



HAL
open science

Bi-functional materials combining energy storage and energy conversion from sunlight

Iryna Sagaidak

► **To cite this version:**

Iryna Sagaidak. Bi-functional materials combining energy storage and energy conversion from sunlight. Other. Université de Picardie Jules Verne, 2019. English. NNT : 2019AMIE0025 . tel-03638202

HAL Id: tel-03638202

<https://theses.hal.science/tel-03638202>

Submitted on 12 Apr 2022

HAL is a multi-disciplinary open access archive for the deposit and dissemination of scientific research documents, whether they are published or not. The documents may come from teaching and research institutions in France or abroad, or from public or private research centers.

L'archive ouverte pluridisciplinaire **HAL**, est destinée au dépôt et à la diffusion de documents scientifiques de niveau recherche, publiés ou non, émanant des établissements d'enseignement et de recherche français ou étrangers, des laboratoires publics ou privés.



Thèse de Doctorat

Mention Chimie
Spécialité Chimie des Solides et Sciences des Matériaux

présentée à l'Ecole Doctorale en Sciences Technologie et Santé (ED 585)

de l'Université de Picardie Jules Verne

par

Iryna SAGAIK

pour obtenir le grade de Docteur de l'Université de Picardie Jules Verne

*Bi-functional materials combining energy storage and
energy conversion from sunlight*

Soutenue le 10 Juillet 2019, après avis des rapporteurs, devant le jury d'examen :

M. E. BAUDRIN, Professeur, UPJV

M. T. DJENIZIAN, Professeur, IMT

M. D. MUÑOZ-ROJAS, Chargé de Recherches CNRS HDR, UGA

M. M. SLIWA, Chargée de Recherches HDR, Ulille

M. F. SAUVAGE, Chargé de Recherches HDR, UPJV

M. A. NGUYEN VAN NHIEN, Professeur, UPJV

Président

Rapporteur

Rapporteur

Examineur

Directeur de thèse

Co-encadrant



To my inner self

Table of Content

General introduction	6
Chapter 1. State of the art on photoelectrochemical energy storage	12
1.1. Solar energy harvesting, conversion, and storage	13
1.1.1. History of photovoltaics	13
1.1.2. Working principles of conventional solar cells and dye-sensitized solar cells	14
1.1.3. Principles of energy storage in electrochemical batteries and capacitors.....	16
1.2. Photorechargeable energy storage devices	18
1.2.1. Devices based on multifunctional charge generation and storage electrode	19
1.2.2. Separate planar sub-devices	21
1.2.2.1. Capacitor storage	22
1.2.2.2. Battery storage	23
1.2.3. Charge generation and storage at the molecular level	30
Conclusions.....	32
References	33
Chapter 2. Evolution of TiO₂ optoelectronic properties upon Li⁺ insertion	38
Introduction	39
2.1. Preliminary work on the photorechargeable anatase TiO ₂ nanoparticles.....	40
2.1.1. Synthesis and characterization of the anatase TiO ₂ nanoparticles.....	40
2.1.2. Formulation of the screen-printable paste and electrode printing procedure	42
2.1.3. Proof-of-concept of quantitative photorechargeable battery electrode based on nanocrystalline anatase TiO ₂ particles	45
2.2. Optical properties of TiO ₂ and Li _x TiO ₂ by UV-visible absorption spectroscopy	49
2.2.1. Absorption spectroscopy and methodology of band gap determination	49
2.2.2. Evolution of TiO ₂ absorption upon lithium insertion	50
2.3. Band edge and charge carrier concentration evolution upon Li ⁺ insertion	56
2.3.1. Mott-Schottky electrochemical impedance spectroscopy theory	56
2.3.2. TiO ₂ flat band potential and charge carrier concentration in different media: aqueous protic and non-aqueous aprotic electrolytes	57
2.3.3. Evolution of the flat band potential and charge carrier concentration upon Li ⁺ insertion into TiO ₂	64

2.4. Photoluminescence spectroscopy basics	68
2.4.1. Steady-state fluorescence of anatase TiO ₂ nanocrystals	69
2.4.2. <i>In situ</i> steady-state fluorescence upon lithiation	71
2.5. Determination of the kinetics of the charge transfer processes in TiO ₂ by TCSPC	75
2.5.1. <i>In situ</i> study of the time-resolved fluorescence of TiO ₂ and Li _{0.6} TiO ₂	76
2.5.2. Kinetics of charge transfer processes in Li _{0.6} TiO ₂ in contact with electrolyte	79
Conclusion.....	82
References.....	84

Chapter 3. Database of optoelectronic properties of common insertion materials and their photoelectrochemistry..... 89

Introduction	90
3.1. Study of transition metal oxides	91
3.1.1. Li ₄ Ti ₅ O ₁₂	91
3.1.2. LiCoO ₂	99
3.1.3. MoO ₃	104
3.1.4. WO ₃	109
3.1.5. CuO	113
3.1.6. Bi ₂ O ₃	117
3.1.7. LiMn ₂ O ₄	122
3.1.8. LiMn _{1/3} Co _{1/3} Ni _{1/3} O ₂	124
3.2. Transition metal sulfides	126
3.2.1. TiS ₂	127
3.2.2. MoS ₂	130
3.2.3. WS ₂	134
3.3. Lithiated polyanions	138
3.3.1. LiFePO ₄	139
3.3.2. LiMnPO ₄	143
3.3.3. LiVPO ₄ F	146
3.4. Fundamental evaluation of the possibility of Li ⁺ photo-insertion / photo-deinsertion reaction	149
3.5. First results on the photoelectrochemistry of chosen insertion materials	151
3.5.1. LiCoO ₂	151
3.5.2. LiFePO ₄	153

3.5.7. $\text{Li}_4\text{Ti}_5\text{O}_{12}$	164
Conclusions	175
References	178
General conclusions	188
Résumé développé de la thèse en Français (Summary in French)	192
Appendix	204
Résumé (Abstract)	208

General introduction

The constant growth of world population along with the enhancement of living standards leads to a continuous increase of the energy demand, forecasted to increase by 30% from current $1.5 \cdot 10^{14}$ kWh/year in the two following decades [1-2]. Around 80% of the currently produced energy is coming from the combustion of fossil fuels, e.g. coal, petroleum and natural gas. However, due to its limited feedstock, its extraction is likely to decline after 2025 [3]. Apart from its limited availability, fossil fuels burning is the main source of carbon dioxide emission into the atmosphere. Counting for 72 % of all the greenhouse gases emitted [4], CO₂ is the main contributor to the climate change with all the threatening consequences of global warming such as sea level elevation, ice melting, more frequent and stronger hurricanes, extreme heat and wildfires, flooding, etc.

Based on numerous scientific reports, the United Nations (UN) framework convention on climate change has been signed in Paris in 2015 by 174 states and the European Union as a political answer to the uprising issues [5]. The agreement stated the aim to keep the maximum of the global temperature rise well below 2°C by tackling the problem of the greenhouse gas emissions. Following shortly after, at the 21st Conference of the Parties to the UN Framework Convention on Climate Change (COP21) the emission-cutting pledges were made by all the 170 countries attending [6]. The adopted strategy of decarbonization is primarily based on the replacement of the fossil fuels by the alternative sustainable and renewable energy sources.

Nowadays, among all the alternative energy sources employed, renewables and nuclear have a 34% share of the total electricity generation [1]. As for the nuclear, even though the CO₂ release in the production cycle is very low (90-140 g of CO₂ per kWh) compared to conventional energy sources (1000-1100 g of CO₂ per kWh for coal), it can hardly be called sustainable because of the finite and toxic nature of the Uranium-235 and the harmful radioactive wastes after nuclear chain reactions. Except for geothermal ($1.3 \cdot 10^{10}$ kWh), most of the renewable energy sources originate directly or indirectly from solar activity. Wind power ($4.9 \cdot 10^{14}$ kWh), bio-energy ($1.1 \cdot 10^{11}$ kWh), hydropower ($1.1 \cdot 10^{12}$ kWh), and marine power ($3.6 \cdot 10^{13}$ kWh) are secondary products of the solar irradiation of the Earth due to the transformation of the solar radiation into thermal heat, photosynthesis, evaporation of the water, and waves respectively (potential energy generation capacities numbers of installed facilities from [7-8]).

The amount of energy produced at the Sun surface is tremendous, ca. $9.5 \cdot 10^{22}$ kWh, as it originates from the hydrogen to the helium gas transformation through the nuclear fusion

reaction. Even taking into account losses due to the back reflections, scattering and absorption in the atmosphere, the energy available for the harvesting at the Earth surface ($1.1 \cdot 10^{18}$ kWh/year assuming 1500 h/year of sunshine) can still easily satisfy the actual yearly energy demand of $1.5 \cdot 10^{14}$ kWh. More than that, the amount of solar energy reaching the earth in one hour ($7.3 \cdot 10^{14}$ kWh) corresponds to the annual energy consumption of the world population.

There are two main reasons explaining why solar is still not the primary energy source despite its credibility. The first is that the light-to-electricity conversion used to be not cost competitive compared to the nuclear or fossil fuels [9], though it has seriously changed over the last years owing to the continuous drop in the cost of silicon-based photovoltaic cells (-86% from 2009 to 2017) in parallel to fossil fuels' price rising (Fig. 1.1) [10]. Nowadays, 50 USD for a megawatt-hour (MWh) of solar energy becomes competitive with the cost of electricity produced from the natural gas (60 USD/MWh) and twice cheaper than that produced from coal (102 USD/MWh). Therefore, even though the introduction of the solar energy still requires substantial financing of new infrastructures and electronic management systems for smart grid implementation, the technology becomes worth the investment in the long-term.

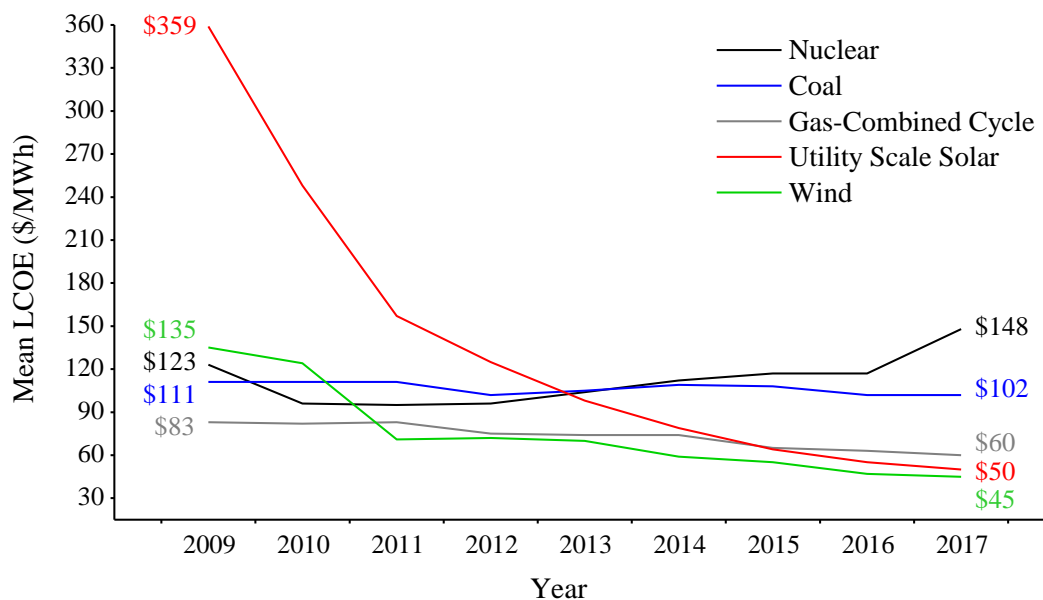


Figure 1.1. Evolution of levelized cost of energy (LCOE) from various sources over time adapted from [10]. Solar mean LCOE values primarily relate to North American alternative energy landscape but reflect broader/global cost declines.

The second issue is more difficult to solve as it concerns the intermittent nature of the solar energy on long time-scale range from second up to day extent (Fig. 1.2). The time-dependent solar energy output and its unpredictability constrains the direct implementation of the photovoltaics as it cannot be produced in a steady and reliable manner to supply society's fluctuating electricity demands at any time. The current application of PV technologies in connection with a grid is possible due to the backup of energy supply from another source (often a stable non-renewable one). It allows to level on time the energy production to the energy demand from customers [11].

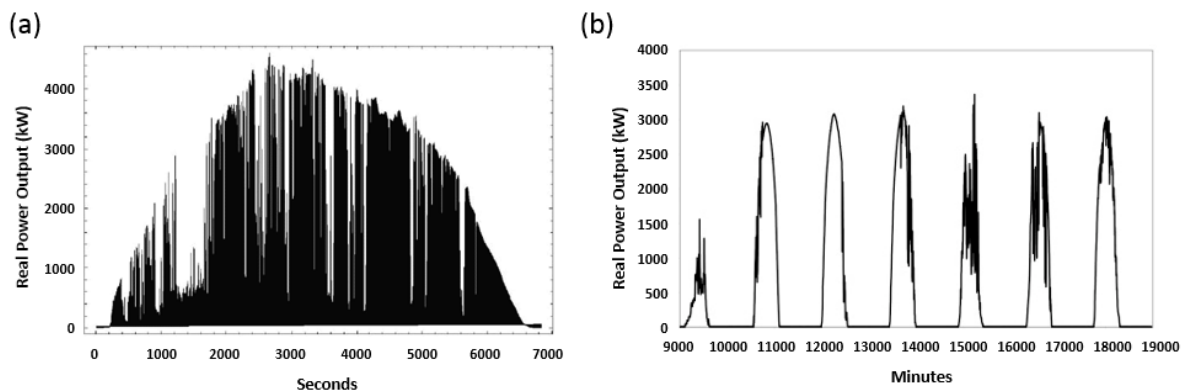


Figure 1.2. Evolution of real power output from a 4.6 MW solar photovoltaic array in Springerville AZ on (a) tenths of seconds over two hours and (b) minutes over a week timescale [12].

For off-grid application, the costly backup energy generation systems, often based on fossil fuels, are required to manage the PV power output disruption [13]. However, constant energy output can be also assured by storage of the excess of energy produced during peak generation or lower demand time for later on-demand supply. The generated energy can be stored chemically (i.e. batteries, capacitors or hydrogen), mechanically (pumped hydroelectric power, compressed air or flywheels), or in thermal systems [14]. Each of these technologies has its application place depending on the employment conditions. However, the most appealing among them is electrochemical storage systems such as batteries due to easy integration, flexibility of storage time, and high versatility from μWh to MWh energy density scale. However, the incorporation of the electrochemical storage part into the PV generation system at least doubles the initial costs, rising up to 28 000 – 33 000 USD for a 5.6 kW PV plant associated with a 3 kW / 6 kWh lithium-ion battery system including installation costs, DC/DC converter/inverter and battery management system [15]. Thus, despite the mature technology,

the cost return time of the installation remains too long (20-30 years) compared to the service lifetime of silicon PV and Li-ion batteries.

With the aim to lower domestic cost of PV installation as well as to prompt new innovation and science streams, the development of a single device combining both energy conversion and storage is highly desirable but also very challenging from a scientific point of view when dealing with the functions gathered at the molecular level. One shorter-term alternative is based on a hybridization of the two technologies. It consists in developing a single device comprising two compartments, one corresponding to PV, such as dye-sensitized solar cell as often proposed, and a lithium-ion battery part sharing a same electrode in common [16]. This approach is potentially less expensive and easier for integration compared to the conventional external coupling. The second approach, inscribed to longer term perspectives, consists in tailoring molecular assembly to combine both sunlight conversion of energy and its chemical storage. This approach was first demonstrated on inorganic materials by Cahen et al. [17] and then Tributsch et al. [18], who highlighted an interfacial light-driven ion transfer in the mixed electronic/ionic semiconductor by making use of the efficient charge separation process within the depletion layer. A direct consequence is that such a mechanism is restricted to the surface, thus representing one important bottleneck of such an approach. To overcome this issue, ca. 5 nm crystalline anatase TiO_2 nanocrystals were synthesized in our group affording to drastically enhance the surface-to-volume ratio [19-20]. As a result, a quantitative photorecharge reaction of the electrode was obtained in ca. 2 hours when exposed to incident standard A.M. 1.5G illumination [21]. This proof-of-concept showed for the first time that the band gap excitation can induce a complete electrode recharge, and paved the way to new scientific and technological direction towards bifunctional materials combining conversion and storage of sunlight power. Nevertheless, further developments call for deepening our current understanding on these photoinduced charge transfer processes in order to maximize the performance in terms of stability and recharge time and developing an appropriate counter-electrode affording a regenerative full photorechargeable Li-ion battery device by collecting free-electron carriers from the photoanode.

One objective of this thesis is to explore what are the optoelectronic properties of most common class of insertion materials which are in discharged or charged states (i.e. lithiated or not) and investigating how these properties are modified during the battery operation (i.e. upon lithium insertion / deinsertion). It has been already discussed in the literature that the potential of intercalated ions can contribute to the electrode free energy causing a shift of the energy band

edges, band gap, and thus affecting the Debye length and interfacial electric field of the space-charge layer [22-23]. With this aim, the second chapter of this thesis is dedicated to describing the results on the in-depth study of the evolution of the optoelectronic properties and dynamics of the ultra-fast charge transfer processes at electrode/electrolyte interface of the anatase TiO₂ upon lithium insertion on the basis of *in situ* / *in operando* experiments using UV-Visible absorption spectroscopy, steady-state and time-resolved fluorescence spectroscopy and Mott-Schottky electrochemical capacitance measurements.

One important obstacle in the development of fully photorechargeable battery system is finding a suitable counter electrode for which optical absorption is complementary to the photoanode, while it has the opposite-type of major carriers and suitable position of conduction and valence bands with respect to the other electrode in order to collect the major carriers. For this reason, the third chapter will describe our work related to the creation of a material database gathering the optoelectronic properties of the most widely used battery electrode materials in order to reveal which materials present potentialities for this application but can also present potentialities for other type of applications such as in the fields of electrochromism or photocatalysis. Three groups of materials are investigated: transition metal oxides (Li₄Ti₅O₁₂, LiCoO₂, MoO₃, WO₃, CuO, Bi₂O₃, LiMn_{1/3}Ni_{1/3}Co_{1/3}O₂), transition metal sulfides (TiS₂, MoS₂, WS₂), and lithiated polyanion structures (LiFePO₄, LiMnPO₄, LiVPO₄F).

References

- [1] International Energy Agency, Key World Energy Statistics, **2017**.
- [2] International Energy Agency, World Energy Outlook, **2017**.
- [3] S. H. Mohr, J. Wang, G. Ellem, J. Ward, and D. Giurco, *Fuel*, **2015**, 141, 120.
- [4] J. G. J. Olivier, K. M. Schure, and J. A. H. W. Peters, *PBL Netherlands Environmental Assessment Agency*, The Hague, **2017**.
- [5] United Nations, United nations framework convention on climate change, **2015**.
- [6] UNFCCC Secretariat, Report of the Conference of the Parties on its twenty-first session, Paris, **2015**.
- [7] World energy council, World Energy Resources, **2016**.
- [8] REN21 Secretariat, Renewables 2017: Global Status Report, Paris, **2017**.

- [9] J. Newman, P. G. Hoertz, C. A. Bonino, and J. A. Trainham, *J. Electrochem. Soc.*, **2012**, 159, 1722–1729.
- [10] LAZARD, Levelized Cost of Energy, **2017**. [Online]. Available: <https://www.lazard.com/perspective/levelized-cost-of-energy-2017/>. [Accessed: 17.04.2019].
- [11] N. S. Lewis, *Science*, **2016**, 351, 6271, 1920.
- [12] J. Apt and A. Curtright, The Spectrum of Power from Utility-Scale Wind Farms and Solar Photovoltaic Arrays, Working Paper CEIC-08-04, Carnegie Mellon Electricity Industry Center, **2008**.
- [13] G. Gowrisankaran, S. S. Reynolds, and M. Samano, *Journal of Political Economy*, **2016**, 124, 4, 1187.
- [14] C. Lupangu and R. C. Bansal, *Renewable and Sustainable Energy Reviews*, **2017**, 73, 950.
- [15] K. Ardani, E. O'Shaughnessy, R. Fu, C. McClurg, J. Huneycutt, and R. Margolis, Installed Cost Benchmarks and Deployment Barriers for Residential Solar Photovoltaics with Energy Storage: Q1 2016, NREL/TP-7A40-67474, 1338670, Dec. **2016**.
- [16] H. Nagai and H. Segawa, *Chem. Comm.*, **2004**, 8, 974.
- [17] G. Hodes, J. Manassen, and D. Cahen, *Nature*, **1976**, 261, 403.
- [18] G. Betz, H. Tributsch, and S. Fiechter, *J. Electrochem. Soc.*, **1984**, 131, 3, 640.
- [19] S. Patra, C. Davoisne, S. Bruyère, H. Bouyanfif, S. Cassaignon, P.-L. Taberna, F. Sauvage, *Part. Part. Syst. Char.* **2013**, 30, 1093.
- [20] S. Patra, C. Davoisne, H. Bouyanfif, D. Foix, and F. Sauvage, *Sci. Rep.*, **2015**, 5, 10928.
- [21] F. Sauvage, C. Andriamiadamanana, C. Laberty, "Dispositif électrochimique autophotorechargeable transparent", EP3075024A1 **2014**.
- [22] H. Tributsch, *Appl. Phys.*, **1980**, 23, 1, 61.
- [23] H. Tributsch, *J. Photochem*, **1985**, 29, 1, 89.

Chapter 1. State of the art on photoelectrochemical energy storage

1.1. Solar energy harvesting, conversion, and storage	13
1.1.1. History of photovoltaics	13
1.1.2. Working principles of conventional solar cells and dye-sensitized solar cells	14
1.1.3. Principles of energy storage in electrochemical batteries and capacitors.....	16
1.2. Photorechargeable energy storage devices.....	18
1.2.1. Devices based on multifunctional charge generation and storage electrode	19
1.2.2. Separate planar sub-devices.....	21
1.2.2.1. Capacitor storage	22
1.2.2.2. Battery storage	23
1.2.3. Charge generation and storage at the molecular level.....	30
Conclusions	32
References	33

1.1. Solar energy harvesting, conversion, and storage

1.1.1. History of photovoltaics

The story of photovoltaics starts back in 1839 when French scientist Edmond Becquerel presented the photoelectric effect to the Academie des Sciences in Paris. In his experiment, generation of a current induced by light action was noticed when illuminating a halogenated metallic electrode connected to a platinum electrode placed in acidic solution [1]. It is only a century later that the first practical photovoltaic cell with worth power conversion efficiency (PCE) of 6 % was developed by Chapin, Fuller, and Pearson based on silicon p-n junction [2]. The discovery of p-n junction has fostered the development of the off-grid energy production devices in the contest of Cold War's spacial programs. Since then, the vast majority of fabricated solar cells are based on either single-crystalline or large grain poly-crystalline silicon. Still nowadays, the PV technology is dominated by p-n silicon hetero-junction technologies with a market share of ca. 90 % owing to the performances, cost and elemental availability as Si is the second most abundant element in Earth. The highest reported PCE value is 26.1% for Si single crystal technology [3] and 26.6% for Si heterostructure [4]. The values are approaching the 32% Shockley-Queisser limit determined for single junction solar cells having a band gap of 1.10 eV (Si) under ASTM G173-03 conditions [5-6].

After the two petrol crisis in the 70's, development of a second generation of solar cells was explored to democratize solar energy to large public using a strategy to reduce modules manufacturing cost with new technologies. This second generation explores thin-film inorganic technologies based on lower cost amorphous or nanocrystalline silicon PV (14.0%) or on polycrystalline chalcogenide III-V and II-VI heterojunction cells, amongst CdTe (22.1%), CuInGaSe (22.9%), and GaAs with a record of 28.9% achieved by Alta Devices (Fig. 1.3) [7-8]. Multi-junctions to panchromatically capture the light through complemental junctions allowed to reach the world record efficiencies of 38.8% using a 5-junction GaInAs/GaInP/GaAs/AlGaInAs/AlGaInP cell under standard A.M.1.5G illumination conditions (100 mW/cm², 1 sun) [9] and as high as 46.0% with a 4-junction solar cell based on GaInP/GaAs//GaInAsP/GaInAs under concentrated sunlight conditions (50.8 W/cm², 500 sun) [10]. Nevertheless, the toxicity of some of these elements, their scarcity and the extremely high production cost of multiple junction modules restrain such technology to laboratories and to spatial applications niche [11].

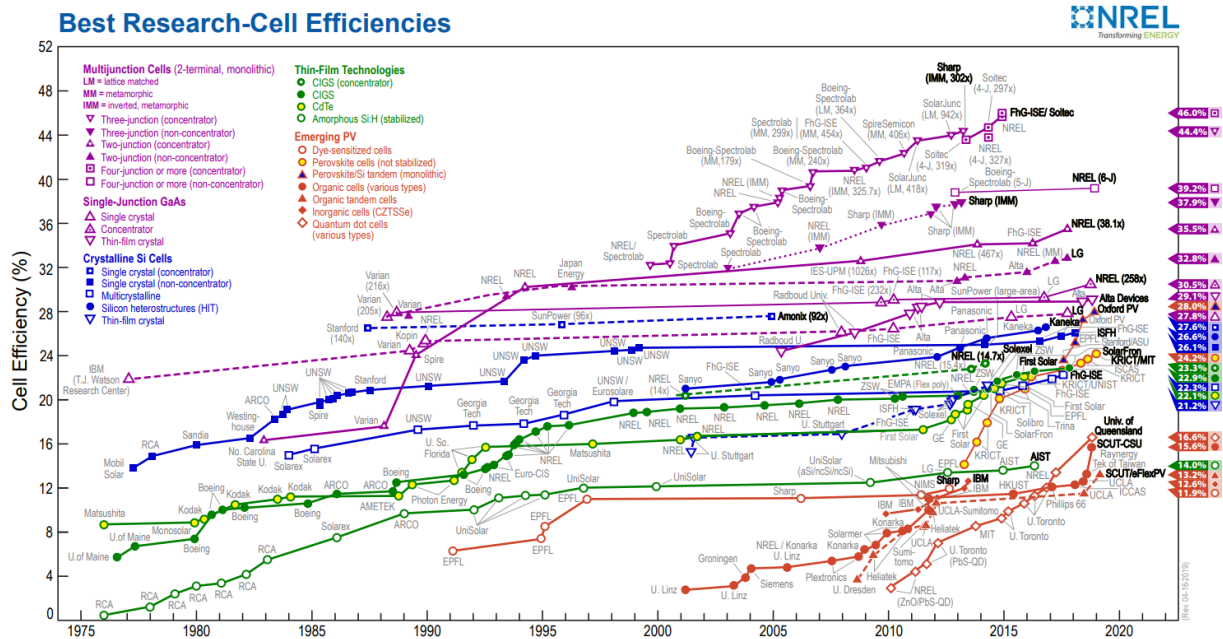


Figure 1.3. Evolution of certified record power conversion efficiencies for existing technologies since 1976 (Data from National Renewable Energy Laboratory from 17.07.2018 [8]).

At the end of the 80's, the development of conducting polymers for organic electronics paved the way towards a third solar cell technology generation which promises low-cost and new market opportunities thanks to roll-to-roll printing processing yielding flexible solar cells. Organic materials also offer an added value with respect to inorganic counterparts owing to their versatility, in particular band gap engineering. This has led to organic photovoltaics (OPV) [12], quantum dots solar cells, which remains inorganic but with the same aim of band gap tunability [13], hybrid organic / inorganic devices such as dye-sensitized solar cells (DSSCs) [14], and more recently halide perovskite solar cells [15]. Among all the above-mentioned technologies, even though not the best performing (PCE = 14.3% [39]), DSSCs stand out as the most mature technology in terms of stability. They also gather advantages in converting very efficiently low diffuse light reaching as high as PCE = 29.3% [40]. In addition, the DSSC technology offers power conversion efficiency independent of external temperature, tunable coloration, bifacial conversion, and semi- to full transparency possibilities.

1.1.2. Working principles of conventional solar cells and dye-sensitized solar cells

Conventional solar cells are based on a p-n junction between either differently doped semiconductor of the same nature (homojunction) or two different types of semiconductor

(heterojunction). When the quantum of light with an energy equal to or greater than the semiconductor's band gap is absorbed, an electron is promoted from the valence band into the conduction band leaving a positively charged hole in the valence band. The formed excitons are diffusing towards the junction. The interfacial electric field is sufficient to dissociate electron-hole pairs, and trigger the transportation of electrons towards the n-type semiconductor and the holes in opposite direction towards the p-type semiconductor [18] (Fig. 1.4). Thus, the p-n junction allows to spatially and energetically separate the excitons while avoiding their recombination, leading to the establishment of a photovoltage which under short-circuit condition drives the carriers towards the external load.

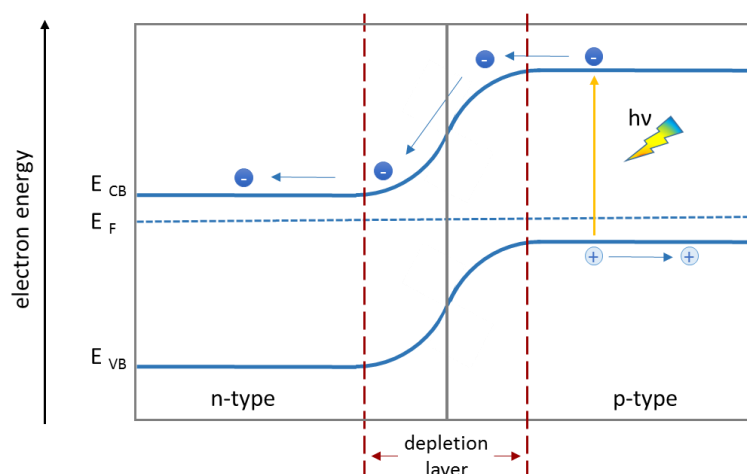


Figure 1.4. Schematic representation of the photoinduced charge separation in the p-n junction.

The working principle of dye-sensitized solar cells has opened a new paradigm in PV field because of (i) the utilization of nanocrystalline particles instead of defect-free single crystals, (ii) a principle relying on electrochemical processes, (iii) no electric field separating the excitons, (iv) separation of charge carrier generation and charge transport processes. The technology is composed of two electrodes, a photoanode and a counter-electrode (CE), separated by a liquid electrolyte containing a redox couple to regenerate the dye (e.g. I_3^-/I^-) (Fig. 1.5) [14]. In the photoanode, light absorption and charge separation take place in the dye molecules, typically based on polypyridyl ruthenium complexes, which are anchored on the wide band gap anatase TiO_2 nanoparticles ($E_g=3.2$ eV). The photogenerated electrons located in the lowest unoccupied molecular orbitals of the dye's (LUMO) are injected from the triplet states of $Ru(+II)$ into the conduction band of TiO_2 . The oxidized dye molecule (S^+) is regenerated by a two-hole transfer process leading to the oxidation of I^- to I_3^- . The free

electrons from TiO_2 are collected and transferred through the back contact towards the counter-electrode to ensure closing the electrochemical loop by reducing I_3^- back to I^- [14, 19].

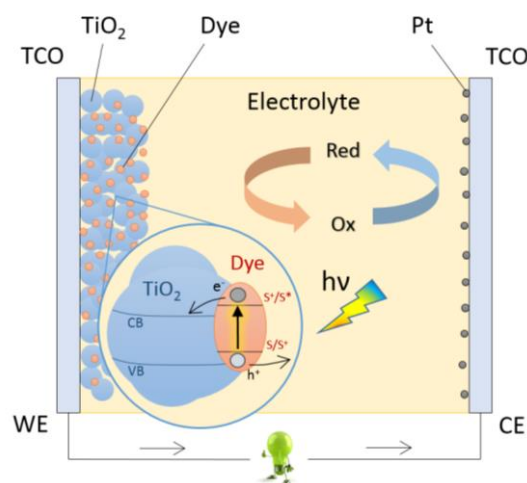


Figure 1.5. Schematic representation of a dye-sensitized solar cell.

1.1.3. Principles of energy storage in electrochemical batteries and capacitors

Electrochemical batteries and capacitors are widely used for nomade applications as a power storage feedstock [20]. The Li-ion battery technology is leading the field owing to higher cell voltage (3.2 - 4.2 V), high energy density (60-200 Wh/kg), low self-discharge (0.03% to 5%), and high stability (>1000 cycles lifespan) [20–22]. The working principle of a battery is based on the conversion of electrical energy stored in a form of a chemical energy by means of redox reactions on transition metal-based electrode materials where the charges are compensated by ion insertion into or deinsertion from the structure. A typical configuration consists of two electrodes, one at high potential (cathode) and one at low potential (anode), separated by a lithium-ion conducting medium (solid or liquid) (Fig. 1.6 (a)). The discharge of the battery is ensured by a release of lithium ions from the negative electrode into the electrolyte with a concomitant lithium insertion into the positive electrode. This leads to a simultaneous transfer of electrons in the same direction via the external circuit. This process can be inverted by imposing an external current such as from the grid to provide the battery recharge.

In supercapacitors, the electrical energy is stored in the form of the surface accumulation of ions [23]. A typical device consists of two conductive high surface-area electrodes separated by an electrolyte solution (Fig. 1.6 (b)). The energy is stored via the Helmholtz double-layer formation at both electrode/electrolyte interfaces by the charge carriers (electrons or holes) from the electrode side and the ions (cations or anions respectively) from electrolyte. This technology

stands out for the high capacitance, fast and reversible charge storage/release function and very high lifespan ($>10^5$ cycles). However, in contrast to electrochemical batteries, supercapacitors offer a high power but a low energy density as showed in the Ragone plot (Fig. 1.7) [24-25].

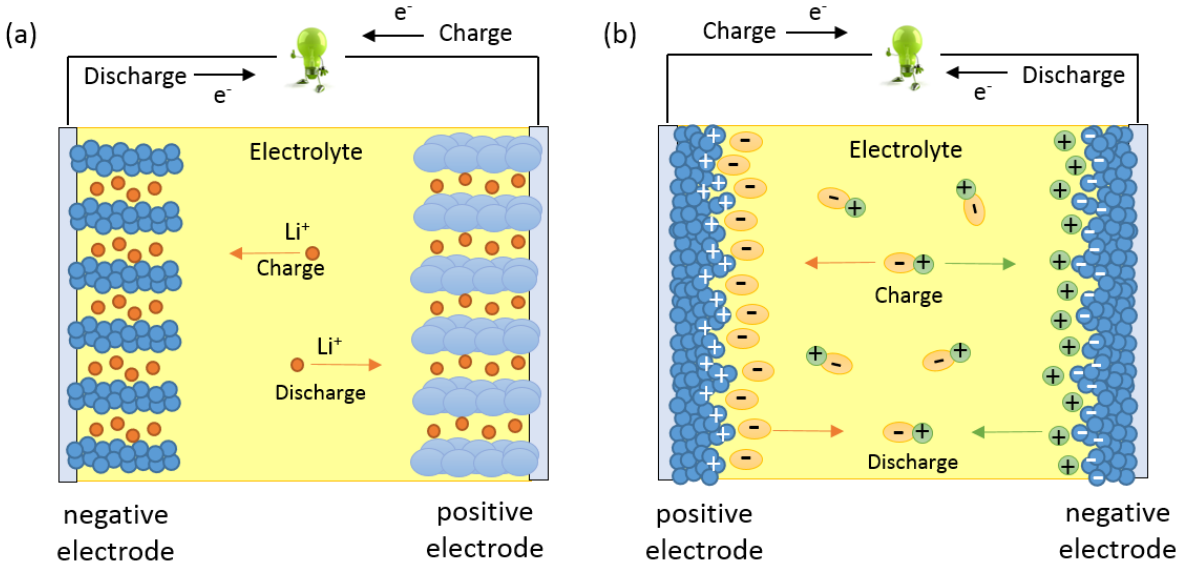


Figure 1.6. Schematic representation of (a) Li-ion battery and (b) an electrochemical supercapacitor.

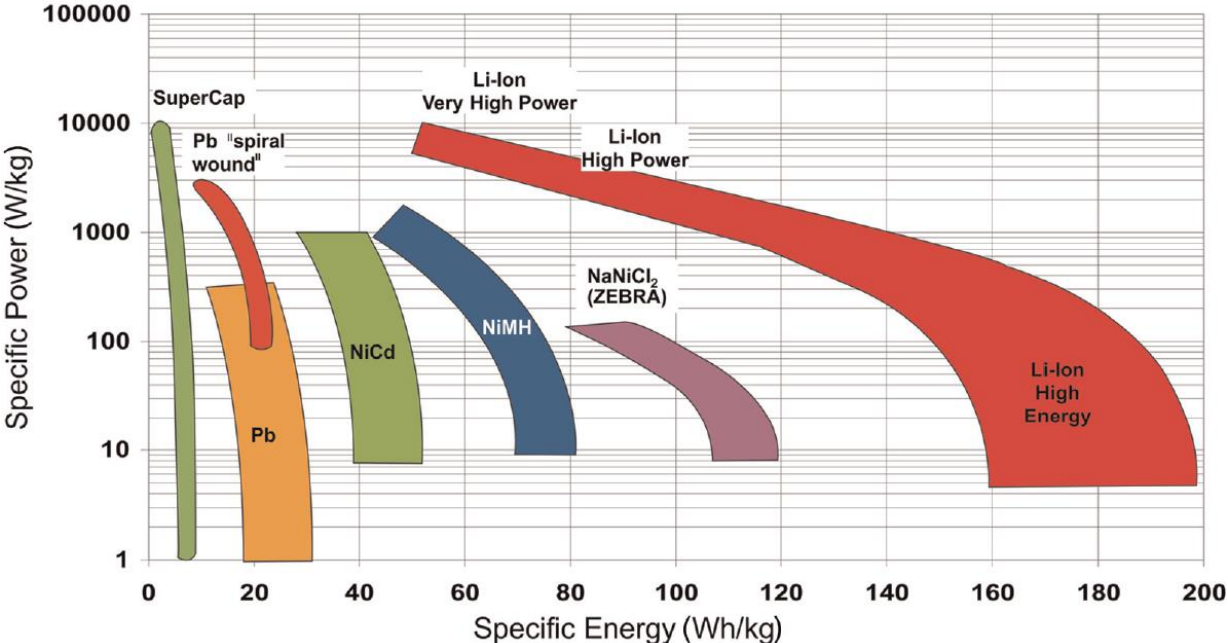


Figure 1.7. Ragone plot for various energy storage devices [25].

1.2. Photorechargeable energy storage devices

As an alternative to the coupling of photovoltaic and energy storage technologies, a range of studies have been carried out aiming at developing a two-in-one solar energy conversion and storage device by means of hybridization of technologies.

Most of such devices reported can be classified into one of the two following sub-groups depending on the engineering of the cell: (i) devices with a multifunctional electrode and (ii) separate planar sub-devices. In the first case, the charge generation material and charge storage material are put in junction forming a multifunctional electrode. The assembly is quite similar to that of a dye-sensitized solar cell (Fig. 1.8 (a)) [26]. Here, charging of the device takes place at the multifunctional electrode at open-circuit condition, and the system is discharged at closed-circuit. In the second case, charge storage and charge separation functions happen at two spatially separated electrodes. Most of these devices are assembled in a three-electrode configuration (Fig. 1.8 (b)) [27]. The photorecharge takes place when the illuminated photoanode is connected to the charge storage electrode. The photogenerated electrons are transferred from the photoanode to the charge storage electrode via the external circuit. The discharge takes place between the charge storage electrode and the internal electrode while leaving the photoanode disconnected.

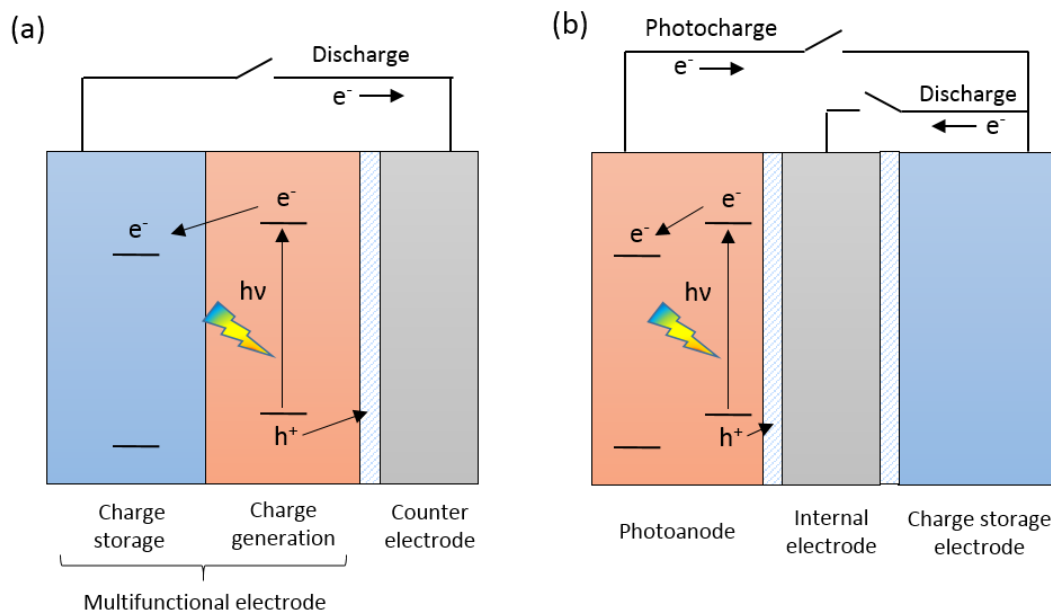


Figure 1.8. Schematic representation of the two configurations proposed for photorechargeable devices based on the use of (a) a multifunctional electrode or (b) spatially separated photoanode and storage electrode.

1.2.1. Devices based on multifunctional charge generation and storage electrode

The first photorechargeable device based on multifunctional electrode was proposed by Miyazaki et al. back in 2000 using TiO₂ and carbon fiber (CF) as energy generation and energy storage materials, respectively [26]. The photorecharge was ensured at the multifunctional electrode at open-circuit condition by means of a charge generation in the anatase TiO₂ particles and its subsequent storage in the carbon fibers leading to the insertion of lithium ions into CFs. The discharge was performed through an external load of 1kΩ at short-circuit condition. The authors reported a rather small discharge capacity of ca. 250 μC/cm² which has been attributed to the low rate of lithiation of the carbon fibers under illumination [28].

The majority of the following devices were assembled accordingly to a dye-sensitized solar cell configuration or at least using a dye-sensitized TiO₂ photoanode to improve light harvesting of the electrode. In 2002, Orel et al. proposed a device including a photoanode composed of two layers: an external layer of nanocrystalline TiO₂ particles sensitized with N3-dye that has a role of carrier generation under illumination and an internal layer of WO₃ nanoparticles that are able to store the electrons throughout lithium insertion in WO₃ (Fig. 1.9) [29]. The intimate contact between these two redox active layers is responsible for self-discharge as mentioned by the authors. This leads to the chemical oxidation of Li_xWO₃ by TiO₂. The device reached an open-circuit voltage of 0.6 V and a discharge capacity of 500 μAh/cm² after 1 hour of photocharging under standard A.M. 1.5G illumination conditions (100 mW/cm²). Later on, Nomiyama et al. proposed a mixture of TiO₂ particles to generate carriers and doped polyaniline (PANI) polymer for a storage function, which is ensured by anions (ClO₄⁻ or SO₄²⁻) transfer from PANI to the electrolyte [30-31]. The authors consider TiO₂/PANI as a promising bifunctional composite because of its good specific capacity between 60 and 120 mAh/g and an energy conversion efficiency over 12% [32]. However, experimentally the overall electricity-to-storage conversion efficiency of the device was reported to be less than 1% owing to the low charge transfer rate between TiO₂ and PANI upon photorecharge. Indeed, the halftime of charge transfer is 10⁻¹ second which is ten times longer than the lifetime of the excited electrons in TiO₂.

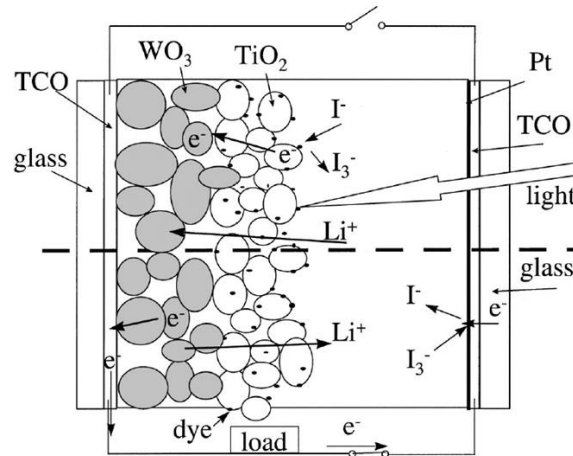


Figure 1.9. Schematic representation of the “photovoltaically self-charging battery” proposed by Orel et al. [29].

In 2013, Nishide et al. proposed an electrode of BODIPY dye (4,4-difluoro-4-bora-3a,4a-diaza-s-indacene) grafted upon anthraquinone (AQ) for charge storage in an aqueous air-battery configuration (Fig. 1.10) [33]. Upon illumination, the photogenerated electrons reduce AQ units to AQ^{2-} with the charge counterbalanced by sodium insertion. The photogenerated holes are oxidizing OH^- ions in the electrolyte leading to the production of O_2 . With a MnO_2 /carbon cathode ensuring the 4-electron reduction of O_2 to OH^- on the other side of the cell, the charge storage capacity reached 166 mAh/g in photorecharge under standard A.M.1.5G illumination and 143 mAh/g for the subsequent discharge with good capacity retention over 50 cycles. Another alternative geometry proposed by Sakurai et al. is based on an air battery configuration composed of $SrTiO_3/LaNi_{3.76}Al_{1.24}$ multifunctional electrode [34]. Photons are absorbed by the perovskite $SrTiO_3$. The photogenerated electrons are transferred to $LaNi_{3.76}Al_{1.24}$ where the energy is stored in a metal hydride form by proton insertion ($LaNi_{3.76}Al_{1.24}H_n$). The holes participate in the oxidation of OH^- species in electrolyte. Platinum catalyst on the other side of the cell is used as a positive electrode to ensure the oxygen reduction. Upon discharge, metal hydride reacts with oxygen generating electric energy and water. After 190 minutes of photorecharge under 100 mW/cm^2 illumination, the device exhibited a discharge capacity of about 950 mAh/g. Discharge and photorecharge can be repeated at least 40 cycles.

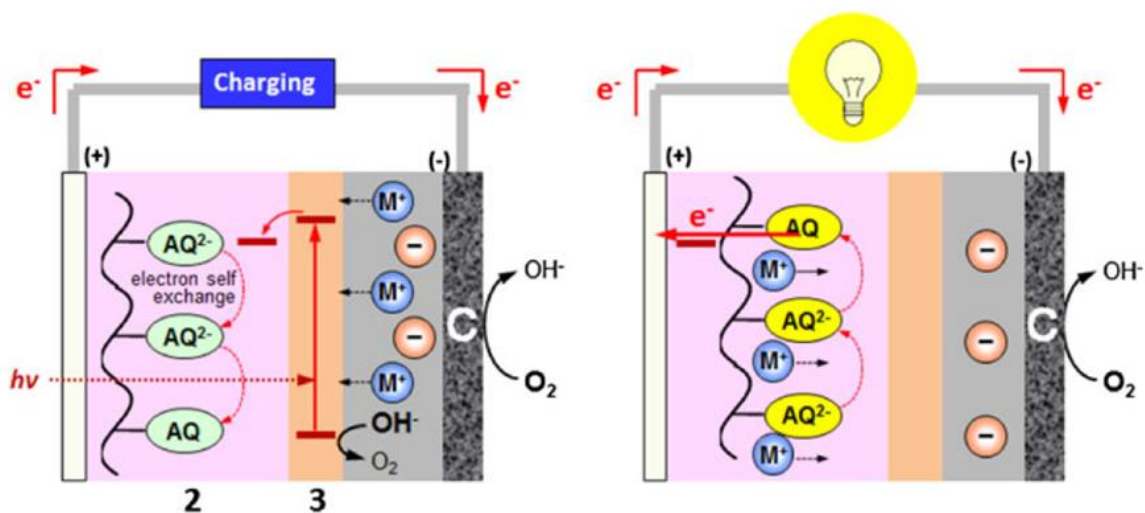


Figure 1.10. Schematic representation of the “organic photorechargeable air battery” proposed by Nishide et al. based on BODIPY-sensitized (3) anthraquinone polymer layers (2) [33].

Finally, Zaghbi et al. recently presented results on N719 dye grafted onto LiFePO_4 electrode [35]. The photorecharge of the electrode was ensured under standard A.M. 1.5G conditions leading to a photorecharge time of ca. 10 hours under O_2 atmosphere and above 100 hours under Ar. The device exhibited 340 mAh/g discharge capacity stable over 15 cycles by combining discharge load and light illumination. The authors suggested that the twice higher capacity than theoretically expected is the result of the two concomitant mechanisms of galvanostatic discharge and photorecharge. Nevertheless, the band alignment and the photorecharge mechanism proposed remain unclear and can be largely debated. This feature will be discussed in more details in Chapter 3.

1.2.2. Separate planar sub-devices

The approach of separate planar sub-devices lies in the presence of two compartments, one photovoltaic (DSSC or OPV) and one for electrochemical storage (battery or capacitor). In most cases, the photoelectrochemical cell is composed of three electrodes. The charge storage electrode alternately plays the role of counter electrode for the photovoltaic compartment and working electrode for the battery part. Below we present these devices dividing them into two sub-groups based on the charge storage type, i.e. capacitor storage or battery storage.

1.2.2.1. Capacitor storage

Most of the photorechargeable devices based on dye-sensitized TiO_2 in combination with capacitive storage electrode are using different forms of carbon. Miyasaka et al. developed an activated carbon (AC) electrode storing energy with a double-layer charge capacitance of 0.69 F/cm^2 using a simple sandwich-type cell architecture (Fig. 1.11) [36]. The device achieved an open circuit voltage of 0.45 V owing to an efficient charge separation ensured by holes scavenging by LiI placed in contact with the photoanode. The photorecharge capacity achieved under standard illumination conditions was $20 \mu\text{Ah/cm}^2$, thus representing 8.0 C/g of activated carbon. This number is 15 times greater than the one obtained with LiI-free photocapacitor. However, the performance was limited by the formation of a Schottky barrier at $\text{TiO}_2/\text{carbon}$ interface which penalizes fast electron transfer from TiO_2 to carbon upon discharge. To overcome this issue, the authors proposed a three-electrode configuration by introducing an internal Pt electrode. By minimizing the inner resistance, they reached 0.8 V open circuit photovoltage and a discharge capacity as high as $130 \mu\text{Ah/cm}^2$ [37-38]. No cyclability data are reported.

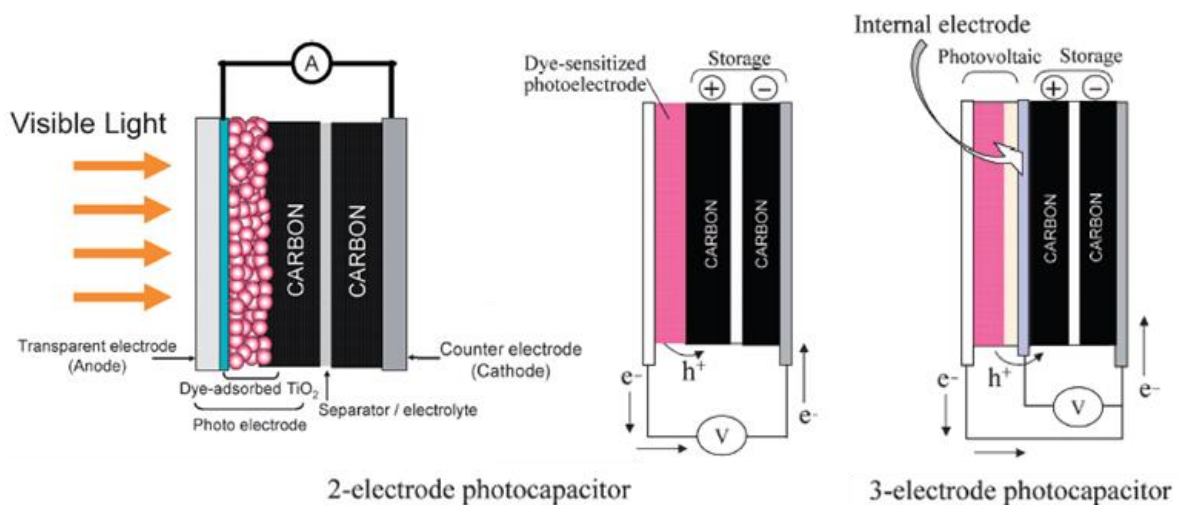


Figure 1.11. Schematic representation of the “carbon-incorporated photocapacitor” proposed by Miyasaka et al. in a two- and three-electrode configuration [38].

The carbon nanotubes (CNT) are known to have a good specific capacitance (54 F/g) and an excellent electrochemical stability [39]. When incorporated into a photorechargeable electrochemical device, it led to the highest solar-to-storage conversion efficiency, corresponding to the overall device efficiency achieved up to date. They reported a value of 5.12% , where a capacitance of 48 F/g was obtained under 100 mW/cm^2 irradiation [40]. The

discharge capacity of $1.36 \mu\text{Ah}/\text{cm}^2$ was maintained over 100 cycles. The incorporation of PANI into CNT electrode increased the electrode's capacitance to $208 \text{ F}/\text{g}$. However, it caused a decrease in the storage capacity from 84% to 70% resulting in a drop of overall device efficiency down to 4.29%. After photorecharge, a discharge capacity of $56 \mu\text{Ah}/\text{cm}^2$ was reached, for which a capacity retention of 80% was obtained after 100 cycles. The combination of poly(3,4-ethylenedioxythiophene) (PEDOT) with the multi-walled carbon nanotubes has also increased the initial capacitance of CNT electrode to $95 \text{ F}/\text{g}$, which corresponds to an energy density of $3.15 \text{ mWh}/\text{g}$ [41]. The authors assign this improvement to originate from a lowering in internal resistance of high surface area and high conductivity PEDOT. When employed alone, PEDOT reached $0.52 \text{ F}/\text{cm}^2$ storage capacity under standard irradiation [42]. However, note that authors have used different units (F/cm^2 vs F/g) which in absence of some information related to the size and loading of the electrode impede a direct comparison between the numbers. Both CNTs and PANI have also been incorporated in combination with dye-sensitized TiO_2 into so-called "energy-fibers" for smart textiles. The device exhibits rather limited performances of up to $3.32 \text{ mF}/\text{cm}^2$ under $100 \text{ mW}/\text{cm}^2$ irradiation [43-44] and $20 \text{ mF}/\text{cm}^2$ under $65 \text{ mW}/\text{cm}^2$ irradiation [45]. Bae et al. presented a single fiber-based device including ZnO nanowires and graphene as principal energy conversion and storage materials. The electrode reaches a storage capacitance of $0.4 \text{ mF}/\text{cm}^2$ after photorecharge under standard A.M. 1.5G conditions [46]. The nanocomposite of PVDF and ZnO nanowires as a capacitive energy storage material in combination with N719-sensitized TiO_2 exhibited $59.4 \text{ mAh}/\text{g}$ storage capacity achieving 3.70% overall device efficiency under standard conditions [47].

Finally, single-walled carbon nanotubes were also incorporated into an OPV device based on P3HT:PCBM (poly(3-hexylthiophene):1-(3-methoxycarbonyl)propyl-1-phenyl[6,6] C_{61}).

This assembly yielded a specific capacitance of $28 \text{ F}/\text{g}$ after 70 seconds of illumination under $100 \text{ mW}/\text{cm}^2$ and 3.39% overall device conversion efficiency [48]. However, only 47% of initial discharge capacity of $4.9 \text{ mAh}/\text{g}$ was maintained after 10 cycles. Using two OPV in series allowed reaching $79.8 \text{ F}/\text{g}$ storage capacity while exhibiting a higher power density of $10 \text{ W}/\text{g}$ and energy density of $5 \text{ mWh}/\text{g}$.

1.2.2.2. Battery storage

A range of other inorganic and organic materials has been used for developing photoelectrochemical devices including a battery. A surface-oxidized tungsten oxide in

combination with a classical DSSC part reached $141 \mu\text{Ah}/\text{cm}^2$ discharge capacity with 0.4 V discharge output voltage after 10 hours of photorecharge under standard illumination conditions (A.M. 1.5G) [49]. Zhao et al. presented a similar device based on nanoparticles of WO_3 and Z907-sensitized TiO_2 which reached 40.6 mAh/g ($24.4 \mu\text{Ah}/\text{cm}^2$) discharge capacity after a photorecharge under $7.5 \text{ mW}/\text{cm}^2$ irradiation during 10 minutes [50]. In the following cycle, the discharge capacity dropped to 34 mAh/g and was further maintained during 4 cycles only. The authors ascribed this capacity loss to the possible reduction of WO_3 to W and side reactions with the electrolyte leading to a SEI formation. Gao et al. presented a photorechargeable battery based on WO_3 -coated carbon nanotubes with a TiN nanotube arrays on Ti mesh as an electrocatalytic electrode for I_3^- to I^- reduction (Fig. 1.12 (a)) [51]. After 30 minutes of photorecharge under $100 \text{ mW}/\text{cm}^2$, the open circuit voltage of the complete device reached 0.7 V and yielded a discharge capacity of $139 \mu\text{Ah}/\text{cm}^2$. In the following cycle, the discharge capacity dropped to $124 \mu\text{Ah}/\text{cm}^2$ (11% loss) and remained stable over 10 cycles. In contrast to the above described three-electrode systems, Jiang et al. presented a photorechargeable device based on tungsten oxide hydrate in a two-electrode assembly [52]. The nano- $\text{WO}_3 \cdot \text{H}_2\text{O}/\text{CNTs}/\text{PVDF}$ composite electrode was combined with N719-sensitized TiO_2 photoanode providing a discharge capacity of $383 \mu\text{Ah}/\text{cm}^2$ after 10 minutes of photorecharge under $100 \text{ mW}/\text{cm}^2$ irradiation. The overall device efficiency was 2.12 %.

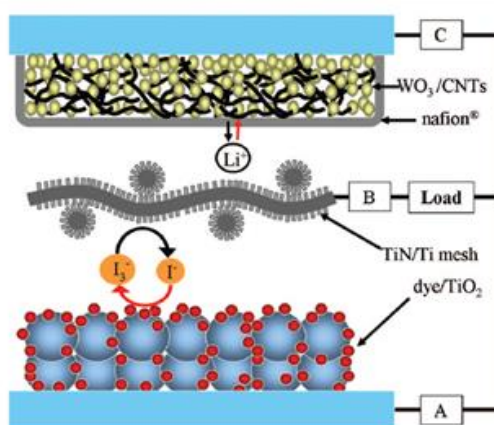


Figure 1.12. Schematic representation of the “solar storable rechargeable air battery” proposed by Gao et al. [51].

An advanced architecture has been proposed by Wang et al. to improve charge collection and lower internal charge transfer resistances. This consists of an intermediate double-sided TiO_2 nanotube array electrode, one side of which is a photoanode of a dye-sensitized solar cell for

charge generation and the other is a charge storage electrode combined with the LiCoO_2 positive electrode in the battery compartment (Fig. 1.13 (a)) [53]. In order to provide high enough photovoltage for the battery recharge, the authors integrated three series-connected tandem N719-N749 DSSCs to afford above 2 V generation under illumination (Fig. 1.13 (b)). Photorecharging power pack under standard illumination for 440 seconds resulted in the voltage rise up to 3 V and a consequent discharge capacity of 33.9 μAh . The entire conversion efficiency of the device was limited to $\sim 0.82\%$, which authors assign to the growing inner resistance of the cell over the operational time.

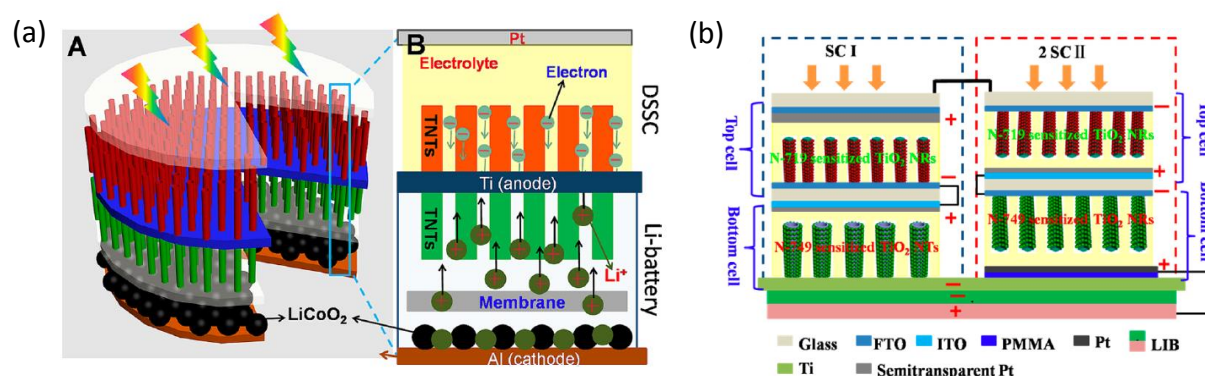


Figure 1.13. Schematic representation of (a) two-compartment photorechargeable device based on double-sided TiO_2 nanotube arrays proposed by Wang et al. and its modification with the three tandem DSSCs integrated in the photovoltaic compartment [53].

A set of organic materials have also been proposed in photorechargeable systems for ensuring the energy storage function. Segawa et al. were first to present the polypyrrole (PPy) as a charge storage electrode in a three-electrode cell [27, 54]. Here, the storage of photogenerated energy is performed by deinsertion of ClO_4^- from the PPy structure. A maximum discharge capacity of 0.5 $\mu\text{Ah}/\text{cm}^2$ was achieved after 30 minutes of photorecharge under standard A.M. 1.5G conditions. This capacity, although low compared to the inorganic counterparts, remained stable over 10 cycles. An overall device energy conversion efficiency of 0.5 to 1% was reported. Gao et al. improved this concept by introducing PEDOT polymer into the DSSC compartment to ensure the dye regeneration by hole trapping and forming $\text{PEDOT}^+\text{ClO}_4^-$ with the anions from the electrolyte (Fig. 1.14) [55]. This photoelectrochemical cell reached 0.76 V open-circuit voltage under standard light conditions. The subsequent discharge capacity was 8.3 mAh/g and a negligible capacity fade of less than 4 % was experienced over 10 cycles. The authors ascribed the limited performances of the device, i.e. solar-to-storage conversion

efficiency of $\sim 0.1\%$, to the low power conversion efficiency (PCE = 0.5%) of the $\text{TiO}_2/\text{PEDOT}$ anode.

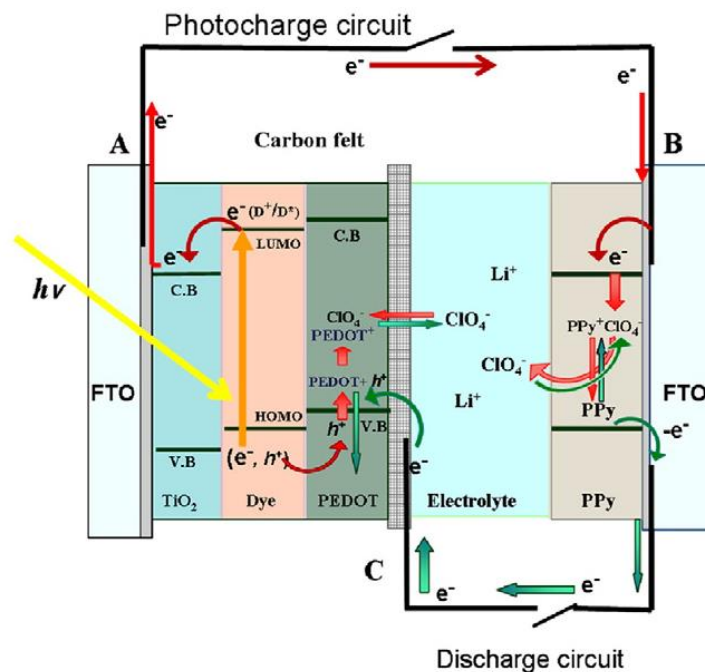


Figure 1.14. Schematic representation of the “photorechargeable battery based on polymeric charge storage electrodes” proposed by Gao et al. [55].

Nishide et al. presented a similar three-electrode device with the integrated polyviologen poly(tripyridiniomesitylene tribromide) (PTPM) storing the photogenerated electrons by means of electrolytic and reductive polymerization [56]. The authors replaced the traditional I_3^-/I^- redox mediator of the DSSC with an aqueous electrolyte containing $\text{TEMPOL}^+/\text{TEMPOL}$ (1-oxyl-2,2,6,6-tetramethyl-4-hydroxypiperidine) redox couple. The cell exhibited a discharge capacity of $0.02 \mu\text{Ah}$ with a constant output voltage of around 0.4 V.

The approach of combining dye-sensitized solar cells with battery has also been extended to redox-flow batteries. The first solar redox flow battery was reported by Gao et al., where an analyte containing Li_2WO_4 particles in aqueous electrolyte performed the faradaic storage function (Fig. 1.15) [57]. Upon illumination, the photogenerated electrons produced in the dye-sensitized TiO_2 particles are used for Li^+ insertion into Li_2WO_4 leading to their reduced form $\text{Li}_{2+x}\text{WO}_4$. The subsequent discharge takes place between the $\text{Li}_{2+x}\text{WO}_4$ particles in the anolyte and LiI species in the catholyte. Lithium transfer between the two compartments is ensured by an intermediate solid conducting LISICON membrane. The authors reported a discharge capacity of $15.1 \mu\text{Ah/mL}$ after a photorecharge under 100 mW/cm^2 irradiation. The device

showed stability over 10 cycles for an optimized current density of $75 \mu\text{A}/\text{cm}^2$. Another photoelectrochemical redox flow battery based on $[\text{Fe}(\text{C}_{10}\text{H}_{15})_2]^+/\text{Fe}(\text{C}_{10}\text{H}_{15})_2$ ferrocene derivatives was introduced by Yang et al. [58]. The authors achieved $53.3 \mu\text{Ah}/\text{mL}$ discharge capacity after a photorecharge of 40 minutes under $40 \text{ mW}/\text{cm}^2$ illumination. A range of other redox couples for solar redox battery have been explored by Madden et al. such as methyl viologen $\text{MV}^{2+}/\text{MV}^+$, $\text{S}_4^{2-}/\text{S}_2^{2-}$, $\text{Cr}^{3+}/\text{Cr}^{2+}$, Fe^{2+}/Fe , and $\text{V}^{3+}/\text{V}^{2+}$ [59]. The integration of polysulfide redox species with N719-sensitized TiO_2 led to a discharge capacity of $240 \mu\text{Ah}/\text{cm}^2$ with a remarkably flat discharge voltage of 0.7 V. However, the authors underline important capacity losses upon cycling, i.e. 20 % loss after three cycles, which according to the authors call for the need to improve electrolyte, dye, and electrode/electrolyte interface stability.

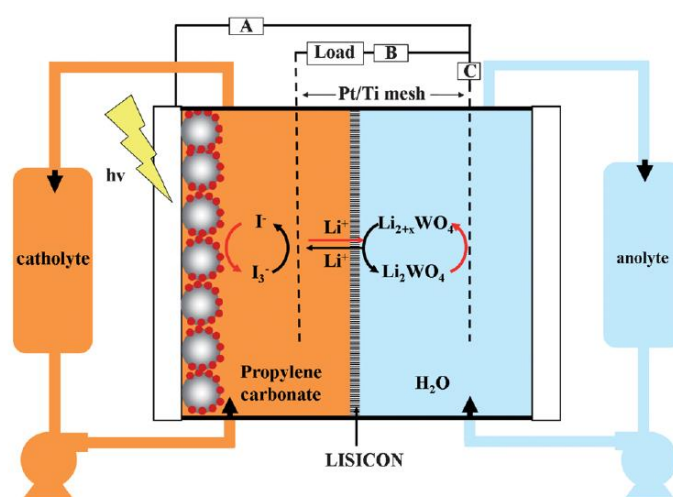


Figure 1.15. Schematic representation of a “solar rechargeable redox flow battery” proposed by Gao et al. [57].

A few studies presented photoelectrochemical devices based on different light harvesting materials and redox couples. Combination of WO_3 -decorated BiVO_4 photoanode and aqueous I_3^-/I^- and $\text{Br}_3^-/\text{Br}^-$ redox couples as catholyte and anolyte respectively resulted in $250 \mu\text{Ah}$ discharge capacity after first photorecharge and 0.4 V output voltage stable over 20 cycles [60]. The overall device efficiency reached 1.25%, however without any precision on the type of light and the power used, thus making the direct comparison with the other device architectures impossible. Utilization of other combinations between absorbers and redox couples have also been presented, i.e. CdS associated to $\text{V}^{3+}/\text{V}^{2+}$ [61] and $\alpha\text{-Fe}_2\text{O}_3$ associated to $\text{Fe}(\text{CN})_6^{3-}/\text{Fe}(\text{CN})_6^{4-}$ [62], however without any further details about overall device performance, discharge capacities, and experimental conditions.

Finally, more advanced designs integrating multiple light absorbers have been presented using two photoelectrodes [63–65]. Probably the most interesting is the device based on Ta_3N_5 photoanode and GaN/Si photocathode (Fig. 1.16), providing the highest up-to-date device photovoltage of 1.5 V [63]. This high voltage allows to operate a 1.2 V alkaline anthraquinone/ferrocyanide redox battery with a 3.0% solar-to-storage conversion efficiency under standard light conditions (A.M. 1.5G). The discharge capacity reached 200 $\mu\text{Ah/mL}$, even though this latter is limited by the catholyte degradation.

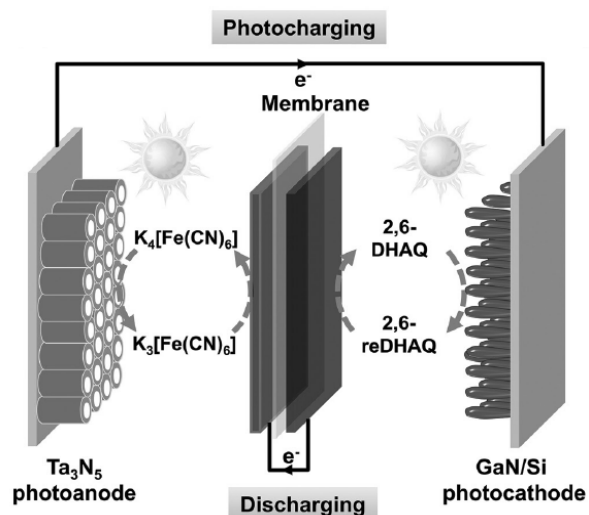


Figure 1.16. Schematic representation of a “solar rechargeable redox battery” proposed by Wang et al. [63].

Jin et al. presented a photorechargeable redox flow battery composed of regenerative silicon solar cell in association with 9,10-anthraquinone-2,7-disulfonic acid (AQDS) and 1,2-benzoquinone-3,5-disulfonic acid (BQDS) based redox couples as catholyte and anolyte, respectively [64]. After a photorecharge under 100 mW/cm^2 during 7.3 hours, the device reached an excellent discharge capacity of 3.5 mAh/mL leading to a solar-to-storage efficiency of 1.7%. Silicon absorber and AQDS-based catholyte have also been studied in combination with $\text{Br}_3^-/\text{Br}^-$ redox couple based anolyte [65]. After a photorecharge under A.M. 1.5G illumination conditions, the battery reached a discharge capacity values of up to 730 $\mu\text{Ah/mL}$ and 0.78 V stable output voltage with a 3.2% solar-to-storage conversion efficiency.

The main characteristics and performances of all above-discussed photoelectrochemical storage devices are gathered in Table 1.1.

Table 1.1. Overview of photorechargeable electric energy storage systems including the overall device discharge performance characteristics and solar-to-storage efficiencies when available.

	Conversion	Storage	Discharge performance	Light power	Solar-to-storage efficiency	Ref.	
Multifunctional electrode	Dye-sensitized TiO ₂	Carbon fibers	Ohmic load discharge	n/a	n/a	[28-28]	
		WO ₃	500 μAh/cm ²	100 mW/cm ²	n/a	[29]	
		PANI	n/a	n/a	<1%	[31]	
	BODIPY-dye	AQ ²⁻ /AQ	143 mAh/g; 0.63 V	100 mW/cm ²	n/a	[33]	
	SrTiO ₃	LaNi _{3.75} Al _{1.24} H _n	950 mAh/g	100 mW/cm ²	n/a	[34]	
	N719-dye	LiFePO ₄	340 mAh/g	100 mW/cm ²	0.06-0.08%	[35]	
Separate planar sub-devices	Dye-sensitized TiO ₂	Activated carbon	130 μAh/cm ² ; 47 mWh/cm ²	100 mW/cm ²	n/a	[36, 38]	
		CNTs	48 F/g; 1.36 μAh/cm ²	100 mW/cm ²	5.12%	[40]	
			0.024 mF/cm ²	100 mWh/cm ²	1.50%	[43]	
			3.32mFcm ²	0.27 mW/cm ²	1.83%	[44]	
	Capacitor storage	CNTs + PANI	208 F/g; 1.36 μAh/cm ²	100 mW/cm ²	4.29%	[40]	
		CNTs + PEDOT	95 F/g; 3.147 mWh/g	100 mW/cm ²	n/a	[41]	
		PANI	20 mF/cm ²	65 mW/cm ²	2.1%	[45]	
		PEDOT	0.52 F/cm ²	100 mW/cm ²	4.37%	[42]	
		PVDF/ZnO	59.4 mAh/g	100 mW/cm ²	3.70%	[47]	
		ZnO NWs	ZnO/graphene	0.4 mF/cm ²	100 mW/cm ²	n/a	[46]
	P3HT:PCBM	CNTs	28 F/g; 0.5 mAh/g	100 mW/cm ²	3.39%	[48]	
	Dye-sensitized TiO ₂	WO ₃	141 μAh/cm ² ; 0.4 V	100 mW/cm ²	n/a	[49]	
			24.4 μAh/cm ²	7.5 mW/cm ²	n/a	[50]	
			0.139 mAh/cm ²	100 mW/cm ²	n/a	[51]	
			385 μAh/cm ²	100 mW/cm ²	2.12%	[52]	
			33.89 μAh	100 mW/cm ²	0.82%	[53]	
		Battery storage	Polypyrrole	0.5 μAh/cm ²	100 mW/cm ²	0.5-1%	[27]
				8.3 mAh/g	100 mW/cm ²	0.10%	[55]
			Polyviologen	0.02 μAh; 0.4 V	>10 mW/cm ²	n/a	[56]
			Li _{2+x} WO ₄ /Li ₂ WO ₄ + I ₃ ⁻ /I ⁻	0.0195 mAh/mL	100 mW/cm ²	n/a	[57]
[Fe(C ₁₀ H ₁₅) ₂] ⁺ /Fe(C ₁₀ H ₁₅) ₂ + I ₃ ⁻ /I ⁻			53.3 mAh/L	40 mW/cm ²	n/a	[58]	
S ₄ ²⁻ /S ₂ ²⁻ + I ₃ ⁻ /I ⁻	240 μWh/cm ² ; 0.7 V	77 mW/cm ²	n/a	[59]			
BiVO ₄	I ₃ ⁻ /I ⁻ + Br ₃ ⁻ /Br ⁻	0.25 mAh; 0.4 V	n/a	1.25%	[60]		

CdS	$V^{3+}/V^{2+} + V^{3+}/VO^{2+}$	n/a	100 mW/cm ²	n/a	[61]
$\alpha\text{-Fe}_2\text{O}_3$	AQDS/AQDSNa ₂ + Fe(CN) ₆ ³⁻ /Fe(CN) ₆ ⁴⁻	n/a	n/a	0.05–0.08%	[62]
Ta ₃ N ₅ + GaN/Si	Anthraquinone + ferrocyanide	200 mAh/L; 1.0 V	100 mW/cm ²	3.00%	[63]
p ⁺ nn ⁺ -Si + n ⁺ np ⁺ -Si	AQDS/AQDSH ₂ + BQDS/BQDSH ₂	3.5 Ah/L; 0.41 V	100 mW/cm ²	1.7%	[64]
n ⁺ p-Si + p ⁺ n-Si	AQDS/AQDSH ₂ + Br ₃ ⁻ /Br ⁻	730 mAh/L	100 mW/cm ²	3.2%	[65]

1.2.3. Charge generation and storage at the molecular level

One longer-term approach to overcome the solar intermittency issue is the development of materials capable of both energy storage and energy conversion at a molecular level. Both organic and inorganic materials have been considered for this application.

The only functional energy harvesting and storage device based on the organic molecule was presented by Samuel et al. inspired by a homojunction OPV cell (Fig. 1.17) [66]. The bi-functional cyanine dendrimer is sandwiched between a hole transporting polymer based on PEDOT/PSS and an aluminum plate to collect the free carriers. Upon light excitation, the electron is trapped in the central indoline unit triggering the movement of I⁻ or PF₆⁻ across the cyanine to the second indoline. This process is reversible. Even though the performances are modest (0.003 $\mu\text{Ah}/\text{cm}^2$), likely because of the low light capture and short lifetime of the charge separation, this work stands for the first proof-of-concept of a photorechargeable device based on molecular energy conversion and storage in an organic molecule.

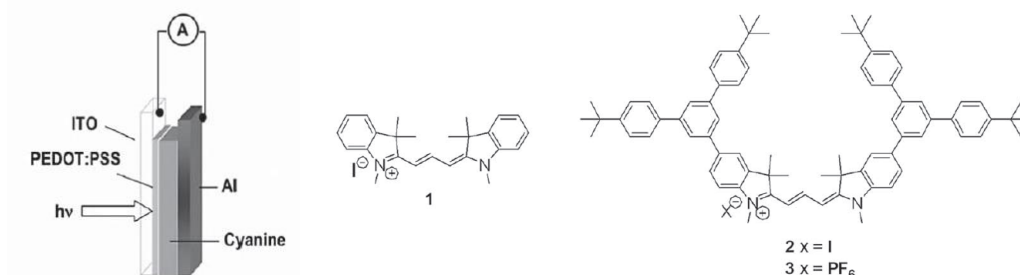


Figure 1.17. Cell configuration and bifunctional organic cyanine dendrimer performing light conversion and charge storage at molecular level proposed by Samuel et al. [66].

The second approach addressed bi-functional inorganic materials and started back in the 80's by Gerischer et al., who extended the fundamental knowledge of the semiconductor/electrolyte

interface and the theory on photoinduced ion transfer reactions through the interface [67–69]. In the same period of time, Cahen et al. were also working in similar direction and reported the first photoelectrochemical system capable of conversion and storage of solar energy based on CdSe electrode, where the partial reversible substitution of Se with S from electrolyte takes place under illumination [70]. A few years later Tributsch et al. experimentally proved the possibility of the light-driven intercalation reactions in p-type layered compounds (ZrS_2 and $ZrSe_2$) and discussed the theoretical prediction of the photoinduced ion deinsertion from the n-type Hf dichalcogenides for simultaneous energy conversion and storage [71], which was experimentally demonstrated a couple of years later [72-73]. However, the main drawback of transition metal dichalcogenides was the too low quantum efficiencies and a quasi-metallic behavior leading to a loss of the photo-effect. Tributsch et al. considered the possibility of using a typical for batteries Li^+ ion for photo-insertion but abandoned the idea because of lithium's low ionization energy and too high electropositivity for the practical use [74]. Therefore, they focused on the Cu^+ insertion systems that are compatible with a copper metal counter-electrode. The most promising performances were achieved on $Cu_{6-x}PS_5I$ [75] and Cu_3PS_4 [74] p-type semiconductors, where Cu^{2+} ion insertion into structure was triggered by homogeneous electron transfer to the transition metal. With similar approach, Tributsch et al. reported a successful proton deinsertion from the n-type $H_xTiO_2(B)$ by the action photogenerated holes oxidizing Ti^{3+} to Ti^{4+} [76]. However, focusing almost exclusively on the photoinduced phenomenon, the storage capability of these systems has been relatively undertreated.

The principle of the photoinduced insertion/deinsertion reaction lies in the effective charge separation in the depletion layer of the semiconductor [68-69]. When a semiconductor electrode is immersed in the electrolyte, the equalization of the Fermi levels between the semiconductor and the electrolyte (chemical potential) takes place (Fig. 1.18). It results in the space charge depletion of the minority charge carriers and bending of semiconductor band edges at the surface. When the light is absorbed in the depletion layer, the photogenerated charges are effectively separated due to the migration of the main charge carriers into the bulk of semiconductor and the minor charge carriers towards the surface. In absence of a suitable redox mediator in the electrolyte, the minor charge carriers accumulate at the semiconductor surface, trigger redox reaction with the transition metal and interfacial ion transfer for charge compensation.

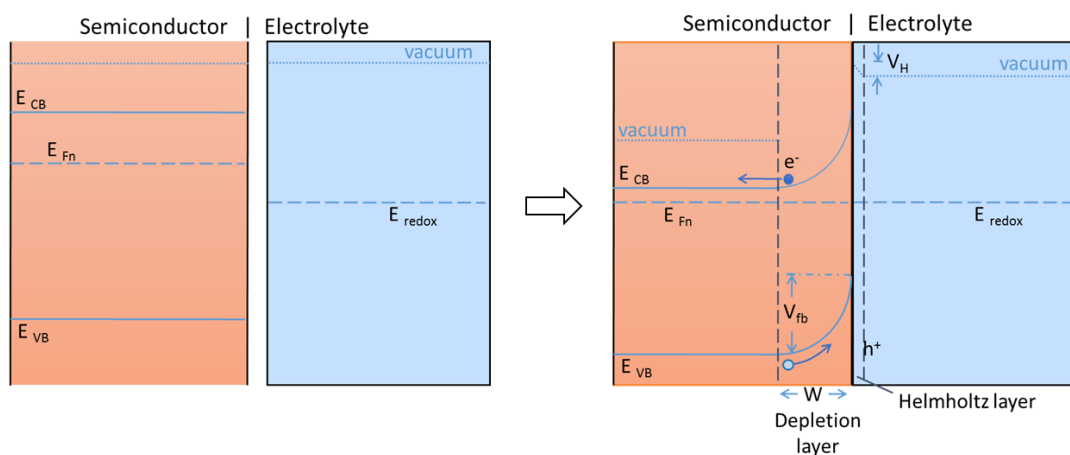


Figure 1.18. Schematic representation of the band bending at the semiconductor/electrolyte interface for an electrolyte containing a redox mediator.

Unfortunately, so far, the interfacial light-driven ion transfer in mixed electronic/ionic semiconductor is only an extreme surface reaction limited to the Debye length (space charge layer width). This was confirmed by Hirakawa et al. on the CuFeTe_2 -based electrode, in which the storage capability was only 0.562 mWh/g, thus representing less than 1% of the theoretical energy density (60 mWh/g) [77].

Conclusions

In this chapter, we presented the evolution of the solar cells development since the discovery of the photo-effect until today. We introduced the principles of the electrochemical energy storage devices, i.e. batteries and capacitors, commonly used to store energy. The concept of combining the two functions to solve solar intermittency or to prolong battery capacity for nomad applications has been reviewed. We presented them into two groups depending on the approach, namely hybridization of two technologies in one device or development of bi-functional materials capable of combining energy conversion and its storage at molecular level.

The main advantage of the solar-to-chemical conversion and storage systems based on hybridization lies in the use of the third generation PV benefiting from the ease of its integration with the storage counterpart and the potential overall cost reduction. Nevertheless, the devices developed so far are highly limited in terms of performances (maximum 1.0 V output voltage and the overall device efficiency of 5.12%) and stability. One of the reasons is that up to now focus has been on the development of the prototypes and hardly any on the optimization of the

system, which often resulted in poorly matched conversion and storage parts leading to inefficient electron transfer. In addition, the issue of battery self-discharge when the PV part is exposed to lower light illumination has never been tackled. One complication in analyzing the publications on photorechargeable devices arises from the different sources of illumination and the different units used to report the performances.

The longer-term and more fundamental second approach to overcome the solar intermittency is based on combining charge generation and charge storage functions as a result of light-induced charge separation within the depletion layer and ion-transfer reaction in a mixed ionic/electronic conductor. Such materials open up new scientific and technological directions that can potentially close the gap between PV and batteries in terms of functions as well as cut the cost of energy conversion and storage device. Currently, the main limitation of such device is the low performances nested either in poor charge separation or in photoelectrochemical reactions confined to the extreme surface of the material.

References

- [1] E. Becquerel, *Compt. Rend. Acad. Sci.*, **1839**, 9, 145.
- [2] D. M. Chapin, C. S. Fuller, and G. L. Pearson, *J. Appl. Phys.*, **1954**, 25, 5, 676.
- [3] F. Haase, C. Hollemann, S. Schäfer, A. Merkle, M. Rienäcker, J. Krügener, R. Brendel, and R. Peibst, *Sol. Energy Mater. Sol. Cells*, **2018**, 186, 184.
- [4] K. Yoshikawa, W. Yoshida, T. Irie, H. Kawasaki, K. Konishi, H. Ishibashi, T. Asatani, D. Adachi, M. Kanematsu, H. Uzu, and K. Yamamoto, *Sol. Energy Mater. Sol. Cells*, **2017**, 173, 37.
- [5] S. Rühle, *Solar Energy*, **2016**, 130, 139.
- [6] W. Shockley and H. J. Queisser, *J. Appl. Phys.*, **1961**, 32, 3, 510.
- [7] T. Wilkins, Alta Devices sets 29.1% solar efficiency record; NASA selects Alta Devices for International Space Station Test, **2018**. [Online]. Available: <https://www.altadevices.com/solar-world-record-nasa-selects-alta-devices/>. [Accessed: 02.05.2019].
- [8] NREL, Best Research-Cell Efficiencies, National Renewable energy laboratory (NREL), **2018**. [Online]. Available: <https://www.nrel.gov/pv/assets/pdfs/best-research-cell-efficiencies-190416.pdf>. [Accessed: 17.03.2019].

- [9] P. T. Chiu, D.C. Law, R.L. Woo, S.B. Singer, D. Bhusari, W.D. Hong, A. Zakaria, J. Boisvert, S. Mesropian, R.R. King, and N.H. Karam, *2014 IEEE 40th Photovoltaic Specialist Conference (PVSC)*, **2014**, 0011.
- [10] F. Dimroth, T.N. Tibbits, M. Niemeyer, F. Predan, P. Beutel, C. Karcher, E. Oliva, G. Siefer, D. Lackner, P. Fuß-Kailuweit, A.W. Bett, *IEEE J. Photovolt.*, **2016**, 6, 1, 343.
- [11] R. R. King, C.M. Fetzer, D.C. Law, K.M. Edmondson, H. Yoon, G.S. Kinsey, D.D. Krut, J.H. Ermer, P. Hebert, B.T. Cavicchi, and N.H. Karam, *2006 IEEE 4th World Conference on Photovoltaic Energy*, **2006**, 2, 1757.
- [12] C. W. Tang, *Appl. Phys. Lett.*, **1986**, 48, 2, 183.
- [13] K. W. J. Barnham and G. Duggan, *J. Appl. Phys.*, **1990**, 67, 7, 3490.
- [14] M. Grätzel, *Nature*, **2001**, 414, 6861, 338.
- [15] A. Kojima, K. Teshima, T. Miyasaka, and Y. Shirai, *Abstracts 210th ECS Meeting*, **2006**, 397.
- [16] K. Kakiage, Y. Aoyama, T. Yano, K. Oya, J. Fujisawa, and M. Hanaya, *Chem. Commun.*, **2015**, 51, 88, 15894.
- [17] M. Freitag, J. Teuscher, Y. Saygili, X. Zhang, F. Giordano, P. Liska, J. Hua, S.M. Zakeeruddin, J.E. Moser, M. Grätzel, and A. Hagfeldt, *Nat. Phot.*, **2017**, 11, 6, 372.
- [18] C. Honsberg and S. Bowden, PVEducation [Online]. Available: <http://www.pveducation.org/>. [Accessed: 18.04.2019].
- [19] A. Hagfeldt, G. Boschloo, L. Sun, L. Kloo, and H. Pettersson, *Chem. Rev.*, **2010**, 110, 11, 6595.
- [20] X. Luo, J. Wang, M. Dooner, and J. Clarke, *Appl. Energy*, **2015**, 137, 511.
- [21] N. Nitta, F. Wu, J. T. Lee, and G. Yushin, *Mater. Today*, 2015, 18, 5, 252.
- [22] G. E. Blomgren, *J. Electrochem. Soc.*, **2017**, 164, 1, 5019.
- [23] R. A. Rightmire, "Electrical energy storage apparatus", US3288641A, **1966**.
- [24] P. Sharma and T. S. Bhatti, *Energy Convers. Manag.*, **2010**, 51, 12, 2901.
- [25] H. Budde-Meiwes, J. Drillkens, B. Lunz, J. Muennix, S. Rothgang, J. Kowal, and D.U. Sauer, *Proc. Inst. Mech. Eng. D J. Automob. Eng.*, **2013**, 227, 5, 761.
- [26] X. Zou, N. Maesako, T. Nomiyama, Y. Horie, and T. Miyazaki, *Sol. Energy Mater. Sol. Cells*, **2000**, 62, 1, 133.
- [27] H. Nagai and H. Segawa, *Chem. Comm.*, **2004**, 8, 974.
- [28] T. Nomiyama, H. Takeuchi, K. Kawazoe, Y. Horie, and T. Miyazaki, *Jpn. J. Appl. Phys.*, **2005**, 44, 7, 5219.

- [29] A. Hauch, A. Georg, U. O. Krašovec, and B. Orel, *J. Electrochem. Soc.*, **2002**, 149, 9, 1208.
- [30] T. Nomiyama, K. Sakamoto, T. Yoshida, A. Kagiya, and Y. Horie, *MRS Proceedings*, **2013**.
- [31] T. Nomiyama, K. Sakamoto, T. Yoshida, A. Kagiya, and Y. Horie, *MRS Online Proceedings Library Archive*, **2014**, 1606.
- [32] T. Nomiyama, K. Sasabe, K. Sakamoto, and Y. Horie, *Jpn. J. Appl. Phys.*, **2015**, 54, 7, 071101.
- [33] K. Oyaizu, Y. Niibori, A. Takahashi, and H. Nishide, *J. Inorg. Organomet. Polymer*, **2013**, 23, 1, 243.
- [34] K. Akuto and Y. Sakurai, *J. Electrochem. Soc.*, **2001**, 148, 2, 121.
- [35] A. Paoletta, C. Faure, G. Bertoni, S. Marras, A. Guerfi, A. Darwiche, P. Hovington, B. Commarieu, Z. Wang, M. Prato, and M. Colombo, *Nat. Commun.*, **2017**, 8, 14643.
- [36] T. Miyasaka and T. N. Murakami, *Appl. Phys. Lett.*, **2004**, 85, 17, 3932.
- [37] T. N. Murakami, N. Kawashima, and T. Miyasaka, *Chem. Commun.*, **2005**, 26, 3346.
- [38] T. Miyasaka, N. Ikeda, T. N. Murakami, and K. Teshima, *Chem. Lett.*, **2007**, 36, 4, 480.
- [39] Y. Cunjiang, M. Charan, R. Jiepeng, W. Bingqing, and J. Hanqing, *Adv. Mater.*, **2009**, 21, 47, 4793.
- [40] Z. Yang, L. Li, Y. Luo, R. He, L. Qiu, H. Lin, and H. Peng, *J. Mater. Chem. A*, **2013**, 1, 3, 954.
- [41] M. Skunik, P. J. Kulesza, N. Vlachopoulos, L. Häggman, and A. Hagfeldt, *ECS Trans.*, **2011**, 35, 25, 93.
- [42] H.W. Chen, C.Y. Hsu, J.G. Chen, K.M. Lee, C.C. Wang, K.C. Huang, and K.C. Ho, *J. Power Sources*, **2010**, 195, 18, 6225.
- [43] T. Chen, L. Qiu, Z. Yang, Z. Cai, J. Ren, H. Li, H. Lin, X. Sun, and H. Peng, *Angew. Chem.*, **2012**, 51, 48, 11977.
- [44] X. Chen, H. Sun, Z. Yang, G. Guan, Z. Zhang, L. Qiu, and H. Peng, *J. Mater. Chem. A*, **2014**, 2, 6, 1897.
- [45] Y. Fu, H. Wu, S. Ye, X. Cai, X. Yu, S. Hou, H. Kafafy, and D. Zou, *Environ. Sci.*, **2013**, 9.
- [46] J. Bae, Y.J. Park, M. Lee, S.N. Cha, Y.J. Choi, C.S. Lee, J.M. Kim, and Z.L. Wang, *Adv. Mater.*, **2011**, 23, 30, 3446.
- [47] X. Zhang, X. Huang, C. Li, and H. Jiang, *Adv. Mater.*, **2013**, 25, 30, 4093.

- [48] G. Wee, T. Salim, Y. M. Lam, S. G. Mhaisalkar, and M. Srinivasan, *Energy Environ. Sci.*, **2011**, 4, 2, 413.
- [49] Y. Saito, S. Uchida, T. Kubo, and H. Segawa, *Thin Solid Films*, **2010**, 518, 11, 3033.
- [50] W. Zhao, X.-F. Wang, E. Zheng, Y. Wei, Y. Sanehira, and G. Chen, *J. Power Sources*, **2017**, 350, 28.
- [51] N. F. Yan, G. R. Li, G. L. Pan, and X. P. Gao, *J. Electrochem. Soc.*, **2012**, 159, 11, 1770.
- [52] X. Huang, X. Zhang, and H. Jiang, *RSC Advances*, **2016**, 6, 99, 96490.
- [53] W. Guo, X. Xue, S. Wang, C. Lin, and Z. L. Wang, *Nano Lett.*, **2012**, 12, 5, 2520.
- [54] H. Segawa, Y. Saito, S. Uchida, T. Kubo, S. Fujita, and T. Isaji, "Three-Pole Two-Layer Photo-Rechargeable Battery", U.S. Patent Application 12/076,913, **2009**.
- [55] P. Liu, H. X. Yang, X. P. Ai, G. R. Li, and X. P. Gao, *Electrochem. Commun.*, **2012**, 16, 1, 69.
- [56] M. Suzuka, S. Hara, T. Sekiguchi, K. Oyaizu, and H. Nishide, *Polymer*, **2015**, 68, 353.
- [57] N. F. Yan, G. R. Li, and X. P. Gao, *J. Mater. Chem. A*, **2013**, 1, 24, 7012.
- [58] P. Liu, Y. Cao, G.-R. Li, X.-P. Gao, X.-P. Ai, and H.-X. Yang, *ChemSusChem*, **2013**, 6, 5, 802.
- [59] M. A. Mahmoudzadeh, A. R. Usqaocar, J. Giorgio, D. L. Officer, G. G. Wallace, and J. D. W. Madden, *J. Mater. Chem. A*, **2016**, 4, 9, 3446.
- [60] Y. Zhou, S. Zhang, Y. Ding, L. Zhang, C. Zhang, X. Zhang, Y. Zhao, and G. Yu, *Adv. Mater.*, **2018**, 1802294.
- [61] J. Azevedo, T. Seipp, J. Burfeind, C. Sousa, A. Bentien, J.P. Araújo, and A. Mendes, *Nano Energy*, **2016**, 22, 396.
- [62] K. Wedege, J. Azevedo, A. Khataee, A. Bentien, and A. Mendes, *Angew. Chem.*, **2016**, 55, 25, 7142.
- [63] Q. Cheng, W. Fan, Y. He, P. Ma, S. Vanka, S. Fan, Z. Mi, and D. Wang, *Adv. Mater.*, **2017**, 29, 26, 1700312.
- [64] W. Li, H.C. Fu, L. Li, M. Cabán-Acevedo, J.H. He, and S. Jin, *Angew. Chem.*, **2016**, 55, 42, 13104.
- [65] S. Liao, X. Zong, B. Seger, T. Pedersen, T. Yao, C. Ding, J. Shi, J. Chen, and C. Li, *Nat. Commun.*, **2016**, 7, 11474.
- [66] A. K. Pandey, P. C. Deakin, J.V. Vuuren, D. Ross, P. L. Burn, and I. D. Samuel, *Adv. Mater.*, **2010**, 22, 35, 3954.
- [67] H. Gerischer, *Surf. Sci.*, **1969**, 13, 1, 265.

- [68] H. Gerischer, *J. Electroanal. Chem. Interfacial Electrochem.*, **1975**, 58, 1, 263.
- [69] H. Gerischer, *J. Electrochem. Soc.*, **1978**, 125, 5, 218.
- [70] G. Hodes, J. Manassen, and D. Cahen, *Nature*, **1976**, 261, 403.
- [71] H. Tributsch, *Appl. Phys.*, **1980**, 23, 1, 61.
- [72] M. Abramovich and H. Tributsch, *J. Electroanal. Chem. Interfacial Electrochem.*, **1982**, 138, 1, 121.
- [73] M. Abramovich and O. Gorochov, *J. Electroanal. Chem. Interfacial Electrochem.*, **1983**, 153, 1, 115.
- [74] G. Betz, S. Fiechter, and H. Tributsch, *J. Appl. Phys.*, **1987**, 62, 11, 4597.
- [75] G. Betz, H. Tributsch, and S. Fiechter, *J. Electrochem. Soc.*, **1984**, 131, 3, 640.
- [76] G. Betz, H. Tributsch, and R. Marchand, *J. Appl. Electrochem.*, **1984**, 14, 3, 315.
- [77] T. Nomiya, H. Kuriyaki, and K. Hirakawa, *Synthetic Metals*, **1995**, 71, 1, 2237.

Chapter 2. Evolution of TiO₂ optoelectronic properties upon Li⁺ insertion

Introduction	39
2.1. Preliminary work on the photorechargeable anatase TiO ₂ nanoparticles.....	40
2.1.1. Synthesis and characterization of the anatase TiO ₂ nanoparticles.....	40
2.1.2. Formulation of the screen-printable paste and electrode printing procedure	42
2.1.3. Proof-of-concept of quantitative photorechargeable battery electrode based on nanocrystalline anatase TiO ₂ particles.....	45
2.2. Optical properties of TiO ₂ and Li _x TiO ₂ by UV-visible absorption spectroscopy	49
2.2.1. Absorption spectroscopy and methodology of band gap determination	49
2.2.2. Evolution of TiO ₂ absorption upon lithium insertion.....	50
2.3. Band edge and charge carrier concentration evolution upon Li ⁺ insertion	56
2.3.1. Mott-Schottky electrochemical impedance spectroscopy theory	56
2.3.2. TiO ₂ flat band potential and charge carrier concentration in different media: aqueous protic and non-aqueous aprotic electrolytes	57
2.3.3. Evolution of the flat band potential and charge carrier concentration upon Li ⁺ insertion into TiO ₂	64
2.4. Photoluminescence spectroscopy basics	68
2.4.1. Steady-state fluorescence of anatase TiO ₂ nanocrystals.....	69
2.4.2. <i>In situ</i> steady-state fluorescence upon lithiation.....	71
2.5. Determination of the kinetics of the charge transfer processes in TiO ₂ by TCSPC.....	75
2.5.1. <i>In situ</i> study of the time-resolved fluorescence of TiO ₂ and Li _{0.6} TiO ₂	76
2.5.2. Kinetics of charge transfer processes in Li _{0.6} TiO ₂ in contact with electrolyte	79
Conclusions	82
References	84

Introduction

The proof-of-concept of an interfacial light-driven ion transfer at the interface between a mixed electronic/ionic semiconductor and electrolyte has been presented by Tributsch et al. in 1984, i.e. photo-insertion of Cu^+ into p-type $\text{Cu}_{6-x}\text{PS}_5\text{I}$ [1]. This opened a new research direction of inorganic materials capable of both solar energy conversion and its storage at the molecular level. As the charge carrier photogeneration is long-lived within the depletion layer of the semiconductor but the main limitation of such a mechanism is nested in its extreme surface reaction limited by the Debye length, which resulted in a maximum storage capacity of only 0.5 Wh/kg as pointed out on CuFeTe_2 by Hirakawa et al. [2]. To overcome such a limitation, the important criteria to consider are: having both efficient electronic and ionic conductivity, good reversibility of ion insertion into / deinsertion from the structure, as well as a high dielectric constant and low donor states to promote effective dissociation of the electron-hole pairs in the depletion layer and to maximize the Debye length (W) into the particle's volume as determined from the solution of Poisson's equation in a radial (r) coordinates (eq. 2.1-2.2) .

$$\frac{1}{r^2} \cdot \frac{d}{dr} \left(r^2 \cdot \frac{d\psi}{dr} \right) = \frac{qN}{\epsilon_r \epsilon_0} \quad (2.1)$$

$$W = \left(\frac{2\Delta\psi \epsilon_r \epsilon_0}{qN} \right)^{1/2} \quad (2.2)$$

where $\Delta\psi$ is the electrical interfacial energy drop in the space charge layer (directly related to the flat band potential V_{fb}), ϵ_0 the permittivity of the vacuum ($8.85 \cdot 10^{-12}$ F/m), ϵ_r the relative permittivity (dielectric constant) of the material to that of the vacuum, q the elementary charge ($1.6 \cdot 10^{-19}$ C), and N the main charge carrier concentration (donor density). One additional approach led at LRCS under the post-doctoral work of Dr. Christian Andriamiadamanana prior to my Ph.D. thesis, was to downsize the particles towards nano-scale to promote the surface-to-volume ratio of the active material and thus to increase the yield of the photoelectrochemical reaction per mass unit.

The anatase polymorph of titanium dioxide appears as an excellent candidate owing to its good semiconducting properties, a high dielectric constant of 31-48 [3-4] and low charge carrier density of 10^{17} - 10^{19} cm^{-3} [5-7]. It displays a reversible lithium insertion / deinsertion process at a redox potential of ca. 1.75 V vs. Li^+/Li making this material attractive as a negative electrode for lithium-ion batteries [8-9]. Prior to this Ph.D. work, we elaborated a synthetic procedure

under room-temperature control yielding to nanocrystalline anatase TiO_2 crystals of ca. 4-5 nm in size [10].

This second chapter starts with a summary of this preliminary work that laid the background for the current thesis, including the details of the nanoparticle TiO_2 synthesis, powder and electrode characterization, and the photoelectrochemical performances. In the following parts, the results gathered during my thesis will be presented and discussed aiming at better understanding of the mechanisms behind the photorecharge as well as the evolution of optoelectronic properties of TiO_2 upon lithium insertion, such as the band edge positions, charge carrier concentration and photoluminescence properties. Finally, this chapter will end with a study led by time-correlated single photon counting experiments to determine precisely the dynamics of the charge transfer processes in TiO_2 and $\text{Li}_{0.6}\text{TiO}_2$ nanocrystals and incorporated in a photo-battery.

2.1. Preliminary work on the photorechargeable anatase TiO_2 nanoparticles

The data and concepts presented below make a part of the research activities led by Dr. Snehangshu Patra and Dr. Christian Andriamiadamanana (Post-doctoral fellows between 2012 and 2015 at LRCS) and Gaspard Bouteau (Ph.D. thesis defended in February 2019).

2.1.1. Synthesis and characterization of the anatase TiO_2 nanoparticles

In order to bypass the surface limitation of the long-lived light-induced charge separation in semiconductor [1], two-step room-temperature synthesis procedure was proposed in our group to shape anatase-type TiO_2 nanoparticles of ca. 4-5 nm in size [10]. In my work, we slightly adapted this procedure as following: 40 mL of $\text{Ti}(\text{iOPr})_4$ (titanium (IV) isopropoxide) was added into 400 mL of distilled water to achieve complete hydrolysis of the alkoxyde precursor. The solution was vigorously stirred for 4 hours. The white precipitate was retrieved by multiple centrifugations with water, ethanol, and then dried in an oven at 60°C overnight. The resulted white powder is x-ray amorphous corresponding to hydrated titanium dioxide $\text{TiO}_2 \cdot 1.6\text{H}_2\text{O}$ as deduced by TGA analysis. The dehydration of powder was performed by adding concentrated sulfuric acid (H_2SO_4) until $\text{pH} = 2$. Thermolysis of the solution was carried out for one week at 60°C under these conditions. The resulting white powder was retrieved by three subsequent centrifugations using distilled water. The high resolution transmission electron micrograph (Fig. 2.1 (a)) showed mostly spherical nanoparticles with an average diameter of around 5 nm.

The x-ray diffraction (XRD) pattern shows successful crystallization of the resulted power after controlled thermolysis leading to an anatase-type of TiO_2 structure in good agreement with the selected area electron diffraction (SAED) (Fig. 2.1(b)). Note that there is a minor content of the brookite polymorph, visible with the small peak at $2\theta = 30.8^\circ$. The presence of this polymorph as a structural impurity is explained by a possible increase of pH during the thermolysis [11]. Using Debye-Scherrer equation, we determined a crystallite size of 4.3 nm based on (004) orientation at $2\theta = 37.8^\circ$ [12].

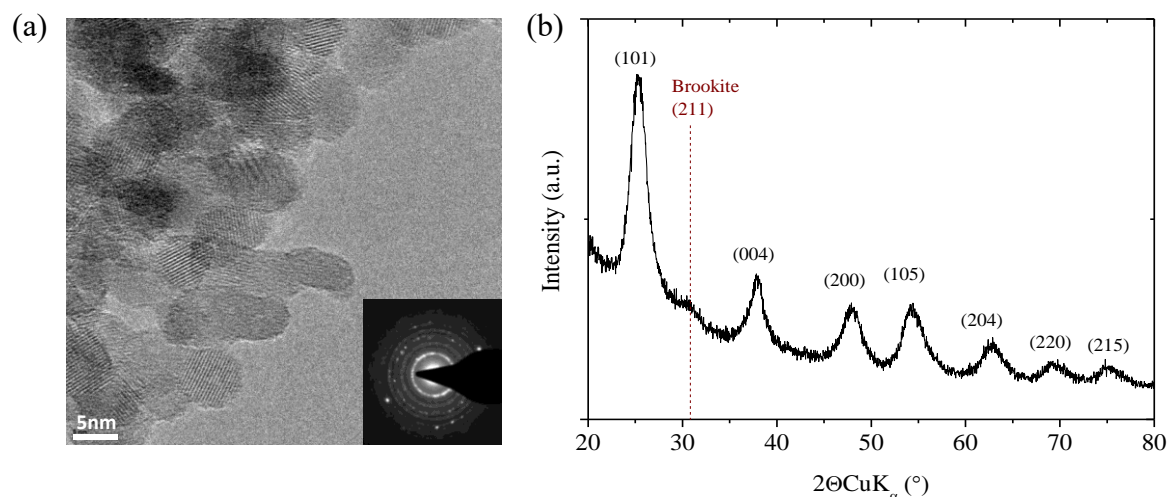


Figure 2.1. (a) High Resolution Transmission Electron Micrograph including SAED pattern and (b) x-ray diffraction pattern of the synthesized anatase TiO_2 powder.

N_2 adsorption-desorption isotherm of these nanoparticles features a type IV isotherm corresponding to a mesoporous network (Fig. 2.2) [13]. Brunauer-Emmett-Teller (B.E.T.) surface area is $248.6 \text{ m}^2/\text{g}$ ($\pm 3.2 \text{ m}^2/\text{g}$, $C_{\text{BET}} = 327$) [14]. The distribution of pores is monomodal centered at 3.5 nm as deduced by Barrett-Joyner-Halenda (BJH) method [15].

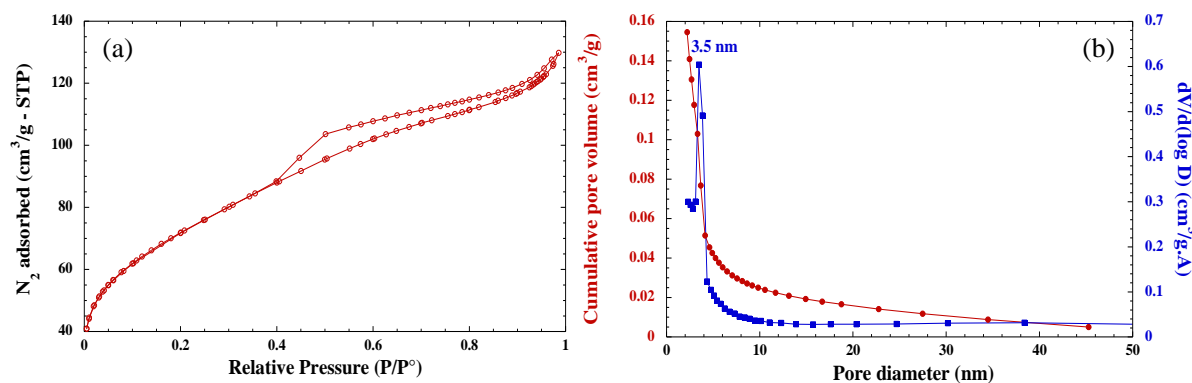


Figure 2.2. (a) N_2 adsorption/desorption isotherm and (b) BJH pore size distribution determined in desorption of the synthesized anatase TiO_2 powder.

2.1.2. Formulation of the screen-printable paste and electrode printing procedure

In order to obtain mesoporous electrodes with reproducible thicknesses in the range of 2-15 μm , size and porosity, we privileged in this work the screen-printing methodology. For this, a printable paste containing the synthesized TiO_2 nanoparticles was prepared. We adapted a protocol reported in the literature for the preparation of dye-sensitized solar cell photoanode [16-17]. For this, 6 g of dry TiO_2 powder was dispersed within 175 mL of distilled water prior acidification by adding 1 mL of HNO_3 (68%, Aldrich)). The solution was stirred at 78°C for 90 minutes with a 45-minute ramp to reach the temperature to allow particle peptization. This can be visualized by the solution color change from white to bluish. The colloidal solution was further dispersed using first Ultra-Turrax homogenizer (for 5 minutes at 25000 rpm) and then an ultrasonic horn with a titanium probe for one minute, alternating every 0.5 seconds ultrasound (at 50% power of 200 W at 20 kHz) and rest. After repeating this procedure three times between homogenizer and high power ultra-sound, the solution was concentrated in rotary evaporator under pressure of 10 mbar at 45°C until an aqueous suspension containing 20 weight percent (wt%) of TiO_2 was obtained. The water and remaining HNO_3 were removed by centrifugation three times using ethanol. Then, 20 wt% of ethylene cellulose 30-50 mPa.s (1.32 g), 34 wt% of ethylene cellulose 5-15 mPa.s (2.28 g) with respect to the initial amount of dry TiO_2 , and 24.3 g of terpineol were added to adjust the viscosity of the paste and final porosity. The mixture was diluted by ethanol to a volume of ca. 130 mL and homogenized by stirring for few hours at 800 rpm. The solution was redispersed following the same procedure as described above (Ultra-Turrax homogenizer and ultrasonic horn) and then concentrated again in the rotary evaporator to reach optimal viscosity for screen-printing. The obtained paste was then homogenized in a three-roll mill system, and heat-treated at 80°C for 4 hours in order to enhance its storage longevity.

The TiO_2 electrodes were screen-printed upon iron-free NSG10 Nippon Sheet Glass FTO. The glass surface was pretreated in 40 mmol/L solution of TiCl_4 at 70°C for 30 minutes. This leads to a few nanometers thick deposit of TiO_2 to enhance the film adhesion of the screen-printed TiO_2 layer onto the FTO substrate. The screen utilized was composed of a network of 90 threads per cm (90T mesh) leading to 16 squares of 16 mm^2 . Three layers of TiO_2 were deposited on the substrate leading to a final thickness of around 10 μm . The printing procedure is the following: printing, mechanical relaxation for 3 minutes and 7 minutes of heat treatment at 110°C on a hot plate to dry the electrodes. The removal of the remaining terpineol and ethyl cellulose, which plays the role of porogen, was carried out in four steps at 325, 375, 450 and

500°C under air according to ramps and step durations schematized in Figure 2.3. These steps follow precisely the thermal degradation stages of the ethyl cellulose. Prior to any use in the photoelectrochemical cell, the electrodes were always dried at 70°C under vacuum overnight. We found reproducibly that working with dry electrodes is important for the photoelectrochemical performances.

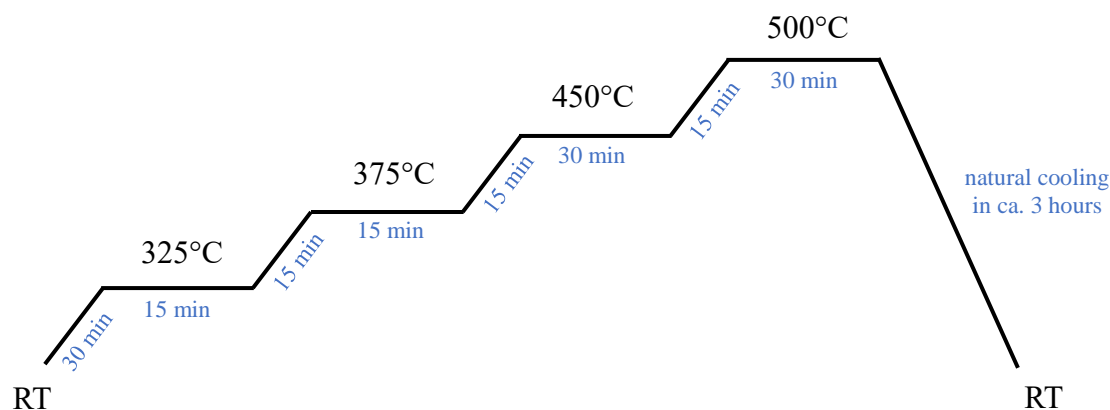


Figure 2.3. Schematic representation of the 4-step heat-treatment procedure to remove ethyl cellulose and terpineol from the screen-printed TiO₂ electrodes.

After the heat-treatment procedure, N₂ adsorption-desorption measurements on the films still show a type IV isotherm (Fig. 2.4 (a)) with a H3 type hysteresis which typically met for porous materials formed from aggregates despite the different dispersion steps led during the paste preparation [13]. This is also visible based on the white color of the printed-electrodes, as discussed below, which shows Mie scattering from small aggregates in the film. The B.E.T. surface area decreases to 135.6 m²/g implying that the heating procedure induces also grain coarsening. The B.J.H. pore distribution in the film indicates a pore size centered at 4 nm in the film with a kind of bimodal distribution leading to an average pore diameter of 7.5 nm (Fig. 2.4. (b)) [15]. The film's porosity was estimated at 57% based on the cumulative pore volume.

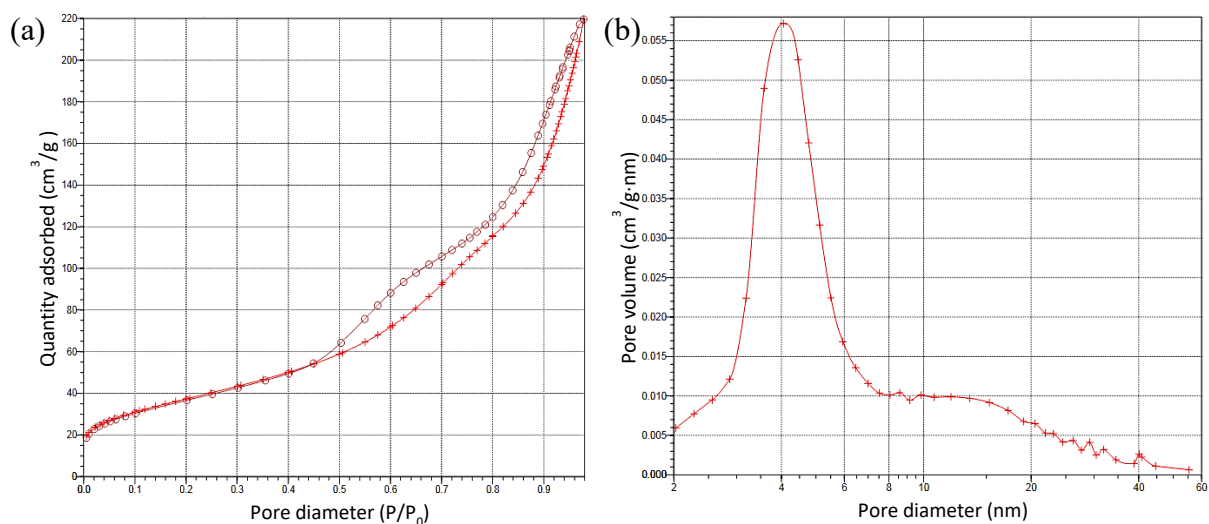


Figure 2.4. (a) N_2 adsorption-desorption isotherm of the screen-printed TiO_2 electrodes and (b) pore size distribution determined by the B.J.H. method.

For all photoelectrochemical experiments, a screen-printed TiO_2 electrode was incorporated into an air-tight double-wall thermostated (at 20°C) photoelectrochemical cell made out of borosilicate (Fig. 2.5). This glass reaches ca. 90% transmittance in the UV and visible range with a cut-off transmittance below 300 nm. The airtight cap was mounted with three platinum wires to one of which the TiO_2 photoanode (WE) was attached by soldering with indium-gallium alloy, and the other two were equipped with crocodile clips. Prior to the cell assembly, the cup with the working electrode and crocodile clips was dried at 70°C under vacuum for at least 6 hours. Meanwhile, the cell body was dried at 100°C in an oven. All the cell components were assembled in an Ar-filled glove box. Two lithium strips were serving as counter (CE) and reference (RE) electrodes. The cell was filled with an electrolyte containing 1 mol/L lithium hexafluorophosphate (LiPF_6) in 1/1 ratio ethylene carbonate (EC) and dimethyl carbonate (DMC) solution from Solvionic. The cup was sealed to the cell by high-vacuum Glisseal grease. The light excitation was ensured by using an Oriel LCS-100 sun simulator equipped with class ABB xenon lamp filtered at AM 1.5G ($100 \text{ mW}/\text{cm}^2$). This light power condition was regularly checked with a silicon reference diode certified at NREL. The photoelectrochemical characterization was carried out using a galvanostat/potentiostat/impedancemeter Modulab[®] XM connected to an optical shutter enabling automatized on/off light exposure.

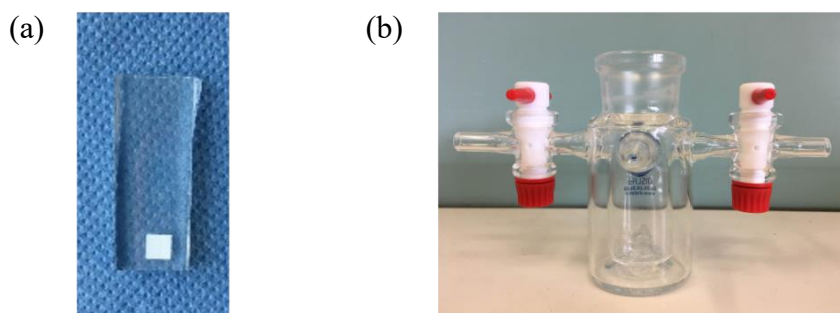


Figure 2.5. (a) Photograph of a mesoporous screen-printed TiO_2 electrode deposited upon the conductive FTO glass substrate and (b) air-tight thermostated borosilicate of the photoelectrochemical cell used in this work.

2.1.3. Proof-of-concept of quantitative photorechargeable battery electrode based on nanocrystalline anatase TiO_2 particles

The downsizing of TiO_2 nanoparticles is known to modify the thermodynamic stability of the polymorphism chemistry in TiO_2 [18-19]. At ambient conditions, rutile is thermodynamically the most stable polymorph followed by brookite and anatase. However, an interesting cross over point in this phase stability is observed when the particle is downsized to nanoscale. Banfield et al. concluded in his work that after crossing the threshold of 14 nm anatase becomes the most stable polymorph [20]. A similar observation was reported by Navrotsky et al. based on calorimetry experiments for particles having a B.E.T. surface area greater than $50 \text{ m}^2/\text{g}$, corresponding to a size limit of around 30 nm assuming spheres [21]. This greater phase stability of the anatase is the result of its lower surface energy which becomes preponderant at the nanoscale, thus ruling the total free Gibbs energy of the system [21-22]. In accordance with literature, our particles of 5 nm demonstrated an increased thermal stability of the anatase polymorph which irreversibly transforms into rutile structure at 1050°C instead of 750°C as deduced from *in situ* x-ray diffraction and Raman spectroscopy [23]. In addition, we demonstrated that the greater structural stability of the anatase TiO_2 is also experienced electrochemically with the occurrence of a complete solid solution domain between TiO_2 and LiTiO_2 , thus bypassing the well-known tetragonal to orthorhombic to quadratic rock-salt phase transitions upon lithium insertion [24]. This led to enhanced electrochemical performances of these nanoparticles in terms of capacity and reversibility [23].

The preliminary work demonstrating the complete photorecharge proof-of-concept of the anatase TiO_2 nanoparticles was carried out in our group by C. Andriamiadamanana (Post-

doctoral fellow 2013-2015) and is herein presented for the sake of clarity to the context of my work [25-26].

The cyclic voltammetry reported in Figure 2.6 compares the electrochemical behavior of TiO₂ nanoparticles under dark and illumination conditions in 1 mol/L LiPF₆ EC/DMC electrolyte at 2 mV/s scan rate. As one can see, under illumination the energy separation between the anodic and cathodic peaks is almost twice lower (469 mV in dark vs. 246 mV under illumination) and is accompanied by the increase of the peak intensity as well as its narrowing. For the first time, it was evidenced that the electrochemical properties of TiO₂ electrode can be modified by light. In this case, light absorption affords to improve the kinetics of the redox processes as a result of the photo-generation of free charge carriers leading to an increase in conductivity [27]. In addition, a slight thermodynamic changes in the system were observed, represented by an increase of equilibrium redox potential from 1.834 V (± 0.009) (vs. Li⁺/Li) in dark to 1.881 V (± 0.004) (vs. Li⁺/Li) under illumination.

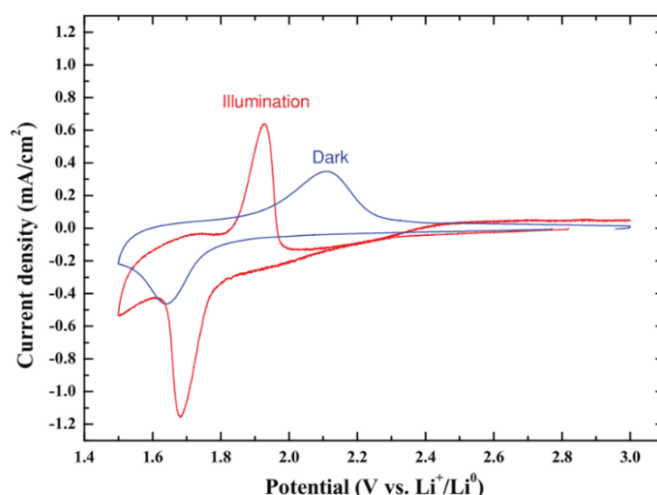


Figure 2.6. Comparison of cyclic voltammetry of the TiO₂ electrode in 1 mol/L LiPF₆ EC/DMC in dark (blue curve) and under illumination (red curve) at 2 mV/s scan rate

In order to evaluate the photorecharge capacity of the electrode, it was first galvanostatically discharged to 1.5 V (vs. Li⁺/Li) at $j = -100 \mu\text{A}/\text{cm}^2$ (corresponding to $\sim C/15$, i.e. one lithium inserted in 15 hours) (Fig. 2.7 (a)). The plateau at 1.8 V vs. Li⁺/Li corresponds to the lithium ion insertion by two-phase reaction between the quadratic anatase Li _{α} TiO₂ ($0 < \alpha < 0.25$) and the orthorhombic Li_{0.5+ δ} TiO₂ ($0 < \delta < 0.15$) [9, 23, 28]. Upon discharge, the electrode's color changes from white to dark blue. It is induced by the lithium insertion into the structure forming Ti³⁺ centers. The quantity of lithium inserted in the structure was estimated to be 0.6 using

inductively coupled plasma - atomic emission spectroscopy (ICP-AES), thus corresponding to a composition of $\text{Li}_{0.6}\text{TiO}_2$. At this discharged state, the potential relaxation behavior of the electrode at open circuit conditions has been compared for one hour between dark and under light illumination. In dark, the electrode's potential reached a steady-state value of 1.92 V vs. Li^+/Li . This corresponds to the potential of the electrode close to equilibrium. The electrode remained dark blue in this condition. The subsequent discharge down to 1.5 V vs. Li^+/Li under darkness revealed a very limited capacity of $46 \mu\text{Ah}/\text{cm}^2$ recuperated. In contrast, when the discharged electrode was left relaxing under illumination under the same other conditions, a faster rise of the electrode potential was observed reaching ca. 3.0 V vs. Li^+/Li . The electrode color changed from dark blue to white and almost full electrode capacity of $608 \mu\text{Ah}/\text{cm}^2$ was retrieved after subsequent discharge (Fig. 2.7 (b)). The complete lithium extraction was also confirmed by ICP-AES. These results demonstrate a quantitative nature of the photo-induced Li^+ deinsertion from the nanoparticle anatase TiO_2 . It gives credit to the downsizing of the particles that provides an answer to the surface limitation issue of the photoinduced ion transfer reaction [2]. This has been further demonstrated in the Ph.D. thesis work of Gaspard Bouteau comparing different particles size of anatase TiO_2 from 4 to 400 nm [29].

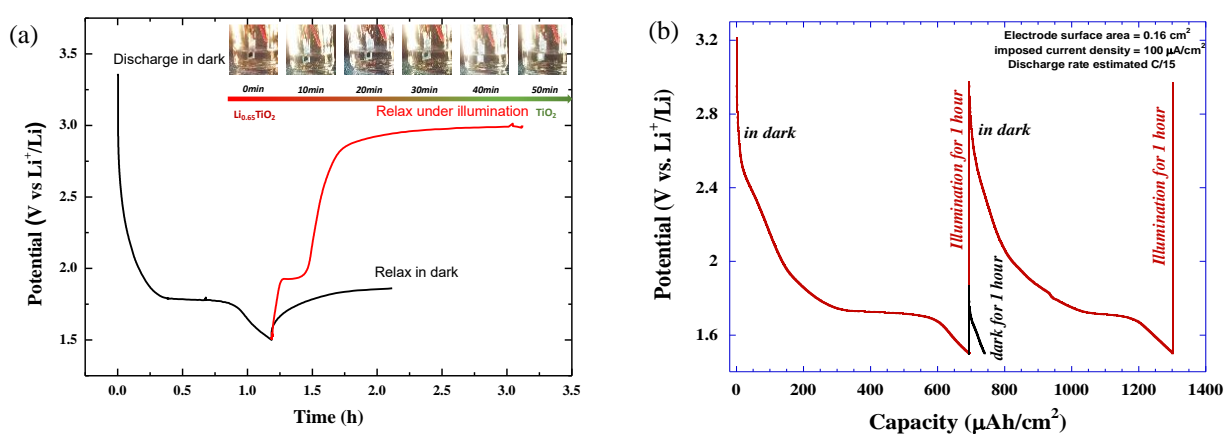
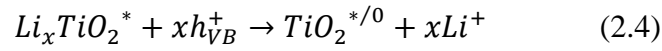
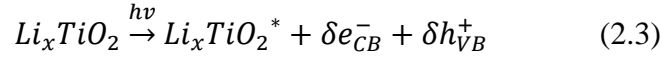


Figure 2.7. Electrochemical properties of anatase TiO_2 nanoparticles in a half-cell configuration: (a) galvanostatic discharge in dark until 1.5 V (vs. Li^+/Li) at C/15 ($j = -100 \mu\text{A}/\text{cm}^2$) followed by either 1 hour open-circuit condition in dark (black curve) or under illumination (red curve), and (b) galvanostatic discharge profile of the electrode after one hour open-circuit condition in dark (black curve) or under illumination (red curve).

Based on the above presented results, the first proposed mechanism to account for the photo-induced recharge of the anatase TiO_2 nanoparticles is as following. The illumination of the Li_xTiO_2 -composition leads to the creation of photogenerated electron-hole pairs in the particle

(eq. 2.3). Considering a model including a depletion layer, which can be questionable given the size of the particles, the holes will drift towards particles' surface where they will onset the oxidation reaction with the transition metal Ti^{3+} to Ti^{4+} and subsequent release of lithium ions out from the crystal structure for charge compensation (eq. 2.4).



On the other side, the electrons in the center of the particle are ideally collected towards the external circuit. However, in our case, the charge collection is not taking place because of the open-circuit condition and the lithium metal foil used at the counter-electrode which is too reductive with respect to the energy of the photogenerated electrons located in the conduction band of TiO_2 (ca. -3.25 eV derived from Mott-Schottky measurements, section 2.3.2). In that configuration, they are scavenged by fluoride-based radicals formed in the electrolyte [29].

When discharged at $j = -100 \mu A/cm^2$ under illumination, the device provides a stable output potential of around 3 V (vs. Li^+/Li), with a remaining white electrode coloration, by virtue of the two antagonist processes: the lithium insertion into TiO_2 triggered by the galvanostatic discharge current and the photo-induced lithium deinsertion from Li_xTiO_2 (Fig. 2.8 (a)). The extracted capacity of the system is in theory infinite if the cell is completely regenerative without any side reactions with the electrolyte. Experimentally, we reached as high as 20 mAh/cm² until the electrode detached from the FTO. The electrolyte acquired an orange coloration indicating some side reactions and modification of solvation of Li^+ and PF_6^- driven by continuous light exposure as recently demonstrated in our group [29]. One additional aspect of the two functions of the electrode, namely sun energy conversion and storage, has been demonstrated through the employment of the device as a photovoltaic cell during the day (simultaneous galvanostatic load under illumination) and as a simple battery in discharge during the night (Fig. 2.8 (b)) [26]. Thus, a constant current can be provided regardless of external light power fluctuation and day/night intermittency over 3 days.

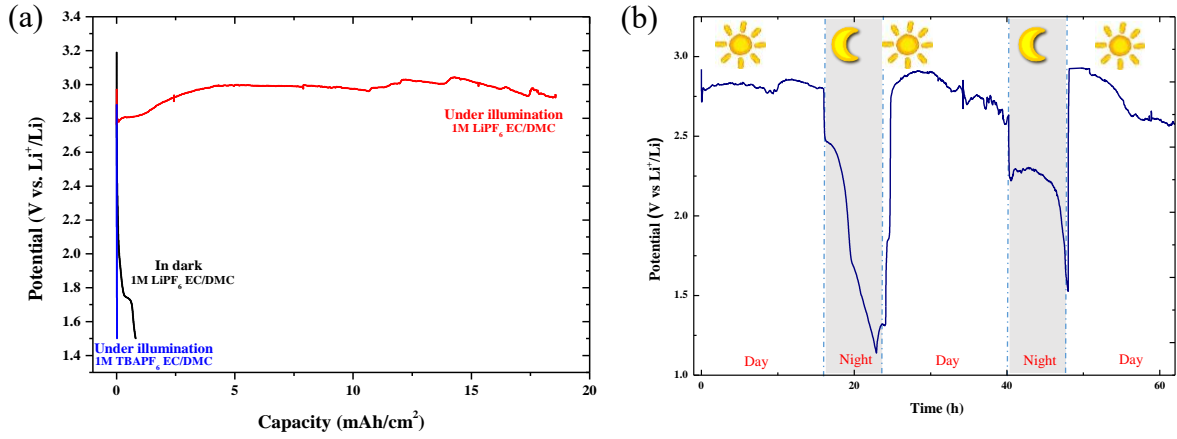


Figure 2.8. (a) A comparison of galvanostatic discharge at $j = -100 \mu\text{A}/\text{cm}^2$ of nanocrystalline anatase TiO_2 electrode in dark (black curve), under illumination (red curve) and under illumination in lithium-free $\text{TBAPF}_6 \text{EC/DMC}$ electrolyte (blue curve). (b) Galvanostatic discharge at $j = -100 \mu\text{A}/\text{cm}^2$ under reproduced intermittent light intensity conditions with a sequence of 16 hours under illumination and 8 hours in dark conditions.

2.2. Optical properties of TiO_2 and $\text{Li}_{0.6}\text{TiO}_2$ by *in situ* UV-visible absorption spectroscopy

In order to evaluate the evolution of the nanoparticle anatase TiO_2 light absorption in general and the band gap value in particular as a function of Li^+ content in the structure, *in situ* spectro-electrochemical experiments were carried out by UV-visible absorption spectroscopy on TiO_2 at different states of discharge.

2.2.1. Absorption spectroscopy and methodology of band gap determination

Light absorption is an intrinsic property of semiconductors. It relates to the energy of interband electronic transitions when the semiconductor is illuminated with an incident photon exceeding the band gap value. As a result, the electrons from the valence band (VB) are promoted to the conduction band (CB) while leaving positive charges in valence band. The correlation between the band gap value and the absorbance onset is typically described by the linear relationship proposed by Tauc, Davis, and Mott [30-31] (eq. 2.5).

$$(h\nu\alpha)^{1/n} = A(h\nu - E_g) \quad (2.5)$$

where h is the Planck's constant ($\text{J}\cdot\text{s}$), ν the frequency of vibration (s^{-1}), α the absorption coefficient, E_g the band gap (eV), A is proportionality constant and n a tabulated constant.

Depending on n value, different types of transitions can be derived: n equals to 1/2 for direct allowed transition, 3/2 for direct forbidden transition, 2 for indirect allowed transition and to 3 for indirect forbidden transition.

In order to determine the band gap value of a non-transmitting material, i.e. powder pressed into a pellet, we used an integration sphere and measured the diffuse reflectance spectrum of the pellet. In this case, the diffuse reflectance is inversely related to the absorption property. The band gap value is then derived from its spectrum using the Kubelka-Munk function ($F(R)$) (eq. 2.6) [32–34].

$$F(R) = \frac{(1 - R)^2}{2R} \quad (2.6)$$

Substitution of α by $F(R)$ gives the Tauc equation [35-36], from which E_g value can be determined from the intercept with the x axis in the $(h\nu ; (h\nu F(R))^{1/n})$ coordinates (eq. 2.7).

$$(h\nu F(R))^{1/n} = B(h\nu - E_g) \quad (2.7)$$

2.2.2. Evolution of TiO₂ absorption upon lithium insertion

Prior to studying the evolution of TiO₂ absorption as a function of the lithium content (depth of discharge), the band gap of the pristine 5 nm anatase TiO₂ powder has been determined by UV-Visible absorption spectroscopy in diffuse reflectance mode. For this, 1 wt% of TiO₂ was mixed into KBr before to be pressed to form a pellet. Figure 2.9 shows the reflectance spectrum recorded between 250 and 800 nm using a matt Teflon sample as a nominal 100% reflectance reference. The high reflectance above 400 nm is in a good agreement with the visual white color of the powder.

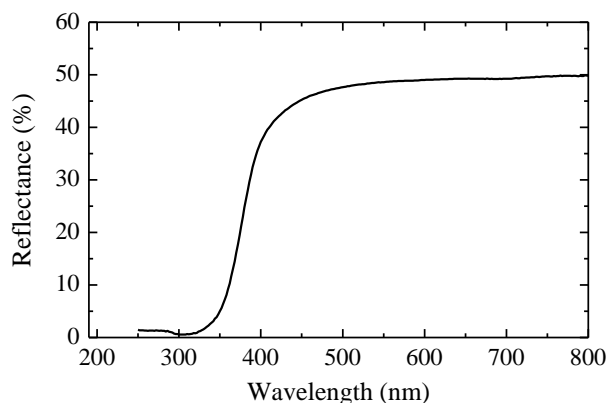


Figure 2.9. Evolution of diffuse reflectance as a function of wavelength for the 5 nm anatase TiO₂ nanoparticles.

The anatase TiO₂ is reported to have an indirect band gap involving the lowest $X_{1,2} \rightarrow \Gamma_1$ transition [37]. Assuming an indirect allowed transition, the Tauc plot leads to a band gap value of 3.24 eV corresponding to $\Gamma_3 \rightarrow X_{1b}$ transition (Fig. 2.10). This value is in a good agreement with both experimental [38–42] and theoretical [37] values reported in literature. The result suggest the absence of any quantum confinement effect at a size of 5 nm particles. This is in good agreement with the literature reporting a threshold value of ca. 2 nm [39].

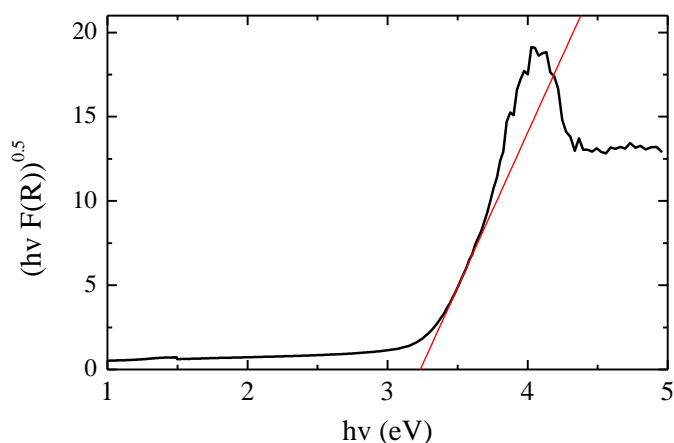


Figure 2.10. Tauc plot for 5 nm anatase TiO₂ particles for an indirect allowed transition ($n=2$).

To provide more insight on the origin and absorption consequences of the electrode's color change from white to deep blue upon lithium insertion into TiO₂, we developed in my work an air-tight three electrodes quartz cuvette allowing spectroelectrochemical experiments on films in transmittance configuration. However, for this study, we replaced the aggregated 5 nm particles by perfectly dispersed 20 nm particles for which screen-printed electrodes of 10 μm thickness are transparent to visible light in agreement with Mie scattering theory. The TiO₂ working electrode was assembled with two lithium strips as counter and reference electrodes. The electrolyte is composed of 1 mol/L LiPF₆ in 1/1 EC/DMC solvent mixture (LP30, Solvionic). The lithium insertion was performed by applying $j = -100 \mu\text{A}/\text{cm}^2$ discharge current using two-channel biologic VSP potentiostat/galvanostat. The transmittance spectra were recorded *in situ* at different states of discharge (Fig. 2.11). The sequence of galvanostatic curves providing these different states of discharge is presented in Figure 2.11 (a). The cumulative discharge curve is composed of a solid-solution domain until ca. 1.75 V (vs. Li⁺/Li) before a well-defined plateau at 1.75 V vs. Li⁺/Li corresponding to a two-phase reaction between lithium poor and lithium richer TiO₂ [9, 28]. The evolution of transmittance spectrum at different TiO₂ states of discharge is presented in Figure 2.11 (b). Before lithium insertion (OCV condition),

there is very little absorption between 400 to 1500 nm in agreement with the white color of TiO_2 . The LP30 electrolyte has an absorption threshold below ca. 250 nm, a value well inferior to the absorption wavelength of $\text{TiO}_2 / \text{Li}_x\text{TiO}_2$ compositions. The electrolyte exhibits also two absorption bands at 890 and 1022 nm, and two much stronger at 1162 nm with a shoulder at 1116 nm and a larger one containing at least 4 components at around 1400 nm. FTO in electrolyte absorbs all wavelengths below 360 nm, a few nanometers before the absorption of TiO_2 nanoparticles. Upon lithium insertion, the main outcome comes from a significant increase of absorption in the visible and infra-red part of light.

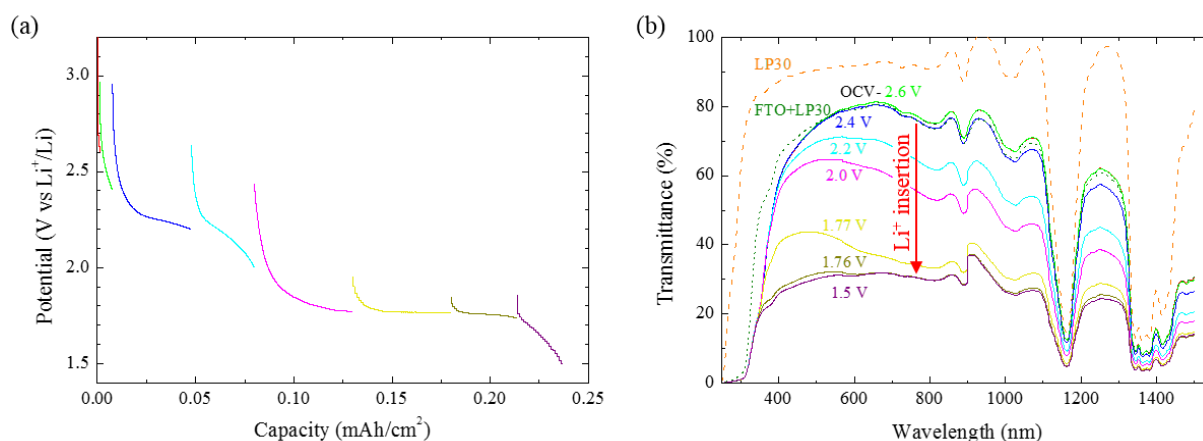


Figure 2.11. *In situ UV-visible absorption experiment of 20 nm nanocrystalline anatase TiO_2 upon lithium insertion: (a) succession of galvanostatic discharge curves and (b) corresponding evolution of transmittance after each discharge step (spectrum of electrolyte and FTO in electrolyte is provided as reference).*

This suggests that the color change from white to dark blue upon lithium insertion into TiO_2 stems from the increased absorption by free electrons in the conduction band. In addition, as the powder remains blue in darkness, this coloration also in part originates from the localization of electrons in the Ti^{3+} centers occupying the 3d metal orbitals. It may be accompanied by an additional contribution from the antibonding O 2p – Ti 4s hybridized orbitals owing to the nanosize of the particles in agreement with Vayssieres et al. [43]. Our result is in agreement with literature, reporting similar evolution of absorption spectra and color change as a function of lithium insertion for $\text{Li}_{4/3}\text{Ti}_{5/3}\text{O}_4$ [44] and WO_3 [45].

The band gap of TiO_2 and $\text{Li}_{0.6}\text{TiO}_2$ electrode inside the electrolyte was derived from the transmittance spectrum when the battery assembled at open circuit voltage (OCV) condition and discharged down to 1.5 V vs. Li^+/Li (Fig. 2.13). The absorption coefficient α was calculated

using a derivation of Beer-Lambert law (eq. 2.8), where % T corresponds to the transmittance value and d is the film thickness.

$$\alpha = (\ln(\frac{100}{\%T}))/d \quad (2.8)$$

The band gap value was derived from the absorbance onset in the Tauc plot in $(h\nu ; (h\nu\alpha)^{1/n})$ coordinates considering an indirect transition in agreement with literature [38–42] (Fig. 2.13). For TiO_2 , two distinct onsets are observed corresponding to lowest indirect $X_1 \rightarrow \Gamma_1$ transition at 2.85 eV and $\Gamma_3 \rightarrow X_{1b}$ transition at 3.21 eV in agreement with literature [37, 42]. Compared to the band gap measured on powder samples, i.e. 3.24 eV, this suggests a noticeable band gap narrowing when TiO_2 is in contact with electrolyte. This can be attributed on the one hand to a Stark effect induced by the specific adsorption of lithium cation on the surface of the particles as demonstrated in the Ph.D. work of Gaspard Bouteau [29], and on the other hand by the coulombic interactions created at the interface between TiO_2 and the high dielectric constant and polarity of the EC/DMC solvent mixture.

This bandgap is maintained until 1.77 V vs. Li^+/Li . At this potential range, the amount of lithium inserted into the anatase structure remains relatively low ($< 0.2 \text{ Li}^+$ per formula unit). The electrochemical phase transition taking place in the plateau at around 1.76 V vs. Li^+/Li contributes to a drastic change in the Tauc plot with a band gap increases. Indeed, for 1.76 V, 1.73 V and 1.5 V vs. Li^+/Li , Li_xTiO_2 exhibits exclusively a transition of 3.21 eV (Fig. 2.12). This higher band gap value upon lithium insertion is attributed to a Burstein-Moss effect. This arises because the electron density increases nearby the conduction band edge of TiO_2 as a result from the continuous formation of Ti^{3+} ($4s^0 3d^1$) upon lithium insertion [46-47].

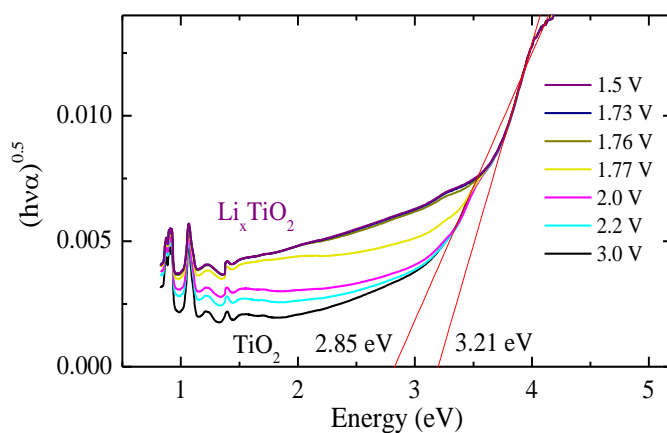


Figure 2.12. Tauc plot of 20 nm anatase TiO_2 electrode at different states of discharge in 1 mol/L LiPF_6 EC/DMC electrolyte. The fitting of the linear part of TiO_2 and Li_xTiO_2 curves and the resulting band gap values are provided for information.

To verify this hypothesis of donor density enhancement upon lithium insertion, the transmittance spectra were fitted by the Drude model. For this, we used an effective mass of electron of 0.4 as reported in literature by Deák et al. [48-49] (eq. 2.9-2.10) (Fig. 2.13).

$$e1 = 1 - \frac{\omega_p^2}{\omega^2 + i\omega} \quad (2.9)$$

$$e2 = \frac{\omega_p^2 \gamma}{\omega(\omega^2 + i\gamma)} \quad (2.10)$$

where $e1$ and $e2$ correspond to real and imaginary part of the complex dielectric function ($\varepsilon = e1 + ie2$), ω is the resonant frequency (in order of 10^{14} Hz), ω_p is the plasmon frequency and γ is the damping constant. Comparison of the TiO₂ data with LP30 and FTO + LP30 reference spectra suggests that the hills and valleys in the transmittance spectra of complete cell stem from the electrolyte absorption (Fig. 2.11 (b)). Therefore, corresponding parts of the spectra were excluded from the Drude model fitting for the sake of simplification. The simulation of the OCV, 2.6 V, and 2.4 V spectra to determine the optical carrier concentration was not successful. Nevertheless, excellent simulation was obtained for the 2.2 V spectrum. This should correspond closely to the pristine TiO₂ structure, as no (or almost no) lithium is normally inserted above this potential.

The evolution of the charge carrier concentration as a function of the depth of discharge is reported in Figure 2.14. The results highlight that lithium insertion into TiO₂ increases by 20 times the charge carrier concentration, from $1.3 \cdot 10^{19} \text{ cm}^{-3}$ to $2.9 \cdot 10^{20} \text{ cm}^{-3}$.

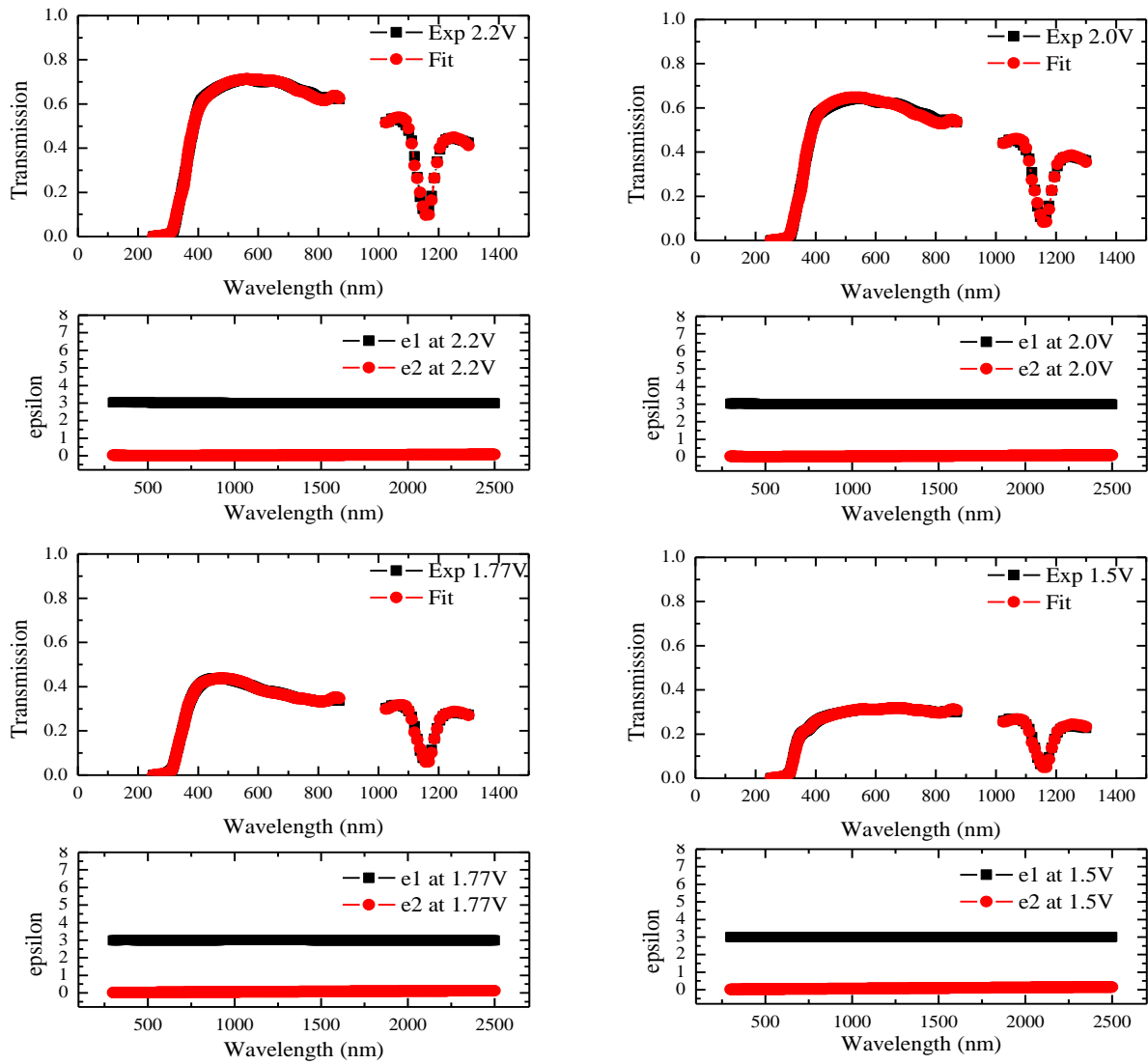


Figure 2.13. Drude model fitting of the transmittance spectra of 20 nm nanocrystalline TiO_2 in 1M LiPF_6 EC/DMC at different depth of discharge: 2.20 V, 2.00 V, 1.77 V and 1.50 V vs. Li^+/Li .

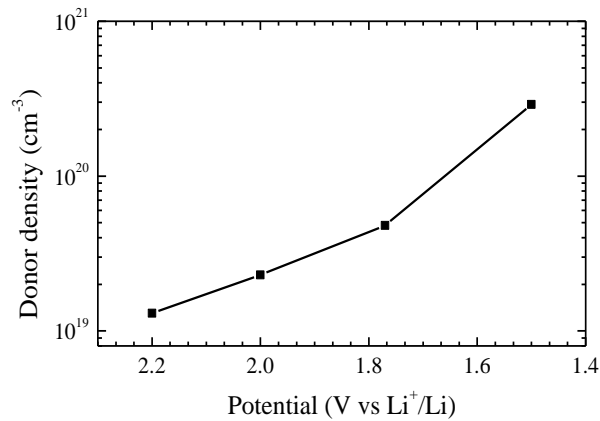


Figure 2.14. Evolution of charge carrier concentration upon lithium insertion in 20 nm anatase TiO_2 nanoparticles determined from the Drude model fitting of the transmittance spectra.

2.3. Band edge and charge carrier concentration evolution upon Li⁺ insertion

The determination of the energy location of the valence and conduction band in TiO₂ and Li_xTiO₂ can be carried out by Mott-Schottky experiments in combination with the steady-state UV-Visible absorption spectroscopy. This approach has been undertaken all along my Ph.D. thesis.

2.3.1. Mott-Schottky electrochemical impedance spectroscopy theory

Mott-Schottky experiments afford through an experimental approach to determine not only the type of main carriers and their concentration but also the flat-band position on the basis of the Schottky barrier establishment at the semiconductor/blocking electrolyte interface [50-51]. The measurement demands a blocking interface. It thus requires the absence of any possible interfacial redox reactions under applied bias voltage which may affect the electrode's built-in capacitance. Under such conditions, the equilibration of the Fermi level in the semiconductor and the chemical potential of the electrolyte leads to the occurrence of band bending (Fig. 2.15 (a)). It consists in the depletion of the main charge carriers (electrons) underneath the electrode surface, thus establishing a Schottky barrier at the semiconductor/electrolyte interface. From the electrolyte side, the Helmholtz layer is formed due to the repulsion of the positively charged ions and attraction of the negatively charged ions in the electrolyte to the electron-depleted surface. This is the case for the n-type semiconductor, and the opposite takes place in the p-type semiconductor.

Mott-Schottky theory assumes the semiconductor to be ideal such as a single-crystal without any intermediate surface states and a negligibly small Helmholtz layer potential drop at the interface. In this case, the interfacial capacitance can be simplified to a pure double-layer capacitance.

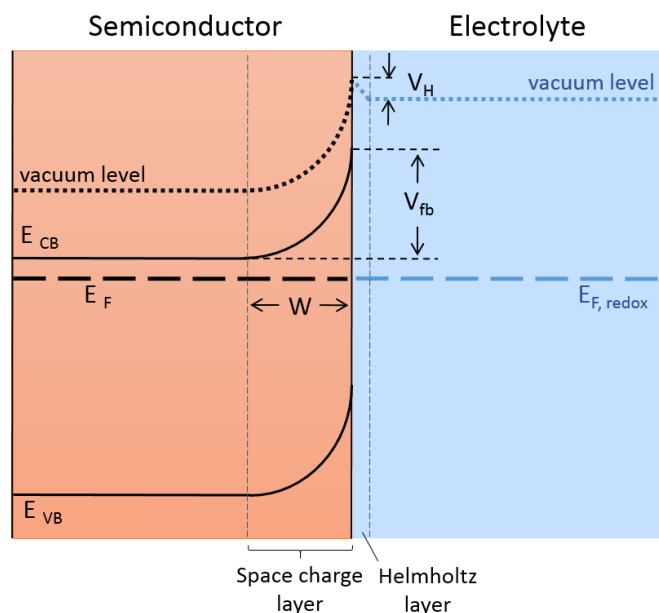


Figure 2.15. Schematic representation of the band bending at n-type semiconductor/electrolyte interface.

2.3.2. TiO₂ flat band potential and charge carrier concentration in different media: aqueous and non-aqueous aprotic electrolytes

Anatase TiO₂ was first studied. For this, 3 μm thick films of 5 nm size particles of anatase TiO₂ were prepared by doctor-blading. The electrolyte was composed of 1 mol/L NaOH in deionized water. The Mott-Schottky capacitance measurements were performed in a three-electrode cell using a saturated calomel electrode and a platinum grid as a reference and counter-electrode, respectively. The most reproducible conditions were obtained in the range of 100 Hz to 1 kHz. No clear frequency dependence was noticed on the electrode's thickness when varying this latter between 3 to 15 μm. The results are reported in Figure 2.16 for a given electrode thickness and for different size of particles, namely 5 nm, 20 nm and 200 nm. To reach reproducible results and lower frequency dependence on the results especially at higher perturbation frequencies (i.e. > 200 Hz), we found crucial to encapsulate FTO to avoid direct contact with the electrolyte. In all experiments, FTO was systematically covered with a layer of silicone resin. Direct contact of FTO to the electrolyte leads also to an increase by almost two orders of magnitude of the carrier density as a result of the predomination of charge carriers from the highly doped SnO₂ layer, which typically has ca. 10²¹ cm⁻³ carrier concentration [52].

Our results show that there is no evident trend for the flat band potential (V_{fb}) and the carrier density (N_d) dependence on the particle size (Fig. 2.16).

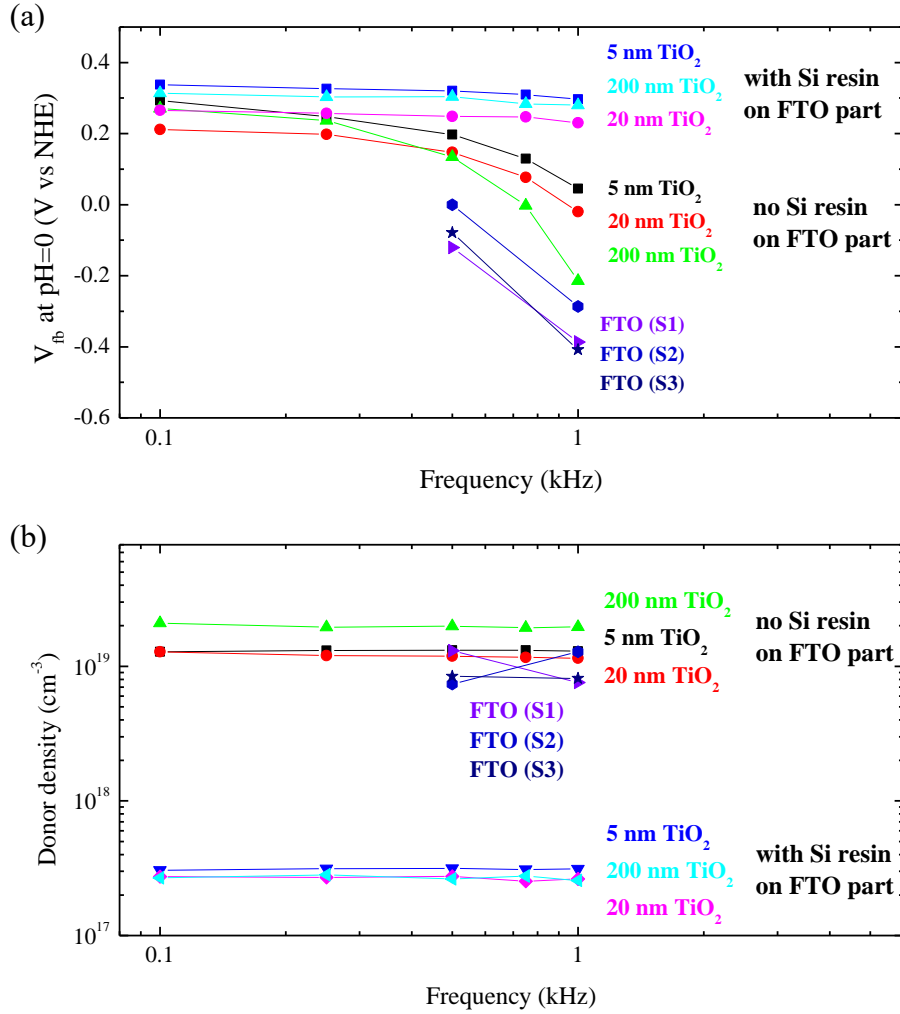


Figure 2.16. Evolution of (a) flat-band potential and (b) donor density as a function of perturbation frequency for different size of anatase TiO₂ particles in 1 mol/L NaOH-based aqueous electrolyte.

The evolution of the flat-band potential and charge carrier concentration as a function of frequency for five identical films composed of 5 nm TiO₂ particles in 1 mol/L NaOH aqueous electrolyte is presented in Figure 2.17 to show the reproducibility of the results. A flat band potential of ca. 0.3 V (vs. NHE) systematically decreases by up to 0.04 V when frequency is increased from 100 Hz to 1 kHz. At the same time, the donor density change is less than 10^{18} cm^{-3} for the values in order of 10^{19} cm^{-3} . The frequency dependence stems from an evolution of the electrical double-layer capacitance at semiconductor/electrolyte interface depending on the excitation frequency. This feature is well-known in literature, albeit too often overshadowed [51, 53]. It can originate from different factors amongst the most important being an evolution of the semiconductor's dielectric constant depending on the frequency, surface punctual defects including surface states or porous / non planar electrode morphology. While

the insignificant changes in the donor density derived from our preliminary experiments suggest a negligible frequency dependence of the dielectric constant of TiO_2 , surface states, high film roughness factor and deep donors states can considerably amplify the frequency dependence in our case by causing a slow response to the applied alternating potential of the charge carriers in the depletion layer. Consequently, one can consider the utilization in our work of mesoporous electrodes including nanocrystalline particles represents a shortfall of our approach in using Mott-Schottky formalism to determine the energy position of the conduction and valence band position and main charge carrier type and concentration.

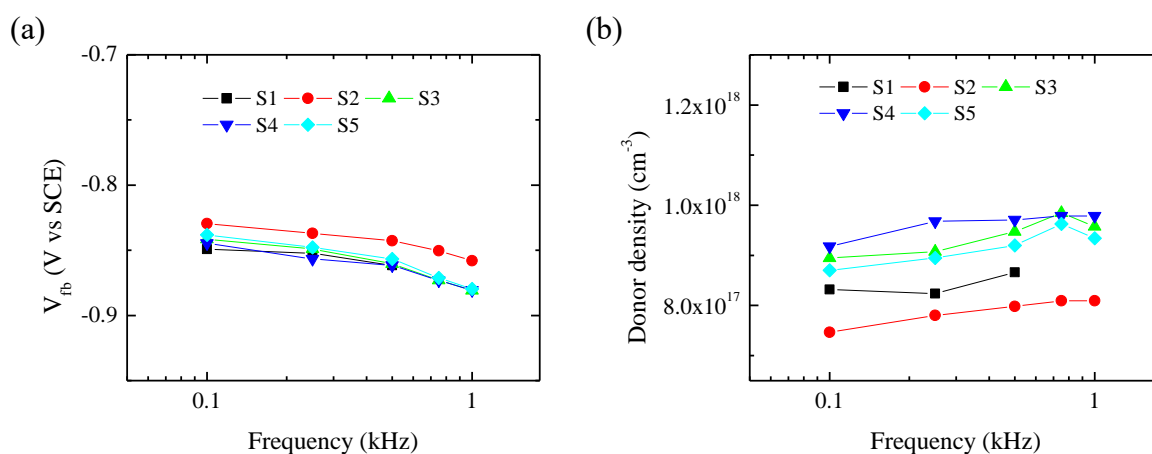


Figure 2.17. Frequency dependence and reproducibility over five fresh samples of (a) the flat band potential and (b) the main charge carrier concentration of the 5 nm anatase TiO_2 nanoparticles measured between 100 Hz and 1 kHz in 1 mol/L NaOH aqueous electrolyte.

Taking into account such a dependency for each set of measurements, all throughout this study, one representative Mott-Schottky plot was selected based on the most reproducible V_{fb} value. The measurement frequency of the chosen data is systematically reported.

Analogous electrochemical experiments were carried out in aprotic non-aqueous electrolyte in order to approach the real properties in photo-batteries. These experiments were performed in argon-filled glove box. The electrolyte is composed of 1 mol/L TBAPF₆ in EC/DMC. The measurements were performed in a two-electrode cell in which a lithium foil was used as both counter and quasi-reference electrode. This lithium quasi-reference electrode's potential was determined from two cyclic voltamperometry measurements on fresh lithium electrodes in Fc^+/Fc electrolyte (Fig. 2.18 (a)). Results show that Li QRE has a stable potential of -3.402 V (± 0.010 V) vs. ferricinium / ferrocene (Fc^+/Fc) redox couple. Laoire et al. reported the redox potential of Fc^+/Fc couple at 3.253 V vs. Li^+/Li in 1 mol/L LiPF_6 in EC/EMC electrolyte on

glassy carbon [54]. Taking this as a reference, the values measured vs. Li QRE can be translated into potentials versus other reference electrodes following the chart presented below (Fig. 2.18 (b)).

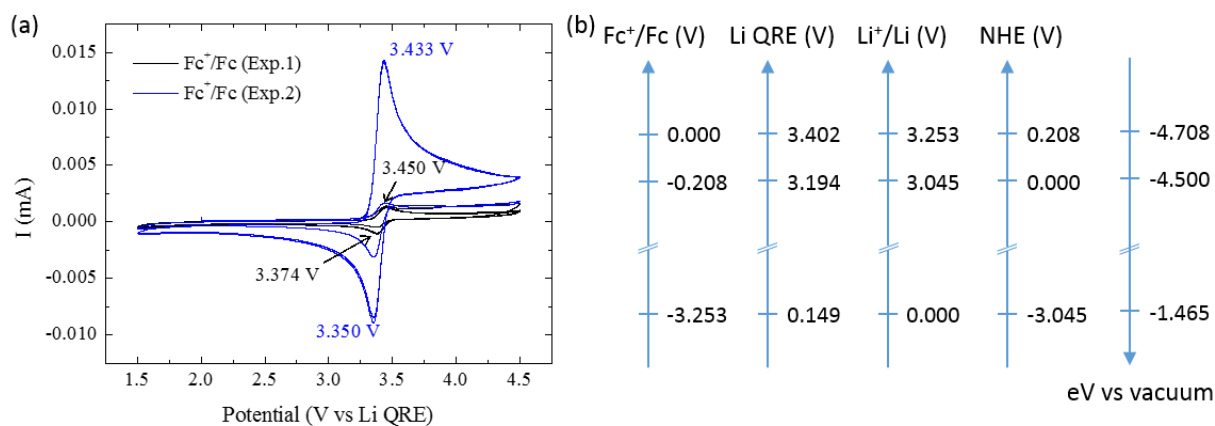


Figure 2.18. (a) Cyclic voltammetry of the Li quasi-reference electrode (QRE) used for Mott-Schottky measurements in non-aqueous aprotic electrolyte containing Fc^+/Fc redox couple in EC/DMC-based electrolyte and (b) a chart representing its energetic position versus conventional reference electrodes.

Similarly to the measurements in aqueous electrolytes, frequency dependence phenomenon was also experienced in 1 mol/L TBAPF₆ EC/DMC electrolyte, i.e. flat-band potential decreases and negligible donor density fluctuation while increasing the frequency (Fig. 2.19). It is important to mention that while carrying out Mott-Schottky measurements of electrodes in a non-aqueous aprotic electrolyte in glovebox, a weakly defined semi-circle was observed in impedance coordinates which may result from the greater length of cables between the cell in glovebox and the impedancemeter. However, due to its low resistive contribution with respect to the total cell impedance and its small capacitance contribution, we assumed its effect into the measurements to be negligible.

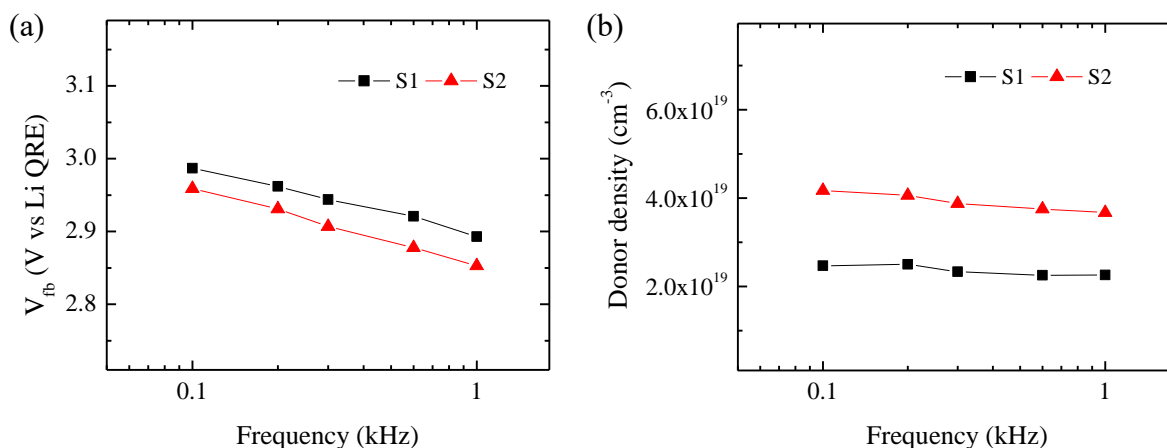


Figure 2. 19. Frequency dependence and reproducibility over two fresh samples (S1 and S2) of (a) the flat band potential and (b) the charge carrier concentration of 5 nm nanocrystalline anatase TiO_2 recorded between 100 Hz and 1 kHz in 1M TBAPF_6 EC/DMC electrolyte.

The representative Mott-Schottky plots for 5 nm nanocrystalline TiO_2 film in aqueous and non-aqueous aprotic electrolytes are presented in Figure 2.20. The linear region of the plot is due to the variation of the space charge layer width in the TiO_2 film, which is expressed in a double-layer capacitance change. In both media, the positive slope of Mott-Schottky plots with a well-defined linear part indicates the n-type behavior of the semiconductor in agreement with common literature [55–57].

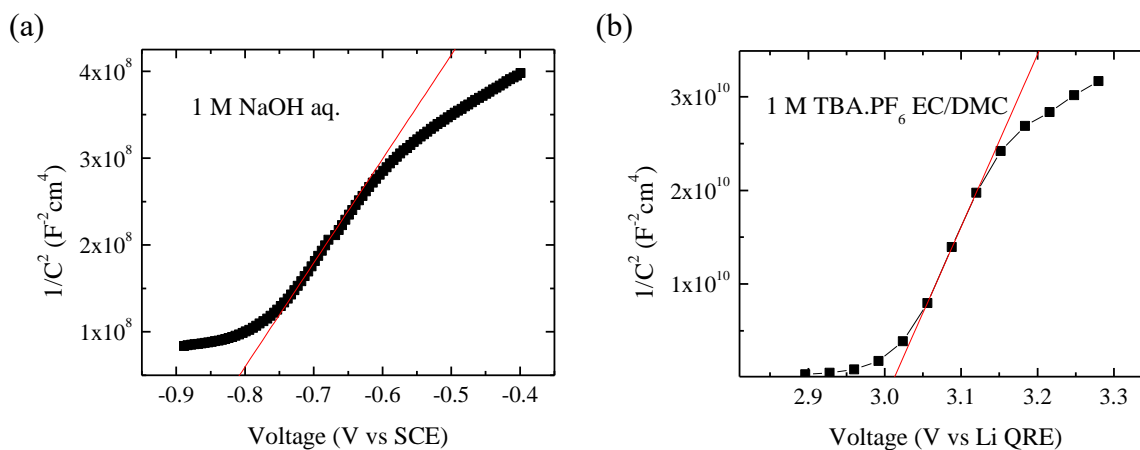


Figure 2.20. Mott-Schottky plot of 5 nm nanocrystalline anatase TiO_2 measured in (a) 1 mol/L NaOH aqueous electrolyte at 750 Hz and (b) 1 mol/L TBAPF_6 EC/DMC electrolyte at 100 Hz.

The values of flat band potential and donor density were derived using the Mott-Schottky equation (eq. 2.11) (Table 2.1):

$$\frac{1}{C^2} = \left(\frac{2}{q\epsilon\epsilon_0NA}\right)\left(V - V_0 - \frac{kT}{q}\right) \quad (2.11)$$

where C is the differential capacitance of the space-charge layer (C), ϵ_0 is the permittivity (dielectric constant) of vacuum, ϵ_r is the relative dielectric constant of material, N is the charge carrier density (cm^{-3}) (N_d , i.e. donor density for n-type semi-conductor and N_a acceptor density for p-type semi-conductor), A is the sample's area (cm^2), V is the electrode potential (V), V_{fb} is the flat band potential (V), k is the Boltzmann's constant ($1.38 \cdot 10^{-23}$ J/K), q is the elementary charge ($1.6 \cdot 10^{-19}$ C), and T is the absolute temperature (K).

Table 2.1. Flat band potential and charge carrier concentration of 5 nm nanocrystalline anatase TiO_2 in 1 mol/L NaOH aqueous electrolyte and 1 mol/L TBAPF₆ EC/DMC electrolyte.

Electrolyte	Flat band potential		Donor density, cm^{-3}
	as measured	recalculated, V vs. NHE	
1 mol/L NaOH aqueous	-0.87 V vs. SCE	-0.63 (pH = 14)	$9.8 \cdot 10^{17}$
1 mol/L TBAPF ₆ EC/DMC	2.99 V vs. Li QRE	-0.20	$2.3 \cdot 10^{19}$

In a 1 mol/L NaOH aqueous solution (pH = 14), the flat band potential value was determined at -0.87 V (vs. SCE). It translates into -0.63 V vs. NHE at pH = 14. This result is in agreement with literature even though a quite large range of values is reported based on various techniques, such as Mott-Schottky measurements (-1.01 to 0.56 V vs. NHE at pH = 14) [7, 58–61], photocurrent measurements (-0.07 V vs. NHE at pH = 14) [62], electron affinity measurements (0.6 V vs. NHE) [63], and calculations (-0.70 V vs. NHE at pH = 14) [64]. The calculation of the donor density considering a dielectric constant of 31 [3-4] leads to a value of $9.8 \cdot 10^{17} \text{ cm}^{-3}$. It also falls in the wide range of values reported in literature from 10^{17} to 10^{19} cm^{-3} [5, 59–61, 65–69]. Such a variation of values can stem from the fact that TiO_2 is often not a single crystal, thus containing intraband gap surface states and can be easily doped by impurities with important consequences on carrier density as a result from its $3d^0$ electronic configuration.

In the non-aqueous aprotic electrolyte, i.e. 1 mol/L TBAPF₆ EC/DMC, a flat band potential of -0.20 V (vs. NHE) was determined. The comparison of the results in different media is difficult because of the establishment of proton specific adsorption-desorption equilibrium in protic solvents and the absence of such in aprotic counterpart. Such an important dependence on the nature of the electrolyte is in agreement with the work reported by Fitzmaurice et al. who

presented a comparable flat-band potential values for measurements in water (-1.03 V vs. NHE at pH = 14) and in non-aqueous protic solvents (-1.2 V vs. NHE for MeOH and -0.9 V vs. NHE for EtOH), but significantly lower values in non-aqueous aprotic solvents (-1.8 V vs. NHE for DMF, -2.0 V vs. NHE for ACN, and -2.1 V vs. NHE for THF) [58]. Interestingly, Fox et al. reported much higher flat band potentials of TiO₂ in DMF (-0.9 V vs. NHE) and THF (-1.0 V vs. NHE) comparable to those measured in water at pH = 14 [70]. To the best of our knowledge, there is no previous literature on the determination of the flat-band potential of TiO₂ in TBAPF₆ EC/DMC electrolyte whereas it represents from a fundamental point of view an interesting approach and data collection to better understand equilibrium of carriers between battery materials with its carbonate-based electrolyte.

Making direct comparison of our results with literature values in other non-aqueous aprotic electrolytes is complicated due to the strong dependence of flat band potential on the nature and concentration of the salt in the electrolyte [58]. Following the conclusion of Fitzmaurice et al. who discussed that anions in the electrolyte have negligible influence on the V_{fb} value, we examined the results obtained in the electrolytes containing the same cation (TBA⁺) and tried to rationalize a trend based on the electrolyte solvent nature. The -0.20 V vs. NHE determined in 1 mol/L TBAPF₆ EC/DMC is much more positive than those reported for 0.2 mol/L TBAP (tetrabutylammonium perchlorate) in different types of solvents, i.e. DMF (-0.9 and -1.8 V vs. NHE), THF (-1.0 and -2.1 V vs. NHE) and ACN (-2.0 V vs. NHE) [58]. Table 2.2 gathers all flat-band potential values reported in the literature for TiO₂ in different aprotic electrolytes including their dielectric constants. This comparison highlights that there is no clear relationship between the flat-band potential and the dielectric constant of the solvent. This is in agreement with the conclusions made by Fox et al. who suggested that V_{fb} in aprotic solvent is constant for a given electrolyte but may depend on the solvent nature in absence of any added protic solute.

Besides the flat-band potential value, the charge carrier concentration can also vary to a large extent. Our results show more than one order of magnitude higher values in EC/DMC-based electrolyte, i.e. $2.3 \cdot 10^{19} \text{ cm}^{-3}$ compared to $9.8 \cdot 10^{17} \text{ cm}^{-3}$ in aqueous solution. This means that depending on the electrolyte nature, this latter can dope the nanocrystals during the Fermi level equalization process.

Table 2.2. Flat-band potential derived from Mott-Schottky measurements in aprotic electrolytes

Solvent	$\epsilon_{\text{solvent}}$	V_{fb} , V vs. NHE	Salt	Ref.
THF	7-8	-2.1	0.2 M TBAP	[58]
		-1.0	unknown	[70]
DMF	37	-1.8	0.2 M TBAP	[58]
		-0.9	unknown	[70]
ACN	37	-1.3	unknown	[70]
		-1.9	0.2 M TBAP	[58]
		-2.1	TBAP	[71]
		-2.0	TBAP	[72]
		-1.8	0.2 M TBAP	[73]
ACN/IPA (4/1)	18-37	-1.7	0.2 M TBAP	[73]
Me ₂ SO	49	-0.7	unknown	[70]
EC/DMC (1/1)	34-41	-0.2	1 M TBAPF ₆	This work

2.3.3. Evolution of the flat band potential and charge carrier concentration upon Li⁺ insertion into TiO₂

The evolution of TiO₂ band edge positions and donor density upon lithium insertion was studied using a similar approach and methodology as aforementioned. For this experiment, a mesoporous film of 10 μm thickness composed of 20 nm nanoparticles of TiO₂ was used to preserve the consistency with the above presented *in situ* UV-visible absorption spectroscopy measurements. We remind that our previous results show no size dependence of the particles on the flat band potential and carrier concentration. The Mott-Schottky capacitance was measured in a two-electrode transparent electrochemical cell using a lithium strip as both counter and quasi-reference electrode (stable at -3.402 V vs. Fc⁺/Fc) in 1 mol/L TBAPF₆ EC/DMC. Lithium insertion was carried out in 1 mol/L LiPF₆ EC/DMC by galvanostatic discharge at $j = -100 \mu\text{A}/\text{cm}^2$ until 1.5 V (vs. Li⁺/Li) to reach final Li_{0.6}TiO₂ composition. The lithiated electrode was then thoroughly rinsed inside the glovebox with DMC to remove all

possible traces of lithium. The electrode was then assembled back into the cell including 1 mol/L TBAPF₆ EC/DMC electrolyte for Mott-Schottky measurements.

As a result of lithium insertion into the structure, there is a noticeable shift of the flat band potential towards positive potentials (Fig. 2.21). This latter moves from 2.84 to 3.36 V vs. Li⁺/Li. To the best of our knowledge, there is no other experimental studies reported in the literature aiming at determining band movements in lithiated phase Li_{0.6}TiO₂ and in aprotic carbonate-based electrolyte. However, in good trend with our results, Fitzmaurice et al. reported a flat band potential increase by 1.14-1.23 V assigned to the lithium insertion into TiO₂ based on absorbance measurements. This was performed in 0.2 mol/L TBAP ACN-based electrolyte containing 10⁻³ mol/L of LiClO₄ supporting electrolyte [58]. It has to be noted that lithium cation in electrolyte is a potential determining ion due to its specific adsorption mechanism, as it is extensively reported in literature for protons [74-75], DMPI⁺ [76], and Li⁺ ions [58, 76–78]. One consequence of this surface adsorption mechanism is the shift of potential towards positive values when increasing the concentration of lithium in agreement with a Nernst law.

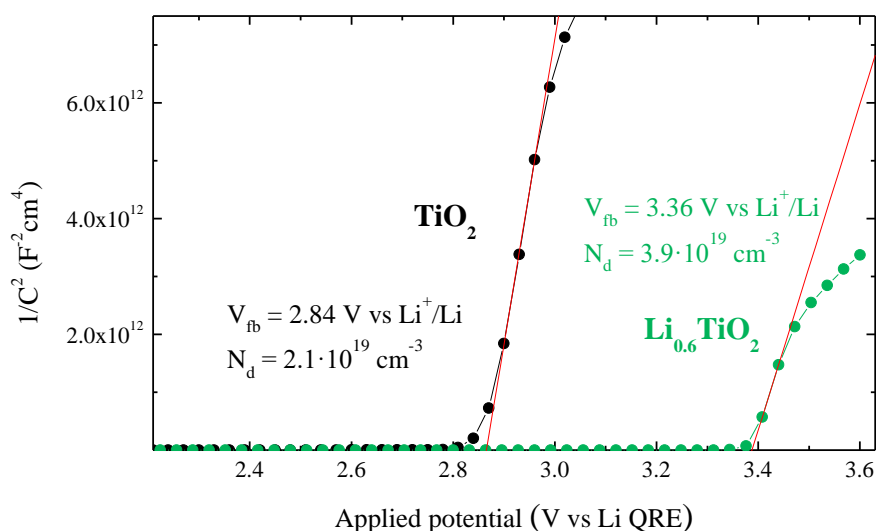


Figure 2.21. Mott-Schottky plot comparing TiO_2 and $\text{Li}_{0.6}\text{TiO}_2$ in 1 mol/L TBAPF₆ EC/DMC electrolyte at 316 Hz perturbation frequency.

Lithium insertion also leads to an increase of carriers' density from $2.1 \cdot 10^{19}$ to $3.9 \cdot 10^{19} \text{ cm}^{-3}$ without any change in the nature of the main carriers. This trend is in good agreement with Van der Krol et al. who reported by Mott-Schottky experiments higher donor densities for lithiated phase, i.e. $8.7 \cdot 10^{17} \text{ cm}^{-3}$, compared to pristine TiO_2 , i.e. $1.4 \cdot 10^{17} \text{ cm}^{-3}$ in 1.0 mol/L LiClO₄ in

propylene carbonate [6]. Even though the reliability of the Mott-Schottky measurements in an ion-conducting electrolyte can be questioned, the authors claimed that the capacitance measured can be entirely attributed to the space charge capacitance based on electrochemical impedance spectroscopy. Even though the charge carrier concentration reported by Van der Krol et al. was calculated using a dielectric constant of 50 for both pristine and lithiated TiO_2 , the authors also report an increase in the dielectric constant of lithiated anatase TiO_2 ($\text{Li}_{0.5}\text{TiO}_2$) to as high as 500 and 900 at a surface region in the film extending to at least 7 nm in depth [6]. A comparable increase in the dielectric constant up to 880 has also been reported upon the proton insertion into the anatase TiO_2 [79]. At the same time, Boschloo et al. attributed the changes in the (C-V) characteristics, from which the dielectric constant is derived, rather to the increase in donor density upon H^+ doping [80]. We support this hypothesis since reaching such a very high dielectric constant is questionable in light of the rather low differences of crystallography between the two phases. In addition, if we consider a dielectric constant of 500 for $\text{Li}_{0.6}\text{TiO}_2$, this would result to a donor density of $2.4 \cdot 10^{18} \text{ cm}^{-3}$; a value lower than TiO_2 which comes in contradiction to results discussed in paragraph 2.2.2 based on Drude model. Consequently, on the basis of these results and knowing that crystal structure is not drastically modified by lithium insertion, we consider that dielectric constant should not vary at all or only to a very low extent. Thus, in the following calculations a dielectric constant of 31 as for TiO_2 was kept constant [3].

One can notice that the charge carrier concentration values derived from the Mott-Schottky experiment are at least one order of magnitude lower than those determined by the Drude model. This discrepancy can be explained by the presence of surface traps and grain boundaries in the nanocrystalline TiO_2 which can be optically excited and not electrochemically because of their shallow position in the band gap that prevents any excitation in a low frequency range of 100 Hz to 1 kHz.

The positive shift of V_{fb} and increase of N_d as above discussed is representative for all the Mott-Schottky experiments in a frequency range from 100 Hz to 1 kHz (Fig. 2.22). $\text{Li}_{0.6}\text{TiO}_2$ follows a similar frequency dependence as discussed above for TiO_2 , i.e. decrease of both flat band potential and carrier concentration values while increasing the small perturbation frequency. However, it seems more pronounced in the determination of the donor density for $\text{Li}_{0.6}\text{TiO}_2$.

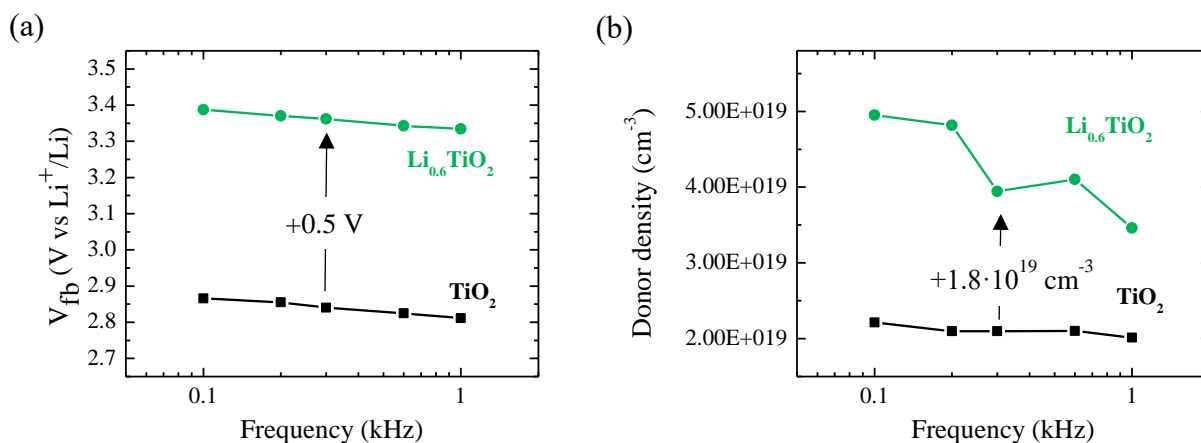


Figure 2.22. Frequency dependence of (a) the flat band potential and (b) charge carrier density of TiO_2 and $\text{Li}_{0.6}\text{TiO}_2$ between 100 Hz and 1 kHz in 1 mol/L TBAPF₆ EC/DMC electrolyte.

The combination of the Mott-Schottky experiment and solid-state UV-Visible absorption spectroscopy enabled evaluation of the energy position of the top of the valence band. Figure 2.23 schematizes the band structure and energy of the band edges for TiO_2 and for its reduced form $\text{Li}_{0.6}\text{TiO}_2$. It shows a lowering in energy of both the valence band by 800 mV from 5.7 V to 6.5 V and conduction band by 500 mV from 2.8 V to 3.3 V (vs. Li^+/Li) upon lithium insertion. This experimental observation gives credit to the DFT calculations reported by Wagemaker et al. who predicted such a movement upon lithium insertion [81]. As a consequence, this means that the photogenerated holes in $\text{Li}_{0.6}\text{TiO}_2$ have a stronger oxidizing character than in TiO_2 counterpart. In this scheme, we also present HOMO and LUMO positions of the electrolyte deduced from both electrochemical cyclic voltamperometry experiments and the optical band gap measurements. The HOMO value is in agreement with literature data even though a broad range of values have been reported for the oxidation potential of PF_6^- between 4.94 V (vs. Li^+/Li) [82] and 6.8 V (vs. Li^+/Li) [83]. Upon illumination of $\text{Li}_{0.6}\text{TiO}_2$, the photogenerated holes oxidize the Ti^{3+} transition metal centers leading to a release of Li^+ out from the structure (i.e. electrode photorecharge). However, in parallel, the oxidizing strength of these holes is sufficient to also oxidize PF_6^- .

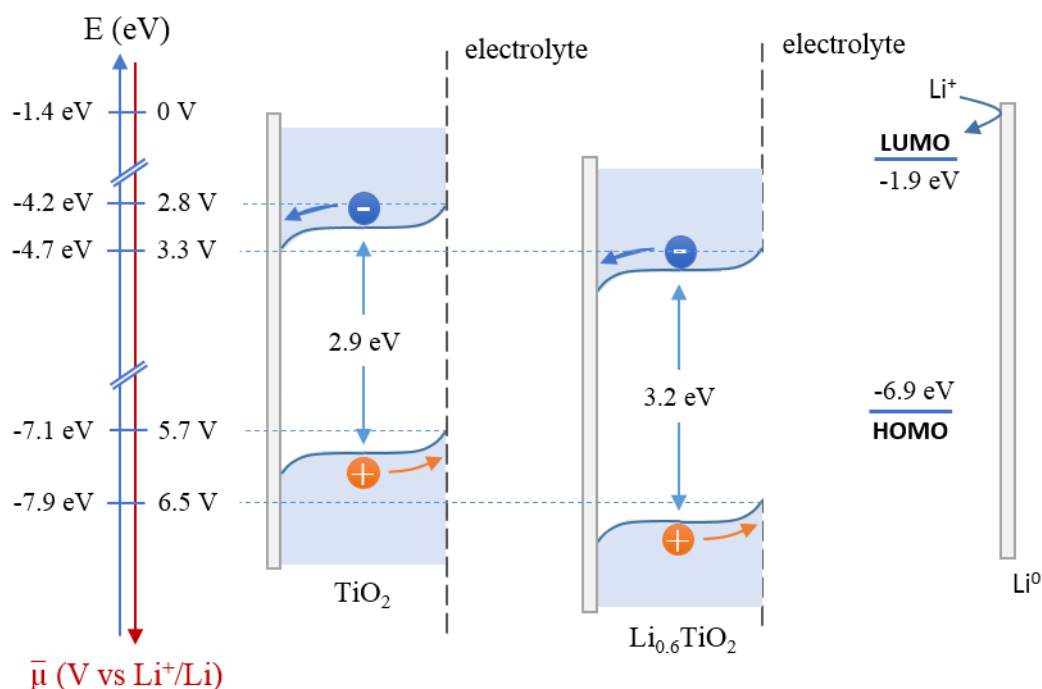


Figure 2.23. Schematic energy diagram of the valence band and conduction band positions of TiO_2 and its discharged form $\text{Li}_{0.6}\text{TiO}_2$ determined in 1 mol/L TBAPF_6 EC/DMC electrolyte. It is compared to HOMO and LUMO positions of the electrolyte (1 mol/L LiPF_6 EC/DMC).

2.4. Fluorescence spectroscopy

The anatase TiO_2 is known to be an excellent UV-absorber ($320 \text{ nm} < \lambda < 410 \text{ nm}$) emitting in the visible range ($430 \text{ nm} < \lambda < 730 \text{ nm}$) [84]. From a practical point of view, better understanding of the material's photoluminescence in the different media can provide further information regarding the excited-state dynamics of the photo-anode depending on its oxidation state and the media.

2.4.1. Photoluminescence spectroscopy basics

Photoluminescence is a physical phenomenon probing photon emission in response to light excitation. It is typically explained by the Jablonski diagram presented in Figure 2.24 [85]. Upon photon absorption, the electron is excited from the ground singlet state (S_0) into the excited singlet states (S_1, S_2, \dots). A non-radiative relaxation from higher energy level to lower lying energy levels such as for instance from S_2 to S_1 or inside S_1 or S_2 excited singlet states is called internal conversion. This is most often an ultra-fast relaxation process taking place in the femtosecond time-scale that can be monitored by transient absorption spectroscopy. The

radiative decay of electrons back to the valence band is called direct band-to-band recombination. However, when dealing with nanocrystalline particles instead of large single crystals, longer photoluminescence processes can also take place through either surface shallow traps or deeper traps in the band gap (ns time-scale). For molecules typically containing heavy metals, non-radiative singlet-to-triplet transitions involving so-called intersystem crossing (ISC) mechanism can also take place. This leads at end to generate very long lifetimes that can reach up to phosphorescence (10^{-6} – 10^2 s). This latter can also take place when very deep trapping of carriers occurs at the defect or impurity sites in the crystal (T_1) [86].

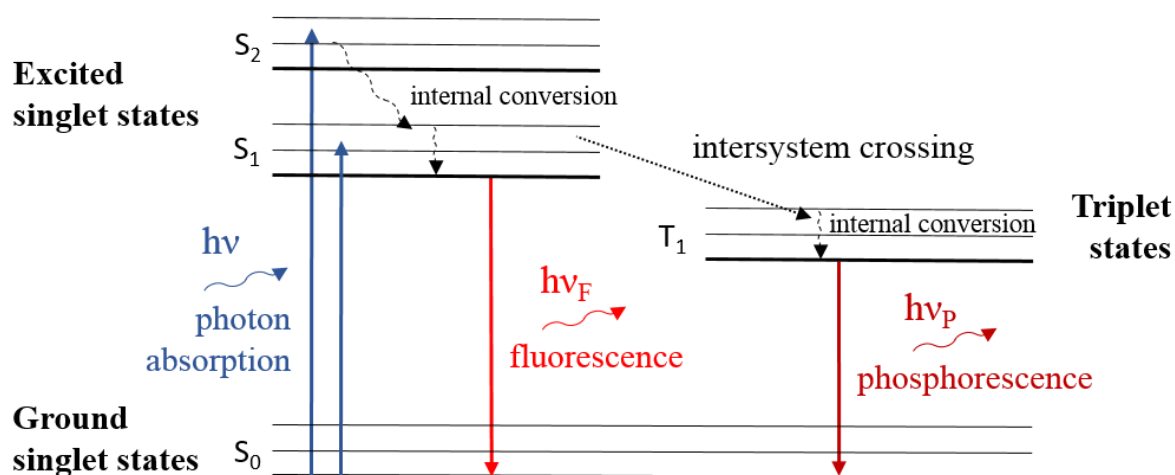


Figure 2.24. Jablonski diagram adapted from reference [85].

2.4.2. Steady-state fluorescence of anatase TiO_2 nanocrystals

The steady-state excitation/emission map of the 5 nm nanocrystalline anatase TiO_2 powder was recorded on FLS980 spectrometer (Edinburgh Instruments) equipped with double excitation/emission monochromators to reduce stray light rejection to less than $1:10^{-10}$. Figure 2.25 (a) shows excitation/emission map of the nanocrystals in the range of exc. 300-700 nm / em. 312-712 nm. The maximum emission is reached at 380 nm excitation wavelength leading to two distinct emission bands at 416 nm and 438 nm (Fig. 2.25 (b)). This corresponds to a Stokes shifts of 36 nm (2277 cm^{-1}) and 58 nm (3485 cm^{-1}) corresponding to the lattice relaxation energy based on the Franck-Condon theory [87]. Our values are close to the 60 nm reported by Niederberger et al. [88], but significantly smaller than the range from 141 to 174 nm as reported in other studies [89–92]. The emission spectrum of TiO_2 can be deconvoluted using a Gaussian function into four bands located at about 413, 435, 450, and 472 nm (Fig. 2.25 (c)). This implies that the radiative recombination takes place through different relaxation pathways. The first

band at 413 nm corresponds to the fluorescence of the self-trapped excitons localized on TiO_6 octahedra in nanocrystalline anatase TiO_2 [93-94]. The broad luminescence over the range of 420-600 nm, comprising the bands 2-4, is attributed to recombination pathways through different distributed surface states [95] and shallow traps in the band gap often associated with oxygen vacancies located 0.51-0.82 eV below the conduction band [42, 94, 96].

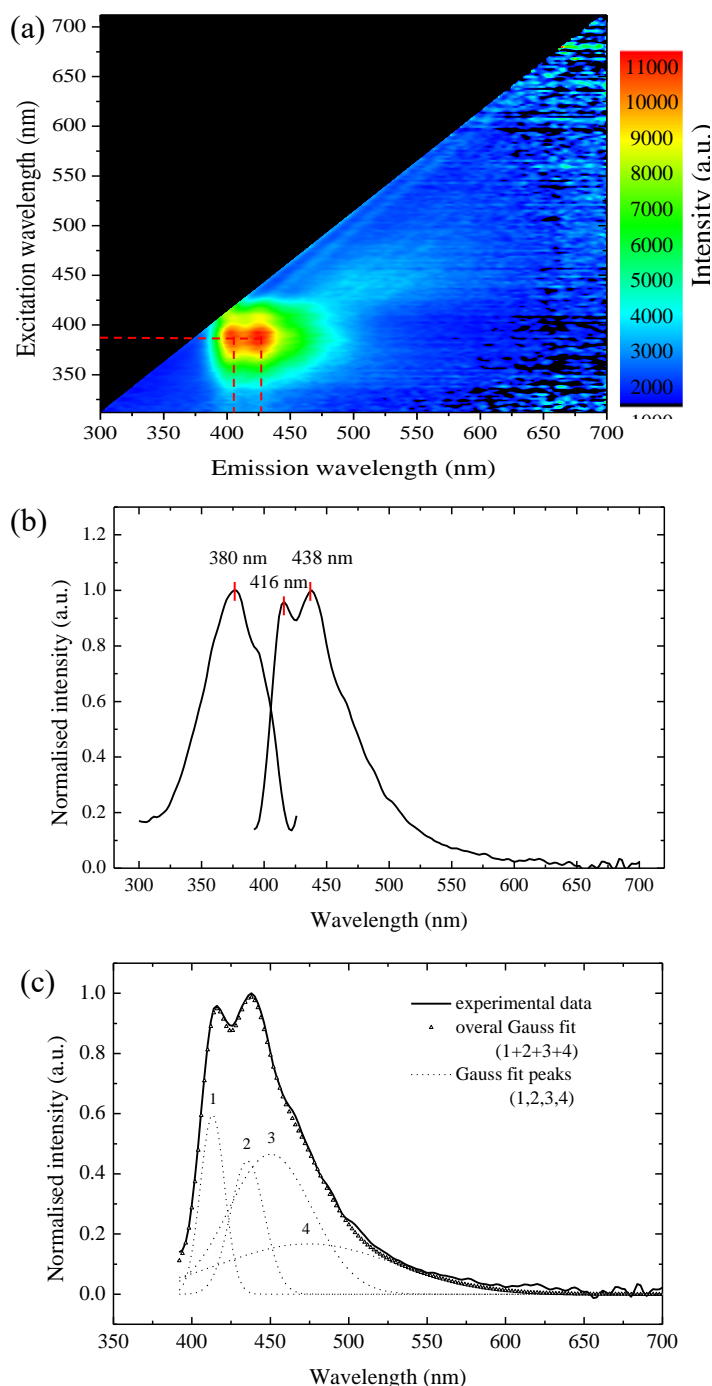


Figure 2.25. Steady-state photoluminescence of 5 nm nano-crystals of anatase TiO_2 particles: (a) excitation / emission map, (b) normalized excitation / emission spectrum at maximum intensity, and (c) deconvolution of the emission spectrum measured at 380 nm excitation wavelength.

The absolute fluorescence quantum yield (QY) of the nanocrystals was determined using both direct and indirect measurement methodologies using an integration sphere (Fig. 2.26 (a)) [97]. As a result, the integration of the fluorescence spectra leads to a value of quantum yield from scratch equal to -0.4 %. The negative sign of the value stems from the very low emission signal close to the noise and the high character of light scattering from the samples. This result highlights the low quantum yield that falls below the detection limit, i.e. <1%. In order to bypass this intrinsic issue, we have attempted to compare the absolute intensities of emission from TiO₂ to that of the scattering barium sulfate reference recorded in a steady-state fluorescence mode at 380 nm excitation wavelength (Fig. 2.26 (b)). Being 100% reflective, the reference emission intensity, i.e. $4 \cdot 10^5$ counts, equals to the full incident light intensity received by TiO₂ upon excitation. The absolute value of TiO₂ emission intensity varying from $1.5 \cdot 10^2$ to a maximum of $1 \cdot 10^3$ counts which in turn represents a fluorescence QY value of 0.25%, thus confirming the very low photoluminescence yield of TiO₂ when the integrating sphere was used. This value is in good agreement with literature, where the quantum yield of anatase TiO₂ at room temperature is reported from 0.25% [98] to 1% [88] by comparison of the wavelength-integrated emission intensity to that of a standard reference molecule.

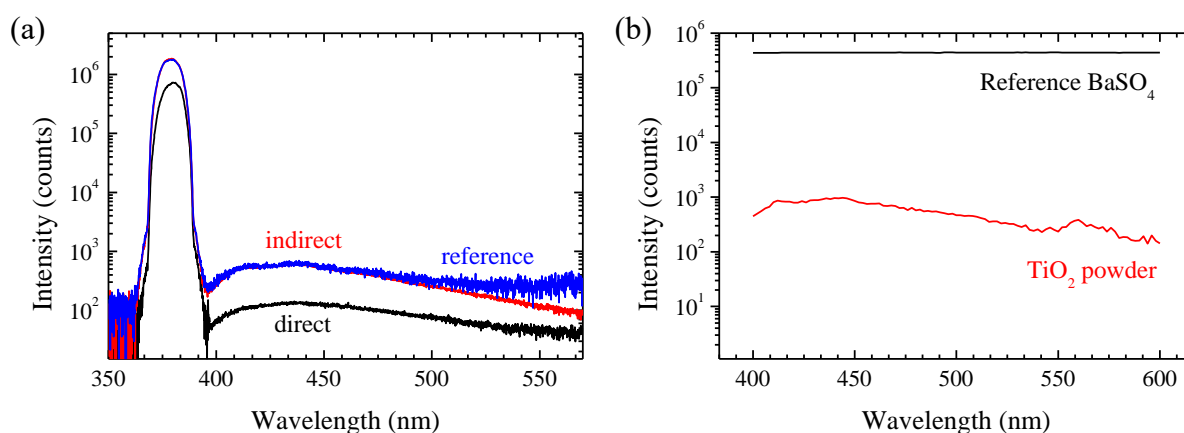


Figure 2.26. Fluorescence of 5 nm nanocrystalline anatase TiO₂ particles: (a) quantum yield spectra measured in direct and indirect mode using an integrating sphere and (b) steady-state emission spectra excited at 380 nm compared to the reference BaSO₄ sample.

2.4.3. *In situ* steady-state fluorescence upon lithiation

The evolution of TiO₂ fluorescence upon lithium insertion was investigated *in situ* by joining the fluorimeter with a two-channel VSP potentiostat/galvanostat (Bio-logic) to maintain a bias voltage during the experiment. For this electro-luminescence experiment, a specific three-electrode air-tight cuvette cell with four sides polished was specifically developed. It is in

principle the same set-up which was used for the UV-Visible absorption spectroscopy reported in section 2.2.3 at the exception of its size which is here 3 x 3 cm. The different fluorescence excitation/emission maps were recorded on screen-printed 12 μm thick anatase TiO_2 film at different depth of discharge (Fig. 2.27). The maps show systematically one principal band for which the maximum is located at 277 nm excitation and 335 nm emission. This energy position differs significantly from TiO_2 powder in air as showed in Figure 2.26.

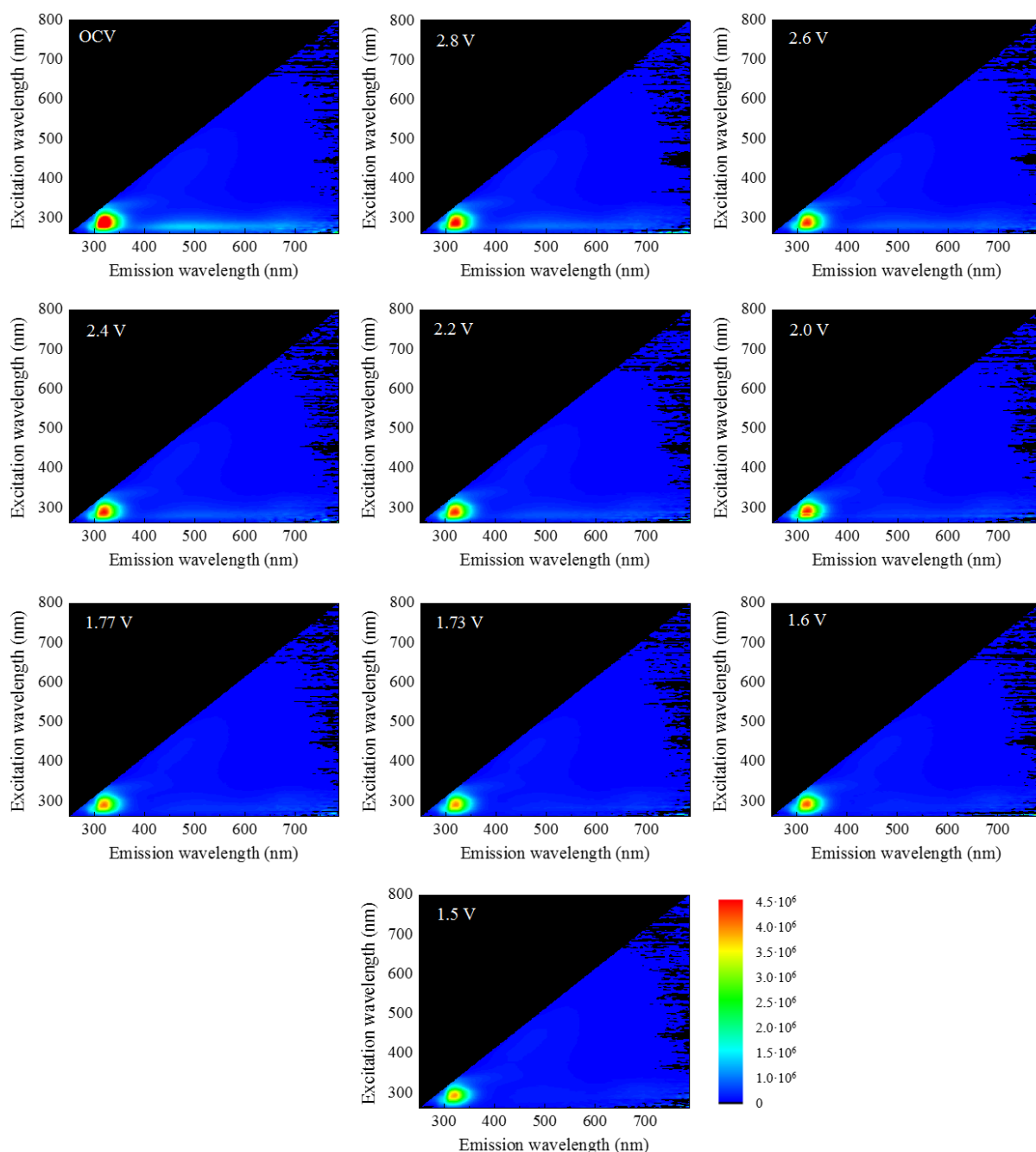


Figure 2.27. Steady-state photoluminescence map of 5 nm nanocrystalline TiO_2 electrode in 1 mol/L LiPF_6 EC/DMC at different depth of discharge. Note that intensity scale is same for all maps.

Looking more closely at the emission spectrum at 277 nm excitation wavelength, one can see two emission bands: a main band at around 335 nm and a second broader and much weaker in intensities at around 500 nm (Fig. 2.28). This latter is hardly visible on the maps due to its low intensity. The maximum of this broad contribution tends to shift towards red from 498 to 515 nm when discharging the electrode in contrast to the first band for which only the intensity is dependent on the electrode's potential (i.e. no effects on the band energy). The first band is attributed to the fluorescence of the solvated Li^+ and PF_6^- in EC/DMC electrolyte (Fig. 2.29 (a)) [99]. The origin of the second band is attributed to deeper trap-mediated fluorescence of TiO_2 nanocrystals in equilibrium with the electrolyte that contains potential-determining cations (i.e. Li^+). In addition, another contribution seems to appear at around 700 nm upon the discharge. It is however ascribed to the measurement noise, the amplitude of which above 630 nm becomes comparable or even higher than the intensity of TiO_2 fluorescence. Interestingly, both TiO_2 and electrolyte fluorescence yields decrease upon lithium insertion in TiO_2 nanocrystals. The quenching of electrolyte luminescence, up to five times in intensity, depending on the bias voltage applied to TiO_2 is surprising at first sight. This result suggests that a part of the radiative energy from the electrolyte is transferred to the electrode, and, that this energy transfer process in benefit to TiO_2 is more efficient when the electrode is lithiated. At same time, the fluorescence QY of the electrode is decreasing when lithiated despite the energy transfer from the electrolyte. This means that the radiative recombination process in Li_xTiO_2 is quenched compared to TiO_2 as one could expect as a result from the hole transfer from Ti^{3+} to Ti^{4+} which is responsible for the electrode's photorecharge.

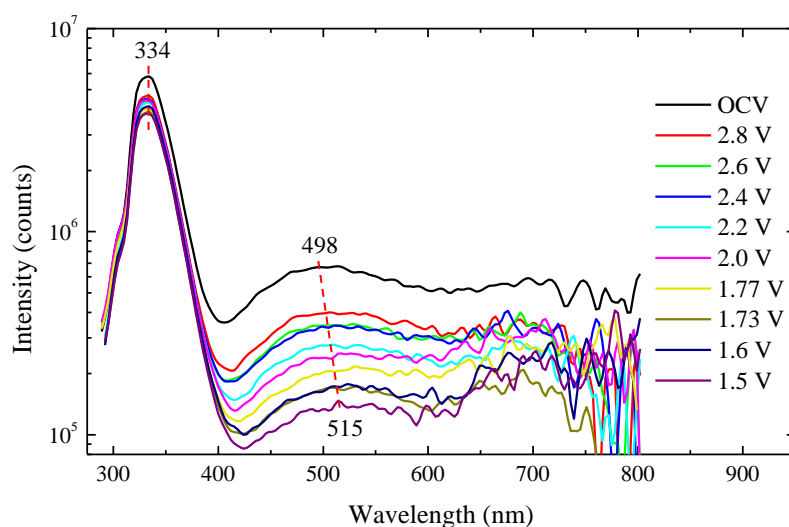


Figure 2.28. Emission spectra of 5 nm nanocrystalline TiO_2 in 1 mol/L LiPF_6 EC/DMC at different depth of discharge (Li^+ insertion) using 277 nm excitation wavelength.

The FRET mechanism is clearly feasible for three reasons. The QY of luminescence of the electrolyte is much greater than TiO_2 ($\text{QY}_{\text{LP30}} = 7.7\%$), the high molecular proximity between solvated Li^+ and PF_6^- responsible for the electrolyte fluorescence and TiO_2 nanocrystals, and thirdly, there is an energy overlap between the emission band of the electrolyte and the excitation band of TiO_2 and $\text{Li}_{0.6}\text{TiO}_2$ nanocrystals.

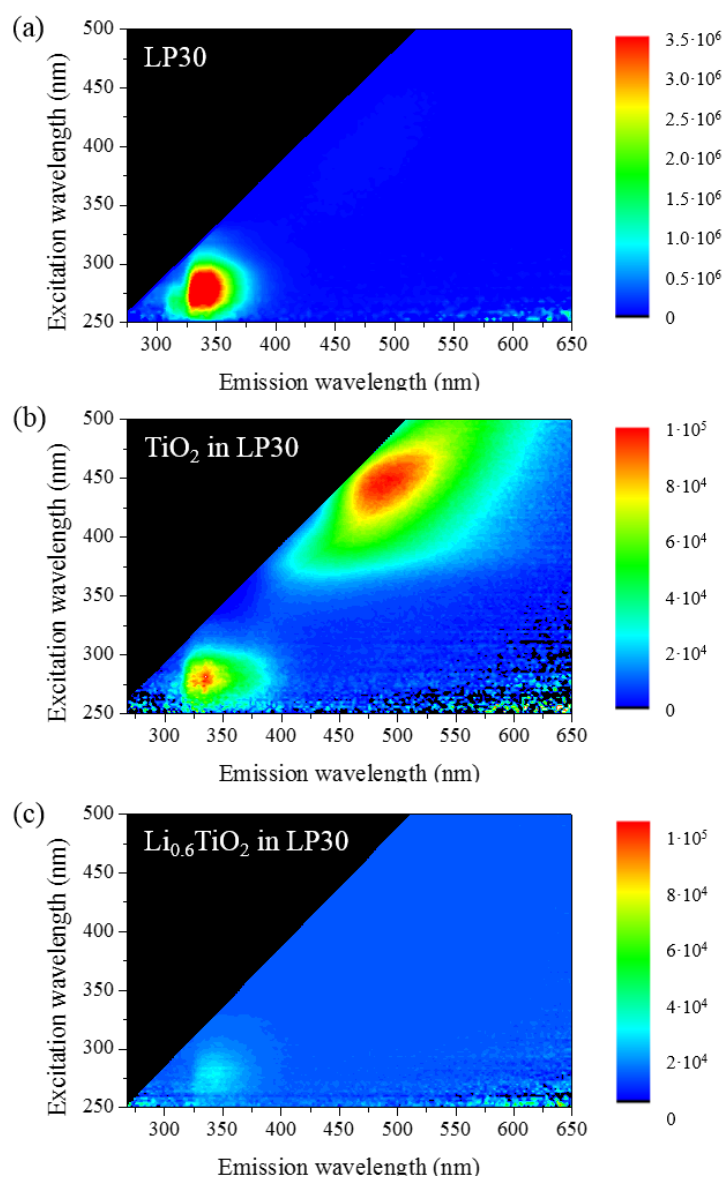


Figure 2.29. Steady-state photoluminescence map of (a) LiPF_6 EC/DMC electrolyte, (b) colloidal solution of TiO_2 in LiPF_6 EC/DMC electrolyte and (c) colloidal solution of $\text{Li}_{0.6}\text{TiO}_2$ in LiPF_6 EC/DMC electrolyte. Note that the intensity scale has been reduced 35 times between (a) and (b-c).

The observed quenching of fluorescence of both TiO_2 and electrolyte is consistent with the fluorescence measurements obtained through a colloidal solution, i.e. without any electrical

bias on electrode, containing either 5 nm TiO₂ or Li_{0.6}TiO₂ in LP30 electrolyte (Fig. 2.29 [29]). In this case, 40 mg of powder was introduced in 3 mL of electrolyte. TiO₂ nanocrystals quench the luminescence of the electrolyte by energy transfer of likely Förster type (FRET) from $3.5 \cdot 10^6$ counts to $1.0 \cdot 10^5$ counts (Fig. 2.29 (a-b)). This process is clearly more efficient in the case of lithiated nanocrystals as observed on biased electrodes. In the case of colloidal solution, we found a nearly total bleaching of the electrolyte ($2.5 \cdot 10^4$ counts) which is prone for an enhanced FRET mechanism in contact with the lithiated particles (Fig. 2.29 (c)). This is consistent with the greater light absorption of the particles when lithiated in agreement with the UV-visible absorption spectra as a function of the depth of discharge reported in Fig. 2.11. This quenching process is thus not originating from any ions drift in the electrolyte or different solvation mechanism induced by the bias voltage. The yield of luminescence of Li_{0.6}TiO₂ is lower as a result from the photorecharge process in agreement with the films and may also in part be due to traps passivation by lithium insertion [100].

2.5. Determination of the kinetics of the charge transfer processes in TiO₂ by TCSPC

The study of the excited-state lifetime(s) can provide key information on evaluating the kinetics of charge recombination and on homogeneous/heterogeneous charge transfer processes when associated to photoluminescence quenching. A very limited number of publications report the dynamics of TiO₂ excited states, either on single crystals [101-102] or on powder suspension in aqueous solutions [103]. During this thesis, time-correlated single-photon counting (TCSPC) technique was used to investigate the radiative relaxation dynamics of TiO₂ and Li_{0.6}TiO₂ excited states in contact with different type of media.

TCSPC working principle is presented in Figure 2.30. It consists of measuring the arrival time of a photon emitted from a sample subsequently to a short-pulse light excitation. This luminescence time is compared to a reference light pulse arrival time itself. Each photon counting event adds up to the intensity number of the corresponding recombination time forming a memory histogram. The originally recorded photon counts versus channels represent the fluorescence intensity versus time, which is typically referred as time-resolved photoluminescence (PL) decay.

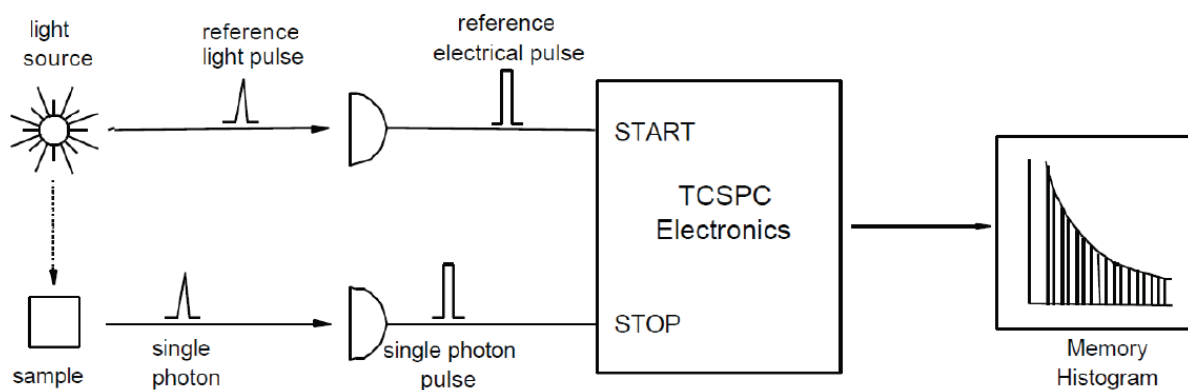


Figure 2.30. Schematic representation of the two-input stopwatch working principle of TCSPC (from Edinburg Instrumets ® TCSPC technical note)

2.5.1. *In situ* study of the time-resolved fluorescence of TiO_2 and $\text{Li}_{0.6}\text{TiO}_2$

Time-correlated single-photon counting measurements of TiO_2 and $\text{Li}_{0.6}\text{TiO}_2$ were performed under argon atmosphere using an EPL-375 picosecond pulsed diode laser as an excitation light source with a pulse width of ca. 75 ps at a frequency rate of 2 MHz. The fluorescence dynamics was recorded at 455 nm emission wavelength using a Peltier-cooled microchannel plate photomultiplier tube (MCP-PMT) Hamamatsu detector (time response < 25 ps). This latter is positioned after the first emission monochromator to minimize light traveling length, therefore to optimize the spectrometer time resolution. The corresponding decays for TiO_2 and $\text{Li}_{0.6}\text{TiO}_2$ are presented in Figure 2.31.

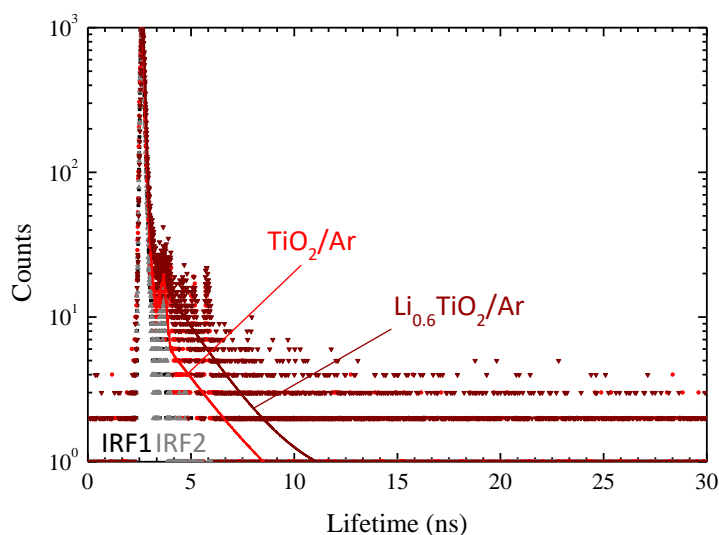


Figure 2.31. Evolution of the photoluminescence decay of TiO_2 and $\text{Li}_{0.6}\text{TiO}_2$ electrodes in an argon filled cuvette cell. The corresponding instrument response function decays IRF1 and IRF2 are presented for information.

The numerical reconvolution of each decay was performed by considering systematically the instrument response function (IRF) determined on 100% refractive BaSO₄ powder. The IRF full width at half maximum (FWHM) was ca. 80 ps. The lifetime values were determined using a multi-exponential mathematical function (eq. 2.12):

$$R(t) = \sum_{i=1}^4 B_i e^{-\frac{t}{\tau_i}} \quad (2.12)$$

This algorithm used in FAST software allows to perform an exponential fit of the decay using up to four fixed lifetime components (τ_i) and corresponding pre-exponential factors (B_i), while automatically excluding the constant background level of the curve. The mathematical reconvolution was carried out resulting in the reduced chi-square (χ^2) of the fits of less than 1.1. In our case, the most robust reconvolution of the decays was obtained by introducing two single-exponential components. The results show that for both TiO₂ and Li_{0.6}TiO₂ a very similar dynamics of excited-states is obtained very close to the IRF value (Table 2.3). The faster contribution is clearly the major, reaching 29 ps after reconvolution. It corresponds to the direct recombination from conduction band down to valence band. This value is at the real limit of the spectrometer capability, but is in good agreement with Bowman et al. who reported an average lifetime of 23 ps for 2 nm TiO₂ nanoclusters based on femtosecond transient absorption spectroscopy [104]. The longer component of ca. 2 ns is physically assigned to the trap-mediated fluorescence process [105]. It shows higher amplitude in the case of lithiated phase, i.e. 18.1% for Li_{0.6}TiO₂ vs. 8.5% for TiO₂. This difference originates from the redistribution of the traps in the band gap subsequently to lithium insertion. However, this result tends to contradict the traps passivation induced by lithium insertion discussed by Tsui et al. [100], but is in agreement with the work of Islam et al. who reported the formation of additional energy levels and trapping sites below the bottom of the conduction band induced by the defect clusters of Li⁺ interstitials and Ti³⁺ electronic species based on atomistic simulation study [106]. In addition to this slight but existing and well-reproducible difference in the photoluminescence decays, we also experienced a tenfold decrease in fluorescence yield for Li_{0.6}TiO₂ in agreement with the steady-state experiments (section 2.4.3).

Table 2.3. Lifetime and amplitude of the fluorescence decay after reconvolution from the IRF of TiO₂ and Li_{0.6}TiO₂ in contact with argon.

	TiO ₂		Li _{0.6} TiO ₂	
	Amplitude, %	Lifetime, ns	Amplitude, %	Lifetime, ns
τ_1	91.5	0.029	81.9	0.029
τ_2	8.5	2.19	18.1	1.96

In a lithium-free electrolyte based on 1 mol/L TBAPF₆ in EC/DMC electrolyte, corresponding to an ionic blocking interface that will prevent any photorecharge mechanism, the photoluminescence decay of TiO₂ was again best fitted with two components leading to a lifetime values of 25 ps (82.1%) and 2.39 ns (17.9%) (Fig. 2.32, table 2.4). The first component is still ascribed to the direct band-to-band recombination while the second to the trap-mediated fluorescence. The lifetime values are very comparable to those under argon except that more traps are involved in the fluorescence process as a result from the built-in depletion layer at the semiconductor/ electrolyte interface. Note that a difference between 29 ps and 25 ps cannot be discussed because of the IRF value of 80 ps. These results suggest the absence of any interfacial charge transfer process between the semiconductor and the electrolyte, or at least down to ca. 20-30 ps.

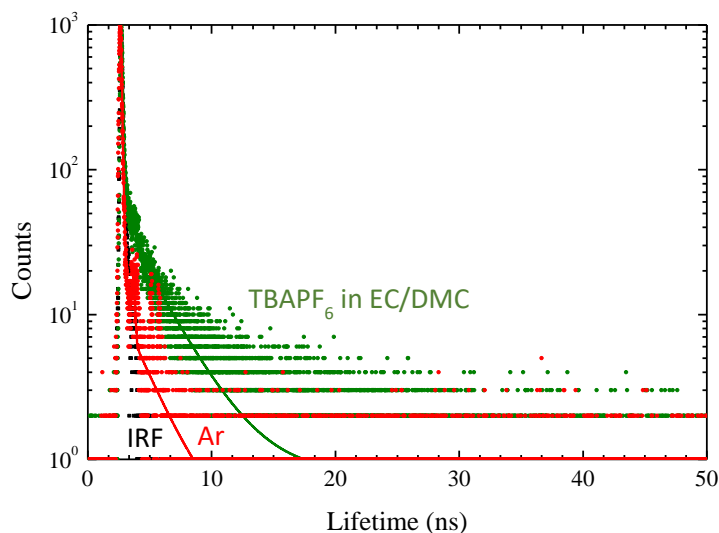


Figure 2.32. Photoluminescence decay of the anatase TiO₂ nanocrystals deposited upon FTO glass in contact with an electrolyte composed of 1 mol/L TBAPF₆ in EC/DMC. The photoluminescence decay of TiO₂ under argon and IRF is provided for comparison.

Table 2.4. Comparison of the lifetime values determined after reconvolution of the photoluminescence decay with the IRF for anatase TiO₂ nanocrystals either in contact with argon or with the electrolyte composed of 1 mol/L TBAPF₆ EC/DMC at open-circuit condition.

	TiO ₂ in contact with argon		TiO ₂ in 1 mol/L TBAPF ₆ EC/DMC	
	Amplitude, %	Lifetime, ns	Amplitude, %	Lifetime, ns
τ_1	91.5	0.029	82.1	0.025
τ_2	8.5	2.19	17.9	2.39

2.5.2. Kinetics of charge transfer processes in Li_{0.6}TiO₂ in contact with an electrolyte

Similar experiments were performed on the discharged composition Li_{0.6}TiO₂. We herein investigated two types of electrolyte, one based on the benchmark organic EC/DMC solvent mixture typically used in batteries (Fig. 2.33 (a)), and a second, more inert, based on EMITFSI ionic liquid (Fig. 2.33 (b)). The electrolytes were tailored by the nature of the added salt to be either ionic-blocking to hamper the electrode photorecharge (TBAPF₆) or ionic-conducting to enable the electrodes' photorecharge (LiPF₆). For the measurements in lithium-free electrolytes, Li_{0.6}TiO₂ was obtained by galvanostatic discharge inside an Ar-filled glove-box at $j = -100 \mu\text{A}/\text{cm}^2$ in LP30 electrolyte until 1.5 V vs. Li⁺/Li. After lithiation, the electrode was thoroughly rinsed with DMC as for the Mott-Shottky experiments. The electrode was then transferred into a TCSPC cuvette filled with the electrolyte and sealed inside the glove-box to ensure its air-tightness. For the lithium-ion conducting electrolytes, the time-resolved electro-luminescence experiments were performed in a three-electrode air-tight cuvette with TiO₂ as a working electrode, and two lithium strips as counter and reference electrode. By combining the galvanostat with the TCSPC spectrometer, the galvanostatic discharge at $j = -100 \mu\text{A}/\text{cm}^2$ down to 1.5 V vs. Li⁺/Li was directly performed inside the spectrometer chamber. Then, the electrode was potentiostatically stabilized at 1.5 V vs. Li⁺/Li until steady-state current close to 0 was obtained before any fluorescence decay was measured. The evolution of the photoluminescence decays of Li_{0.6}TiO₂ electrode in lithium ion-blocking and lithium ion-conducting electrolytes based on either EC/DMC solvent mixture or EMITFSI ionic liquid is presented in Figure 2.33.

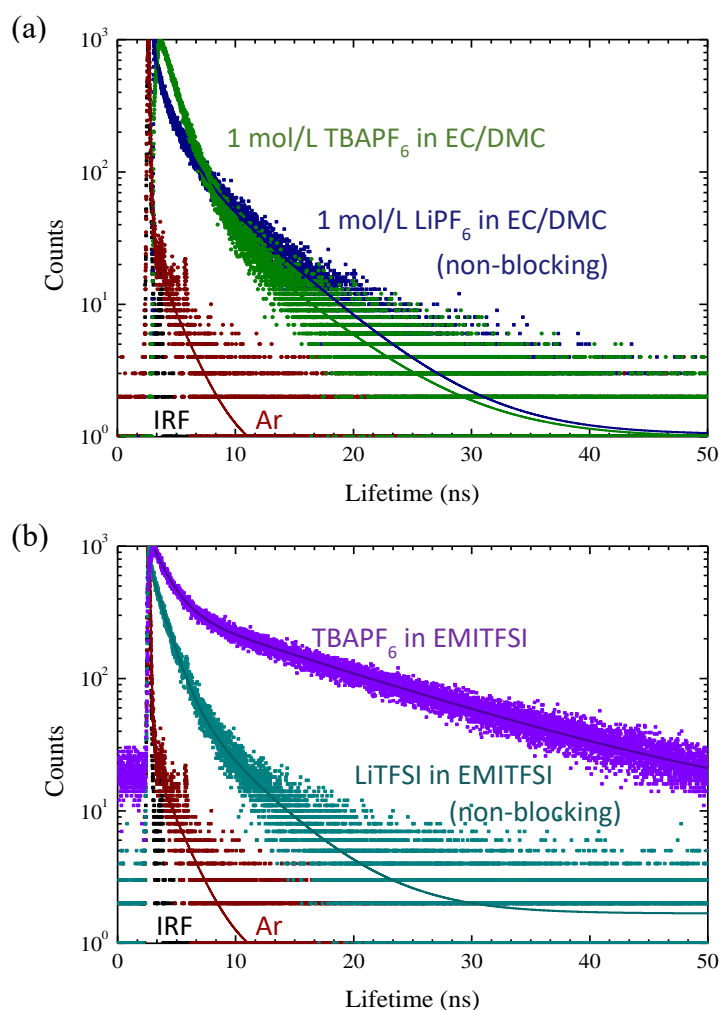


Figure 2.33. Evolution of the photoluminescence decay of $\text{Li}_{0.6}\text{TiO}_2$ electrode in (a) EC/DMC mixture or (b) EMITFSI ionic liquid based electrolytes containing or not lithium ions. The decay of $\text{Li}_{0.6}\text{TiO}_2$ in argon and IRF are provided for comparison.

When the photoluminescence of $\text{Li}_{0.6}\text{TiO}_2$ nanocrystals is measured in contact with EC/DMC and EMITFSI-based electrolytes, we observed significantly longer decays compared to Argon. This stems from the contact of the nanocrystals with a liquid interface of higher dielectric constant which tends to trap the electrons on the predominant surface of the particles. Indeed, the interfacial contact with the electrolyte hinders the band-to-band recombination to the benefit of slower processes through traps. This may also be the result of the Li^+ and/or TBA^+ cations forming “quasi-particles” with trapped electrons in the surface of the particles, thus prolonging the excited-state lifetime [107–109]. In both media, Li^+ -containing electrolyte’s decays are faster than those determined in lithium-free electrolytes. The reconvolution of the PL decays in lithium-based electrolytes requires systematically the means of a third fast contribution

suggesting the occurrence of an additional fast charge transfer process which we attribute to the hole transfer to Ti^{3+} that is responsible for the electrode's photorecharge (Table 2.5). This hole transfer is fast, requiring 145 ps in EC/DMC-based electrolyte, accounting for 7.8% of the total decay, and within 97 ps in EMITFSI ionic liquid representing 12.5% of the total decay. The difference in the amplitude tends to suggest that the photogenerated hole transfer process is more favorable in more inert EMITFSI ionic liquid media than in the EC/DMC-based electrolyte.

Table 2.5. Reconvolution results of the time-correlated single photon counting decays recorded on $Li_{0.6}TiO_2$ in EC/DMC and EMITFSI based electrolytes with or without Li^+ -containing salt.

	1 mol/L TBAPF ₆ EC/DMC		1 mol/L LiPF ₆ EC/DMC		1 mol/L TBAPF ₆ EMITFSI		1 mol/L LiPF ₆ EMITFSI	
	Amplitude, %	Lifetime, ns	Amplitude, %	Lifetime, ns	Amplitude, %	Lifetime, ns	Amplitude, %	Lifetime, ns
τ_1	-	-	7.8	0.145	-	-	12.5	0.097
τ_2	77.9	1.34	38.5	1.33	30.6	1.49	58.4	1.21
τ_3	22.1	5.88	53.7	5.44	69.4	14.6	29.1	4.85

The type of solvent influences the trap-mediated fluorescence mostly in terms of amplitude in the decay and less in terms of the lifetimes. This is likely due to a redistribution of energy and density of states of the intra-band gap traps. The longer lifetime is obtained in EMITFSI ionic liquid which reaches up to 14.6 ns with an amplitude of 69.4%. Along this line, we have evidenced experimentally a Stark-Lo Surdo effect on our nanocrystalline anatase TiO_2 particles induced by the specific adsorption of lithium cation upon the surface of the particles which is visible on the excitation/emission spectrum (Fig. 2.34), band gap value from 2.90 eV to 3.60 eV for TiO_2 in pure DMC and in highly concentrated 1.5 M of $LiPF_6$. Stark-Lo Surdo effect has also important consequences in the photoluminescence dynamics which we think is a beneficial mechanism for the electrode's photorecharge.

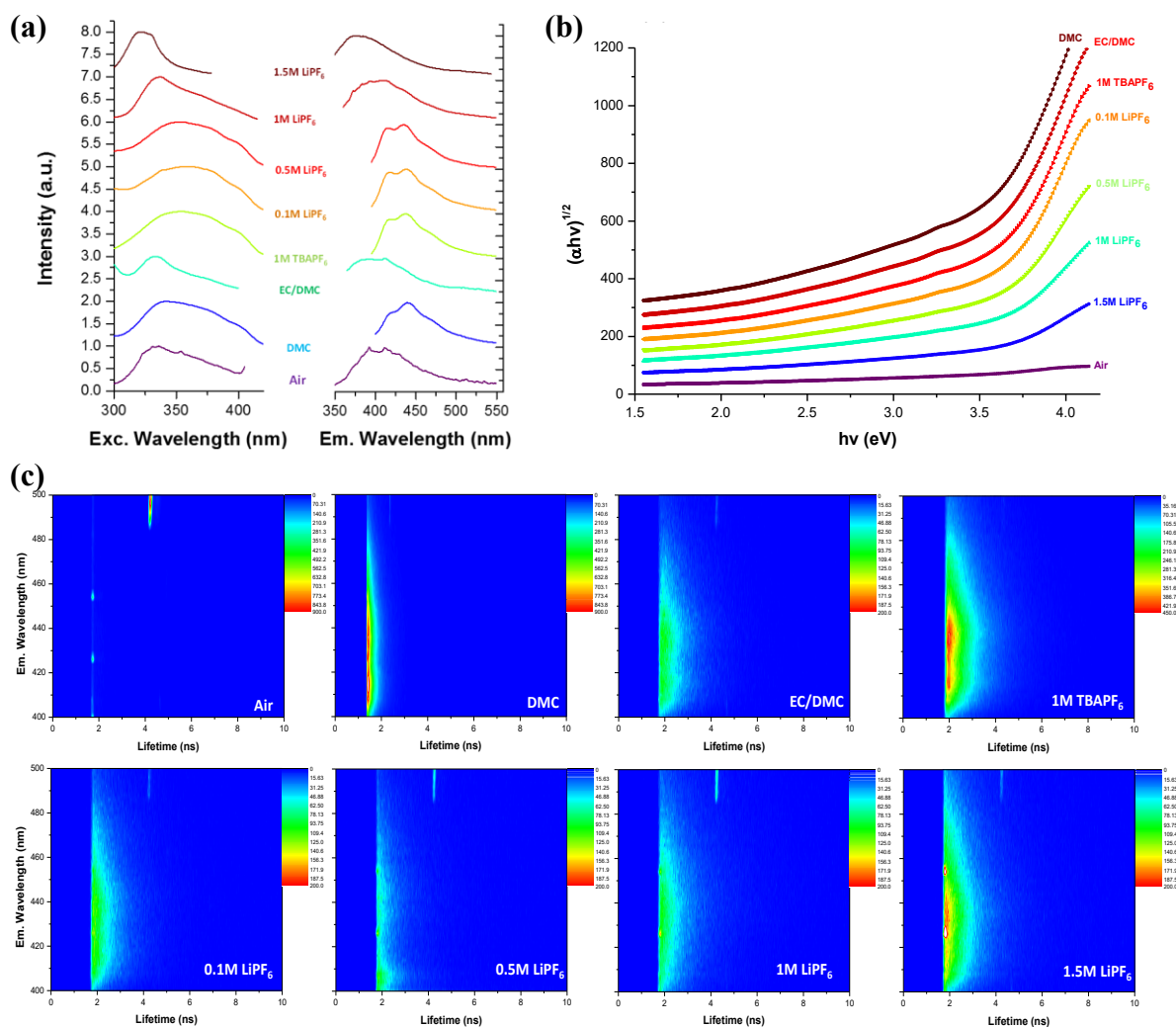


Figure 2.34. (a) Steady-state excitation/emission spectrum, (b) Tauc plot, and (c) time-resolved emission spectroscopy of 5 nm nanocrystalline anatase TiO_2 film in contact with different types of electrolytes.

Conclusions

This chapter firstly described the preliminary work leading to the first proof-of-concept of a complete photorechargeable electrode based on $\text{TiO}_2/\text{Li}_{0.6}\text{TiO}_2$. To achieve this, we developed a low-temperature synthesis yielding to nanocrystals of anatase TiO_2 of 5 nm size. Such a downsizing of the particles affords to maximize the surface reactivity with respect to the volume which is one key to ensure a quantitative photorecharge process. This part of the thesis memoire focused on the study of the processes behind the effective charge separation in $\text{Li}_{0.6}\text{TiO}_2$ nanoparticles triggering photo-induced lithium deinsertion out from the structure. For this, we specifically developed a photoelectrochemical cell which allowed us to study *in situ* the evolution of the optoelectronic properties of TiO_2 upon lithium insertion.

By means of UV-visible absorption spectroscopy, we established that the color change from white to dark blue upon lithium insertion into TiO_2 is associated on the one hand with an increase of the bandgap value, which can be ascribed to Burstein-Moss effect, and on the other hand with the rise of absorbance in both visible and near-infrared part of the light spectrum. This increased absorbance is assigned to the optical absorption of free electron carriers in the conduction band of TiO_2 and the electrons localization into the Ti^{3+} centers occupying the 3d metal orbitals.

In order to determine the band edge positions, which is an important parameter to consider in photochemistry, and their evolution upon lithium insertion, Mott-Schottky measurements on both TiO_2 and $\text{Li}_{0.6}\text{TiO}_2$ were performed in TBAPF_6 -based ionic blocking electrolyte. The results highlight a positive 0.5 V shift in potential of the conduction band. This is accompanied by one order of magnitude increase in charge carrier concentration. In addition, our results stress a strong influence of the flat band potential and carrier concentration depending on the protic or aprotic nature of the electrolyte.

To grasp insights into the dynamics of the excited states of TiO_2 and $\text{Li}_{0.6}\text{TiO}_2$ in different types of electrolyte, we used steady-state fluorescence spectroscopy and time-correlated single photon counting spectroscopy. In this chapter, we identified that in addition to the direct band-to-band recombination which takes place in the range of 29 ps for both TiO_2 and $\text{Li}_{0.6}\text{TiO}_2$, a significant part of the luminescence stems from the recombination through shallow traps associated with oxygen vacancies and surface states when included inside the electrolyte ($\tau > 1$ ns). Upon lithium insertion into the structure, we highlighted a quenching of electrolyte luminescence attributed to FRET mechanism from the electrolyte excited states to TiO_2 and even more efficient to $\text{Li}_{0.6}\text{TiO}_2$ nanoparticles owing to its greater absorption properties. Lithium insertion into TiO_2 also substantially quenches the luminescence of the particles. Finally, on the basis of time-correlated single photon counting experiment comparing the dynamics of excited state of $\text{Li}_{0.6}\text{TiO}_2$ in contact with either a lithium ion-blocking electrolyte or lithium-based electrolyte, we were able to evaluate that the hole transfer to Ti^{3+} is in a range of 100 ps, namely 145 ps in EC/DMC-based electrolyte and 97 ps in EMITFSI based ionic liquid and the existence of Stark-Lo Surdo effect as a result from lithium specific adsorption on the surface of the anatase TiO_2 which modifies the band gap value, the vertical excitation $E_{0,0}$, excitation/emission spectra and the dynamics of the excited states relaxation.

References

- [1] G. Betz, H. Tributsch, S. Fiechter, *J. Electrochem. Soc.*, **1984**, 131, 640.
- [2] T. Nomiya, H. Kuriyaki, and K. Hirakawa, *Synthetic Metals*, **1995**, 71, 1, 2237.
- [3] S. Roberts, *Phys. Rev.* **1949**, 76, 1215.
- [4] A. Eucken, A. Büchner, *Z. Phys. Chem.*, **1935**, 27B, 321.
- [5] P. J. Cameron, L. M. Peter, *J. Phys. Chem. B*, **2003**, 107, 14394.
- [6] R. van de Krol, A. Goossens, J. Schoonman, *J. Phys. Chem. B*, **1999**, 103, 7151.
- [7] M. Tomkiewicz, *J. Electrochem. Soc.*, **1979**, 126, 1505.
- [8] S. Y. Huang, L. Kavan, I. Exnar, M. Grätzel, *J. Electrochem. Soc.*, **1995**, 142, L142.
- [9] G. Sudant, E. Baudrin, D. Larcher, J.-M. Tarascon, *J. Mater. Chem.*, **2005**, 15, 1263.
- [10] S. Patra, C. Davoisne, S. Bruyère, H. Bouyanfif, S. Cassaignon, P.-L. Taberna, F. Sauvage, *Part. Part. Syst. Char.*, **2013**, 30, 1093.
- [11] A. Pottier, S. Cassaignon, C. Chanéac, F. Villain, E. Tronc, J.-P. Jolivet, *J. Mater. Chem.*, **2003**, 13, 877.
- [12] A. L. Patterson, *Phys. Rev.*, **1939**, 56, 978.
- [13] K. S. W. Sing, *Pure Appl. Chem.*, **1985**, 57, 603.
- [14] S. Brunauer, L. S. Deming, W. E. Deming, E. Teller, *J. Am. Chem. Soc.*, **1940**, 62, 1723.
- [15] E. P. Barrett, L. G. Joyner, P. P. Halenda, *J. Am. Chem. Soc.*, **1951**, 73, 373.
- [16] S. Ito, P. Chen, P. Comte, M. K. Nazeeruddin, P. Liska, P. Péchy, M. Grätzel, *Prog. Photovolt. Res. Appl.*, **2007**, 15, 603.
- [17] S. Ito, T. N. Murakami, P. Comte, P. Liska, C. Grätzel, M. K. Nazeeruddin, M. Grätzel, *Thin Solid Films*, **2008**, 516, 4613.
- [18] M. R. Ranade, A. Navrotsky, H. Z. Zhang, J. F. Banfield, S. H. Elder, A. Zaban, P. H. Borse, S. K. Kulkarni, G. S. Doran, H. J. Whitfield, *Proc. Natl. Acad. Sci. U.S.A.*, **2002**, 99, 6476.
- [19] S. J. Smith, R. Stevens, S. Liu, G. Li, A. Navrotsky, J. Boerio-Goates, B. F. Woodfield, *Am. Mineral.*, **2009**, 94, 236.
- [20] H. Zhang, J. F. Banfield, *J. Mater. Chem.*, **1998**, 8, 2073.
- [21] A. Navrotsky, *Geochem. Trans.*, **2003**, 4, 34.
- [22] H. Zhang, J. F. Banfield, *Chem. Rev.*, **2014**, 114, 9613.
- [23] S. Patra, C. Davoisne, H. Bouyanfif, D. Foix, F. Sauvage, *Sci. Rep.*, **2015**, 5, 10928.
- [24] R. J. Cava, D. W. Murphy, S. Zahurak, A. Santoro, R. S. Roth, *J. Solid State Chem.*, **1984**, 53, 64.

- [25] C. Andriamiadamanana, I. Sagaidak, G. Bouteau, C. Davoisne, C. Laberty-Robert, F. Sauvage, *Advanced Sustainable Systems*, **2018**, 2(5), 1700166.
- [26] F. Sauvage, C. Andriamiadamanana, C. Laberty, "Dispositif électrochimique autophotorechargeable transparent", EP3075024A1, **2014**.
- [27] A. M. Eppler, I. M. Ballard, J. Nelson, *Physica E Low Dimens. Syst. Nanostruct.*, **2002**, 14, 197.
- [28] M. Wagemaker, W. J. H. Borghols, F. M. Mulder, *J. Am. Chem. Soc.*, **2007**, 129, 4323.
- [29] G. Bouteau, Etude des propriétés de l'interface semi-conducteur / électrolyte sous illumination pour batteries à ion-lithium photo-rechargeables. Ph.D. thesis, University of Picardie Jules Verne, **2019**.
- [30] E. A. Davis, N. F. Mott, *Phil. Mag.*, **1970**, 22, 0903.
- [31] J. Tauc, R. Grigorovici, A. Vancu, *Physica Status Solidi (b)*, **1966**, 15, 627.
- [32] P. Kubelka, *J. Opt. Soc. Am.*, **1948**, 38, 448.
- [33] P. Kubelka, *J. Opt. Soc. Am.*, **1954**, 44, 330.
- [34] P. Kubelka, F. Munk, *Z. Tech. Phys.*, **1931**, 12, 593.
- [35] J. Tauc, *North-Holland Publ. Co.*, **1972**.
- [36] N. F. Mott, E. A. Davis, *Electronic Processes in Non-Crystalline Materials*, New York: Oxford University Press, **1979**.
- [37] N. Daude, C. Gout, C. Jouanin, *Phys. Rev. B*, **1977**, 15, 3229.
- [38] W. Hu, L. Li, G. Li, C. Tang, L. Sun, *Cryst. Growth Des.*, **2009**, 9, 3676.
- [39] S. Monticone, R. Tufeu, A. V. Kanaev, E. Scolan, C. Sanchez, *Appl. Surf. Sci.*, **2000**, 162–163, 565.
- [40] D. K. Pallotti, L. Passoni, P. Maddalena, F. Di Fonzo, S. Lettieri, *J. Phys. Chem. C*, **2017**, 121, 9011.
- [41] K. M. Reddy, S. V. Manorama, A. R. Reddy, *Mater. Chem. Phys.*, **2003**, 78, 239.
- [42] N. Serpone, D. Lawless, R. Khairutdinov, *J. Phys. Chem.*, **1995**, 99, 16646.
- [43] L. Vayssieres, C. Persson, J.-H. Guo, *Appl. Phys. Lett.*, **2011**, 99, 183101.
- [44] K. Kanamura, T. Umegaki, H. Naito, Z. Takehara, T. Yao, *J. Appl. Electroch.*, **2001**, 31, 73.
- [45] I. Porcheras, E. Bertran, *Thin Solid Films*, **2000**, 377–378, 8.
- [46] E. Burstein, *Phys. Rev.*, **1954**, 93, 632.
- [47] T. S. Moss, *Proc. Phys. Soc. B*, **1954**, 67, 775.
- [48] H. A. Huy, B. Aradi, T. Frauenheim, P. Deák, *Phys. Rev. B*, **2011**, 83, 155201.
- [49] H. A. Huy, B. Aradi, T. Frauenheim, P. Deák, *J. Appl. Phys.*, **2012**, 112, 016103.

- [50] R. Beranek, *Advances in Physical Chemistry*, **2012**, 2011, e786759.
- [51] F. Cardon, W. P. Gomes, *J. Phys. D: Appl. Phys. Advances in Physical Chemistry*, 1978, 11, L63.
- [52] H. Bisht, H.-T. Eun, A. Mehrstens, and M. A. Aegerter, *Thin Solid Films*, **1999**, 351, 1, 109.
- [53] E. C. Dutoit, R. L. Van Meirhaeghe, F. Cardon, W. P. Gomes, *Berichte der Bunsengesellschaft für physikalische Chemie*, **1975**, 79, 1206.
- [54] C. O. Laoire, E. Plichta, M. Hendrickson, S. Mukerjee, K. M. Abraham, *Electrochim. Acta*, **2009**, 54, 6560.
- [55] W. Meyer, *Physik. Z.*, **1935**, 36, 749.
- [56] W. Meyer, H. Neldel, *Physik. Z.*, **1937**, 1014.
- [57] R. G. Breckenridge, W. R. Hosler, *Phys. Rev.*, **1953**, 91, 793.
- [58] G. Redmond, D. Fitzmaurice, *J. Phys. Chem.*, **1993**, 97, 1426.
- [59] E. C. Dutoit, F. Cardon, W. P. Gomes, *Berichte der Bunsengesellschaft für physikalische Chemie*, **1976**, 80, 475.
- [60] C. Gutierrez, P. Salvador, *Journal of Electroanalytical Chemistry and Interfacial Electrochemistry*, **1982**, 138, 457.
- [61] V. Spagnol, E. Sutter, C. Debiemme-Chouvy, H. Cachet, B. Baroux, *Electrochim. Acta*, **2009**, 54, 1228.
- [62] K. L. Hardee, A. J. Bard, *J. Electrochem. Soc.*, **1977**, 124, 215.
- [63] D. O. Scanlon, C. W. Dunnill, J. Buckeridge, S. A. Shevlin, A. J. Logsdail, S. M. Woodley, C. R. A. Catlow, M. J. Powell, R. G. Palgrave, I. P. Parkin, G. W. Watson, T. W. Keal, P. Sherwood, A. Walsh, A. A. Sokol, *Nat. Mater.*, **2013**, 12, 798.
- [64] M. A. Butler, D. S. Ginley, *J. Electrochem. Soc.*, **1978**, 125, 228.
- [65] F. Cao, G. Oskam, P. C. Searson, J. M. Stipkala, T. A. Heimer, F. Farzad, G. J. Meyer, *J. Phys. Chem.*, **1995**, 99, 11974.
- [66] R. Hengerer, L. Kavan, P. Krtil, M. Grätzel, *J. Electrochem. Soc.*, **2000**, 147, 1467.
- [67] L. Kavan, K. Kratochvilová, M. Grätzel, *J. Electroanal. Chem.*, **1995**, 394, 93.
- [68] R. O'Hayre, M. Nanu, J. Schoonman, A. Goossens, *J. Phys. Chem. C*, **2007**, 111, 4809.
- [69] P. E. De Jongh, D. Vanmaekelbergh, *Phys. Rev. Lett.*, **1996**, 77, 3427.
- [70] Kabir-ud-Din, R. C. Owen, M. A. Fox, *J. Phys. Chem.*, **1981**, 85, 1679.
- [71] A. B. Heinzl, D. M. Teschner, R. Schumacher, *Berichte der Bunsengesellschaft für physikalische Chemie*, **1981**, 85, 1117.

- [72] A. Molinari, A. Maldotti, R. Amadelli, *Chem. Eur. J.*, **2014**, 20, 7759.
- [73] R. Schumacher, D. M. Teschner, A. B. Heinzl, *Berichte der Bunsengesellschaft für physikalische Chemie*, **1982**, 86, 1153.
- [74] G. Rothenberger, J. Moser, M. Graetzel, N. Serpone, D. K. Sharma, *J. Am. Chem. Soc.*, **1985**, 107, 8054.
- [75] M. S. Whittingham, *Science*, **1976**, 192, 1126.
- [76] S. Nakade, T. Kanzaki, W. Kubo, T. Kitamura, Y. Wada, S. Yanagida, *J. Phys. Chem. B*, **2005**, 109, 3480.
- [77] Y. Bai, J. Zhang, Y. Wang, M. Zhang, P. Wang, *Langmuir*, **2011**, 27, 4749.
- [78] S. Yang, J. Wang, H. Kou, H. Xue, H. Wang, *Electrochemistry*, **2011**, 2, 015.
- [79] M. F. Weber, L. C. Schumacher, M. J. Dignam, *J. Electrochem. Soc.*, **1982**, 129, 2022.
- [80] G. K. Boschloo, A. Goossens, J. Schoonman, *J. Electrochem. Soc.*, **1997**, 144, 1311.
- [81] M. Wagemaker, A. Van Der Ven, D. Morgan, G. Ceder, F. M. Mulder, G. J. Kearley, *Chemical Physics*, **2005**, 317, 130.
- [82] V. R. Koch, L. A. Dominey, C. Nanjundiah, M. J. Ondrechen, *J. Electrochem. Soc.*, **1996**, 143, 798.
- [83] M. Ue, M. Takeda, M. Takehara, S. Mori, *J. Electrochem. Soc.*, **1997**, 144, 2684.
- [84] H. Tang, Electronic properties of anatase TiO₂ investigated by electrical and optical measurements on single crystals and thin films. Ph.D. thesis, EPFL, **1995**.
- [85] A. Jabłoński, *Z. Physik*, **1935**, 94, 38.
- [86] F. Clabau, X. Rocquefelte, T. Le Mercier, P. Deniard, S. Jobic, M.-H. Whangbo, *Chem. Mater.*, **2006**, 18, 3212.
- [87] T. Makino, Y. Segawa, M. Kawasaki, Y. Matsumoto, H. Koinuma, M. Murakami, R. Takahashi, *J. Phys. Soc. Jpn.*, **2003**, 72, 2696.
- [88] M. Niederberger, M. H. Bartl, G. D. Stucky, *Chem. Mater.*, **2002**, 14, 4364.
- [89] N. Hosaka, T. Sekiya, S. Kurita, *Journal of Luminescence*, **1997**, 72–74, 874.
- [90] H. Tang, K. Prasad, R. Sanjinès, P. E. Schmid, F. Lévy, *J. Appl. Phys.*, **1994**, 75, 2042.
- [91] H. Tang, H. Berger, P. E. Schmid, F. Lévy, *Solid State Commun.*, **1994**, 92, 267.
- [92] M. Watanabe, T. Hayashi, *J. Lumin.*, **2005**, 112, 88.
- [93] Y. Lei, L. D. Zhang, G. W. Meng, G. H. Li, X. Y. Zhang, C. H. Liang, W. Chen, S. X. Wang, *Appl. Phys. Lett.*, **2001**, 78, 1125.
- [94] L. V. Saraf, S. I. Patil, S. B. Ogale, S. R. Sainkar, S. T. Kshirsager, *Int. J. Mod. Phys. B*, **1998**, 12, 2635.
- [95] L. Forss, M. Schubnell, *Appl. Phys. B*, **1993**, 56, 363.

- [96] G. Redmond, D. Fitzmaurice, M. Graetzel, *J. Phys. Chem.*, **1993**, 97, 6951.
- [97] J. C. de Mello, H. F. Wittmann, R. H. Friend, *Adv. Mat.*, **1997**, 9, 230.
- [98] N. D. Abazović, M. I. Čomor, M. D. Dramićanin, D. J. Jovanović, S. P. Ahrenkiel, J. M. Nedeljković, *J. Phys. Chem. B*, **2006**, 110, 25366.
- [99] G. Bouteau, A. N. Van-Nhien, M. Sliwa, N. Sergent, J.-C. Lepretre, G. Gachot, I. Sagaidak, F. Sauvage, *Scientific reports*, **2019**, 9, 135.
- [100] L. Tsui, M. Saito, T. Homma, G. Zangari, *J. Mater. Chem. A*, **2015**, 3, 360.
- [101] H. Tang, H. Berger, P. E. Schmid, F. Lévy, G. Burri, *Solid State Commun.*, **1993**, 87, 847.
- [102] K. Wakabayashi, Y. Yamaguchi, T. Sekiya, S. Kurita, *J. Lumin.*, **2005**, 112, 50.
- [103] K. Fujihara, S. Izumi, T. Ohno, M. Matsumura, *J. Photochem. and Photobiol. A: Chemistry*, **2000**, 132, 99.
- [104] D. P. Colombo, K. A. Roussel, J. Saeh, D. E. Skinner, J. J. Cavaleri, R. M. Bowman, *Chem. Phys. Lett.*, **1995**, 232, 207.
- [105] L. Cavigli, F. Bogani, A. Vinattieri, L. Cortese, M. Colocci, V. Faso, G. Baldi, *Solid State Sci.*, **2010**, 12, 1877.
- [106] C. L. Olson, J. Nelson, M. S. Islam, *J. Phys. Chem. B*, **2006**, 110, 9995.
- [107] N. Kopidakis, E. A. Schiff, N.-G. Park, J. van de Lagemaat, A. J. Frank, *J. Phys. Chem. B*, **2000**, 104, 3930.
- [108] S. Nakade, S. Kambe, T. Kitamura, Y. Wada, S. Yanagida, *J. Phys. Chem. B*, **2001**, 105, 9150.
- [109] D. Nistér, K. Keis, S.-E. Lindquist, A. Hagfeldt, *Sol. Energ. Mat. Sol. C.*, **2002**, 73, 411.

Chapter 3. Database of optoelectronic properties of common insertion materials and their photoelectrochemistry

Introduction	90
3.1. Study of transition metal oxides	91
3.1.1. $\text{Li}_4\text{Ti}_5\text{O}_{12}$	91
3.1.2. LiCoO_2	99
3.1.3. MoO_3	104
3.1.4. WO_3	109
3.1.5. CuO	113
3.1.6. Bi_2O_3	117
3.1.7. LiMn_2O_4	122
3.1.8. $\text{LiMn}_{1/3}\text{Co}_{1/3}\text{Ni}_{1/3}\text{O}_2$	124
3.2. Transition metal sulfides	126
3.2.1. TiS_2	127
3.2.2. MoS_2	130
3.2.3. WS_2	134
3.3. Lithiated polyanions	138
3.3.1. LiFePO_4	139
3.3.2. LiMnPO_4	143
3.3.3. LiVPO_4F	146
3.4. Fundamental evaluation of the possibility of Li^+ photo-insertion / photo-deinsertion reaction.	149
3.5. First results on the photoelectrochemistry of chosen insertion materials	151
3.5.1. LiCoO_2	151
3.5.2. LiFePO_4	153
3.5.3. $\text{Li}_4\text{Ti}_5\text{O}_{12}$	164
Conclusions	175
References	178

Introduction











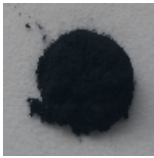

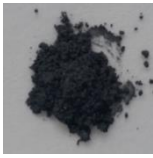
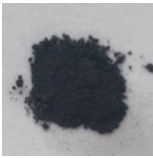
Most of the information related to the optoelectronic properties of inorganic materials reported in literature is connected to either water-splitting, solar fuel generation or photocatalysis applications [1–5]. Only few materials known for their lithium insertion properties are presented, namely TiO_2 , WO_3 , CuO , V_2O_5 , Bi_2O_3 , and BiVO_4 . For photoelectrochemical applications, the position of both valence band and conduction band is critical as it controls the reductive and oxidizing strength of the photogenerated carriers and defines the possibility for electrons or holes to be transferred to the transition metal and to the counter-electrode [6–9]. In contrast, when employed for batteries application [10], the redox potential and crystal structure to evaluate ionic conduction pathways and number of available sites for lithium to be accommodated are the most important criteria. Consequently, for the majority of insertion materials developed for batteries, no or little information is reported on the band gap value, band edge positions, or even charge carrier nature and its concentration. Moreover, with the exception of TiO_2 , which is a reference material for a broad range of applications, no studies are reported aiming at measuring these characteristics in non-aqueous aprotic solvents such as those typically used as electrolytes in batteries. This latter is important as the position of band edges is known to vary significantly depending on doping [11–13], surface states [14], and the nature of electrolyte in contact [15].

This chapter focuses on the creation of a database gathering the optoelectronic properties of the most widely used battery electrode materials. This database enables to evaluate the potentiality of a material for photobattery application and it represents an interesting contribution to the field of photocatalysis. Some first results related to photobatteries are discussed at the end of the chapter.

Three groups of materials were chosen for this study (Table 3.1):

- transition metal oxides ($\text{Li}_4\text{Ti}_5\text{O}_{12}$, LiCoO_2 , MoO_3 , WO_3 , CuO , Bi_2O_3 , LiMn_2O_4 , $\text{LiMn}_{1/3}\text{Ni}_{1/3}\text{Co}_{1/3}\text{O}_2$),
- transition metal sulfides (TiS_2 , MoS_2 , WS_2),
- lithiated polyanions (LiFePO_4 , LiMnPO_4 , LiVPO_4F).

Table 3.1. Visual aspects of the different classes of materials studied in this work.

Transition metal oxides			Transition metal sulfides	Lithiated polyanions
Li ₄ Ti ₅ O ₁₂	LiCoO ₂	MoO ₃	TiS ₂	LiFePO ₄
				
WO ₃	CuO	Bi ₂ O ₃	MoS ₂	LiMnPO ₄
				
LiMn ₂ O ₄	LiMn _{1/3} Co _{1/3} Ni _{1/3} O ₂		WS ₂	LiVPO ₄ F
				

3.1. Study of transition metal oxides

3.1.1. Li₄Ti₅O₁₂

The spinel lithium titanate Li₄Ti₅O₁₂ attracted much attention as an anode material for Li-ion batteries owing to its theoretical gravimetric capacity of 175 mAh/g, bi-phasic plateau at 1.5 V (vs. Li⁺/Li), high power, and excellent cycling stability owing to almost zero volume change between Li₄Ti₅O₁₂ and Li₇Ti₅O₁₂ [16-17]. One major disadvantage of Li₄Ti₅O₁₂ is its poor electronic conductivity ($\sigma < 10^{-13}$ S/cm) [18], which stems from the empty Ti⁴⁺ 3d orbital, and low lithium-ion diffusion coefficient ($\sim 10^{-12}$ cm²/s) [19]. Its crystal structure, crystallizing in cubic phase with Fd $\bar{3}$ m space group, is often presented in a form of Li_{8a}[Ti_{5/3}Li_{1/3}]_{16d}O₄, denoting that 75 % of lithium ions are located at tetrahedral (8a) sites, while the rest of the lithium ions and titanium occupy octahedral (16d) sites (Fig. 3.1). The oxygen ions are located at 32e sites.

The XRD pattern of Li₄Ti₅O₁₂ powder was successfully refined and indexed into the spinel structure with the Fd $\bar{3}$ m space group (Fig. 3.2 (a)). The lattice cell parameter determined is

$a = 8.3588(3) \text{ \AA}$ ($V_{\text{cell}} = 584 \text{ \AA}^3$), in good agreement with the value reported by Dolotko et al. [20]. The sample is free of any impurities based on x-ray diffraction.

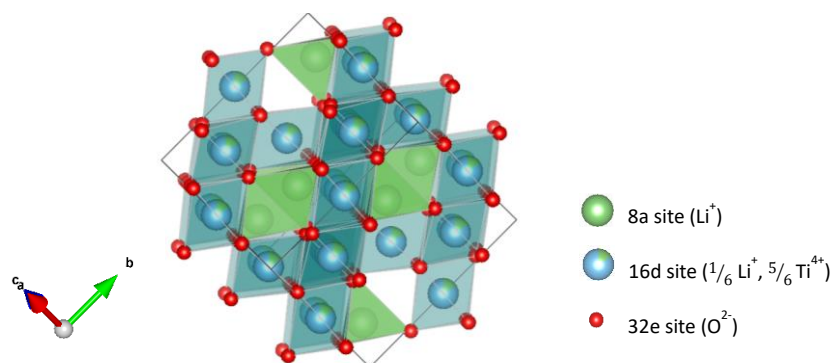


Figure 3.1. Crystal structure of the spinel $\text{Li}_4\text{Ti}_5\text{O}_{12}$.

The SEM study of the powder revealed a spherical morphology composed of aggregated particles ranging between 5 to 20 μm (Fig. 3.2 (b)). The primary particles have a size ranging between 300 and 600 nm (Fig. 3.2 (c)). The high-resolution TEM (HR-TEM) micrograph confirms an entire crystallinity of the particles for which the selected area electron diffraction (SAED) pattern is in agreement with XRD (Fig. 3.2 (d-e)).

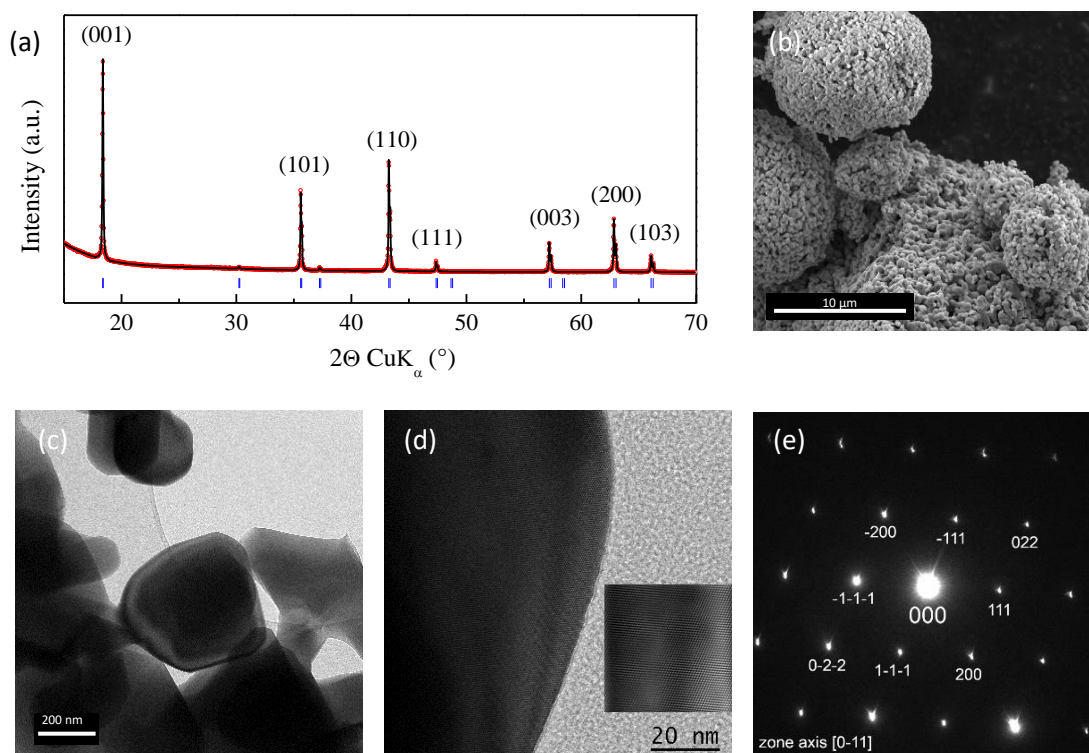


Figure 3.2. (a) Full pattern matching refinement of x-ray diffractogram of $\text{Li}_4\text{Ti}_5\text{O}_{12}$, (b) scanning electron microscopy image, (c) transmission electron micrograph, (d) high-resolution transmission electron micrograph, and (e) selected area electron diffraction pattern of the particles.

Figure 3.3 (a) presents the diffuse reflectance spectrum of $\text{Li}_4\text{Ti}_5\text{O}_{12}$ recorded over the range of 1800 nm down to 200 nm. For this, 1 wt% of $\text{Li}_4\text{Ti}_5\text{O}_{12}$ was mixed within KBr before to be pressed into a pellet. Note that this ratio was kept for all materials herein studied unless mentioned otherwise. An absorption tail is observed at around 400 nm suggesting a wide band gap in agreement with the white color of the particles. The band gap value was determined from the Tauc plot using Kubelka-Monk function. Assuming an indirect allowed transition, the band gap energy of $\text{Li}_4\text{Ti}_5\text{O}_{12}$ is 3.79 eV, which is in agreement with the white color of the particles (Fig. 3.3 (b)). It is 4.05 eV if we assume a direct transition (Fig. 3.3 (c)). Our results are significantly higher than 1.7 - 2.3 eV reported by early calculations [21–24], but close to 3.87 eV reported recently by Verde et al. based on DOS calculations [25]. The obtained values are also in agreement with the 3.8 eV indirect band gap reported by Ge et al. based on diffuse reflectance measurements [26] and with the range of 3.5 - 3.8 eV band gap with a direct allowed transition reported by a number of other authors [27–29].

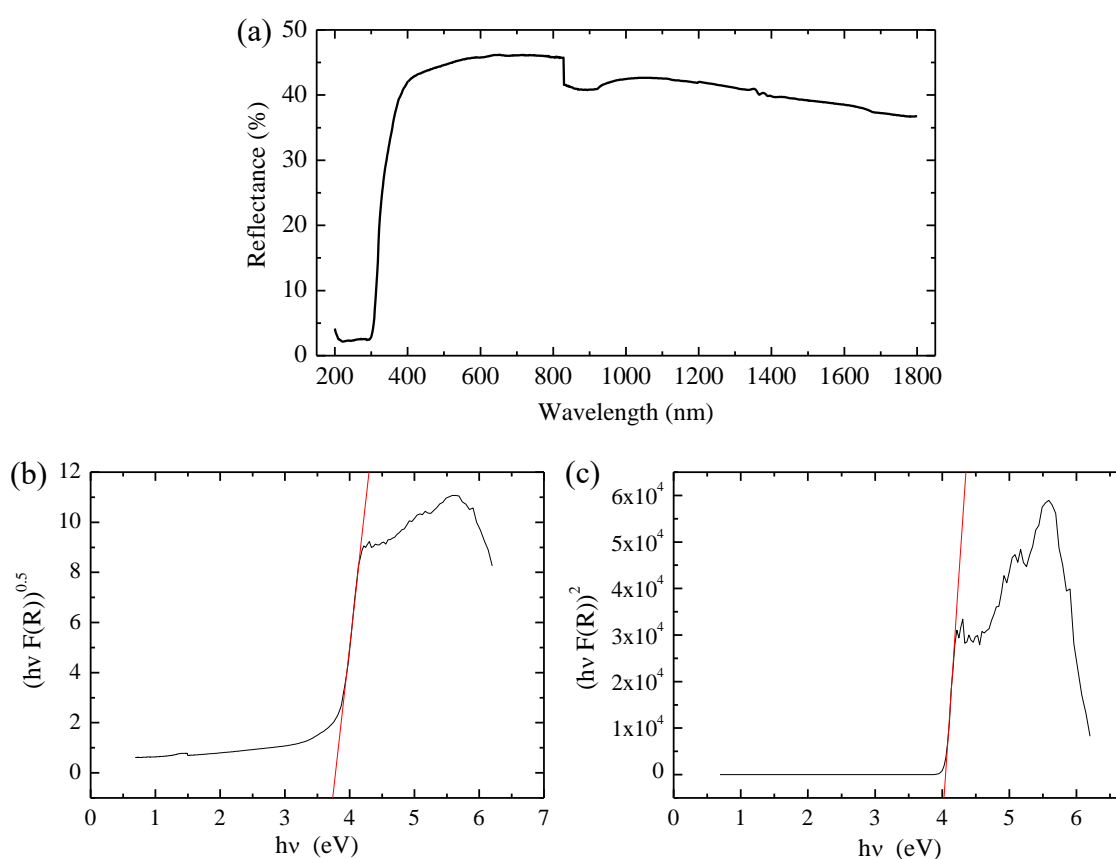


Figure 3.3. (a) Evolution of diffuse reflectance of $\text{Li}_4\text{Ti}_5\text{O}_{12}$ as a function of wavelength and corresponding Tauc plot assuming (b) an indirect allowed band gap transition ($n=2$) and (c) direct allowed band gap transition ($n=0.5$).

The conclusion of a direct vs. indirect nature of the bandgap is often experimentally not so straightforward. However, some correlations were found between the band gap transition nature and the shape of the plot of the absorption coefficient vs. wavelength [30–33]. For a direct transition, the absorbance increases slowly by contrast to an indirect transition for which the absorbance change becomes steep. Taking into account the inverse relation between absorbance and reflectance in opaque materials, thus, the steep reflectance onset of $\text{Li}_4\text{Ti}_5\text{O}_{12}$ suggests an indirect band gap.

The flat band potential as well as the charge carrier type and concentration in $\text{Li}_4\text{Ti}_5\text{O}_{12}$ was determined as previously from the Mott-Schottky plot in two different kinds of blocking electrolytes, i.e. aqueous (protic) and non-aqueous aprotic. For this, a film with $12\ \mu\text{m}$ thickness was prepared by doctor-blading. In aqueous electrolyte, we carried out a set of measurements in different electrolytes, namely in NaOH and in TBANO_3 at different pH values adjusted by adding a small quantity of HNO_3 . We then chose one representative measurement based on quality of the Mott-Schottky curve and the highest reproducibility of the flat band potential (V_{fb}) and the charge carrier concentration (N) values. The frequency dependence of the Mott-Schottky curves for $\text{Li}_4\text{Ti}_5\text{O}_{12}$ and for the other materials described in this chapter follows the same trend as observed for TiO_2 , i.e. a decrease of V_{fb} and negligible changes in N as a function of frequency in the range from 100 Hz to 1 kHz. This is experienced for measurements in both aqueous and non-aqueous aprotic electrolytes. Figure 3.4 presents the Mott-Schottky plots of $\text{Li}_4\text{Ti}_5\text{O}_{12}$ in aqueous and in non-aqueous aprotic EC/DMC-based electrolytes. In both media, the positive slope of the Mott-Schottky curve confirms the n-type nature of conductivity in agreement with literature [26, 34].

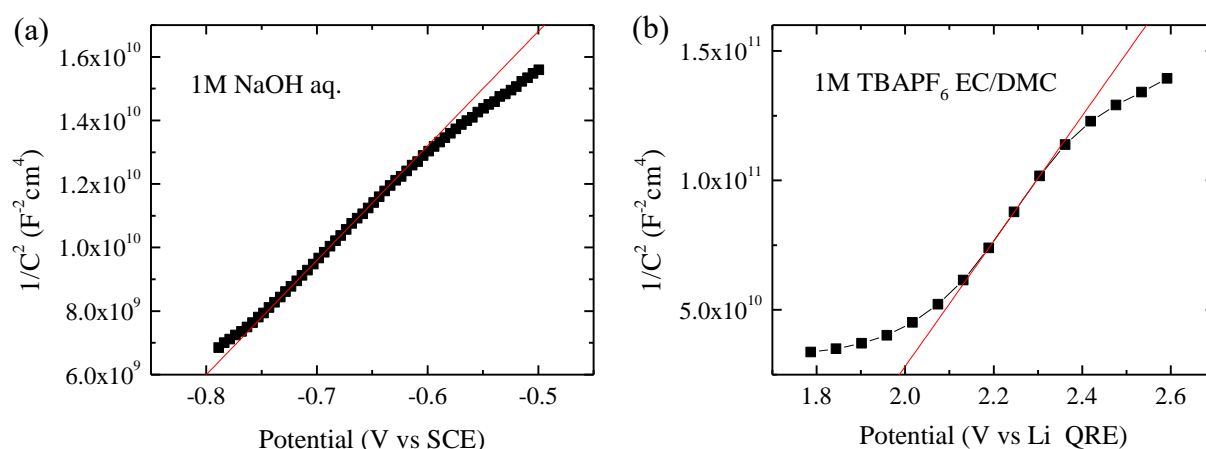


Figure 3.4. Mott-Schottky plot of $\text{Li}_4\text{Ti}_5\text{O}_{12}$ measured in (a) 1 mol/L NaOH aqueous electrolyte at 250 Hz and (b) 1 mol/L TBAPF₆ EC/DMC electrolyte at 200 Hz.

The flat band potential and donor density value of $\text{Li}_4\text{Ti}_5\text{O}_{12}$ is summarized in table 3.2. In 1 mol/L NaOH aqueous solution (pH = 14), the flat band potential is situated at - 0.99 V vs. SCE, which translates into -0.76 V vs. NHE. This value is 0.37 V lower than the one reported by Ge et al. (- 1.13 V vs. NHE at pH = 14) in 0.2 mol/L Na_2SO_4 aqueous solution. In a non-aqueous aprotic electrolyte, based on 1 mol/L TBAPF₆ in EC/DMC, we obtained a flat band potential of 1.86 V vs. Li QRE, which represents - 1.34 V vs. NHE. To the best of our knowledge, this is the first report on the flat band potential determination of $\text{Li}_4\text{Ti}_5\text{O}_{12}$ in a non-aqueous aprotic solvent.

Table 3.2. Flat band potential and charge carrier concentration of $\text{Li}_4\text{Ti}_5\text{O}_{12}$ in 1 mol/L NaOH aqueous and 1 mol/L TBAPF₆ EC/DMC electrolytes.

Electrolyte	Flat band potential		Charge carrier concentration, cm^{-3}
	as measured	recalculated, V vs. NHE	
1 mol/L NaOH in H_2O	- 0.99 V vs. SCE	- 0.76 (pH = 14)	$2.7 \cdot 10^{18}$
1 mol/L TBAPF ₆ in EC/DMC	1.86 V vs. Li QRE	-1.34	$6.9 \cdot 10^{19}$

Considering the n-type conductivity and assuming the close proximity of the fermi level to the conduction band, the flat band potential corresponds to the lower edge of the conduction band. Taking into account the bandgap of 3.79 eV, the valence band edge was calculated as 3.03 V in aqueous electrolyte and 2.45 V in non-aqueous aprotic electrolyte denoting a considerable influence of the nature of the electrolyte on the band edge positions in $\text{Li}_4\text{Ti}_5\text{O}_{12}$ (Fig. 3.5).

The charge carrier concentration was determined by considering a dielectric constant of 20 as the average of the values reported by Zhang et al. [35] and Liu et al. [36] based on the microwave dielectric properties measurements (Table 3.2). In 1 mol/L NaOH aqueous electrolyte, donor density was determined as $2.7 \cdot 10^{18} \text{ cm}^{-3}$. In contrast, a significantly higher value of $6.9 \cdot 10^{19} \text{ cm}^{-3}$ is obtained when measured in 1 mol/L TBAPF₆ EC/DMC. This indicates that the donor density of $\text{Li}_4\text{Ti}_5\text{O}_{12}$ measured in non-aqueous aprotic electrolyte is more than one order of magnitude higher than in the aqueous electrolyte. Such a trend was also observed in chapter II for TiO_2 (see section 2.3.2).

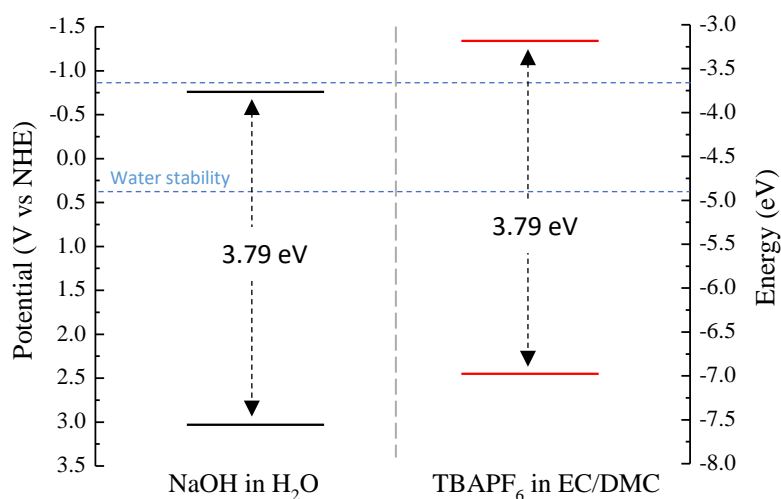


Figure 3.5. Representation of the band edge positions of $\text{Li}_4\text{Ti}_5\text{O}_{12}$ film in aqueous electrolyte at $\text{pH} = 14$ (in black) and in non-aqueous aprotic EC/DMC-based electrolyte (in red).

The steady-state photoluminescence map of $\text{Li}_4\text{Ti}_5\text{O}_{12}$ powder was recorded between 270-800 nm in excitation and 278-808 nm in emission using a front-face configuration (0.5 nm excitation / 0.5 nm emission slits) (Fig. 3.6 (a)). The maximum of emission is reached for an excitation at 333 nm leading to a broad asymmetric band at 728 nm (Fig. 3.6 (b)). Our results are in relatively good agreement with the fluorescence data reported by Wen et al. who obtained a strong emission at 716 nm when excited at 325 nm [37]. The very large Stokes shift of 395 nm (16294 cm^{-1}) is assigned to the presence of deep traps in the bandgap through which most of the energy relaxation is taking place in a non-radiative way (i.e. phonon dispersion and heat dissipation, etc.).

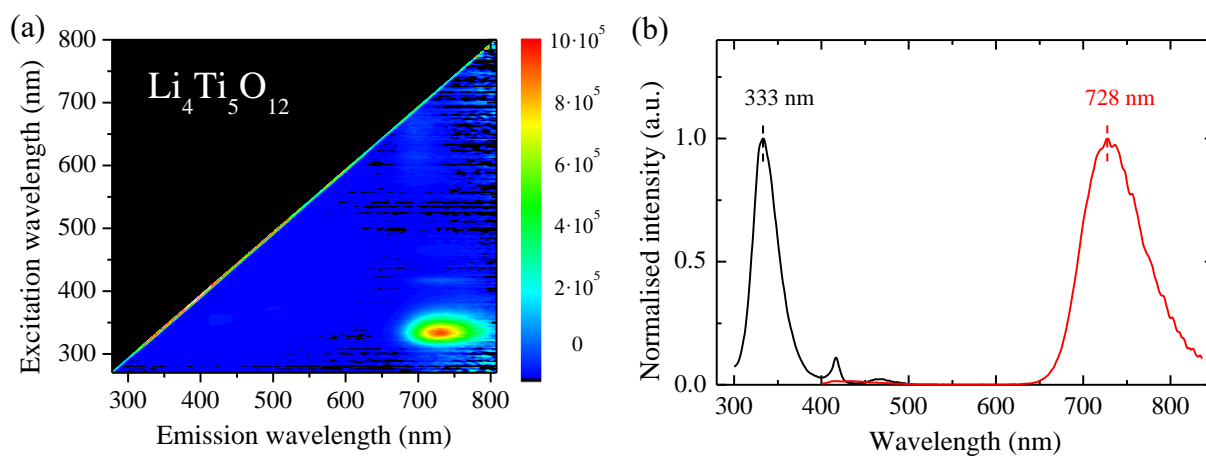


Figure 3.6. Steady-state (a) excitation/emission map and (b) normalized excitation/emission spectra of nanocrystalline $\text{Li}_4\text{Ti}_5\text{O}_{12}$ powder.

The absolute fluorescence quantum yield of $\text{Li}_4\text{Ti}_5\text{O}_{12}$ powder was measured using an integrating sphere combining both direct and indirect measurements (Fig. 3.7). The quantum yield of -0.57% derived from the measurement suggests that the value lies in the error bar range due to the highly reflective sample nature. Thus, we conclude that the quantum yield must be below the detection limit of the set-up, i.e. < 1%.

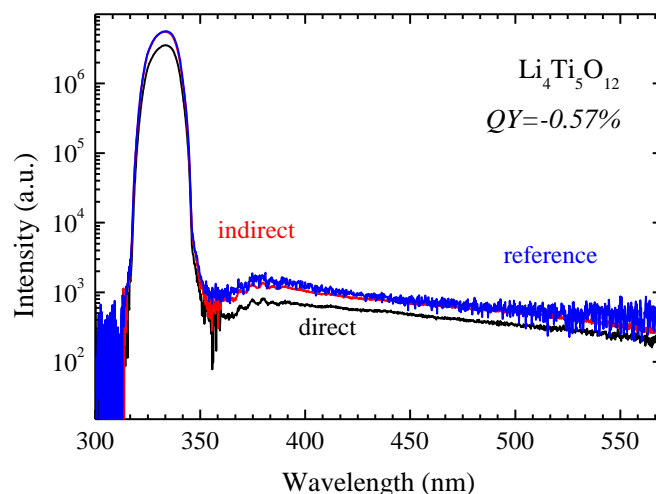


Figure 3.7. Quantum yield fluorescence spectra of $\text{Li}_4\text{Ti}_5\text{O}_{12}$ particles measured in direct and indirect method using an integrating with BaSO_4 as a reference sample.

The dynamics of the excited states in $\text{Li}_4\text{Ti}_5\text{O}_{12}$ was investigated by time-correlated single-photon counting technique using a pulsed laser diode of 375 nm. The luminescence decay was probed at 728 nm emission (Fig. 3.8). For this experiment, a longpass filter of 695 nm was used to exclude any artefacts from excessive light scattering from the sample. The recorded photoluminescence decay is much longer than the IRF decay (20-30 ps). The long tail of the decay suggests the presence of a long-lived component. Note that with this sample an abnormally high background was systematically observed for which the origin is not yet completely understood.

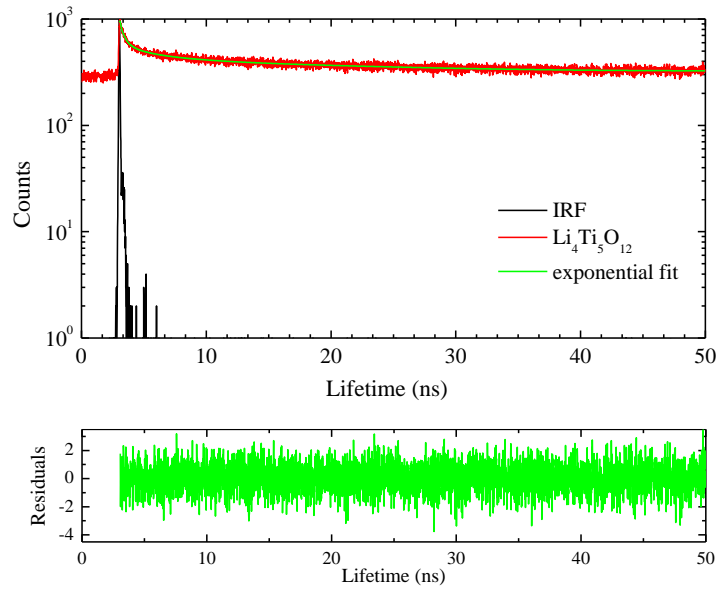


Figure 3.8. Evolution of the PL decay of $\text{Li}_4\text{Ti}_5\text{O}_{12}$ powder and its fit after reconvolution with the IRF measured on BaSO_4 . The residuals' distribution of the exponential fit is reported for information.

The decay was the best fitted using a stretch exponential function (eq. 2.10) including three components leading to a reduced chi-square (χ^2) value of 1.025. The results after reconvolution of the IRF decay are presented in Table 3.3. The fast component at 0.10 ns cannot be related to a direct band-to-band recombination due to the large Stokes shift. Therefore, all the three components, i.e. 0.10, 3.00 and 27.87 ns, are assigned to a very deep trap-mediated fluorescence. A low amplitude of the first component reaching only 6.9% indicates that a very small portion of recombination takes place through the shallow trap states. The 61.0% and 32.1% of the total fluorescence amplitude belonging to the second and third components supports the radiative recombination through the deep traps. This can also explain the origin of the very low quantum yield of $\text{Li}_4\text{Ti}_5\text{O}_{12}$.

Table 3.3. Results after reconvolution of the time-correlated single photon counting decay recorded on $\text{Li}_4\text{Ti}_5\text{O}_{12}$ powder using stretched exponential function (375 nm excitation, 728 nm emission).

Component	Pre-exponential factor B_i	Amplitude, %	Lifetime, ns
τ_1	0.114	6.9	0.10
τ_2	0.035	61.0	3.00
τ_3	0.004	32.9	27.87

3.1.2. LiCoO₂

LiCoO₂ is the most common positive electrode used in lithium-ion batteries owing to its excellent cycling stability and high intercalation / de-intercalation potential of around 4 V (vs. Li⁺/Li) [38-39]. Its structure consists of edge sharing CoO₆ octahedra forming layers separated by lithium cations ensuring a good bi-dimensional ionic conduction (Fig. 3.9). One of the main drawbacks of this material is the irreversible structural change taking place upon de-intercalation above 0.5 Li⁺ extracted inducing a phase transition to a hexagonal close-packed structure of CoO₂ above 4.5 V, which limits the practical capacity to around 140 mAh/g [54].

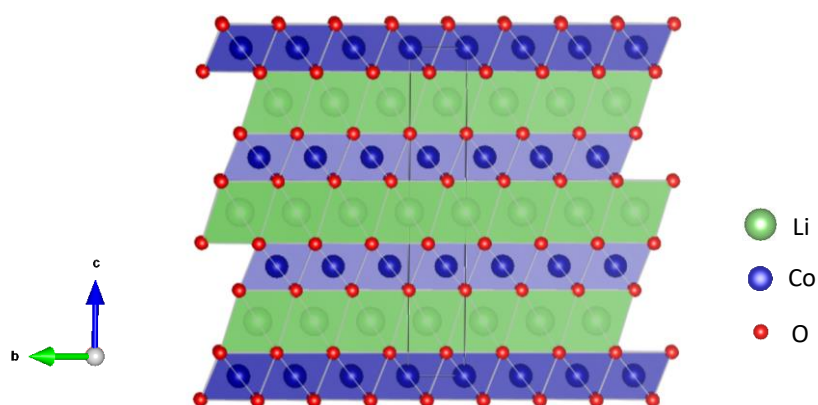


Figure 3.9. Crystal structure representation of LiCoO₂ in (011) plane.

Figure 3.10 (a) shows the x-ray diffraction pattern of LiCoO₂ powder used in this study. All diffraction peaks are indexed into the rhombohedral R-3m space group with lattice cell parameters of $a = b = 2.8149(3)$ Å, $c = 14.050(51)$ Å ($V_{\text{cell}} = 96$ Å³). These values are in good agreement with those reported for instance by Shinova et al. [40]. The diffraction peaks are intense and narrow indicating excellent crystallinity with large crystallite size. The SEM micrographs show well-separated particles having no specific morphology and the size ranging from 2 to 20 μm. There are also spherical nanosized particles of ca. 50 nm (Fig. 3.10 (b-c)).

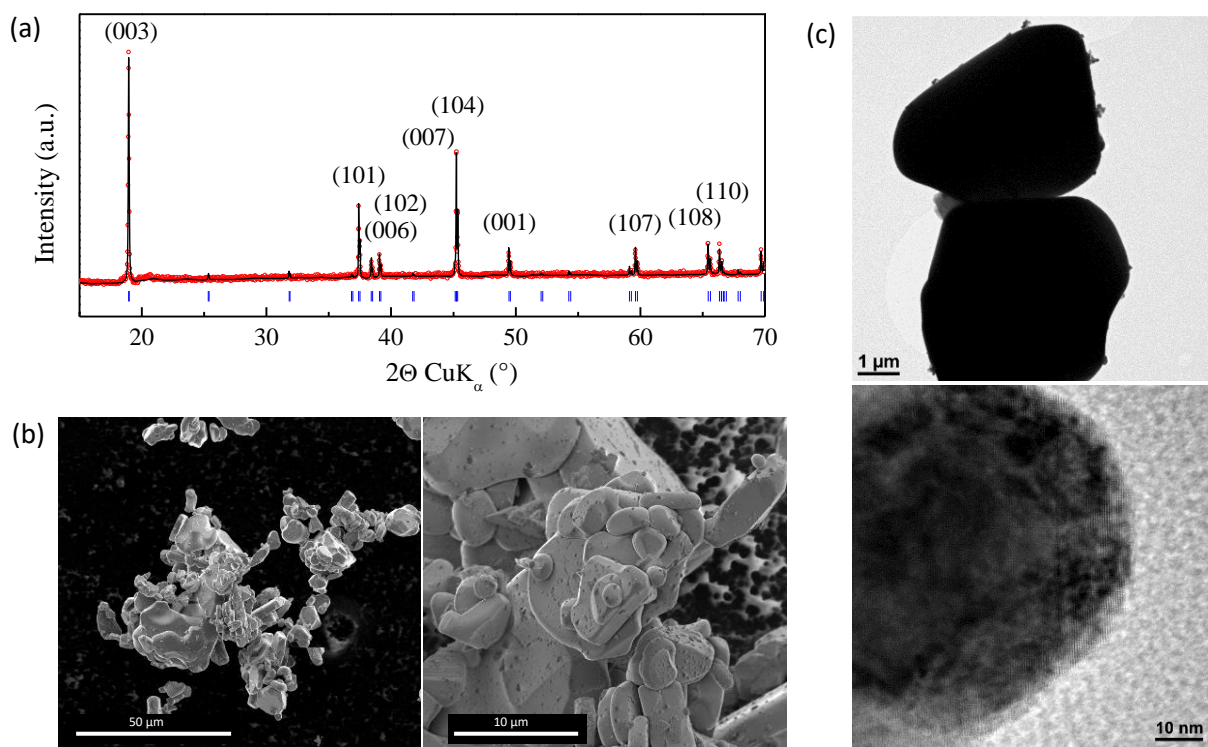


Figure 3.10. (a) Full-pattern matching of x-ray diffraction profile, (b) scanning electron microscopy images, and (c) transmission electron micrograph of LiCoO_2 .

The band gap of LiCoO_2 was evaluated as previously described assuming an indirect allowed transition (Fig. 3.11 (a)). A very low optical band gap of 0.79 eV was determined in agreement with black colour of the particles (Fig. 3.11 (b)). In this case, there is no uncertainties on the origin of the transition since a direct allowed transition would lead to a value of 5.17 eV which should provide a white powder (Fig. 3.11 (c)). In literature, a direct band gap value of LiCoO_2 has been reported between 2.3 to 2.5 eV based on optical absorption spectra measurements [41] and photocurrent spectra onset determination [42]. However, the sluggish increase of reflectance suggests the indirect nature of the optical transition.

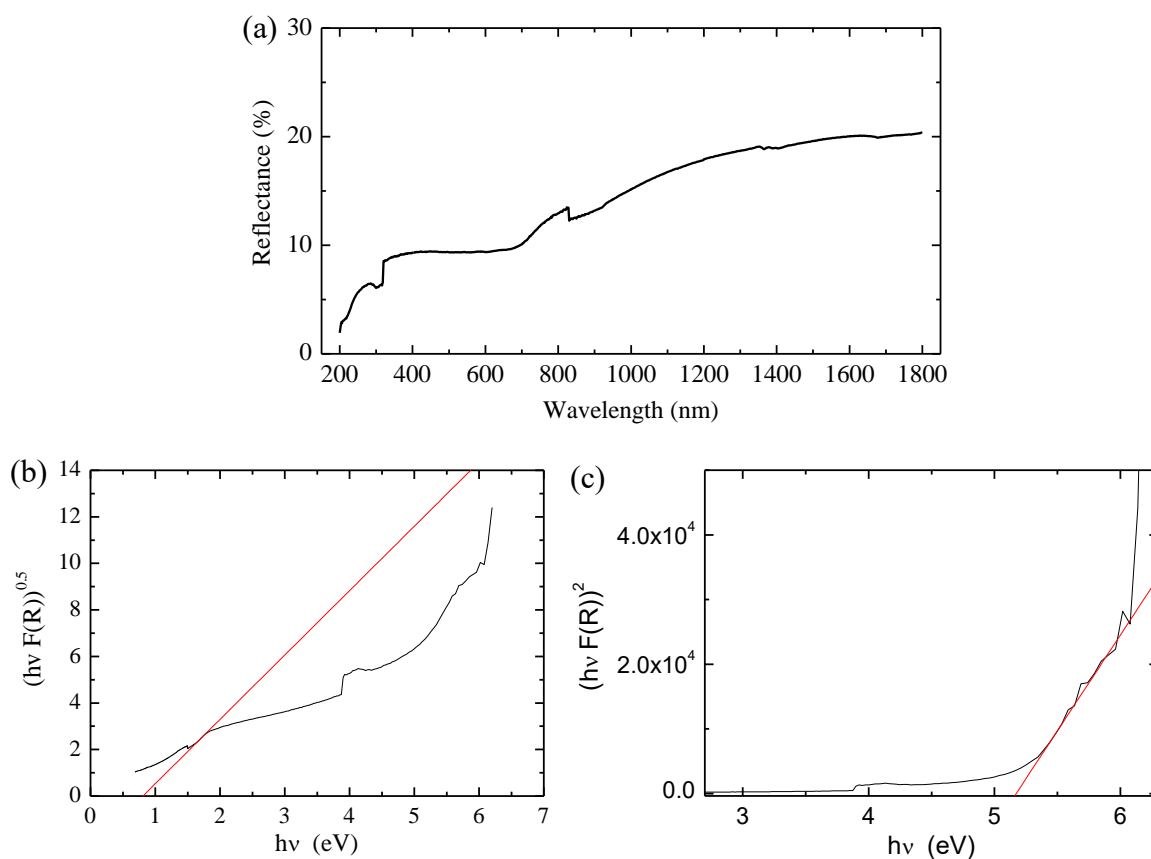


Figure 3.11. (a) Evolution of diffuse reflectance of LiCoO₂ powder as a function of wavelength and (b) corresponding Tauc plot assuming an indirect allowed transition ($n=2$) and (c) a direct allowed transition ($n=0.5$).

The Mott-Schottky measurements were carried out on 18 μm thick LiCoO₂ films prepared by doctor blading in aqueous and non-aqueous aprotic electrolytes. Representative Mott-Schottky plots are provided in Figure 3.12. First observation is that the slope of the Mott-Schottky transition is dependent on the electrolyte nature. LiCoO₂ shows a n-type conductivity when measured in aqueous 0.5 mol/L TBANO₃ electrolyte. However, it turns to be a p-type semiconductor in non-aqueous aprotic 1 mol/L TBAPF₆ EC/DMC electrolyte. To the best of our knowledge, this is the first report of a conductivity-type dependence on the nature of the electrolyte. This result suggests that LiCoO₂ is a weak degenerated semiconductor for which the Fermi level is close to the middle of the band gap. Tukamoto et al. reported that LiCoO₂ is a p-type semiconductor based on ac and dc measurements in controlled atmosphere (air, 1% O₂, and argon). This type of conduction is ascribed to the presence of a small proportion of Co⁴⁺ ions which acts as a dopant increasing hole concentration and its mobility [43]. Rosolen et al. reported a p-type conductivity based on photocurrent measurements in LiClO₄ PC/DMC

electrolyte, which agrees well with our results in non-aqueous aprotic electrolyte [42]. LiCoO_2 has also been reported by Menetrier et al. to be p-type based on thermopower measurements [44]. It is worth to mention that we can exclude the possibility of lithium / proton exchange in aqueous electrolyte, as we repeated the Mott-Schottky measurements in aqueous electrolytes at different pH from 1 to 14 without any visible change in the slope. Note that such a verification has been made for all other sensitive materials which showed a conductivity-type changeover depending on the electrolyte nature (i.e. MoS_2 and WS_2 presented in the following). This means that the donor or acceptor character depends on the electrolyte nature during the Fermi level equalization for such weak degenerated semiconductor, i.e. when the concentration of electrons is relatively comparable to the concentration of holes.

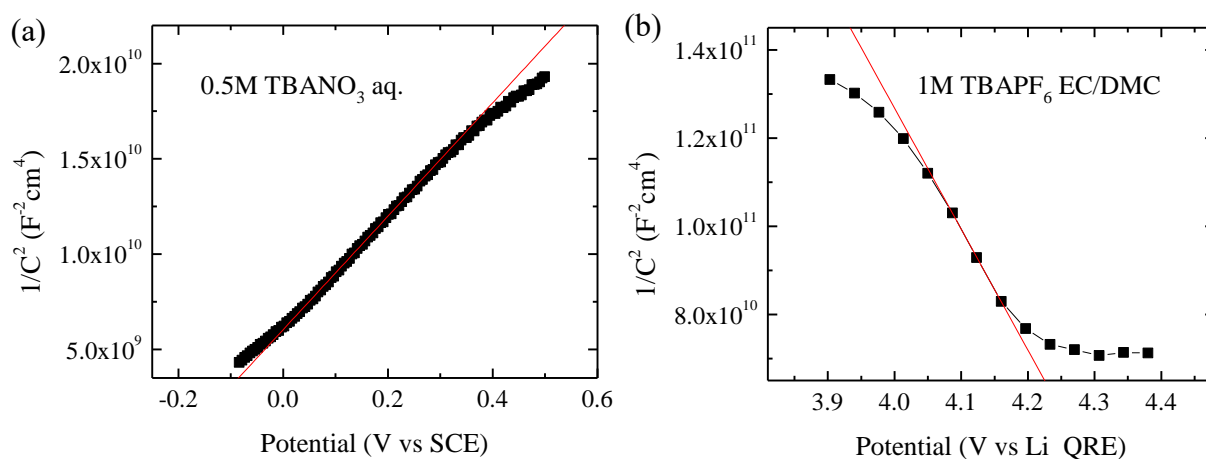


Figure 3.12. Mott-Schottky plot of LiCoO_2 measured at 100 Hz in (a) 0.5 mol/L TBANO_3 aqueous electrolyte and (b) 1 mol/L TBAPF_6 EC/DMC electrolyte.

The flat band potential and donor density values derived from the Mott-Schottky plots are presented in Table 3.4. In 0.5 mol/L TBANO_3 aqueous solution (pH = 1.65), we measured a flat band potential at -0.21 V vs. SCE which corresponds to -0.72 V vs. NHE at pH = 14 considering Nernst equation. This value corresponds to the lower edge of the conduction band. When measured in a non-aqueous aprotic 1 mol/L TBAPF_6 EC/DMC solution, the flat band potential is at 4.44 V vs. Li QRE, corresponding to 1.24 V vs. NHE. In contrast to non-aqueous aprotic electrolyte, this value is attributed to the position of the higher edge energy of the valence band because of the conductivity-type changeover. Considering the band gap of 0.79 eV, the lower conduction band edge is positioned at 0.37 V vs. NHE, which is 1.09 V lower compared to 1 mol/L TBAPF_6 EC/DMC (Fig. 3.13).

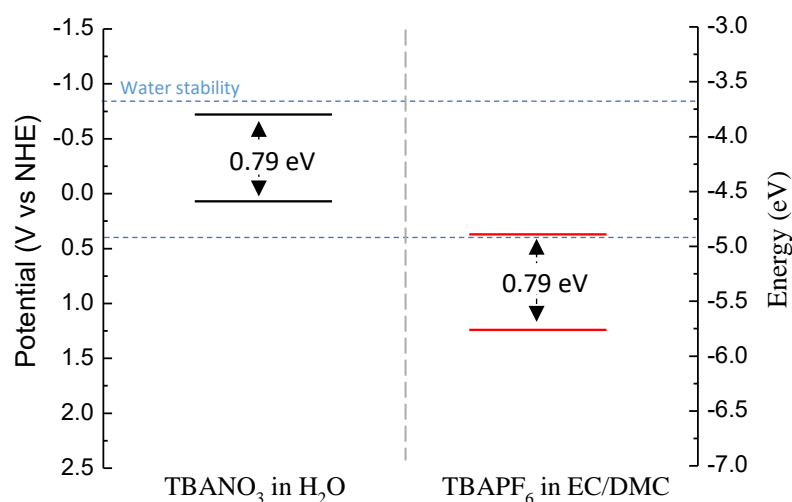


Figure 3.13. Representation of the band edge positions of LiCoO_2 film in aqueous electrolyte at $\text{pH} = 14$ (black) and in non-aqueous aprotic EC/DMC-based electrolyte (red).

The charge carrier concentration of LiCoO_2 for each experiment was determined by considering a dielectric constant of 2. This value was proposed by Khatun et al. [45] and Nageswara Rao et al. [46] (Table 3.4). In 0.5 mol/L TBANO_3 aqueous solution we determined a concentration of n-type charge carriers of $4.9 \cdot 10^{19} \text{ cm}^{-3}$ compared to $2.6 \cdot 10^{20} \text{ cm}^{-3}$ of holes in 1 mol/L TBAPF_6 EC/DMC electrolyte. This latter value is almost one order of magnitude lower than the value of 10^{21} cm^{-3} reported by Mizutani et al. based on termopower measurements [47]. As one can see, the concentration of electrons and holes is not considerably different which supports our explanation driving the n-type vs. p-type changeover.

Table 3.4. Flat band potential and charge carrier concentration of LiCoO_2 in 0.5 mol/L TBANO_3 aqueous electrolyte and 1 mol/L TBAPF_6 EC/DMC electrolyte.

Electrolyte	Flat band potential			Charge carrier concentration, cm^{-3}
	as measured	Recalculated		
		V vs. NHE	V vs. NHE at $\text{pH}=14$	
0.5 mol/L TBANO_3 in H_2O	- 0.23 V vs. SCE	0.01 (at $\text{pH}=1.65$)	-0.72	$4.9 \cdot 10^{19}$
1 mol/L TBAPF_6 in EC/DMC	4.44 V vs. Li QRE	1.24	-	$2.6 \cdot 10^{20}$

Unfortunately, the photophysical properties of LiCoO_2 could not be measured because of the too low bandgap value. This would correspond at best to an excitation band at around 1570 nm, which is not appropriate with a Xe lamp source for excitation and far from the detection limit of a PMT-type detector (ca. 850 nm). Note that this will be the case for all the materials having a band gap value lower than 1.5 eV presented in this study.

3.1.3. MoO_3

MoO_3 was one of the first materials studied for lithium-ion battery owing to its layered structure. Each layer is formed by two sheets of MoO_6 octahedra sharing corners along [001] and [100] directions, and connected together by edge sharing along [001] direction (Fig. 3.14). The layers are alternatively stacked along the c-axis and maintained by electrostatic van der Waals' forces. This two-dimensional structure allows a reversible intercalation of ca. 1.5 lithium per molybdenum transition metal [48-49], resulting in a lithiated phase (Li_xMoO_3) with a good electronic conductivity (10^{-2} S/cm) and Li^+ diffusion coefficient (10^{-10} cm^2/s) [50-51].

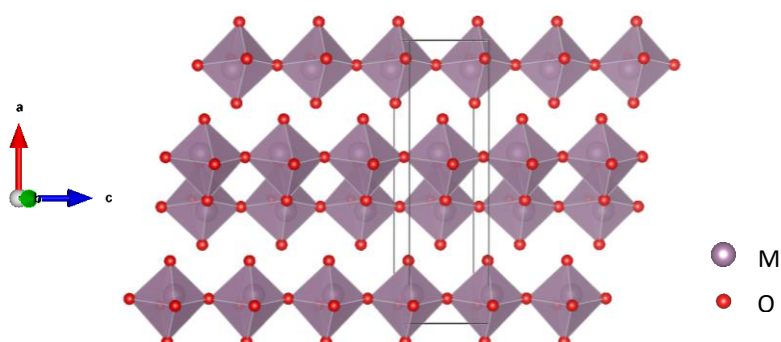


Figure 3.14. Crystal structure representation of MoO_3 according to (101) plane.

The XRD pattern of MoO_3 powder is presented in Figure 3.15 (a). The diffractogram shows single phase, which was successfully indexed with the $Pnma$ space group (orthorhombic lattice). The refined lattice cell parameters are $a = 13.825(8)$ Å, $b = 3.694(6)$ Å, $c = 3.954(6)$ Å ($V = 202$ Å³). These values are in good agreement with literature [52]. The particles have no specific morphology (Fig. 3.15 (b)). Their size is ranging from 50 to 500 nm without being agglomerated. The surface of the particles is well-crystallized without any sign of amorphous regions (Fig. 3.15 (c-d)).

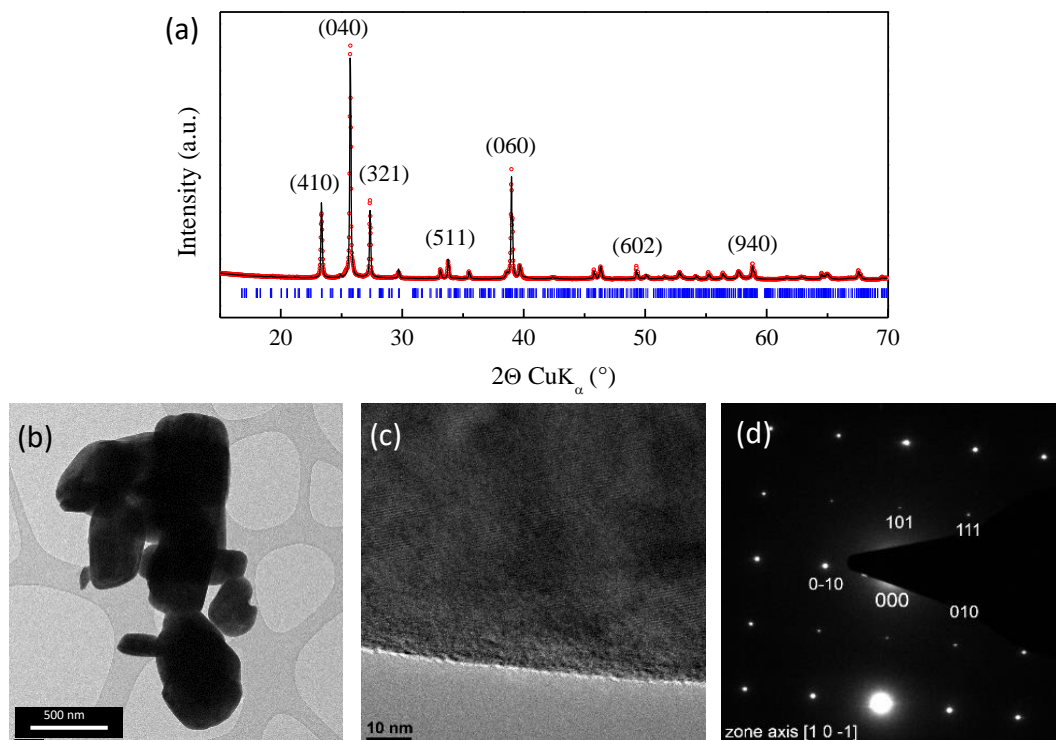


Figure 3.15. (a) Full pattern matching refinement of x-ray diffraction pattern of MoO_3 with its corresponding (b,c) transmission and high-resolution transmission electron micrographs and (d) selected area electron diffraction pattern.

Figure 3.16 (a) shows the evolution of the reflectance as a function of wavelength for MoO_3 between 200 and 1800 nm. Assuming an indirect allowed transition, which we argue to be the case based on the steepness of the transition, we found a band gap of 2.93 eV (Fig. 3.16 (b)). This value is in good agreement with the value of 2.9 eV reported by Anwar et al. based on absorbance measurements [53] and 3.05 eV reported by Zhao et al. based on transmittance measurements [54]. If we assume MoO_3 to have a direct transition, we then obtain a band gap of 3.49 eV, which is not consistent with the yellow colour of the particles. The values reported in the literature in this case are also very dispersed, between 3.15 eV [55] and 4.1 eV [56] based on optical measurements, and 1.95 eV [57] and 3.87 eV when calculated [56].

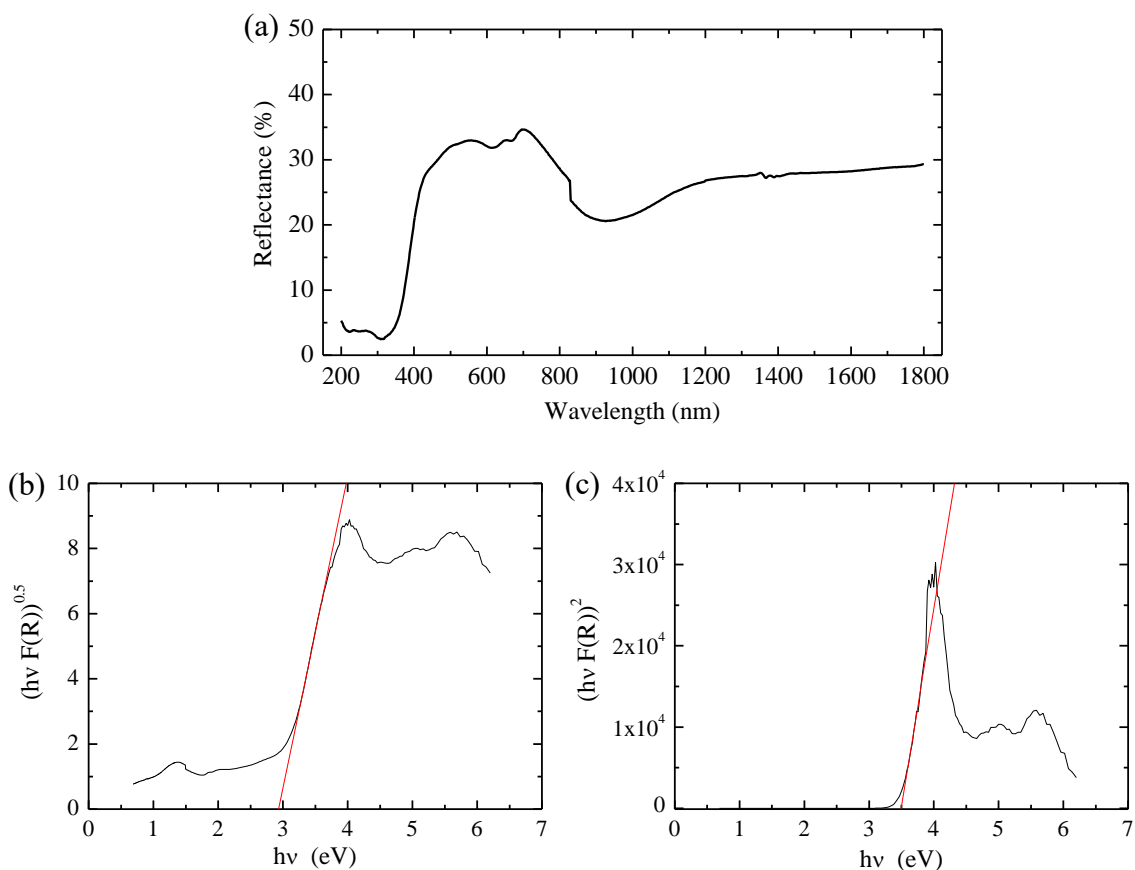


Figure 3.16. (a) Evolution of diffuse reflectance of MoO₃ powder as a function of wavelength using an integrating sphere and corresponding Tauc plot assuming (b) an indirect allowed transition ($n=2$) and (c) a direct allowed transition ($n=0.5$).

The representative Mott-Schottky plots of 13 μm doctor-bladed MoO₃ films are presented in Figure 3.17. In both aqueous and non-aqueous aprotic EC/DMC-based electrolytes, the positive slope of the Mott-Schottky curve shows a n-type conductivity of material. This is in good agreement with Kroger et al. who reported strong n-type conduction based on the determination of the Fermi level position by combining ultraviolet photoemission spectroscopy (UPS) and inverse photoemission spectroscopy (IPES) techniques [58].

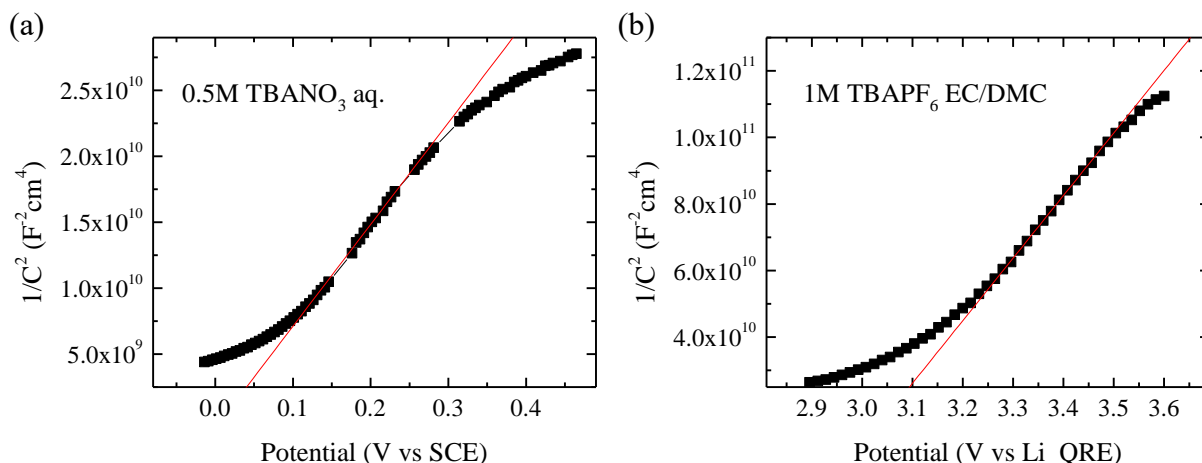


Figure 3.17. Mott-Schottky plot of MoO_3 measured in (a) 0.5 mol/L TBANO_3 aqueous electrolyte at 250 Hz and (b) 1 mol/L TBAPF_6 EC/DMC electrolyte at 200 Hz.

The flat band potential and donor density values are gathered in Table 3.5. The flat band potential is situated at -0.01 V vs. SCE in 0.5 mol/L TBANO_3 aqueous solution at pH = 8.84. It corresponds to -0.08 V vs. NHE at pH = 14 considering Nernst dependence [59-60]. There is a lack of convergence in literature regarding the position of the band edge energy of MoO_3 . Tong et al. reported a conduction band edge at -2.2 V (vs. NHE) based on the UPS measurements [61]. Using same technic, other studies reported a value between 0.4 and 1.3 V (vs. NHE) [62-63], and even up to 2.3 V (vs. NHE) by Kroger et al. based on UPS and IPES measurements [58] and Greiner et al. based on UPS [64]. Such an inconsistency in values may stem from different levels of surface defects as UPS measurements in only sensitive to the extreme surface by contrast to Mott-Schottky experiments which is less surface sensitive even though it is an interfacial measurement. Our result lies in the middle of this wide range of flat-band potential values.

In 1 mol/L TBAPF_6 EC/DMC electrolyte, the flat band potential was measured at 2.94 V vs. Li QRE, which corresponds to -0.26 V vs. NHE. There are no reports on the flat-band potential of MoO_3 in non-aqueous aprotic solvent in literature. Taking into account the bandgap of 2.93 eV, the valence band edge of MoO_3 is determined at 2.85 V (vs. NHE) in aqueous electrolyte and at 2.67 V (vs. NHE) in non-aqueous aprotic electrolyte (Fig. 3.18).

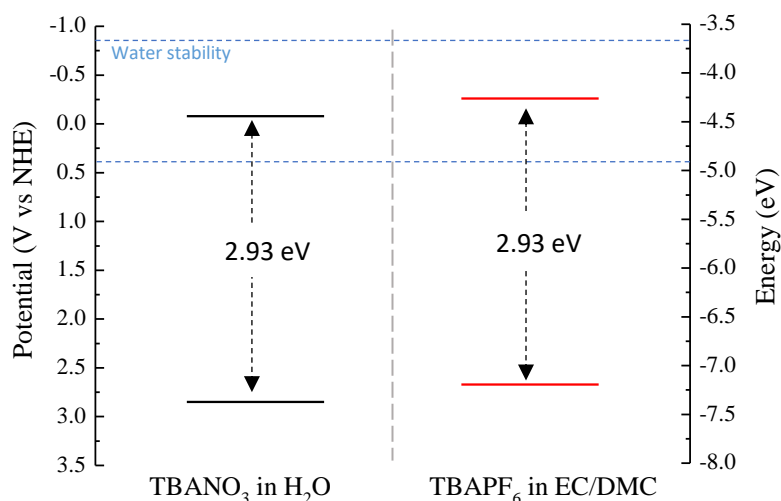


Figure 3.18. Representation of the band edge positions of MoO_3 in aqueous electrolyte recalculated at $\text{pH} = 14$ (black) and in non-aqueous aprotic EC/DMC-based electrolyte (red).

The charge carrier concentration of MoO_3 was determined using a dielectric constant of 6 as proposed by Lajaunie et al. based on calculations [65]. In 0.5 mol/L TBANO_3 aqueous solution, a charge carrier concentration of $4.1 \cdot 10^{18} \text{ cm}^{-3}$ was determined. This is in a good agreement with the value of $1.5 \cdot 10^{18} \text{ cm}^{-3}$ reported by Nadkarni et al. based on the alternating current measurements [66-67]. In 1 mol/L TBAPF_6 EC/DMC electrolyte, we found a significantly higher donor concentration of $1.2 \cdot 10^{20} \text{ cm}^{-3}$, which is almost two orders of magnitude higher compared to aqueous electrolyte.

Table 3.5. Flat band potential and charge carrier concentration of MoO_3 in 0.5 mol/L TBANO_3 aqueous electrolyte and in 1 mol/L TBAPF_6 EC/DMC electrolyte.

Electrolyte	Flat band potential			Charge carrier concentration, cm^{-3}
	as measured	recalculated		
		V vs. NHE	V vs. NHE at $\text{pH}=14$	
0.5 mol/L TBANO_3 in H_2O	-0.01 V vs. SCE	0.23 ($\text{pH}=8.84$)	-0.08	$4.1 \cdot 10^{18}$
1 mol/L TBAPF_6 in EC/DMC	2.94 V vs. Li QRE	-0.26	-	$1.2 \cdot 10^{20}$

Interestingly, we found that MoO_3 gives no fluorescence in the range of 250 to 800 nm. This means that all energy relaxation from the excited states proceeds according to non-radiative mechanisms or that the low luminescence is quenched by the particles agglomeration. Such a behavior is not intrinsic to MoO_3 but has also been encountered in other materials presented in the following, i.e. WO_3 , Bi_2O_3 , LiFePO_4 , LiMnPO_4 , and LiVPO_4F .

3.1.4. WO_3

Tungsten trioxide is a well-known wide band gap semiconductor, which has attracted attention for its electrochemical and electrochromic properties. This material found extensive applications in smart windows [68], gas sensors [69], electronic displays [70], and photocatalysis [71-72]. The WO_6 octahedra are forming a corner-sharing structure allowing open diffusion channels for alkali cation insertion (Fig. 3.19). Its main advantage is the high reversible electrode capacity reported to maintain ca. 650 mAh/g over 100 cycles for lithium-ion batteries [73].

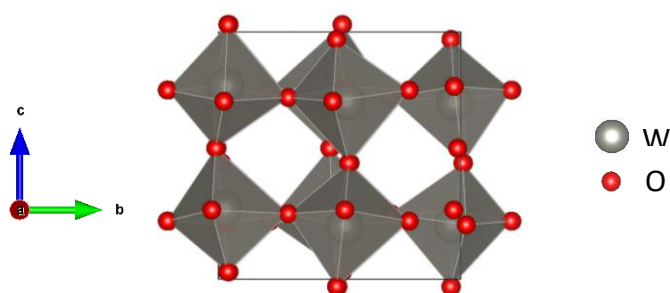


Figure 3.19. Crystal structure representation of WO_3 according to (011) plane.

The refined x-ray diffractogram of WO_3 powder is presented in Figure 3.20 (a). All diffraction peaks are indexed into pure monoclinic phase with a $P2_1/n$ space group. The lattice cell parameters are $a = 7.300(6)$ Å, $b = 7.538(8)$ Å, $c = 7.689(6)$ Å, and $\beta = 90.89^\circ$ ($V = 423$ Å³) in a good agreement with the literature [74]. The transmission electron micrograph depicts spheroidal particles with an average size of 40-80 nm (Fig. 3.20 (b)). The high-resolution TEM (HR-TEM) micrograph shows good crystallinity without the presence of any amorphous region in the samples (Fig. 3.20 (c-d)).

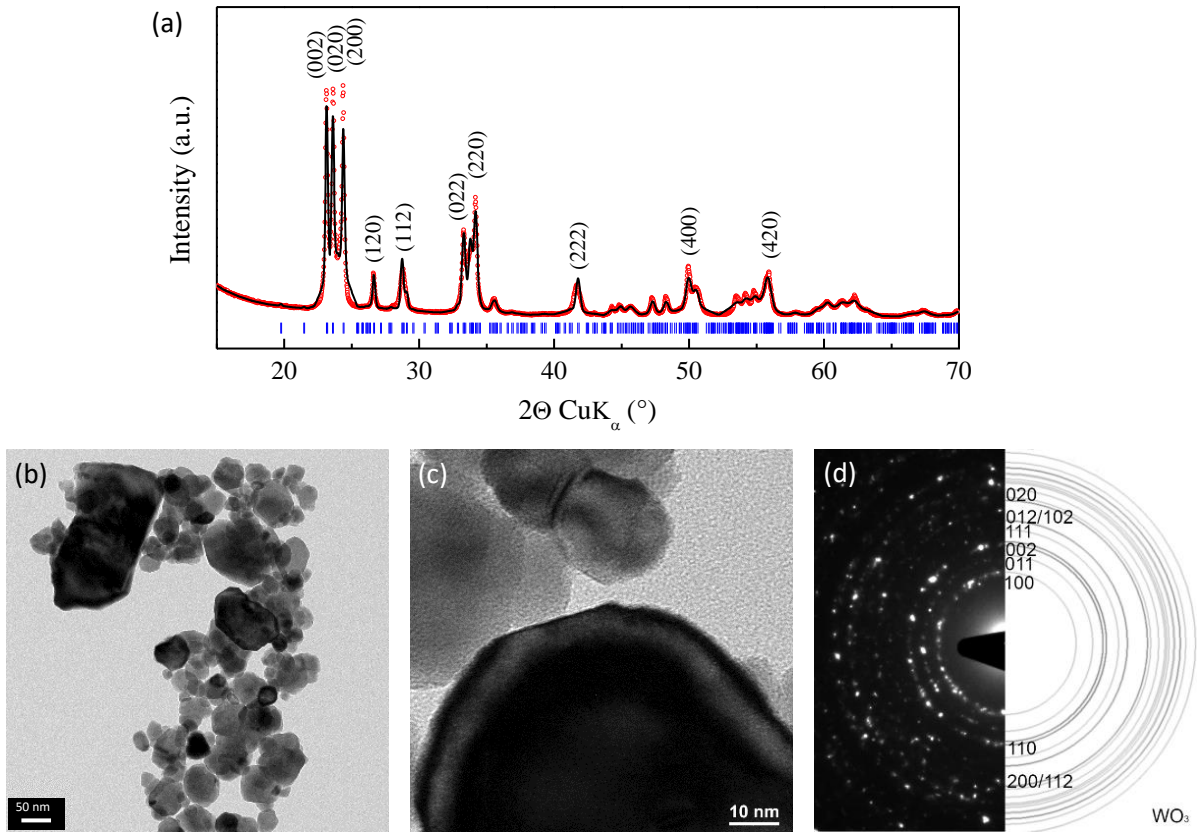


Figure 3.20. (a) Full pattern matching of x-ray diffraction pattern of WO_3 with the corresponding (b,c) transmission electron micrograph and high-resolution transmission electron micrograph, and (d) selected area electron diffraction pattern.

WO_3 band gap was determined to be 2.49 eV assuming an indirect allowed transition (Fig. 3.21 (a-b)). This result lies close to the lower edge of the 2.51 - 2.87 eV indirect band gap values reported in literature based on optical measurements [75–79]. In the case when we assume a direct transition, a band gap of 3.52 eV is obtained, which is not consistent with the yellow/green coloration of the particles (Fig. 3.21 (c)).

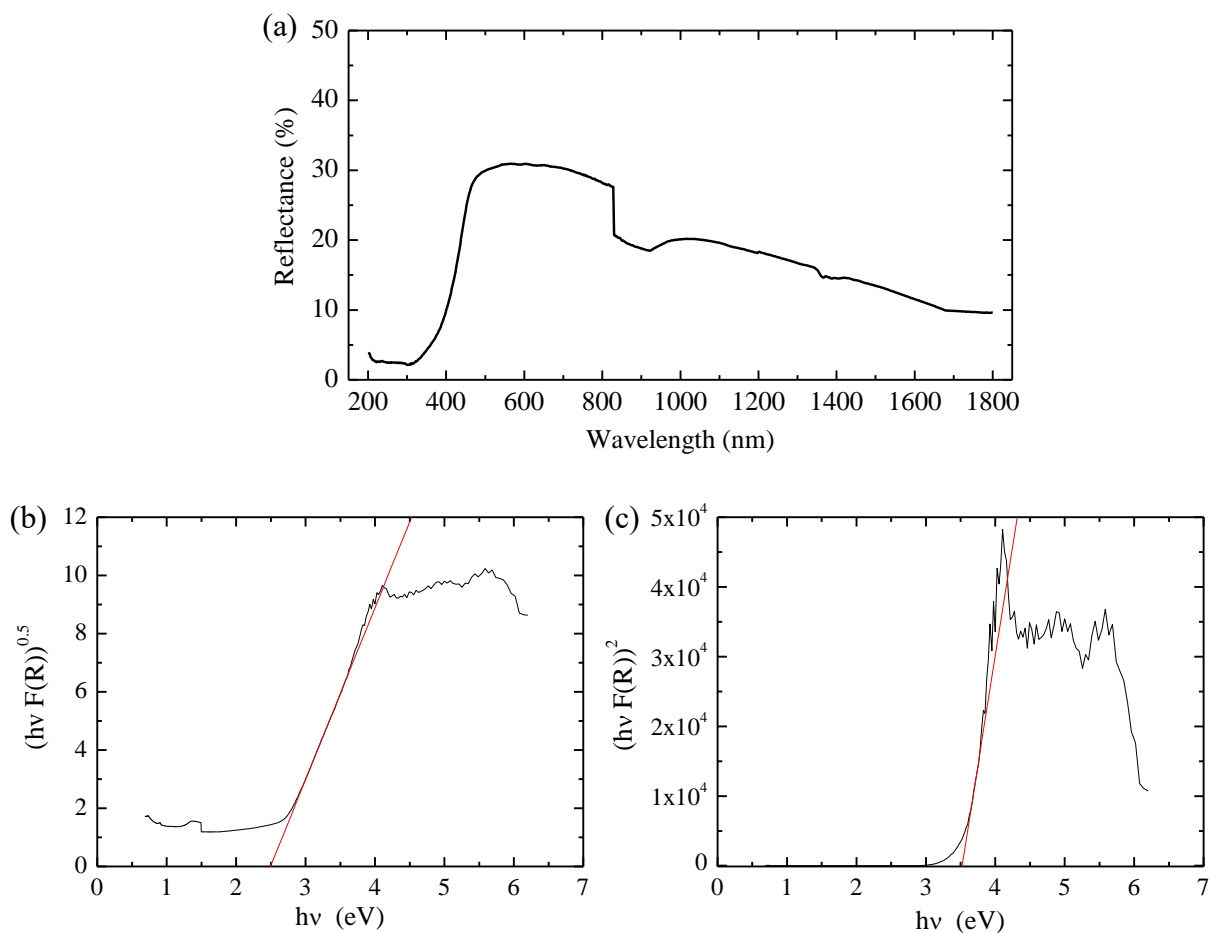


Figure 3.21. (a) Evolution of diffuse reflectance of WO_3 nanoparticles as a function of wavelength and corresponding Tauc plot assuming (b) an indirect allowed transition ($n=2$) and (c) a direct allowed transition ($n=0.5$).

The Mott-Schottky plots of 5 μm doctor-bladed WO_3 films recorded in two different electrolytes are presented in Figure 3.22. It shows a n-type conductivity in both aqueous 0.5 mol/L $TBANO_3$ electrolyte and non-aqueous aprotic 1 mol/L $TBAPF_6$ EC/DMC-based electrolyte. This is in agreement with literature based on Mott-Schottky measurements carried out in Na_2SO_4 and H_2SO_4 aqueous electrolytes [80–82] and thermopower measurements [83].

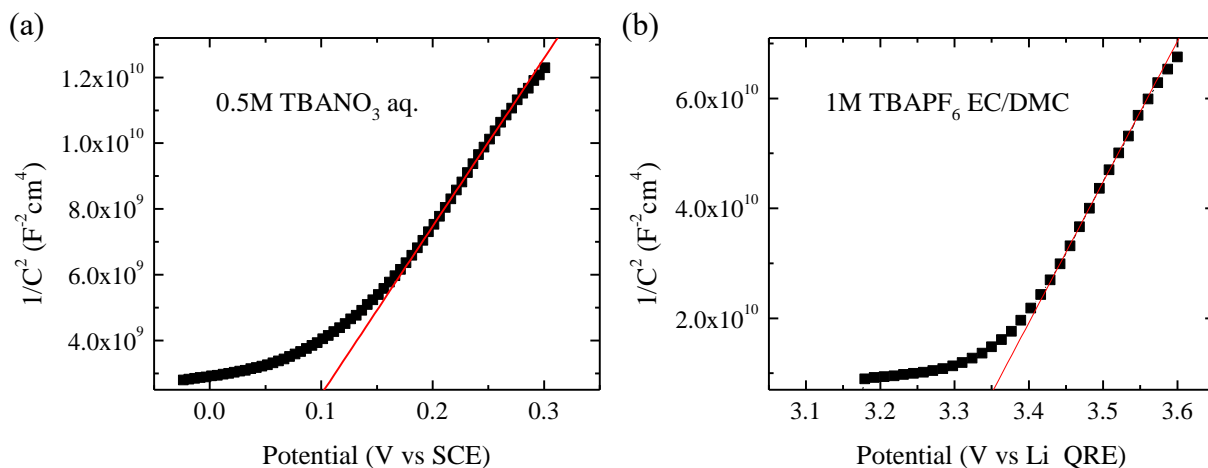


Figure 3.22. Mott-Schottky plot of WO_3 measured in (a) 0.5 mol/L TBANO_3 aqueous electrolyte at 250 Hz and (b) 1 mol/L TBAPF_6 EC/DMC electrolyte at 100 Hz.

The flat band potential and charge carrier concentration values are gathered in Table 3.6. In 0.5 mol/L TBANO_3 aqueous solution (pH = 1.65), we obtained a flat band potential of 0.03 V vs. SCE which corresponds to -0.46 V vs. NHE at pH = 14 assuming Nernst equation [59-60]. Our result lies in the broad range of values reported between - 0.22 and - 0.59 V (vs. NHE at pH = 14) in literature [80, 82] based on Mott-Schottky measurements in Na_2SO_4 and H_2SO_4 -based electrolytes. In a non-aqueous aprotic electrolyte, the flat band potential value was equal to 3.22 V vs. Li QRE, thus corresponding to 0.03 V vs. NHE. These results indicate that the conduction band of WO_3 is 0.49 eV lower in non-aqueous aprotic electrolyte (Fig. 3.23).

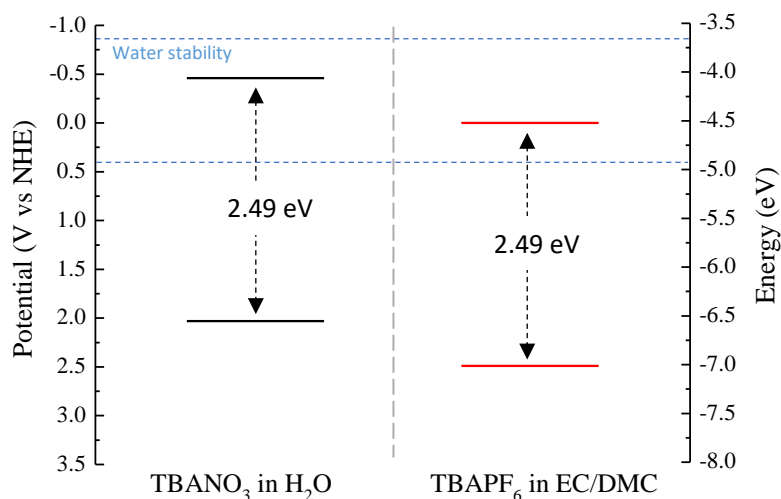


Figure 3.23. Representation of the band edge positions of WO_3 film measured in aqueous electrolyte and recalculated to pH = 14 (black) and in non-aqueous aprotic EC/DMC-based electrolyte (red).

The charge carrier concentration of WO_3 was determined with the dielectric constant of 20 as proposed by Wang et al. (Table 3.6) [80]. A value of $1.4 \cdot 10^{18} \text{ cm}^{-3}$ was extracted in 0.5 mol/L TBANO_3 aqueous electrolyte and $2.8 \cdot 10^{19} \text{ cm}^{-3}$ in 1 mol/L TBAPF_6 EC/DMC. This indicates that more than one order of magnitude higher WO_3 donor density is obtained in non-aqueous aprotic electrolyte. Our value determined in aqueous electrolyte is one to two orders of magnitude lower than those reported in literature in Na_2SO_4 and H_2SO_4 aqueous electrolytes, i.e. from 10^{19} to 10^{20} cm^{-3} [80–82].

Table 3.6. Flat band potential and charge carrier concentration of WO_3 in 0.5 mol/L TBANO_3 aqueous electrolyte and 1 mol/L TBAPF_6 EC/DMC electrolyte.

Electrolyte	Flat band potential			Charge carrier concentration, cm^{-3}
	as measured	recalculated		
		V vs. NHE	V vs. NHE at pH=14	
0.5 mol/L TBANO_3 in H_2O	0.03 V vs. SCE	0.27 (pH=1.65)	-0.46	$1.4 \cdot 10^{18}$
1 mol/L TBAPF_6 in EC/DMC	3.22 V vs. Li QRE	0.03	-	$2.8 \cdot 10^{19}$

3.1.5. CuO

Cupric oxide is an interesting negative electrode material for Lithium-ion batteries because of its high gravimetric capacity of ca. 600 mAh/g obtained through a conversion reaction involving $\text{Cu}^{\text{II}} / \text{Cu}^0$ redox couple according to a plateau at 1.3 V vs. Li^+/Li [84], [85]. CuO has a tenorite-type structure with a square planar coordination of copper by oxygen in a monoclinic crystal structure, forming a zigzag Cu–O chains oriented along the $[10\bar{1}]$ and $[101]$ directions (Fig. 3.24).

The refinement of x-ray diffraction pattern of CuO shows single phase that crystallizes into a monoclinic-type structure with C2/c space group (Fig. 3.25 (a)). The refined lattice cell parameters are $a = 4.690(8) \text{ \AA}$, $b = 3.420(16) \text{ \AA}$, $c = 5.131(3) \text{ \AA}$, and $\beta = 99.54^\circ$ ($V = 81 \text{ \AA}^3$). These values are in good agreement with the values reported by Chaudhary et al. [86].

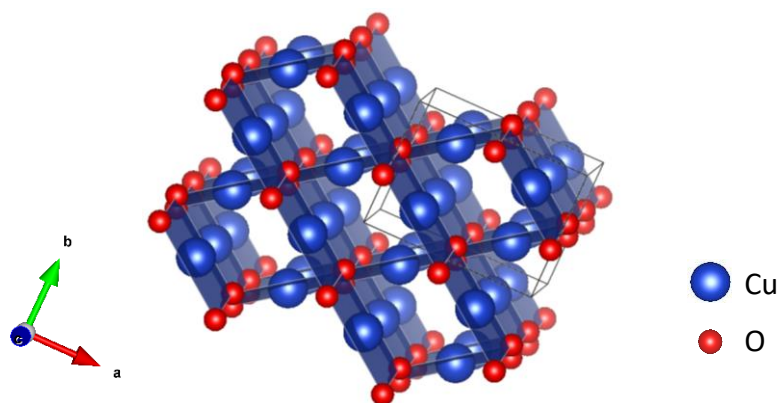


Figure 3.24. Crystal structure representation of CuO.

The TEM study revealed that the powder consists of well-separated particles with close to spherical morphology without presence of any amorphous regions. The particle size is ranging between 20 and 100 nm. (Fig. 3.25 (b-c)).

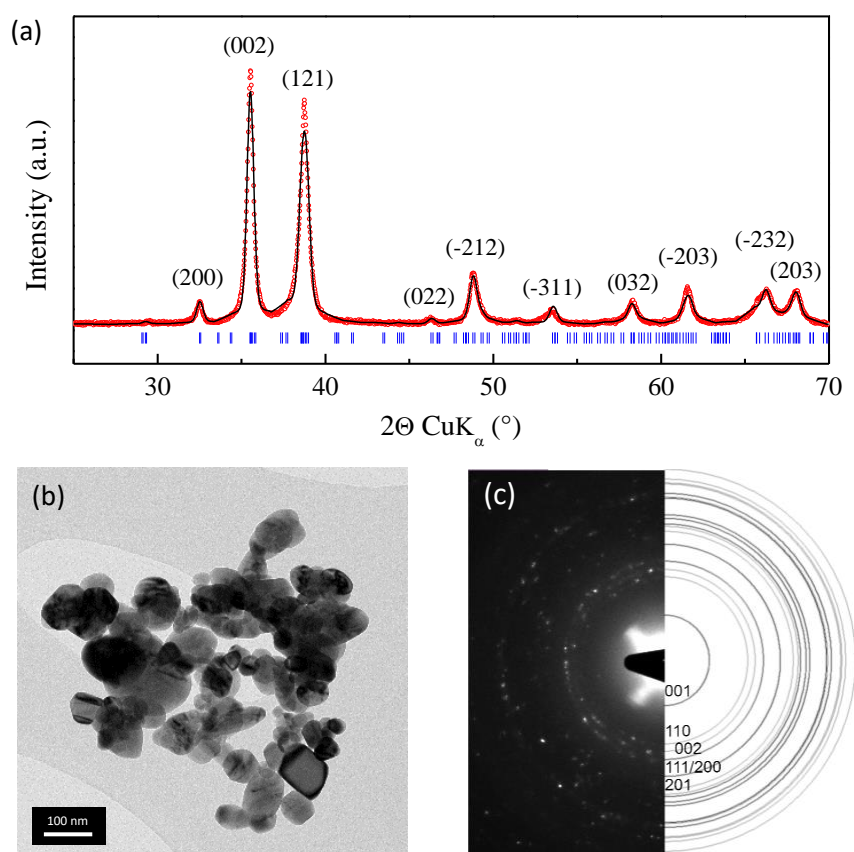


Figure 3.25. (a) Full pattern matching refinement of x-ray diffraction profile of CuO powder with corresponding (b) transmission electron micrograph and (c) high-resolution transmission electron micrograph with (d) selected area electron diffraction pattern.

The band gap value of CuO was determined from the diffuse reflectance spectrum considering both indirect allowed and direct allowed transitions (Fig. 3.26). Assuming that CuO has an indirect allowed transition, we determined a band gap value of 1.19 eV (Fig. 3.26 (b)). This result is in good agreement with the 1.2 eV calculated from the high temperature intrinsic conductivity measurements reported by Jeong et al. [87]. The value also lies in the bottom of the wide range of values reported in literature between 1.20 eV and 1.79 eV based on the absorption spectroscopy measurements assuming an indirect allowed transition [88–92]. Assuming a direct allowed transition, the band gap is equal to 1.66 eV (Fig. 3.26 (c)). This value is considerably lower than the values reported in literature for a direct allowed transition ranging from 2.4 to 3.2 eV [88, 92, 93]. However, the slow change in the reflectance spectrum suggests the indirect nature of the transition and the 1.19 eV band gap comes in a good agreement with the black color of the powder.

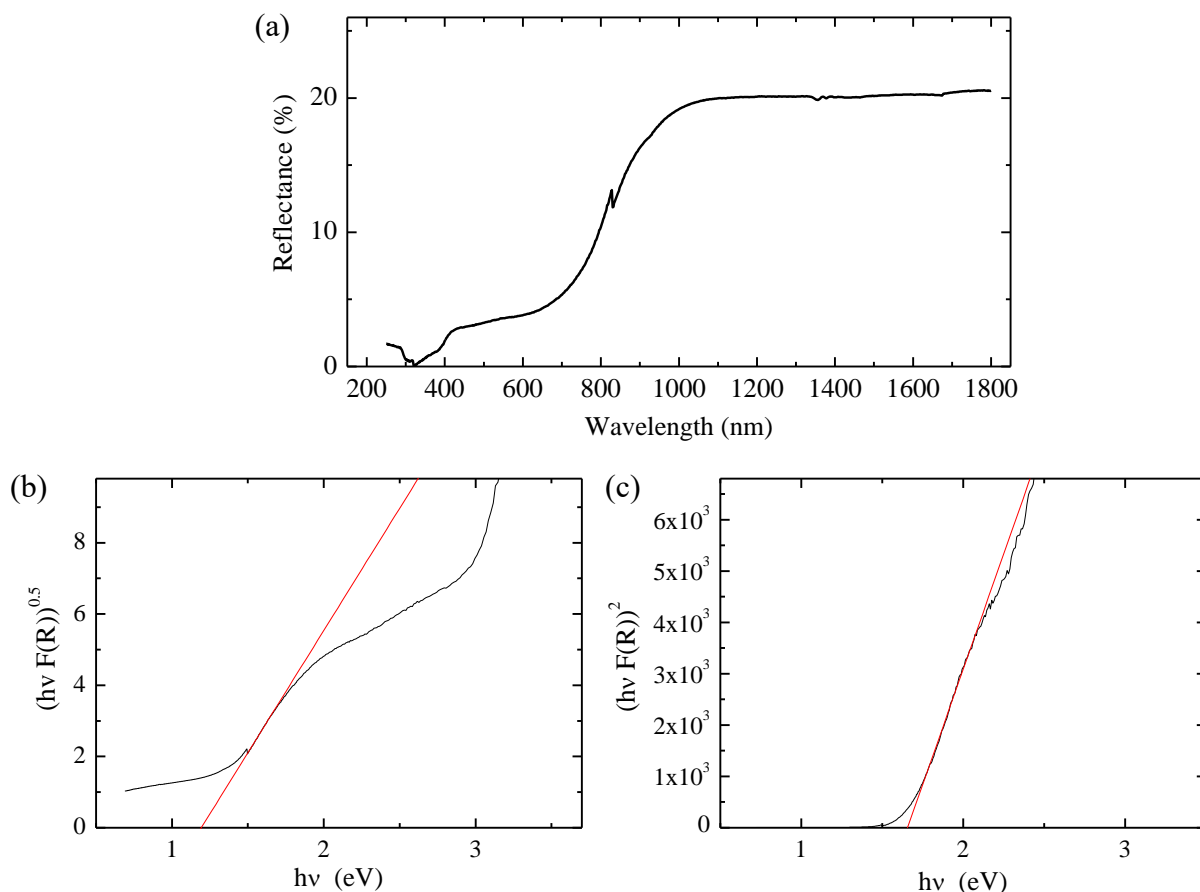


Figure 3.26. (a) Evolution of diffuse reflectance of CuO powder as a function of wavelength. The corresponding Tauc plot is reported assuming (b) an indirect allowed transition ($n=2$) and (c) a direct ($n=0.5$) allowed transition.

To determine the position of conduction and valence band, as well as the type of conductivity, Mott-Schottky impedance was measured on 3 μm thick films deposited on FTO by doctor blading. When measured in a range of aqueous protic electrolytes including NaOH, KOH, Na_2HPO_4 , and TBANO_3 at different pH values, the obtained Mott-Schottky plots were not reproducible. Apart from the significant shift in the Mott-Schottky onset, which can vary to an extent of 0.4, in certain cases, the slope of the curve was changing from positive at lower potentials to negative at higher potentials. This traduces either some kind of side reactions taking place in the electrode depending on the applied potentials, or it can be associated with a crossover change of n to p-type conductivity depending on the applied voltage owing to relative comparable density of holes and electrons in CuO. In addition, for half of the electrodes, we faced issues of bad adhesion onto the FTO substrate leading to the film pilling off at the end of the experiment. In contrast, in 1 mol/L TBAPF₆ EC/DMC electrolyte, a reproducible Mott-Schottky plot was successfully obtained (Fig. 3.27). The negative slope of the linear part of the plot indicates a p-type conductivity in agreement with literature [87–89]. This p-type conductivity stems from the existence of copper vacancies that facilitate hole conduction through Cu-O planar rectangles.

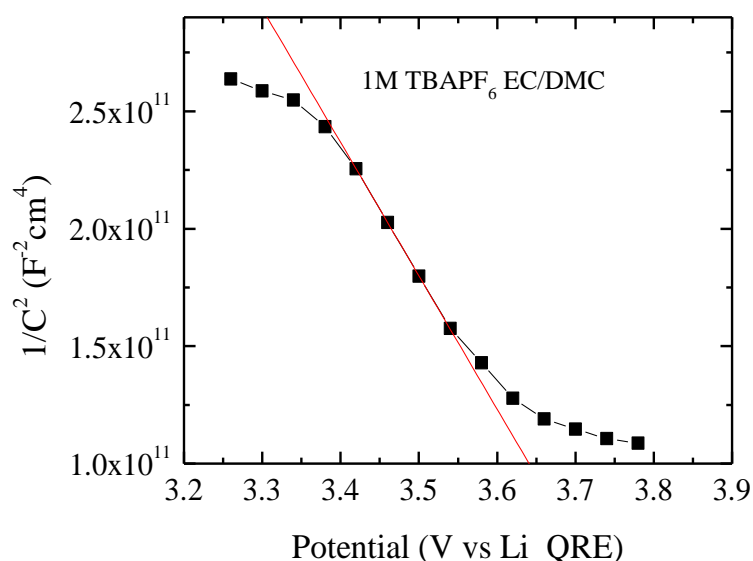


Figure 3.27. Mott-Schottky plot of CuO measured in 1 mol/L TBAPF₆ EC/DMC electrolyte at 300 Hz.

The flat band potential and donor density values are gathered in Table 3.7. We found a flat band potential at 3.80 V vs. Li QRE, which corresponds to the top of valence band position at 0.60 V vs. NHE. The values reported in literature are only based on Mott-Schottky experiments in aqueous electrolytes. The values lie between -1.33 and 0.23 V vs. NHE at pH = 14 [87–90, 94].

Taking into account the 1.19 eV band gap of the material, the position of the conduction band edge is - 0.59 V vs. NHE (Fig. 3.28).

Table 3.7. Flat band potential and charge carrier concentration of CuO in 1 mol/L TBAPF₆ EC/DMC electrolyte.

Electrolyte	Flat band potential		Charge carrier concentration, cm ⁻³
	as measured	Recalculated	
1 mol/L TBAPF ₆ in EC/DMC	3.80 V vs. Li QRE	0.60 V vs. NHE	2.7·10 ¹⁹

A hole concentration of 2.7·10¹⁹ cm⁻³ has been determined based on the dielectric constant of 10 as reported by Nakaoka et al. [89]. This number is in good agreement with the values reported in literature between 4.0·10¹⁸ to 4.0·10²⁰ cm⁻³ [87–89].

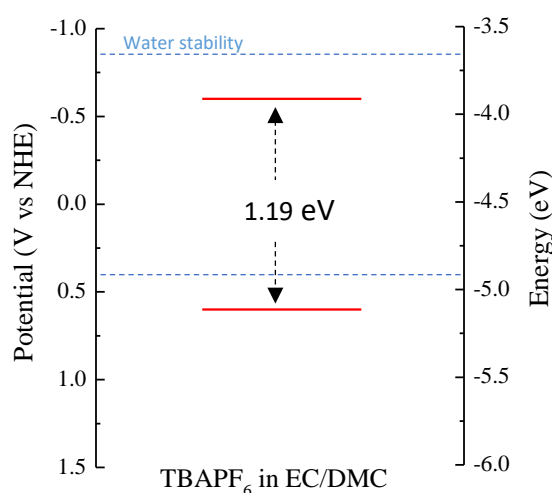


Figure 3.28. Band edge positions of CuO film in non-aqueous aprotic EC/DMC-based electrolyte.

3.1.6. Bi₂O₃

Bismuth oxide is a wide band gap semiconductor that can be used as anode material for lithium-ion batteries. It delivers a gravimetric capacity of ca. 357 mAh/g obtained through a conversion reaction involving Bi^{+III} / Bi⁰ redox processes [95]. Among all the existing polymorphic forms of Bi₂O₃, monoclinic α - and tetragonal β -Bi₂O₃ are the most important. In both cases, the crystal structure is constituted by the equivalently distant layers, parallel to the (011) plane. The tetragonal β -Bi₂O₃ comes of particular interest for lithium-insertion because of the large tunnels

along the a- and c-direction as a result of the different coordination polyhedra sharing only corners in the three-dimensional array (Fig. 3.29) [96].

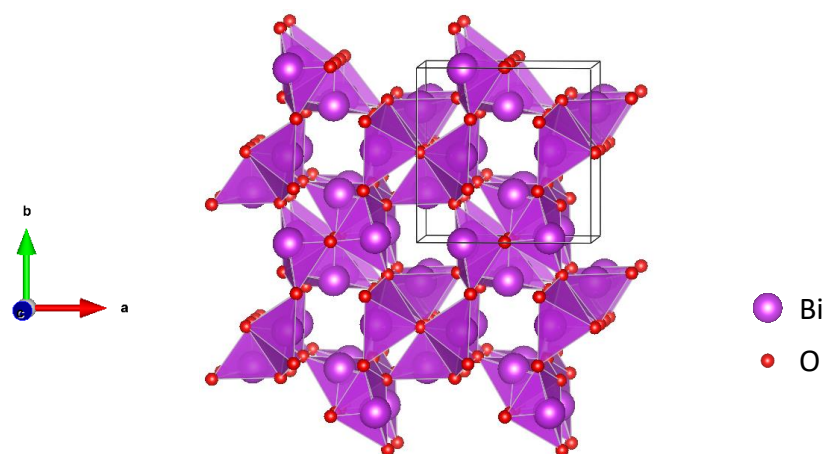


Figure 3.29. Crystal structure representation of β - Bi_2O_3 .

The full-pattern matching refinement of the XRD diffractogram is presented in Figure 3.30 (a). It has intense and sharp diffraction peaks, which indicates a high degree of crystallinity. All the diffraction peaks are corresponding to the tetragonal form (β -phase) within $P\bar{4}2_1c$ space group. The refined lattice cell parameters are $a = b = 7.741(5) \text{ \AA}$ and $c = 5.634(6) \text{ \AA}$ ($V_{\text{cell}} = 338 \text{ \AA}^3$). They are in perfect agreement with those reported by Blower et al., i.e. $a = b = 7.739(1) \text{ \AA}$ and $c = 5.636(1) \text{ \AA}$ [97]. The TEM micrograph reveals spherical morphology of the particles with a diameter ranging between 50 and 200 nm (Fig. 3.30 (b)). A good crystallinity of the particles is proved by the high-resolution TEM micrograph, which show the absence of any amorphous region and confirm the β -phase (Fig. 3.30 (c-d)).

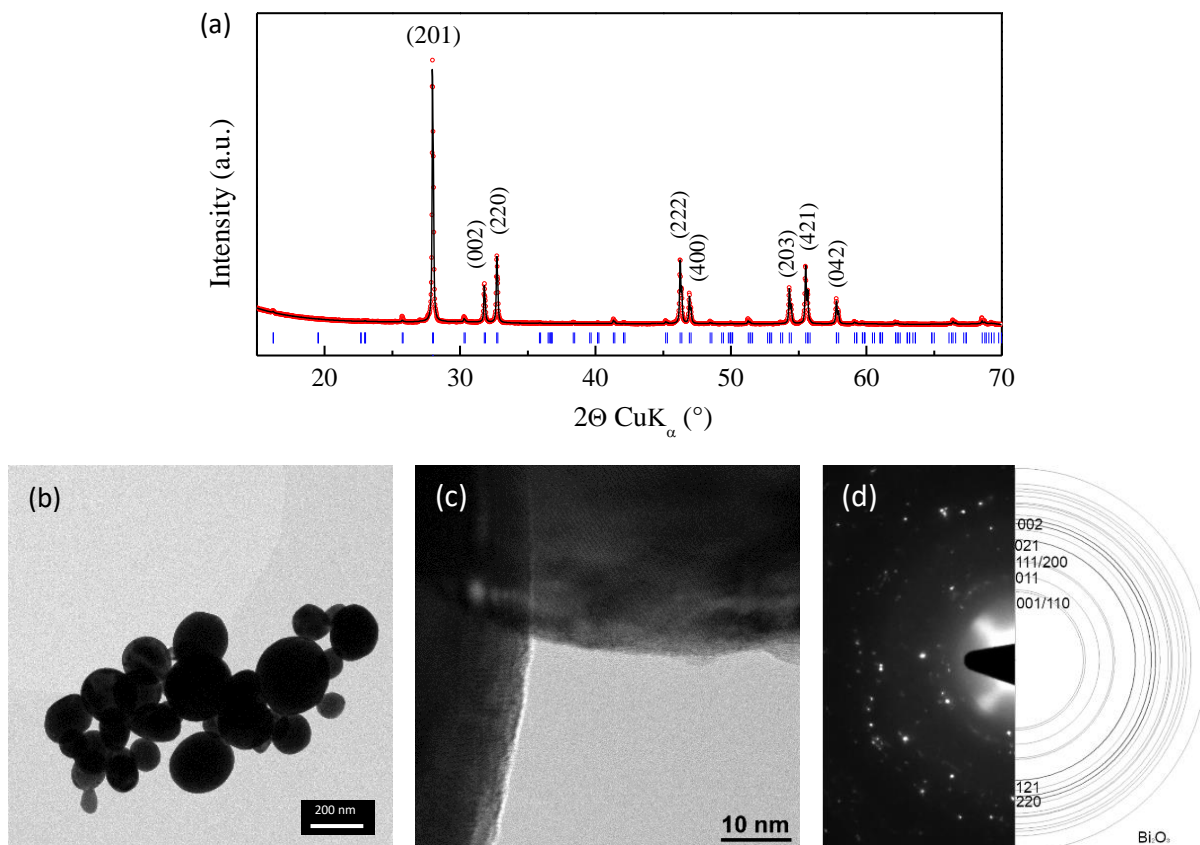


Figure 3.30. (a) Full pattern matching refinement of x-ray diffraction pattern of Bi_2O_3 and corresponding (b) transmission electron micrograph and (c,d) high-resolution transmission electron micrograph and selected area electron diffraction pattern.

The band gap of Bi_2O_3 was also determined from diffuse reflectance experiments (Fig. 3.31 (a)). An absorption edge is observed at around 650 nm. The reflectance maximum is in the NIR region attaining 35% under this experimental condition. We determined a band gap value of 0.98 eV assuming an indirect allowed transition (Fig. 3.31 (b)). This is significantly lower than the values of 2.08 eV reported by Chitrada et al. [98] and 2.15 eV reported by Schlesinger et al. [99] both based on the optical absorption measurements. Assuming a direct allowed transition, a band gap of 2.12 eV is obtained (Fig. 3.31 (c)). This value is closer to the broad range of values reported in literature from 2.26 to 2.88 eV based on the optical absorption spectroscopy measurements [98-104].

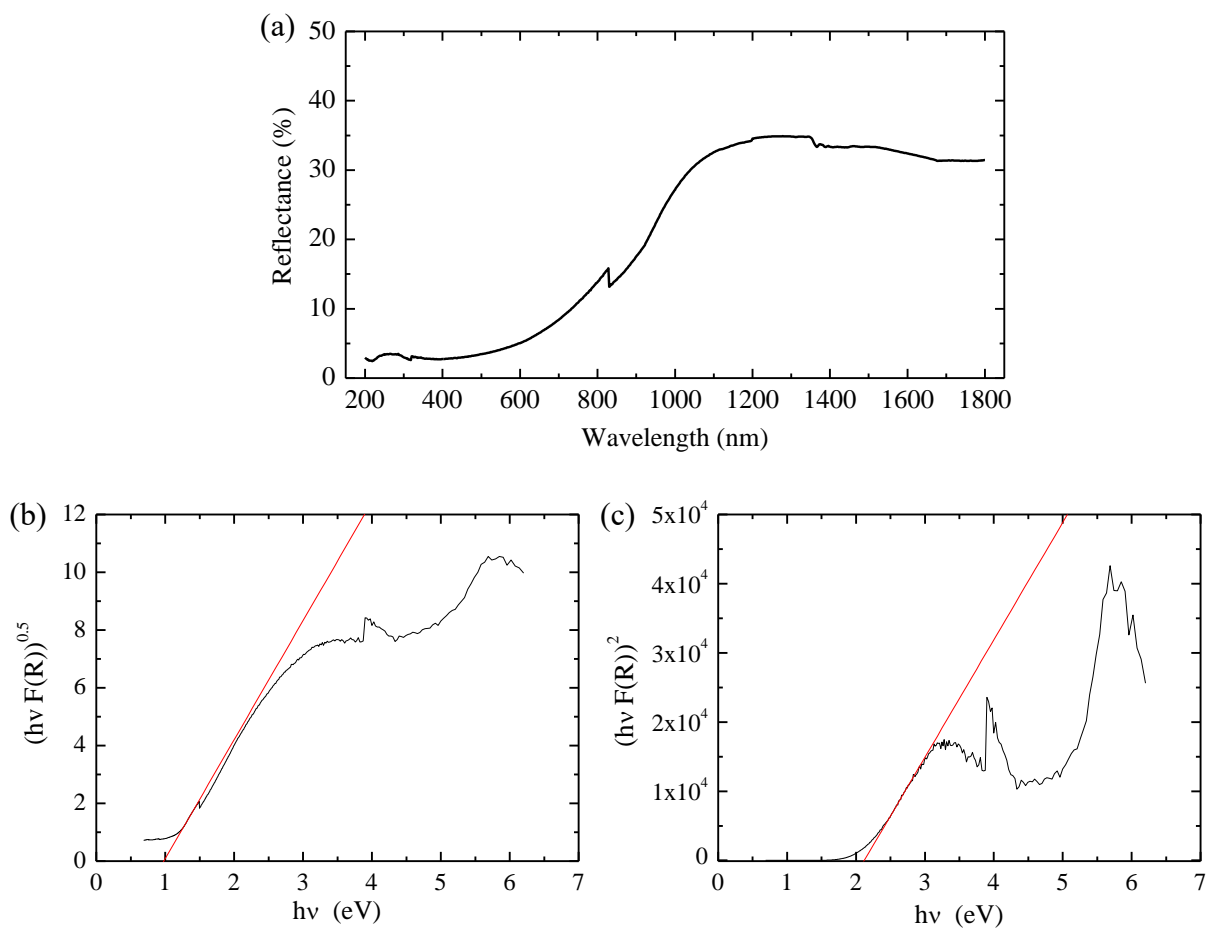


Figure 3.31. (a) Evolution of diffuse reflectance of Bi_2O_3 powder as a function of wavelength and corresponding Tauc plot assuming (b) an indirect allowed transition ($n=2$) and (c) a direct allowed transition ($n=0.5$).

Figure 3.32 presents the Mott-Schottky plots of 5 μm thick doctor-bladed Bi_2O_3 films in either aqueous electrolyte (a) or non-aqueous aprotic EC/DMC-based electrolyte (b). The positive slope of the curves indicates a n-type conductivity in agreement with previous literature (Fig. 3.32) [94, 98, 105].

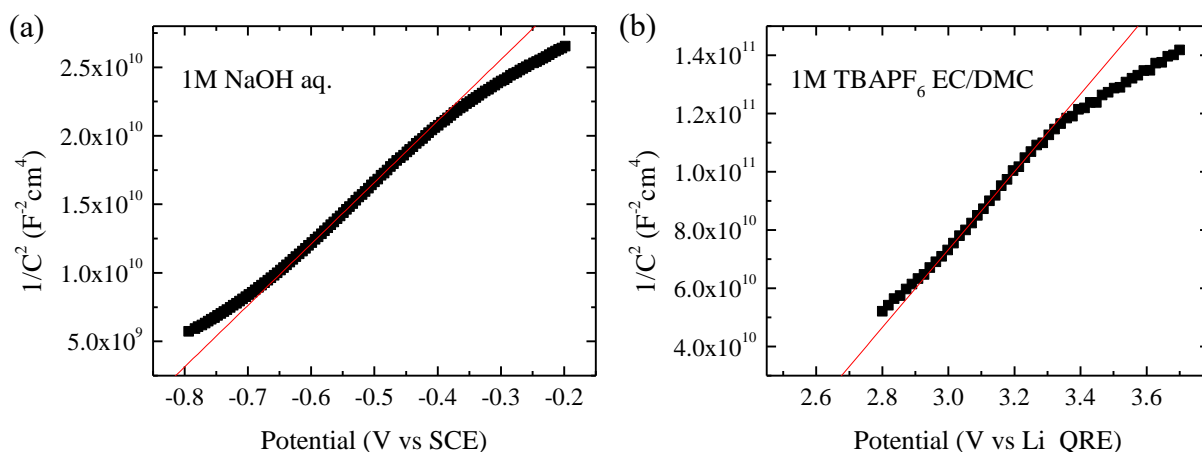


Figure 3.32. Mott-Schottky plot of Bi_2O_3 measured at 500 Hz in (a) 1 mol/L NaOH aqueous electrolyte and (b) 1 mol/L TBAPF₆ EC/DMC electrolyte

The flat band potential and donor density values of Bi_2O_3 are tabulated in Table 3.8. In 1 mol/L NaOH aqueous electrolyte (pH = 14), the flat band potential is equal to - 0.90 V vs. SCE, which corresponds to - 0.66 V vs. NHE. This value is in agreement with - 0.67 V (vs. NHE at pH = 14) reported by Haira et al. [105] and lies in the range of values reported by Chitrada et al. from - 0.57 to - 0.54 V (vs. NHE at pH = 14) based on Mott-Schottky measurements in 1 mol/L KOH aqueous electrolyte [106]. In non-aqueous aprotic electrolyte, the flat band potential is 2.42 V vs. Li QRE. This corresponds to - 0.77 V vs. NHE. The results indicate that Bi_2O_3 has lower flat band potential and consequently higher band edge energies when measured in non-aqueous aprotic electrolyte compared to an aqueous electrolyte (Fig. 3.33).

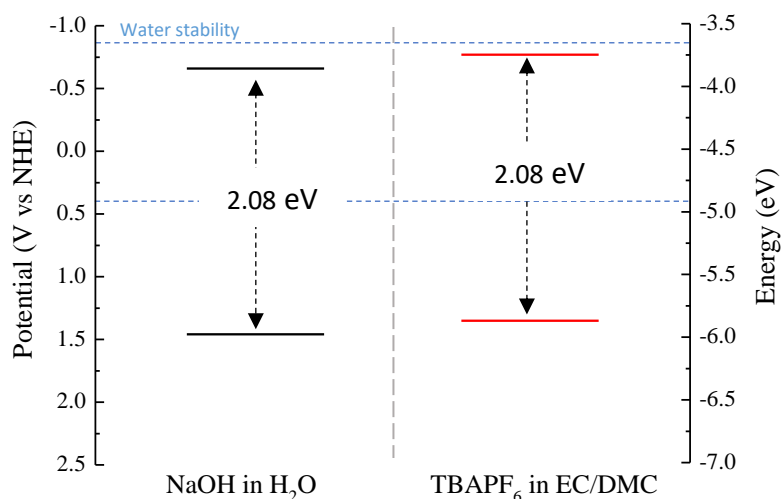


Figure 3.33. Representation of the band edge positions of Bi_2O_3 film measured in aqueous electrolyte at pH = 14 (black) and in non-aqueous aprotic EC/DMC-based electrolyte (red).

The charge carrier concentration in Bi_2O_3 was calculated assuming a dielectric constant of 32 as reported in literature [107] (Table 3.8). A donor density of $9.9 \cdot 10^{17} \text{ cm}^{-3}$ has been determined in aqueous electrolyte, in agreement with literature [98, 108], and $3.3 \cdot 10^{19} \text{ cm}^{-3}$ in non-aqueous aprotic electrolyte. Once again, we found a more than one order of magnitude increase of the carrier concentration in non-aqueous electrolyte. This is the first report determining the flat band potential, carrier type and concentration of Bi_2O_3 in such media.

Table 3.8. Flat band potential and charge carrier concentration of Bi_2O_3 in 1 mol/L NaOH aqueous electrolyte and 1 mol/L TBAPF₆ EC/DMC electrolyte.

Electrolyte	Flat band potential		Charge carrier concentration, cm^{-3}
	as measured	recalculated	
		V vs. NHE	
1 mol/L NaOH in H_2O	-0.90 V vs. SCE	-0.66 (pH=14)	$9.9 \cdot 10^{17}$
1 mol/L TBAPF ₆ in EC/DMC	2.42 V vs. Li QRE	-0.77	$3.3 \cdot 10^{19}$

3.1.7. LiMn_2O_4

Lithium manganese oxide LiMn_2O_4 is one of the most studied cathode material for lithium-ion batteries because of its high redox potential of ca. 4 V vs. Li^+/Li , natural abundance of Mn, and easy synthetic procedure, despite its quite low gravimetric capacity of 120 mAh/g [109-110]. LiMn_2O_4 crystallizes into a cubic spinel structure, which consists of cubic close-packed arrangements of oxygen atoms at the 32e sites, lithium occupying half of the 8a sites, and Mn^{3+} and Mn^{4+} ions occupying 1/8 of the octahedral 16d sites (Fig. 3.34). The empty sites in the $[\text{Mn}_2\text{O}_4]^-$ framework represent a diamond type network of tetrahedral 8a and octahedral 16c sites, which share common faces and edges and form 3D open channels for Li^+ ion diffusion.

The full pattern matching refinement of LiMn_2O_4 diffractogram is presented in Figure 3.35 (a). All diffraction peaks can be indexed into Fd-3m space group. The refined lattice cell parameter is $a = 8.238(3) \text{ \AA}$ ($V_{\text{cell}} = 559 \text{ \AA}^3$) in agreement with the value of $a = 8.2404(2)$ reported by Mukai et al. [111]. The SEM micrograph shows particles with octahedral morphology and very inhomogeneous particle size ranging from ca. 500 nm to 5 μm (Fig. 3.35 (b)). Significant level of particles agglomeration is observed.

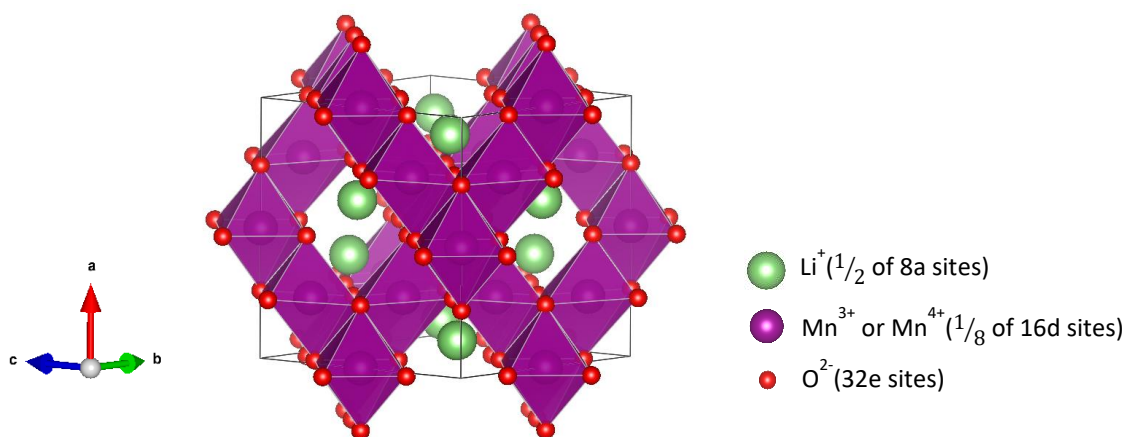


Figure 3.34. Crystal structure representation of the spinel LiMn_2O_4 .

The high-resolution TEM micrograph confirms a good crystallinity of the particles and the absence of any amorphous regions in the bulk or surrounding the particles (Fig. 3.35(c)). The SAED pattern can be successfully indexed into the spinel structure (Fig. 3.35(d)).

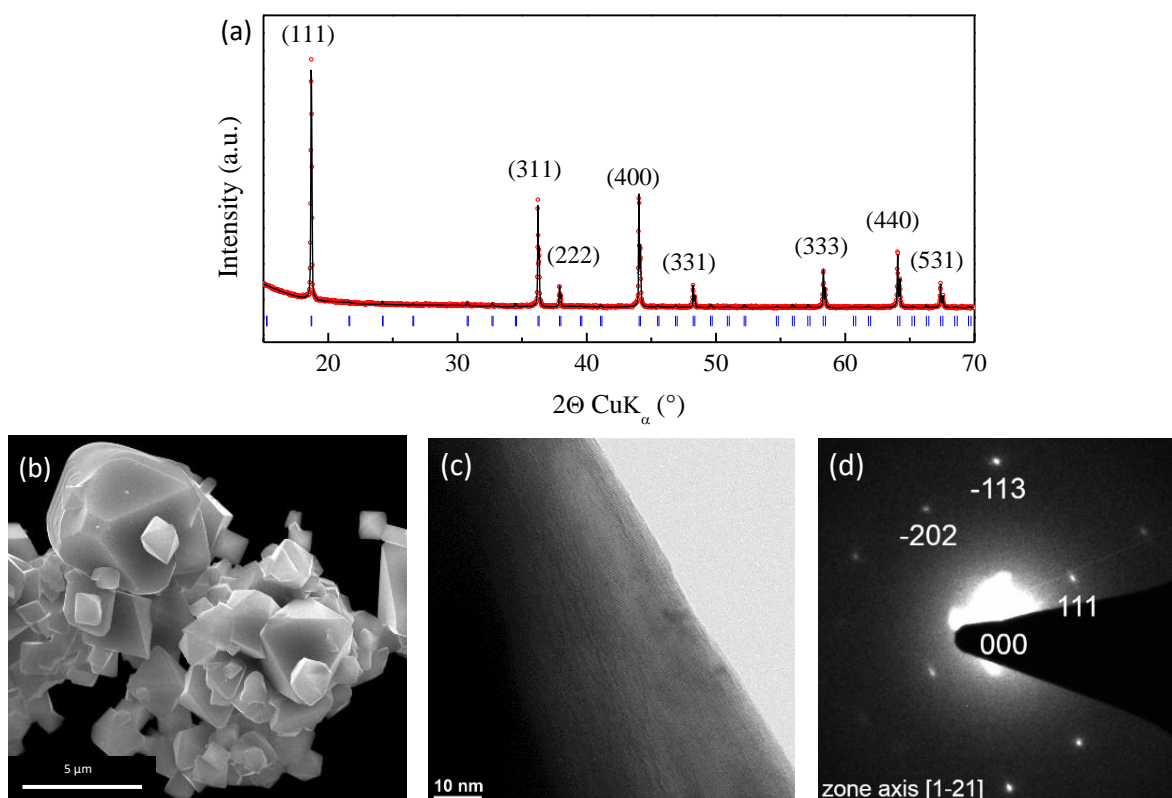


Figure 3.35. (a) Full pattern matching of x-ray diffraction pattern of LiMn_2O_4 powder and corresponding (b) scanning electron micrograph and (c,d) high-resolution transmission electron micrograph and selected area electron diffraction pattern.

The diffuse reflectance spectrum of LiMn_2O_4 is presented in Figure 3.36. The band structure seems to be either of a not semiconducting nature or to have a smaller band gap value than 0.7 eV (> 1800 nm). This contrasts with literature, which reports a direct band gap value between 1.16 to 1.20 eV from experimental optical absorption [112-113]. DFT calculations predicts from the calculation of the DOS a band gap lower than 1.0 eV [114-115].

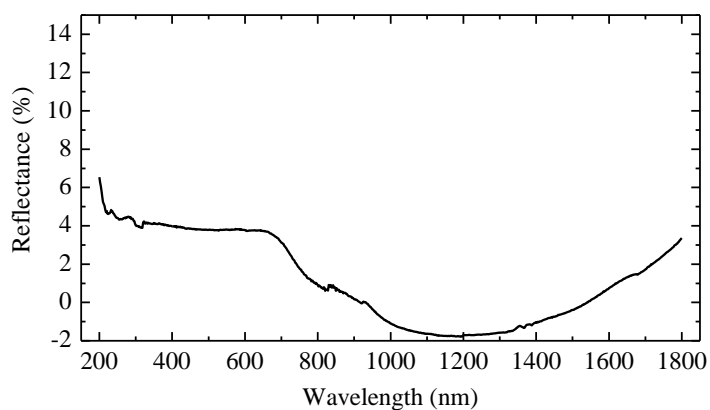


Figure 3.36. Evolution of diffuse reflectance of LiMn_2O_4 powder as a function of wavelength.

3.1.8. $\text{LiMn}_{1/3}\text{Co}_{1/3}\text{Ni}_{1/3}\text{O}_2$

$\text{LiMn}_{1/3}\text{Co}_{1/3}\text{Ni}_{1/3}\text{O}_2$ is currently one of the most important battery cathode materials because of its high discharge capacity of ~ 250 mAh/g and high redox potential of ca. 4 V vs. Li^+/Li [116-117]. Its layered O_3 -type structure consists of a cubic close-packed arrangement where oxygen ions and transition-metal ions occupy alternating layers in octahedral sites, creating 2D pathways for lithium insertion (Fig. 3.37).

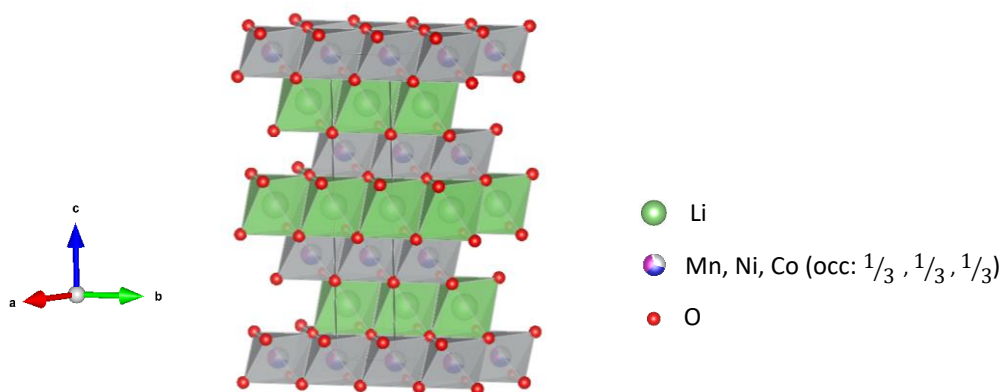


Figure 3.37. Schematic representation of $\text{LiMn}_{1/3}\text{Co}_{1/3}\text{Ni}_{1/3}\text{O}_2$ crystal structure.

The full pattern matching refinement of the x-ray diffraction pattern of $\text{LiMn}_{1/3}\text{Co}_{1/3}\text{Ni}_{1/3}\text{O}_2$ is presented in Figure 3.38 (a). All the diffraction peaks are assigned to R-3m space group corresponding to a rhombohedral lattice. The refined lattice cell parameters are $a = 2.859(2) \text{ \AA}$ and $c = 14.155(9) \text{ \AA}$ ($V_{\text{cell}} = 100 \text{ \AA}^3$) in agreement with literature [118]. The SEM and TEM micrographs show agglomerates ranging from 5 to 10 μm , which are composed of primary 0.5-1.5 μm crystalline particles (Fig. 3.38 (b-c)). The HR-TEM micrograph shows a good crystallinity of the material from center to the edges of the particles with the absence of any amorphous regions (Fig. 3.38 (d)). The SAED pattern is successfully indexed into R-3m space group (Fig. 3.38 (e)).

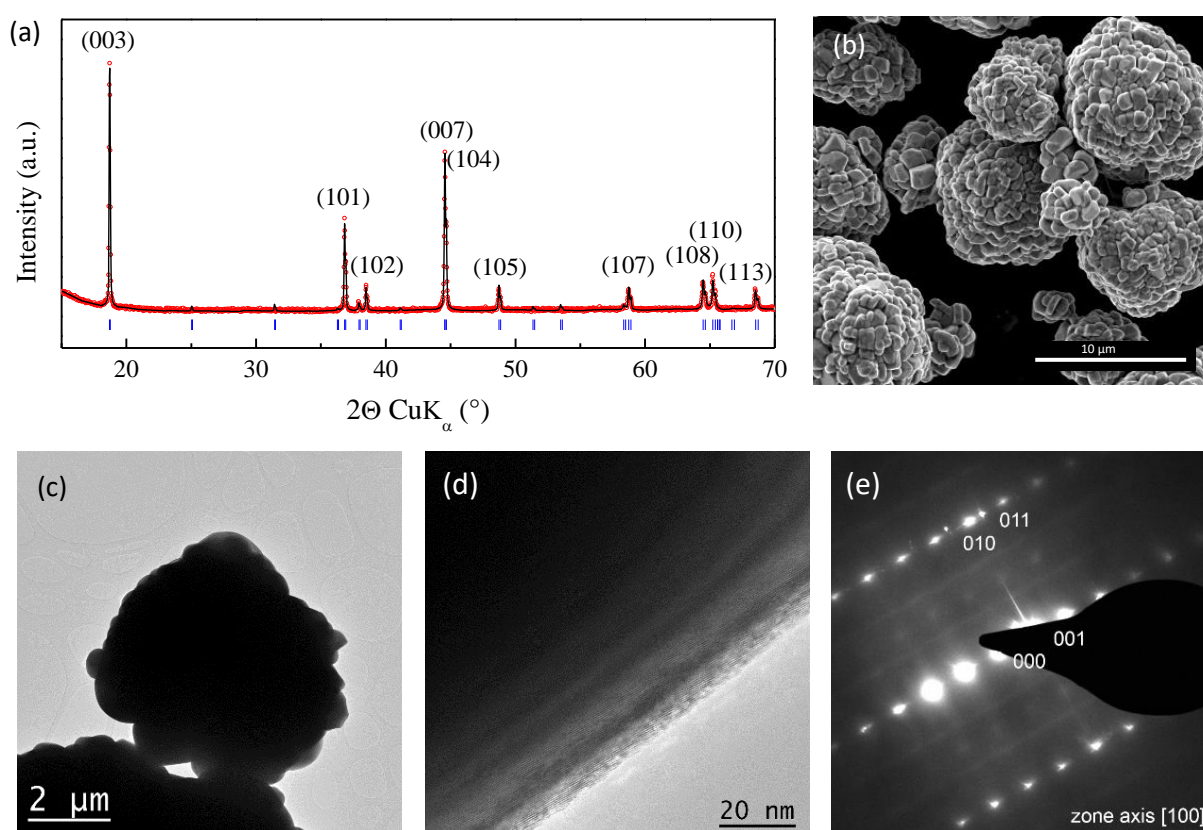


Figure 3.38. (a) Full pattern matching refinement of the x-ray diffraction pattern of $\text{LiMn}_{1/3}\text{Co}_{1/3}\text{Ni}_{1/3}\text{O}_2$ with the corresponding (b) scanning electron micrograph, (c) transmission electron micrograph and (d,e) high-resolution transmission electron micrograph including the selected area electron diffraction pattern.

Similarly to LiMn_2O_4 , we did not achieve to determine the optical band gap of $\text{LiMn}_{1/3}\text{Co}_{1/3}\text{Ni}_{1/3}\text{O}_2$ from the diffuse reflectance spectrum owing to the absence of a clear absorption transition below 1800 nm ($> 0.7 \text{ eV}$) (Fig. 3.39). To the best of our knowledge,

there are no reports related to the determination of the $\text{LiMn}_{1/3}\text{Co}_{1/3}\text{Ni}_{1/3}\text{O}_2$ band gap value in literature.

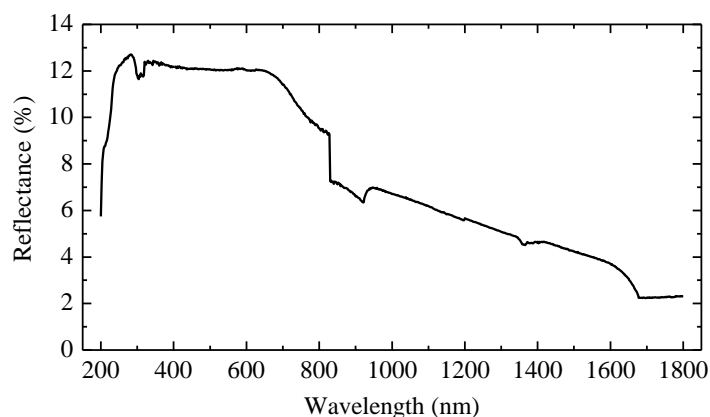


Figure 3.39. Evolution of diffuse reflectance of $\text{LiMn}_{1/3}\text{Ni}_{1/3}\text{Co}_{1/3}\text{O}_2$ powder as a function of wavelength.

3.2. Transition metal sulfides

The layered transition metal sulfides (MS_2) are among the first materials studied for their ability to reversibly insert / deinsert lithium cations [119-120]. Their structure is typically constituted of layers, each of which is composed of transition-metal ions in edge-shared interstices between the pairs of close-packed anion planes (Fig. 3.40). These hexagonally close packed MS_2 layers are held together by Van der Waals forces enabling lithium intercalation between the layers. Among the family of transition metal sulfides, TiS_2 is particularly attractive owing to its low molecular weight and good electrical conductivity stemming from high charge carrier concentration of $\sim 10^{20} \text{ cm}^{-3}$ [49, 121-122].

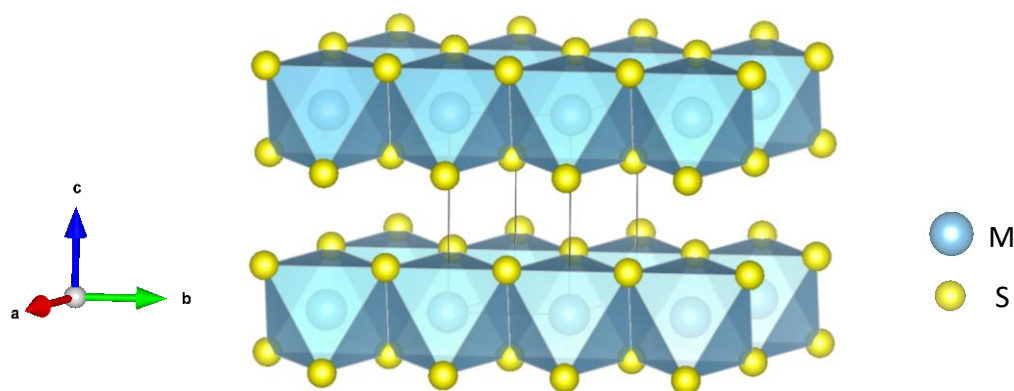


Figure 3.40. Crystal structure representation of layered MS_2

3.2.1. TiS₂

The refined x-ray diffractogram of TiS₂ is presented in Figure 3.41 (a). All diffraction peaks are indexed with P-3m1 space group corresponding to a tetragonal unit cell. The lattice cell parameters refined are $a = b = 3.407(3)$ Å and $c = 5.695(6)$ Å ($V_{\text{cell}} = 57$ Å³), in a good agreement with the values of $a = b = 3.407(2)$ Å and $c = 5.695(3)$ Å reported by McKelvy et al. [123]. The scanning electron micrograph reveals a nano-platelet morphology ranging from 5 to 15 μm in size (Fig. 3.41 (b)). The HR-TEM micrograph confirms a good crystallinity of the particles until the edges (Fig. 3.41 (c)). It also reveals the presence of pores in the particles as showed in the micrograph by semi-transparent “bubbles” in the core of the particle. The selected area electron diffraction pattern was indexed into TiS₂ (Fig. 3.41 (e)). The electron diffraction pattern recorded over a particle consists of differently oriented sheets of TiS₂ according to the same zone axis as showed by the absence of some reflections in the SAED pattern.

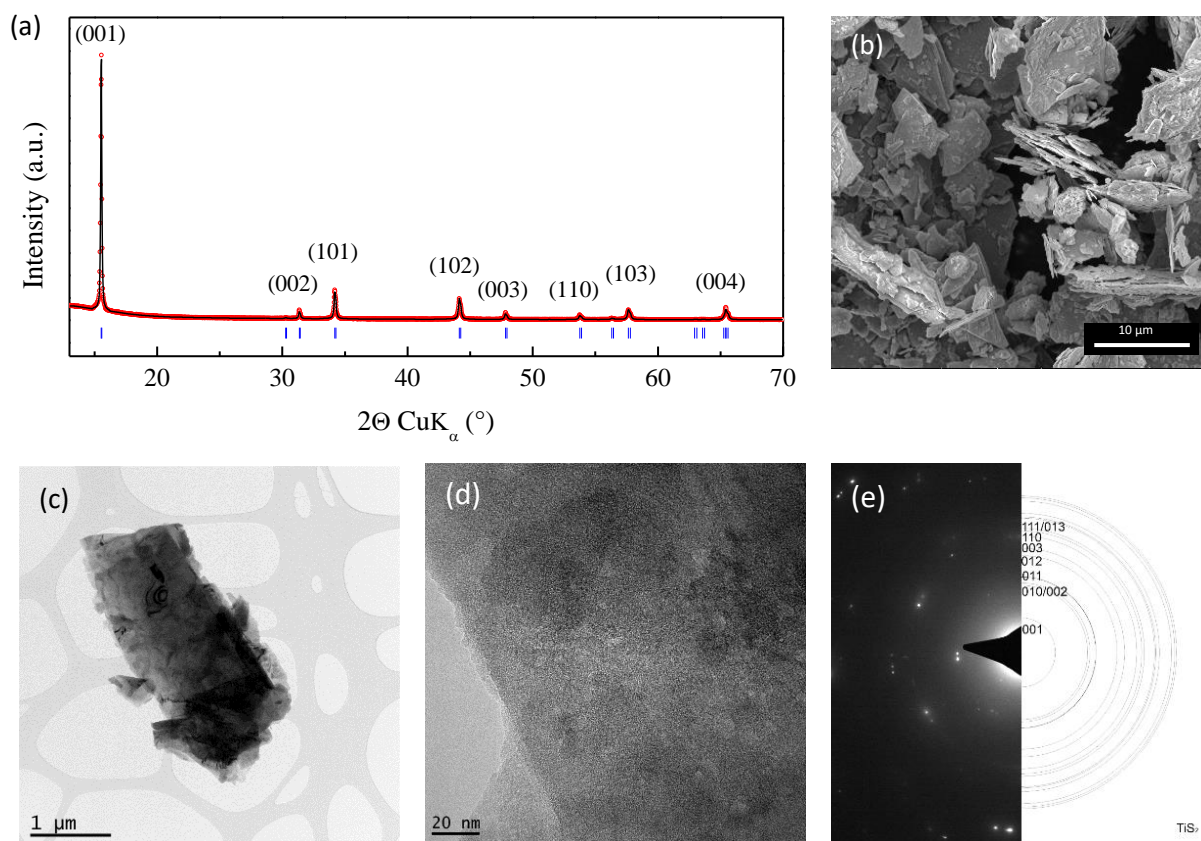


Figure 3.41. (a) Full pattern matching refinement of x-ray diffraction pattern of TiS₂ and corresponding (b) scanning electron micrograph, (c) transmission electron micrograph and (d,e) high-resolution transmission electron micrograph with selected area electron diffraction pattern.

Figure 3.42 presents the diffuse reflectance spectrum of TiS_2 powder. The absence of any absorption edge below 1800 nm suggests that the band structure is not of a semiconducting nature. Indeed, even though TiS_2 is theoretically a semiconductor, it has always been experimentally found to have a semi-metallic nature. This is supported by most of DFT calculations on the electronic structure of TiS_2 which suggest TiS_2 to be an indirect band overlap semimetal [124–130]. It was also supported by the experimental studies reporting that TiS_2 is a metal or semimetal with an indirect overlap of the bottom of the conduction band and the top of the valence band ranging from 0.2 to 1.5 eV [131–135]. This semi-metallic behavior is assigned to the access of the titanium metal electrons filling the d-type conduction band of the material [136–137].

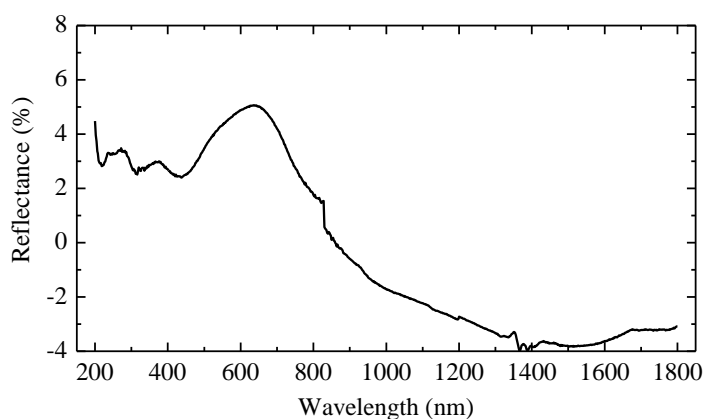


Figure 3.42. Evolution of diffuse reflectance of TiS_2 powder as a function of wavelength.

In order to determine, if possible, the band edge position of TiS_2 and type of conduction, the Mott-Schottky measurements of 12 μm doctor-bladed film were carried out. The representative Mott-Schottky plots in aqueous electrolyte and in non-aqueous aprotic EC/DMC-based electrolyte are reported in Fig. 3.43. In both cases, the positive slope of the Mott-Schottky curve indicates a n-type conductivity in agreement with Hall measurements reported in literature [122, 138, 139]. The success of the Mott-Schottky measurements is quite surprising taking into account the inability to determine the band gap value from the diffuse reflectance measurements. It suggests that there is probably a narrow band gap (< 0.7 eV), allowing the equalization of the Fermi level of TiS_2 and the electrolyte.

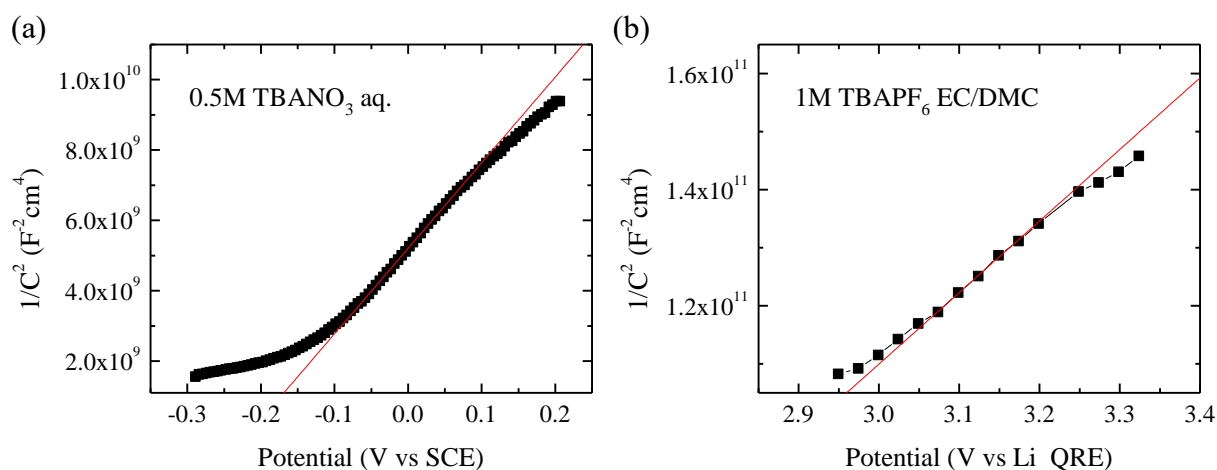


Figure 3.43. Mott-Schottky plot of TiS_2 measured at 500 Hz in (a) 0.5 mol/L TBANO_3 aqueous electrolyte and (b) 1 mol/L TBAPF_6 EC/DMC electrolyte.

Table 3.9 gathers the flat band potential and donor density values derived from the Mott-Schottky equation (eq. 2.7). A flat band potential of -0.24 V vs. SCE was determined in 0.5 mol/L TBANO_3 aqueous solution (pH = 3.45). The value translates into -0.62 V vs. NHE at pH = 14 [59-60]. In the non-aqueous aprotic electrolyte, we obtained a flat band potential of 2.01 V vs. Li QRE, which corresponds to -1.18 V vs. NHE. No data is reported in literature regarding the flat band potential of TiS_2 .

Table 3.9. Flat band potential and charge carrier concentration of TiS_2 in 0.5 mol/L TBANO_3 aqueous electrolyte and 1 mol/L TBAPF_6 EC/DMC electrolyte.

Electrolyte	Flat band potential			Charge carrier concentration, cm^{-3}
	as measured	Recalculated		
		V vs. NHE	V vs. NHE at pH=14	
0.5 mol/L TBANO_3 in H_2O	-0.24 V vs. SCE	0.00 (pH=3.45)	-0.62	$4.2 \cdot 10^{18}$
1 mol/L TBAPF_6 in EC/DMC	2.01 V vs. Li QRE	-1.18	-	$6.9 \cdot 10^{19}$

To calculate the charge carrier concentration, a dielectric constant of 15 was assumed by us, taking as a first hypothesis of a similar ratio between the dielectric constant of TiS_2 and TiO_2 with respect to WS_2 ($\epsilon=8$) and WO_3 ($\epsilon=20$), i.e. roughly 2:1. A donor density of $4.2 \cdot 10^{18} \text{ cm}^{-3}$ was obtained in 0.5 mol/L TBANO_3 aqueous electrolyte and $6.9 \cdot 10^{19} \text{ cm}^{-3}$ in 1 mol/L TBAPF_6

EC/DMC (Table 3.9). As previously observed, the charge carrier concentration in non-aqueous aprotic electrolyte is one order of magnitude higher compared to the aqueous counterpart. At the same time, these values are one to two orders of magnitude lower compared to the values from $1.1 \cdot 10^{20}$ to $2.8 \cdot 10^{20} \text{ cm}^{-3}$ reported in literature based on calculations from Hall coefficient measurements [122, 123, 134, 138, 139]. This tends to suggest that the dielectric constant of TiS_2 might be far from assumed value of 15.

3.2.2. MoS_2

Figure 3.44 (a) exhibits the full pattern matching refinement of the XRD pattern of MoS_2 . All diffraction peaks were successfully indexed into hexagonal crystal structure of $P6_3/mmc$ space group. The obtained cell parameters are $a = b = 3.160(7) \text{ \AA}$ and $c = 12.294(9) \text{ \AA}$ ($V_{\text{cell}} = 106 \text{ \AA}^3$). They are in good agreement with the results reported by Bronsema et al. [140]. The electron micrographs show that the particles display a nanoflake-like morphology with flakes diameter ranging from 1 to $10 \mu\text{m}$ without amorphous domain at the particles surface (Fig. 3.44 (b-d)). The SAED pattern is consistent with MoS_2 crystal structure (Fig. 3.44 (e)).

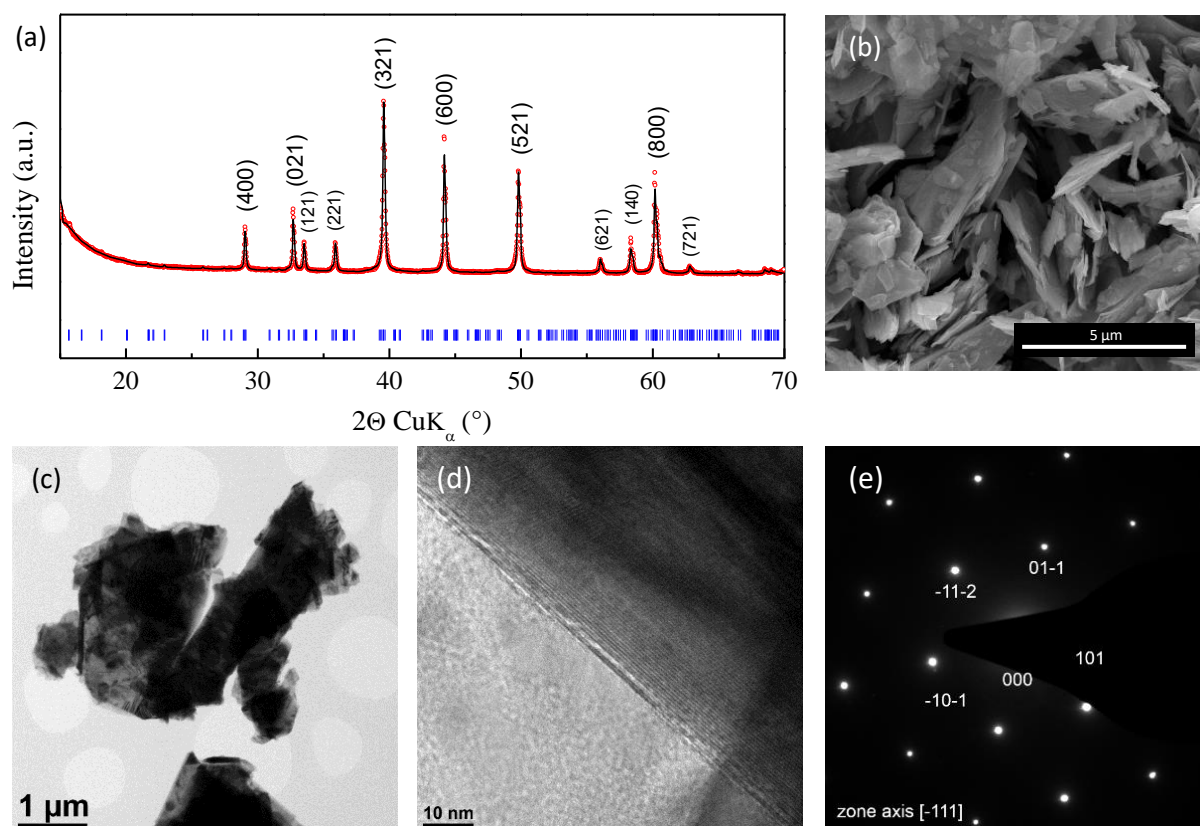


Figure 3.44. (a) Full pattern matching refinement of x-ray diffraction pattern of MoS_2 and (b) scanning electron micrograph, (c) transmission electron micrograph and (d,e) high-resolution transmission electron micrograph including selected area electron diffraction pattern.

The band gap of MoS₂ was determined from the diffuse reflectance spectrum, which shows an absorption tail in the visible range (Fig. 3.45 (a)). A band gap value of 1.52 eV was determined from the Tauc plot assuming an indirect allowed transition (Fig. 3.45 (b)). The literature reports values of 1.68 eV determined from absorption measurements [141] and 1.75 eV based on photocurrent study [142]. DFT calculations predict an indirect bandgap nature between 1.04 eV to 1.29 eV based on the DOS calculation under vacuum [143–147]. The indirect bandgap is consistent with the slow increase of reflectance near the absorption threshold.

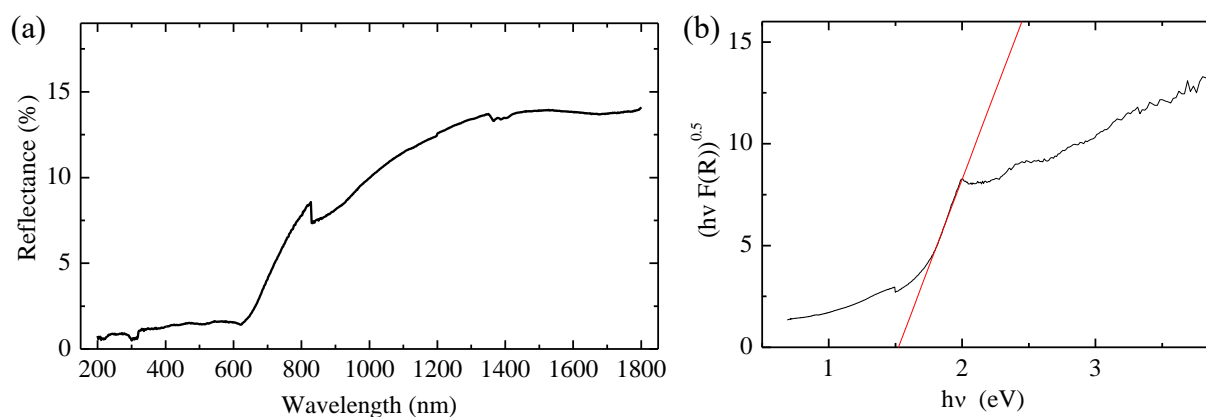


Figure 3.45. (a) Evolution of diffuse reflectance of MoS₂ powder as a function of wavelength and corresponding Tauc plot assuming (b) an indirect allowed transition ($n=2$).

The Mott-Schottky measurements were carried out on 4 μm thick films of MoS₂ made by doctor blading. The representative Mott-Schottky plots are presented in Figure 3.46 within the two types of electrolyte. The results show that the slope of the Mott-Schottky curve is a function of the electrolyte nature, i.e. n-type conductivity in aqueous 0.5 mol/L TBANO₃ electrolyte and p-type conductivity in non-aqueous aprotic 1mol/L TBAPF₆ EC/DMC-based electrolyte. It is well-known in literature that MoS₂ can exist in both n- and p-type conduction depending on doping [148–152] and the experimental conditions [153-154]. However, this is the first time that a crossover in the main charge carrier in MoS₂ crystals depending on the electrolyte nature is reported. These results suggest that MoS₂ is a weak degenerated semiconductor for which the Fermi level is close to the middle of the band gap, resulting in a comparable concentration of electron and hole carriers as previously observed in LiCoO₂.

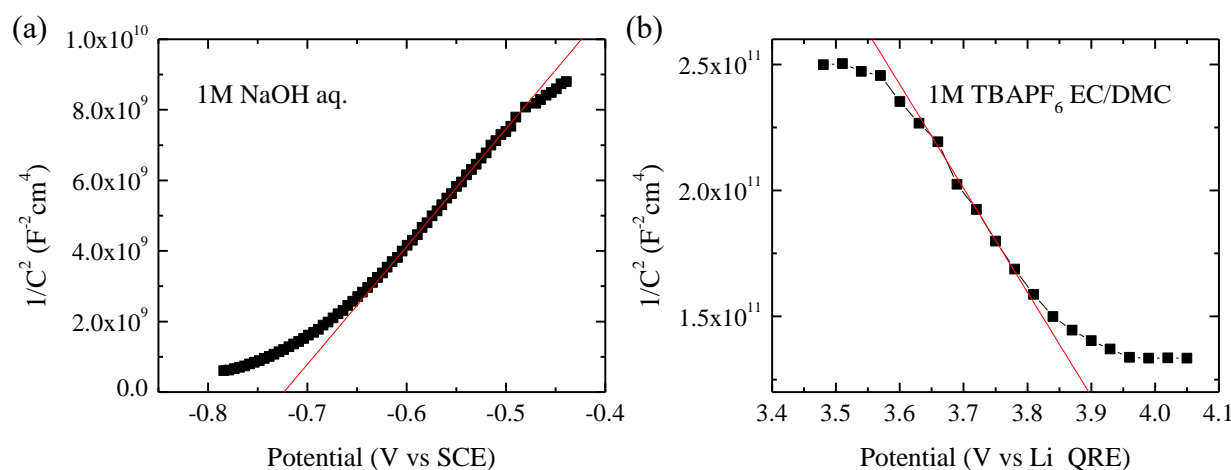


Figure 3.46. Mott-Schottky plot of MoS_2 measured at 100 Hz in (a) 1 mol/L NaOH aqueous electrolyte and (b) 1 mol/L TBAPF_6 EC/DMC electrolyte.

The flat band potential and donor density of MoS_2 is gathered in Table 3.10. In 1 mol/L NaOH aqueous solution (pH = 14), the flat band potential is equal to - 0.75 V vs. SCE, thus at - 0.51 V vs. NHE corresponding to the lower edge of the conduction band. By contrast, when measured in a non-aqueous aprotic electrolyte, the flat band potential value becomes 4.20 V vs. Li QRE, corresponding to 1.01 V vs. NHE for the higher edge of the valence band. This result confirms very well the band gap value of 1.52 eV, showing no or little effect of the solvent on the band gap transition of MoS_2 . In other words, these results show that the band edge positions of MoS_2 are not affected neither by the electrolyte nature nor by the change in semiconductivity type (Fig. 3.47). Nevertheless, our result is lower than the flat band potential of - 0.24 V vs. NHE reported by Anand for n-type MoS_2 in a mixture of K_2SO_4 , KI, I_2 , H_2SO_4 in water (electrolyte pH not indicated) [141]. On the other hand, our value is 0.21 V higher than the flat band potential reported by Schneemeyer et al. based on photocurrent measurements of n-type MoS_2 in 0.1 M $[\text{Et}_4\text{N}]\text{Cl}$ / 0.1 M $[\text{n-Bu}_4\text{N}]\text{ClO}_4$ in CH_3CN electrolyte [142].

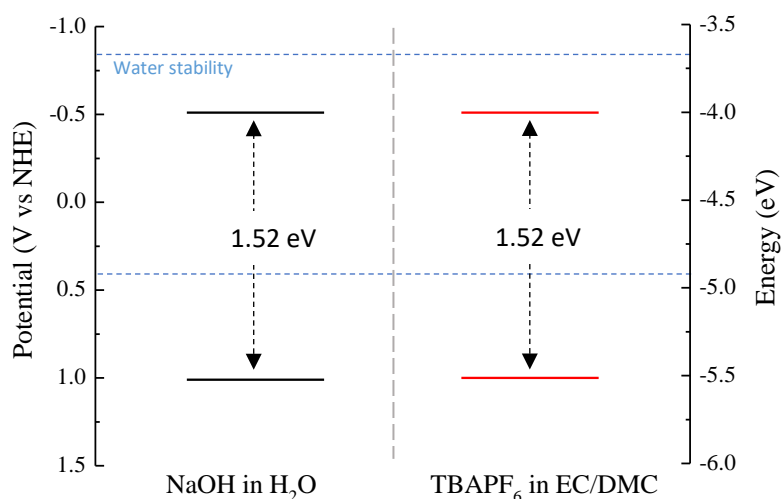


Figure 3.47. Representation of the band edge positions of MoS_2 film measured in aqueous electrolyte at $\text{pH} = 14$ (black) and in non-aqueous aprotic EC/DMC-based electrolyte (red).

The charge carrier concentration of MoS_2 in both media was calculated with a dielectric constant of 11 based on the calculations reported in literature (Table 3.10) [143, 155, 156]. In 0.5 mol/L TBANO_3 aqueous electrolyte, we determined an electron concentration of $3.0 \cdot 10^{18} \text{ cm}^{-3}$. This value is one order of magnitude lower than that reported by Anand et al., i.e. $3.5 \cdot 10^{19} \text{ cm}^{-3}$ [141]. In 1 mol/L TBAPF_6 EC/DMC, the hole carrier concentration is $4.0 \cdot 10^{19} \text{ cm}^{-3}$. This number lies in the middle of the $10^{17} - 10^{19} \text{ cm}^{-3}$ range reported for p-type MoS_2 based on thermopower measurements [147].

Table 3.10. Flat band potential and charge carrier concentration of MoS_2 in 1 mol/L NaOH aqueous electrolyte and 1 mol/L TBAPF_6 EC/DMC electrolyte.

Electrolyte	Flat band potential		Charge carrier concentration, cm^{-3}
	as measured	recalculated	
		V vs. NHE	
1 mol/L NaOH in H_2O	-0.75 V vs. SCE	-0.51 (pH=14)	$3.0 \cdot 10^{18}$
1 mol/L TBAPF_6 in EC/DMC	4.20 V vs. Li QRE	1.01	$4.0 \cdot 10^{19}$

3.2.3. WS₂

The full-pattern matching refinement of WS₂ x-ray diffractogram shows an important preferential orientation along (001) planes. All observed diffraction peaks can be indexed into the hexagonal lattice of P6₃/mmc space group (Fig. 3.48 (a)). The refined lattice cell parameters are $a = b = 3.154(5)$ Å and $c = 12.362(12)$ Å ($V_{\text{cell}} = 106$ Å³). These values are very close to the isostructural MoS₂ previously investigated, and are in good agreement with the values reported in literature [157], [158]. The SEM micrograph shows nanoplates morphology with a particle size ranging from 200 nm to 6 micrometers (Fig. 3.48 (b-c)). This morphology is responsible for the preferential orientation observed. The HR-TEM study confirms that there are no amorphous regions on the sample, especially at the surface of the particles (Fig. 3.48 (d)). The SAED pattern shows single crystal electron diffraction with an indexation in agreement with XRD (Fig. 3.48 (e)).

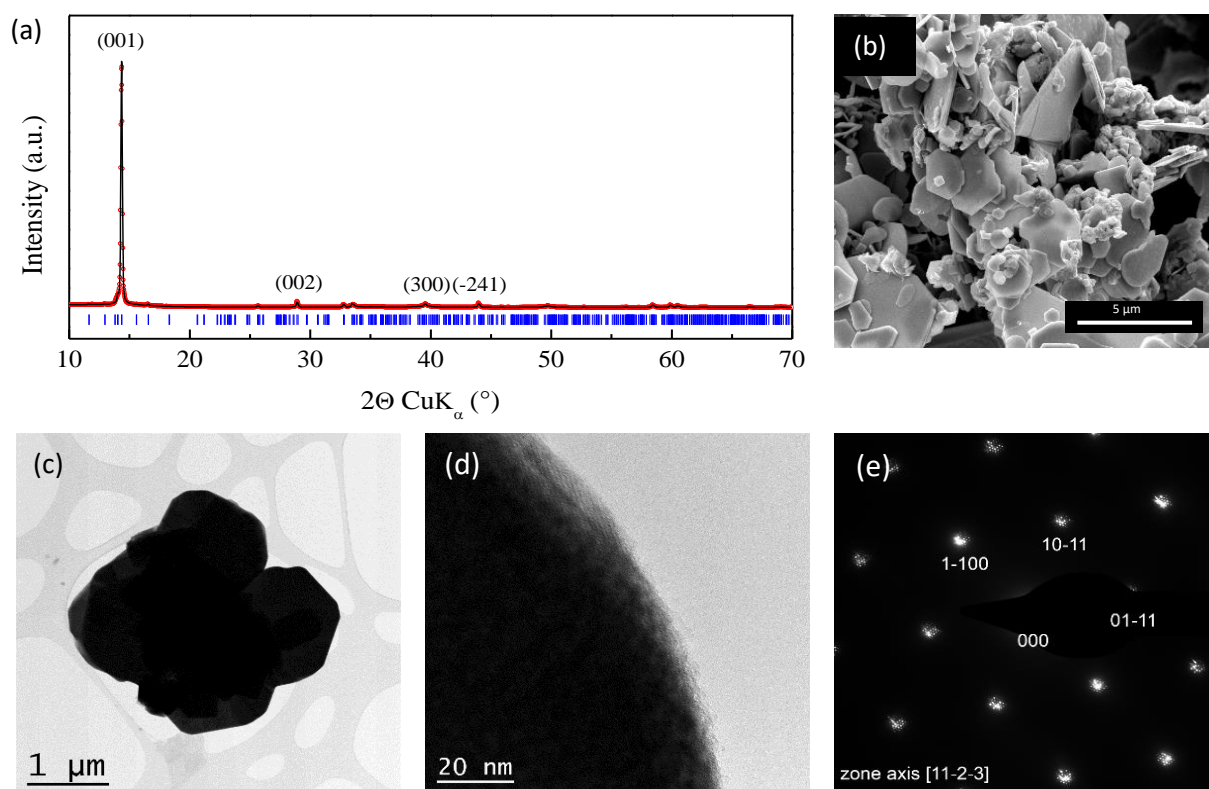


Figure 3.48. (a) Full pattern matching refinement of x-ray diffraction pattern of WS₂ and corresponding (b-d) scanning, transmission and high resolution transmission electron micrograph of the sample with its (e) selected area electron diffraction pattern.

WS₂ particles show a very broad reflectance within the NIR light portion (Fig. 3.49 (a)). Assuming an indirect allowed transition, a band gap value of 0.82 eV is determined from the

corresponding Tauc plot (Fig. 3.49 (b)). This value is lower than those predicted by DFT calculations [146, 159, 160] and experimentally determined values between 1.12 eV and 1.30 eV based on different techniques such as absorption spectroscopy [161], photoelectrochemical study [162], and measurements of the gate-voltage dependence of the source-drain current in an ambipolar ionic liquid-gated transistor [163]. At the same time it is 0.97 eV higher than 1.79 eV indirect band gap reported by Kam et al. based on the photocurrent spectroscopy measurements [164]. Assuming a direct transition would lead to a value of 1.31 eV (Fig. 3.29 (c)). Nevertheless, the very broad reflectance onset clearly suggests an indirect transition.

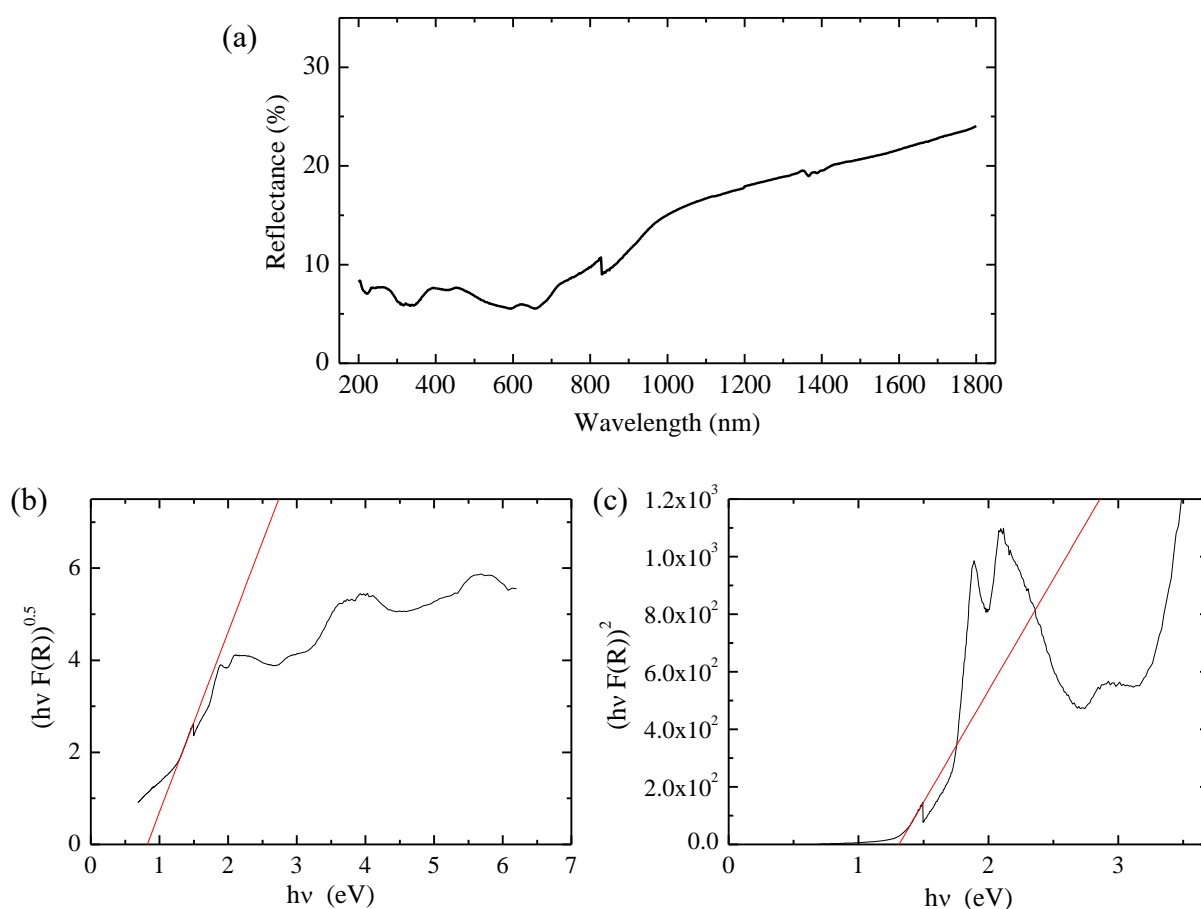


Figure 3.49. (a) Evolution of diffuse reflectance of WS_2 powder as a function of wavelength and corresponding Tauc plot assuming (b) an indirect allowed transition ($n=2$) and (c) a direct allowed transition ($n=0.5$).

Mott-Schottky experiments were carried out on a 4 μm thick doctor-bladed film (Figure 3.50). Interestingly, as it was the case for MoS_2 and $LiCoO_2$, WS_2 shows a changeover in the conductivity type depending on the electrolyte nature. A n-type conductivity is observed in

aqueous 1 mol/L NaOH electrolyte and a p-type conduction appears in non-aqueous aprotic 1mol/L TBAPF₆ in EC/DMC. This changeover suggests a weak extrinsic semi-conduction in WS₂ in which the process of Fermi level equalization control either a n-type conduction (hole transfer) or a p-type conduction (electron transfer) depending on the electrolyte nature. Single crystals WS₂ is reported in the literature to be n-type [165]. However, both n- and p-type conductivity are reported for polycrystalline WS₂ samples [161, 162, 166–169]. This changeover is mainly controlled by the synthetic method leading to different levels of punctual defects driven mainly by the sulfur stoichiometry. The literature also reports that the nature of semi-conduction in WS₂ can be easily changed by a careful control in aliovalent doping [170–172] or by changing the bias voltage during thermopower measurements as demonstrated by Kawai et al. on nanotubes [173].

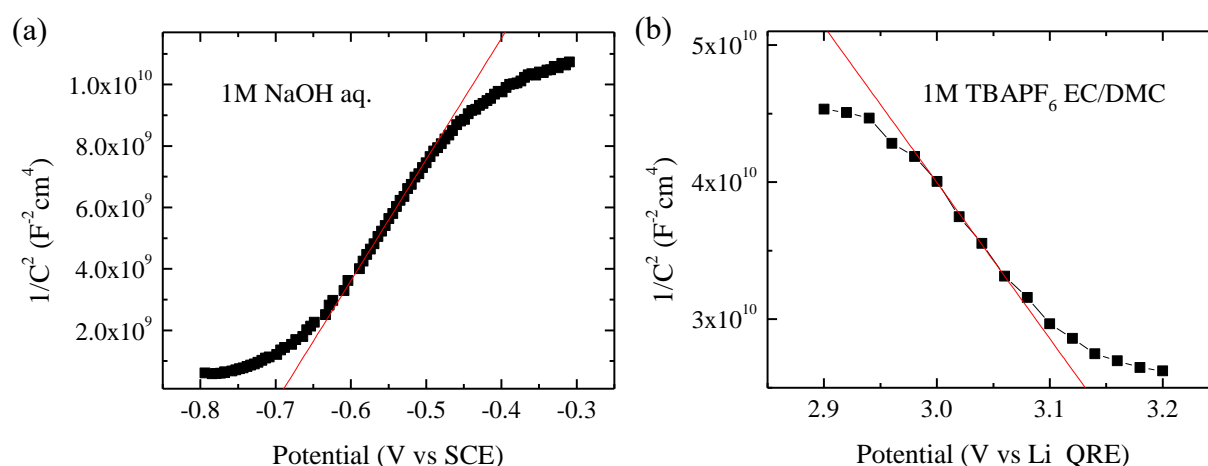


Figure 3.50. Mott-Schottky plot of WS₂ measured at 100 Hz in (a) 1 mol/L NaOH aqueous electrolyte and (b) 1 mol/L TBAPF₆ EC/DMC electrolyte.

The flat band potential and donor density values are reported in Table 3.11. In 1 mol/L NaOH aqueous electrolyte (pH = 14), the flat band potential of WS₂ is equal to -0.72 V vs. SCE, which corresponds to -0.48 V vs. NHE. This value is comparable to -0.45 V vs. NHE at pH = 14 reported in literature for the n-type WS₂ by Morrish et al. [166] and is ca. 0.35 V more positive than that reported by Bassaid et al. [167] based on Mott-Schottky measurements in Na₂SO₄ aqueous electrolytes. This value of flat band potential corresponds to the lower edge of the conduction band. When measured in a non-aqueous aprotic electrolyte, the flat band potential is at 3.34 vs. Li QRE, corresponding to a higher edge of the valence band at 0.15 V vs. NHE. In literature, all measurements on p-type WS₂ were carried out in aqueous electrolyte, giving p-type semi-conduction and a large range of values for the valence band position from 0.00 to

0.87 V vs. NHE at pH = 14 based either on Mott-Schottky experiments [161, 167, 168] or photoelectrochemical measurements [170, 174]. Taking into account the bandgap of 0.82 eV, the lower conduction band edge is calculated as -0.67 V vs. NHE. This denotes that there is solvation effect on the flat band potential in WS₂ of 0.19 eV higher in 1 mol/L TBAPF₆ EC/DMC electrolyte (Fig. 3.51).

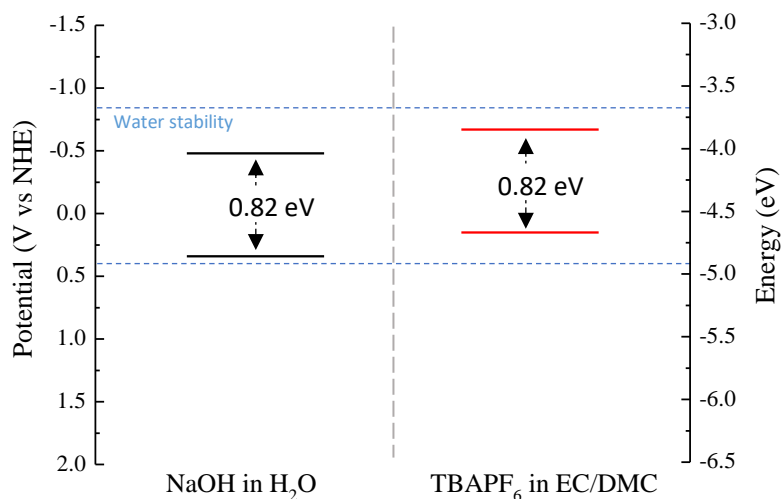


Figure 3.51. Representation of the band edge positions of WS₂ film measured in aqueous electrolyte at pH = 14 (black) and in non-aqueous aprotic EC/DMC-based electrolyte (red).

Charge carrier concentration of WS₂ for each experiment was determined assuming a dielectric constant of 8 [167] (Table 3.11). An electron density of $6.7 \cdot 10^{18} \text{ cm}^{-3}$ is obtained in 1 mol/L NaOH aqueous electrolyte in agreement with the broad range of values reported in literature [166-167]. A strong p-type doping is experienced in 1 mol/L TBAPF₆ EC/DMC with a hole density of $1.8 \cdot 10^{20} \text{ cm}^{-3}$. This value is very comparable to the $1.2 \cdot 10^{20} \text{ cm}^{-3}$ hole concentration determined by Wang et al. based on termopower measurements [175].

Table 3.11. Flat band potential and charge carrier concentration of WS₂ in 1 mol/L NaOH aqueous and 1 mol/L TBAPF₆ EC/DMC-based electrolytes.

Electrolyte	Flat band potential		Charge carrier concentration, cm^{-3}
	as measured	recalculated V vs. NHE	
1 mol/L NaOH in H ₂ O	-0.72 V vs. SCE	-0.48 (pH=14)	$4.2 \cdot 10^{18}$
1 mol/L TBAPF ₆ in EC/DMC	3.34 V vs. Li QRE	0.15	$1.8 \cdot 10^{20}$

3.3. Lithiated polyanions

LiFePO_4 and LiMnPO_4 are isostructural and belong to the family of olivine (LiMPO_4 , $M = \text{Fe}^{2+}, \text{Mn}^{2+}, \text{Co}^{2+}, \text{Ni}^{2+}$). These two materials are very attractive as high rate cathodes for lithium-ion batteries operating at 3.42 V and 4.13 V (vs. Li^+/Li). They have lower environmental impact and lower cost by substituting cobalt by iron or manganese [176-177]. The olivine structure consists of a corner-sharing MO_6 octahedra and edge shared LiO_6 octahedra localized along the b-axis linked together by PO_4 tetrahedra forming a three-dimensional architecture (Fig. 3.52).

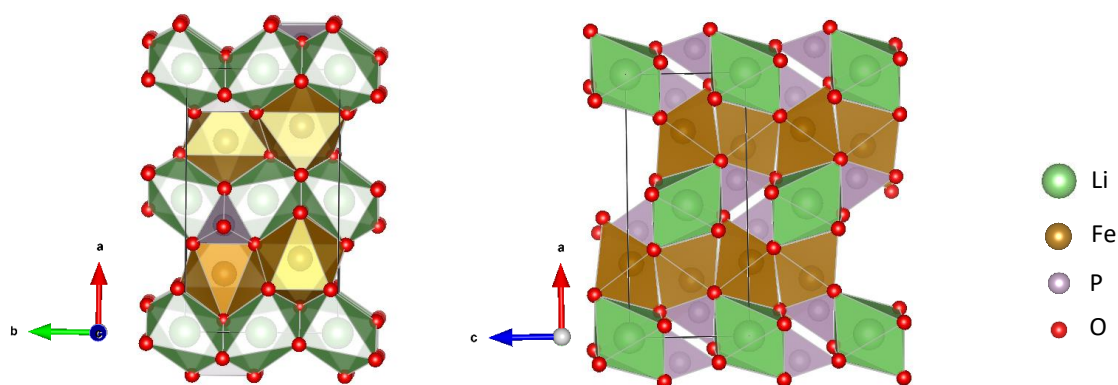


Figure 3.52. Crystal structure representation of LiMPO_4 materials down to $[001]$ and $[010]$ directions.

LiVPO_4F is another polyanion based on fluorophosphate, which was found also promising as cathode materials in lithium-ion batteries owing to its operating redox potential of 4.2 V (vs. Li^+/Li) [178-179]. It crystallizes into a tavorite-like structure composed of distorted chains of VO_4F_2 octahedra sharing two fluorine atoms, which are connected by corner-sharing PO_4 tetrahedra through the O atom (Fig. 3.53).

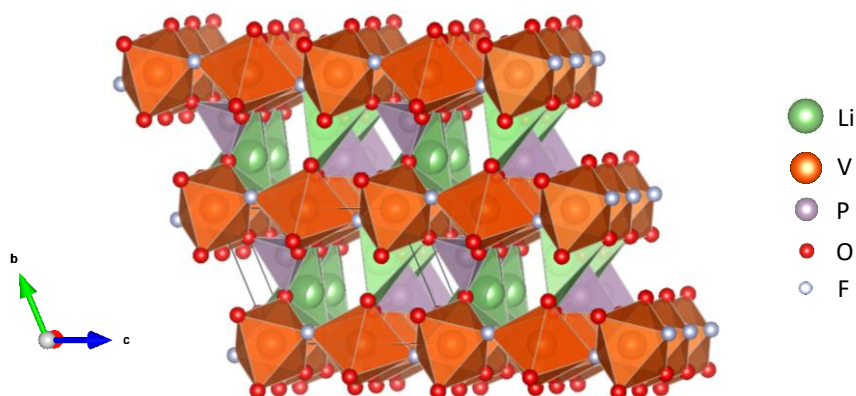


Figure 3.53. Crystal structure representation of LiVPO_4F down to $[100]$ direction.

3.3.1. LiFePO₄

The full-pattern matching refinement of LiFePO₄ is presented in Figure 3.54 (a). All diffraction peaks are corresponding to the orthorhombic lattice of LiFePO₄ adopting Pnma space group. The lattice cell parameters refined are $a = 10.332(9)$ Å, $b = 6.019(3)$ Å and $c = 4.704(5)$ Å ($V_{\text{cell}} = 293$ Å³) in agreement with the literature [180]. The SEM study revealed particles without well-defined morphology and broad size distribution ranging from few micrometers to ca. 80 μm (Fig. 3.54 (b)). The HR-TEM micrograph and SAED pattern confirm the XRD indexation and the absence of amorphous regions in the particles (Fig. 3.54 (d-e)).

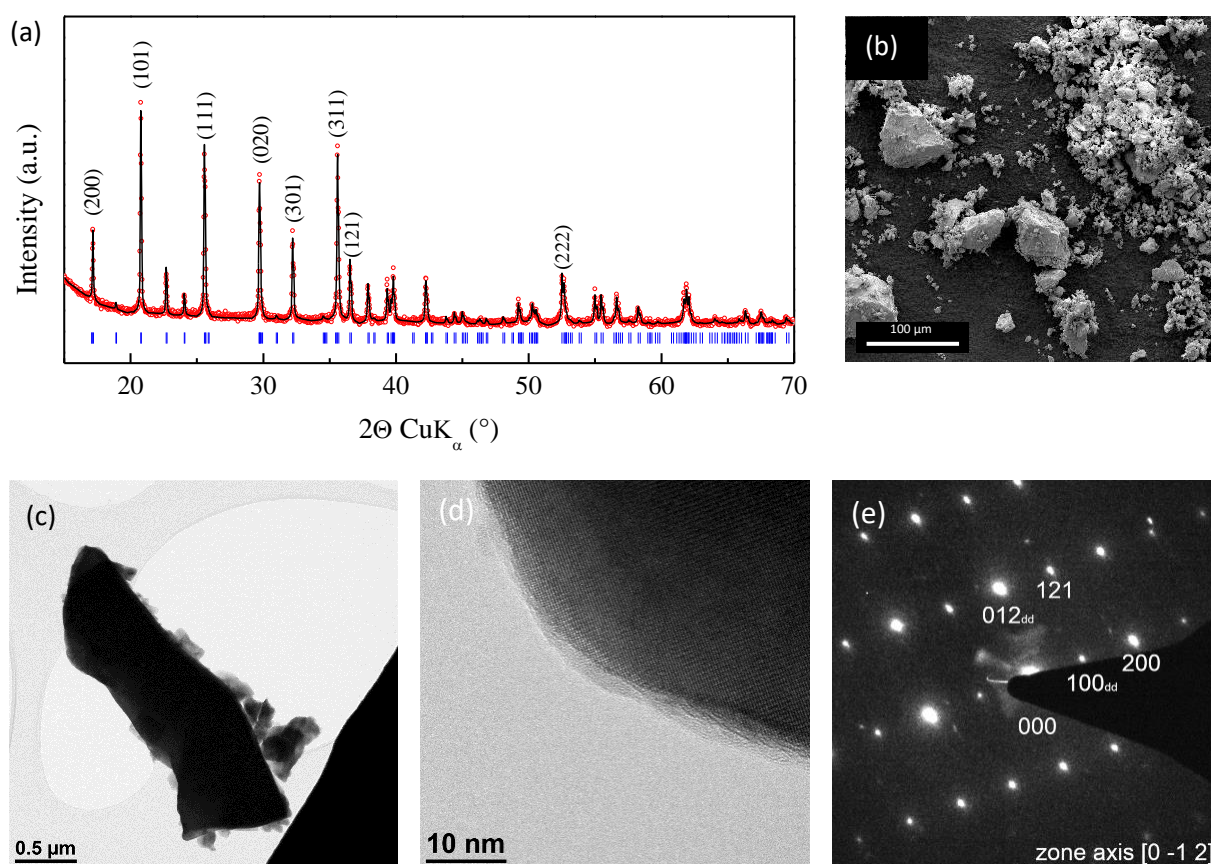


Figure 3.54. (a) Full pattern matching refinement of x-ray diffraction profile of LiFePO₄, (b) scanning electron micrograph, (c) transmission electron micrograph and (d,e) high-resolution transmission electron micrograph including selected area electron diffraction pattern.

The optical band gap of LiFePO₄ powder was determined to be 1.96 eV if we assume an indirect transition or 3.11 eV for a direct transition (Fig. 3.55 (a-c)). The band structure of LiFePO₄ is still controversial in literature. The electronic band calculations based on the traditional density functional theory (DFT) within the localized density approximation (LDA) and generalized

gradient approximation (GGA) report a band gap between 0.1 and 1 eV [181–183] which is not really consistent with the colour of the material (sand to green depending on the particles size). In contrast, more recently, Zhou et al. reported a large band gap value of 3.7 eV calculated using GGA method adding Hubbard U term (GGA+U) [184]. These authors support their calculations by experimental data based on the diffuse reflectance measurements leading to a band gap value of 3.8 eV determined as the absorption onset and 4.0 eV using the Kubelka-Monk function. Shi et al. reported a band gap of 3.2 eV based on same DFT method (GGA+U) [185]. Our 3.11 eV direct band gap value comes in agreement with these calculations. The light sand-like colour of the particles is consistent with such a bandgap value.

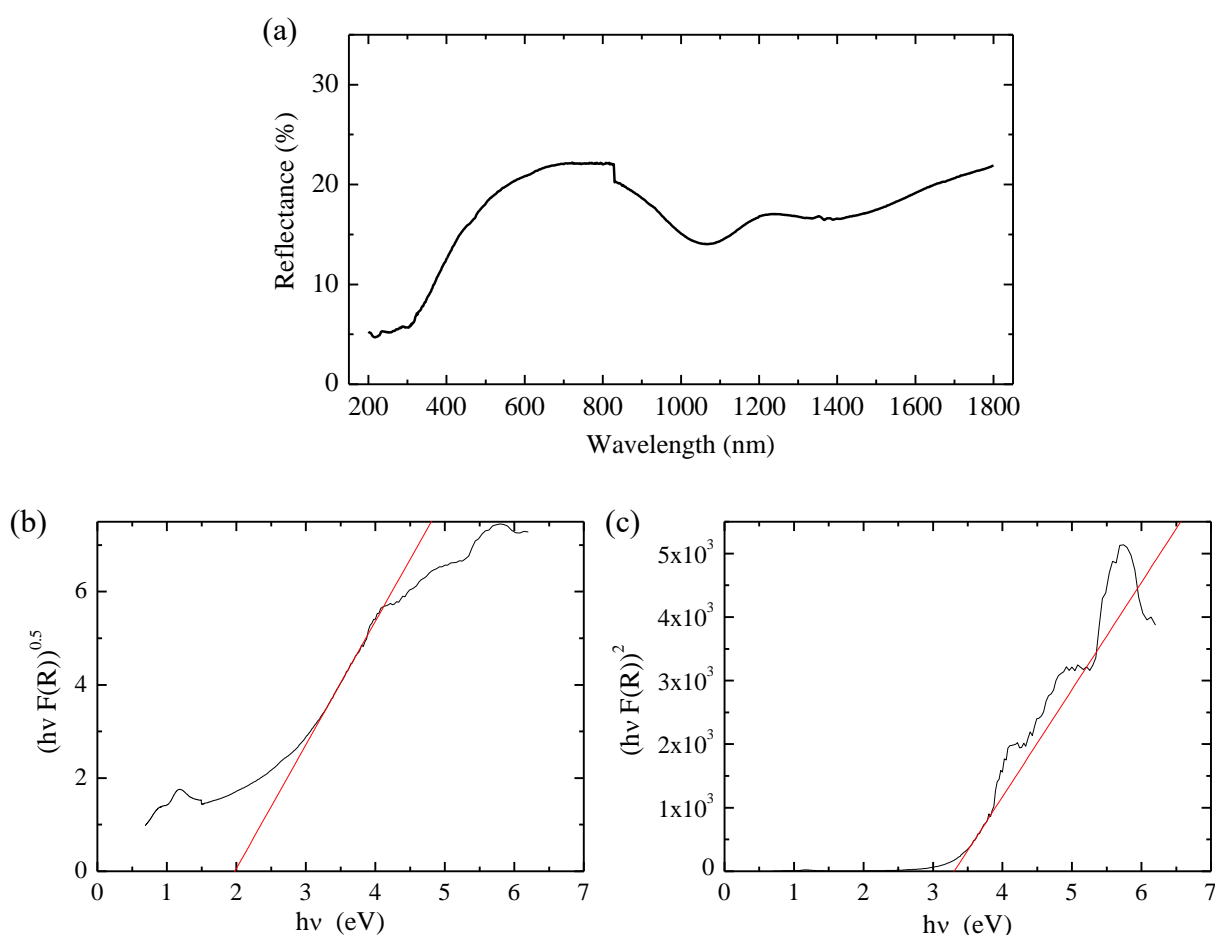


Figure 3.55. (a) Evolution of diffuse reflectance of LiFePO_4 powder as a function of wavelength and corresponding Tauc plot assuming (b) an indirect allowed transition ($n=2$) and (c) a direct allowed transition ($n=0.5$).

The flat band potential and the charge carrier concentration of LiFePO_4 were determined by Mott-Schottky analysis using 80 μm thick doctor-bladed films (Figure 3.56). In both aqueous and non-aqueous aprotic EC/DMC-based solutions, the positive slope of the Mott-Schottky

curve indicates n-type conductivity in agreement with Xu et al. [186]. However, these authors underline that a p-type conductivity may arise in the case of extrinsic doping owing to the higher mobility of the holes. N-type conductivity has also been observed by other studies reporting a negative sign in Seebeck coefficient [187-188]. All these results tends to disapprove the assumptions made on p-type conductivity mechanism in LiFePO_4 [189-190].

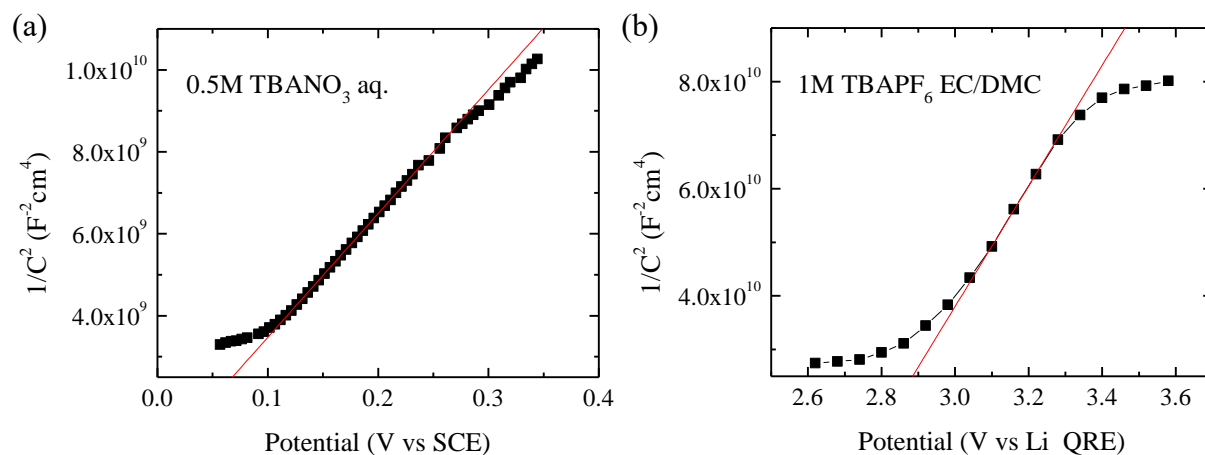


Figure 3.56. Mott-Schottky plot of LiFePO_4 measured in (a) 0.5 mol/L TBANO_3 aqueous electrolyte at 250 Hz and (b) 1 mol/L TBAPF_6 EC/DMC electrolyte at 100 Hz.

Table 3.12 gathers the flat band potential and donor density values. In 0.5 mol/L TBANO_3 aqueous electrolyte (pH = 1.65), we obtained a flat band potential of -0.04 V vs. SCE, which translates into -0.53 V vs. NHE at pH = 14. When measured in a non-aqueous aprotic 1 mol/L TBAPF_6 EC/DMC electrolyte, the flat band potential is equal to 2.62 V vs. Li QRE, corresponding to -0.58 V vs. NHE. Both values, corresponding to the bottom of the conduction band, are very close to each other, suggesting a low solvation effect on the band position. Our results are much more negative than the unrealistic 3.0 V vs. NHE conduction band edge reported based on calculations by Paoletta et al. [191]. Combining the Mott-Schottky and UV-visible spectroscopy results, the band positions of LiFePO_4 are reported in the two media in Figure 3.57.

Table 3.12. Flat band potential and charge carrier concentration of LiFePO_4 in 0.5 mol/L TBANO_3 aqueous solution and 1 mol/L TBAPF_6 EC/DMC electrolyte.

Electrolyte	Flat band potential			Charge carrier concentration, cm^{-3}
	as measured	Recalculated		
		V vs. NHE	V vs. NHE at pH=14	
0.5 mol/L TBANO_3 in H_2O	-0.04 V vs. SCE	0.20 (pH=1.65)	-0.53	$1.9 \cdot 10^{19}$
1 mol/L TBAPF_6 in EC/DMC	2.62 V vs. Li QRE	-0.58	-	$3.9 \cdot 10^{20}$

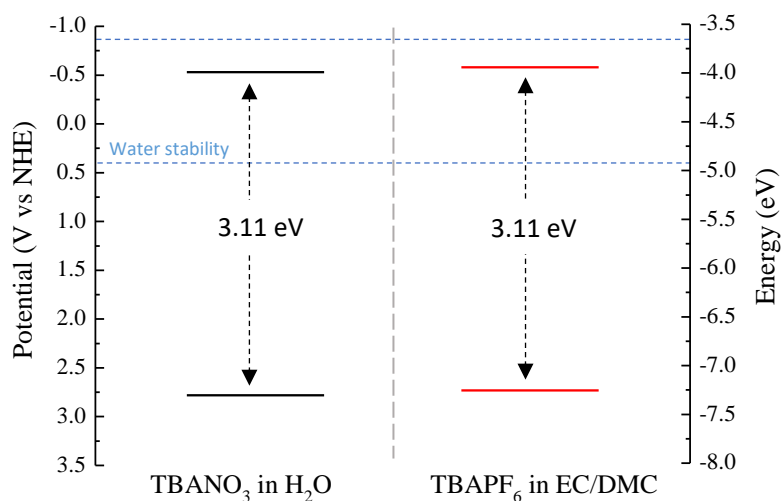


Figure 3.57. Representation of the band edge positions of LiFePO_4 measured in aqueous electrolyte and recalculated to $\text{pH} = 14$ (black) and in non-aqueous aprotic EC/DMC-based electrolyte (red).

The charge carrier concentration of LiFePO_4 for each experiment was calculated with a dielectric constant of 3 based on the complex permittivity calculations from the impedance data by Bharathi et al. [188] (Table 3.12). In 0.5 mol/L TBANO_3 aqueous electrolyte, we obtained $1.9 \cdot 10^{18} \text{ cm}^{-3}$ donor charge carrier concentration. This is two orders of magnitude lower than the donor density derived from the measurements in 1 mol/L TBAPF_6 EC/DMC, i.e. $3.9 \cdot 10^{20} \text{ cm}^{-3}$. To the best of our knowledge, this is the first report of the charge carrier concentration of LiFePO_4 .

3.3.2. LiMnPO₄

Similar to LiFePO₄, the XRD pattern of LiMnPO₄ was refined using same space group leading to the lattice cell parameters of $a = 10.460(9)$ Å, $b = 6.100(6)$ Å and $c = 4.744(5)$ Å ($V_{\text{cell}} = 303$ Å³) in agreement with Koleva et al. [192]. The cell volume is ca. 3% greater than LiFePO₄ owing to the larger ionic radii of Mn²⁺ ($r = 97$ pm) than Fe²⁺ ($r = 92$ pm) in high spin configuration. The SEM study revealed the nanoflake morphology of LiMnPO₄ particles, which are forming aggregates of up to 10 μm in diameter (Fig. 3.58 (b)). The size of the primary particles is ranging from 20 to 200 nm (Fig. 3.58 (c)). The high-resolution TEM micrograph and SAED pattern confirms that particles are single crystals of LiMnPO₄ without the presence of amorphous regions (Fig. 3.58 (d-e)).

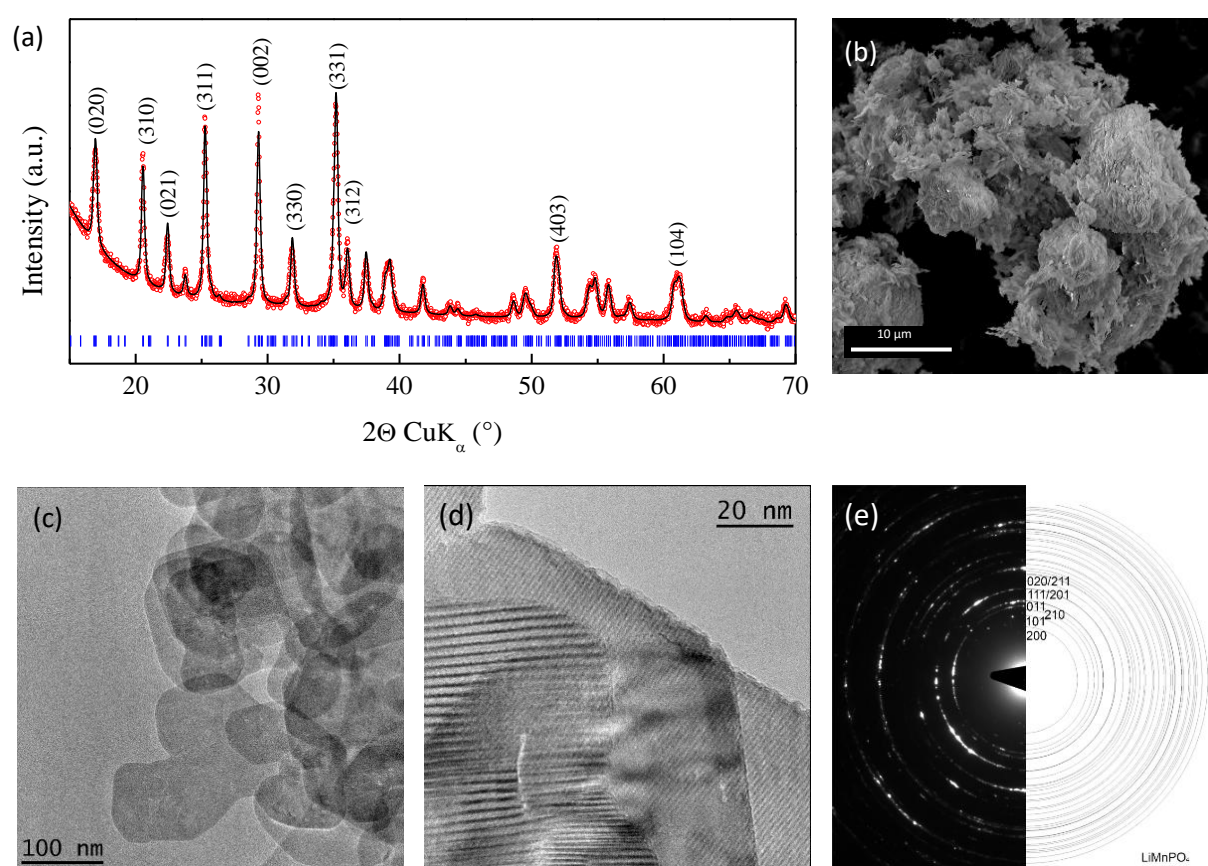


Figure 3.58. (a) Full pattern matching refinement of x-ray diffraction pattern of LiMnPO₄ with its corresponding (b) scanning electron micrograph, (c) transmission electron micrograph and (d,e) high-resolution transmission electron micrograph including selected area electron diffraction pattern.

Figure 3.59(a) shows that LiMnPO₄ has good reflecting properties in all visible and NIR part of light. Using Kubelka-Monk function, the optical band gap for an indirect allowed transition

is rather difficult to determine precisely as we can extrapolate an onset at ca. 2.22 eV followed by a more marked transition above 5 eV (Fig. 3.59 (b)). For a direct electronic transition, the extrapolation of the linear part of $(hvF(R))^2$ curve results in a 5.19 eV intercept. However, zooming in shows that there is also a small transition onset at around 3.93 eV, which has a low absorption coefficient compared to that of the 5.19 eV transition. We argue that LiMnPO_4 has a direct band gap nature based on the Tauc plots. Our value is in agreement with 3.8 - 4.0 eV reported by Xu et al. based on GGA+U calculations [184]. It is however significantly higher than 1.7 to 1.9 eV calculated by other groups [181, 182, 193]. It is recognized in literature that LiMnPO_4 has a stronger insulating character than LiFePO_4 , thus consistent with the greater band gap value [187].

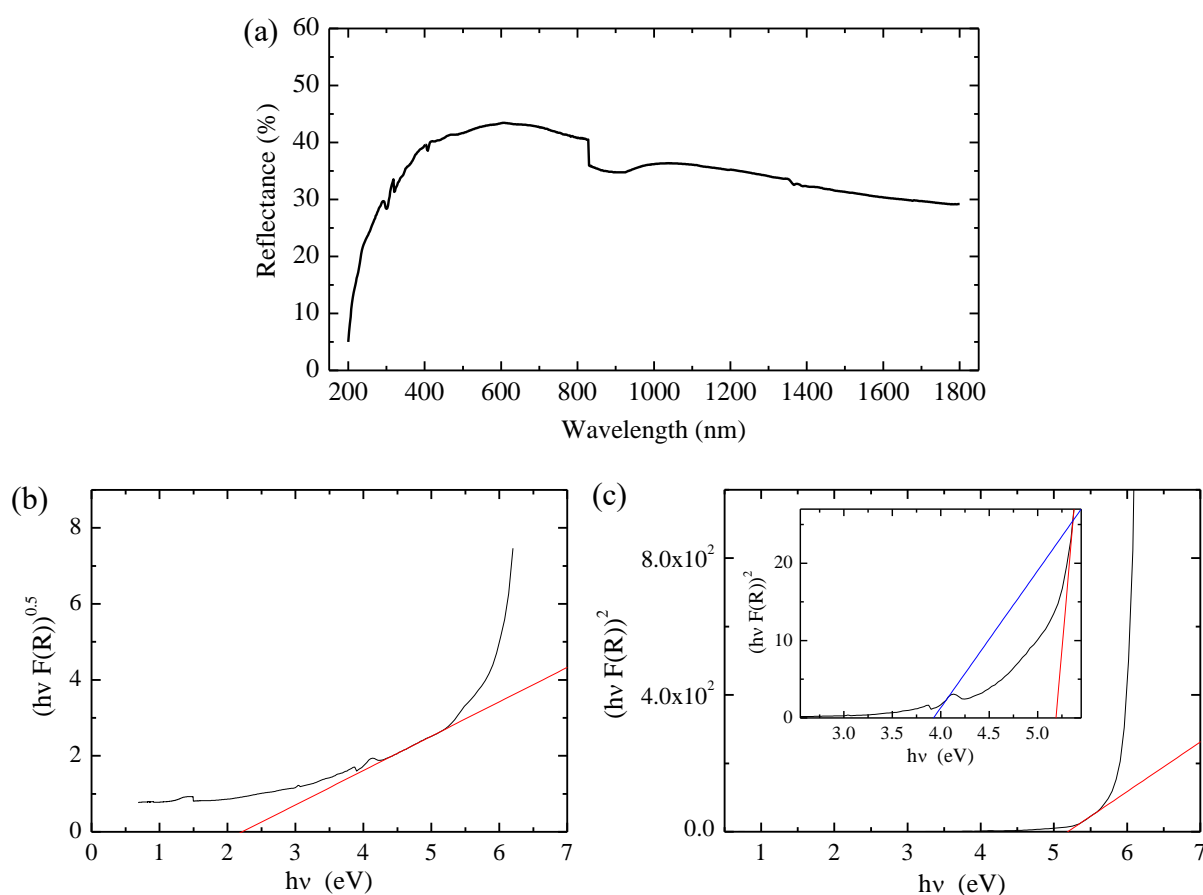


Figure 3.59. (a) Evolution of diffuse reflectance of LiMnPO_4 powder as a function of wavelength and corresponding Tauc plot assuming (b) an indirect allowed transition ($n=2$) and (c) a direct allowed transition ($n=0.5$).

The Mott-Schottky experiments were performed on 5 μm thick doctor-bladed film. The measurements carried out in a range of aqueous electrolytes based on NaOH or TBANO_3 at

different pH values were not successful due to a lack of reproducibility in the results as similarly observed for CuO, LiMn₂O₄ and LiMn_{1/3}Co_{1/3}Ni_{1/3}O₂. In contrast, there were no problems of reproducibility in 1 mol/L TBAPF₆ EC/DMC electrolyte. A representative Mott-Schottky plot is reported in Figure 3.60. The negative slope of the plot confirms that LiMnPO₄ is a n-type semi-conductor.

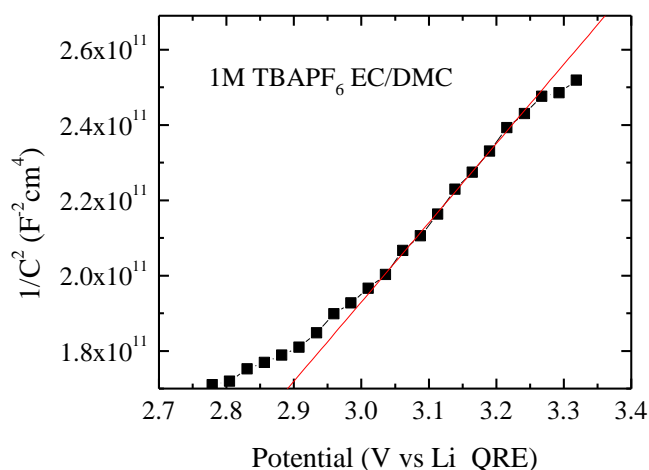


Figure 3.60. Mott-Schottky plot of LiMnPO₄ measured in 1 mol/L TBAPF₆ EC/DMC electrolyte at 300 Hz.

Using the Mott-Schottky equation, the flat band potential and donor density of LiFePO₄ were determined (Table 3.13). The flat band potential, corresponding to the position of the bottom of the conduction band, was measured at 2.07 V vs. Li QRE, which translates into -1.12 V vs. NHE. Taking into consideration a 3.93 eV band gap, the top of the valence band should be at 2.81 V vs. NHE. This shows that compared to LiFePO₄ both conduction band and valence band of LiMnPO₄ are destabilized in energy by 0.54 eV and 0.24 eV, respectively. (Fig. 3.61). A charge carrier concentration of $2.2 \cdot 10^{20} \text{ cm}^{-3}$ was determined using a dielectric constant similar to LiFePO₄ as an approximation [188]. This value is two times lower than in LiFePO₄ ($3.9 \cdot 10^{20} \text{ cm}^{-3}$). To the best of our knowledge, this is the first report on the flat-band potential and donor density in LiMnPO₄.

Table 3.13. Flat band potential and charge carrier concentration of LiMnPO_4 in 1 mol/L TBAPF_6 EC/DMC electrolyte.

Electrolyte	Flat band potential		Charge carrier concentration, cm^{-3}
	as measured	recalculated	
1 mol/L TBAPF_6 in EC/DMC	2.07 V vs. Li QRE	-1.12 V vs. NHE	$2.2 \cdot 10^{20}$

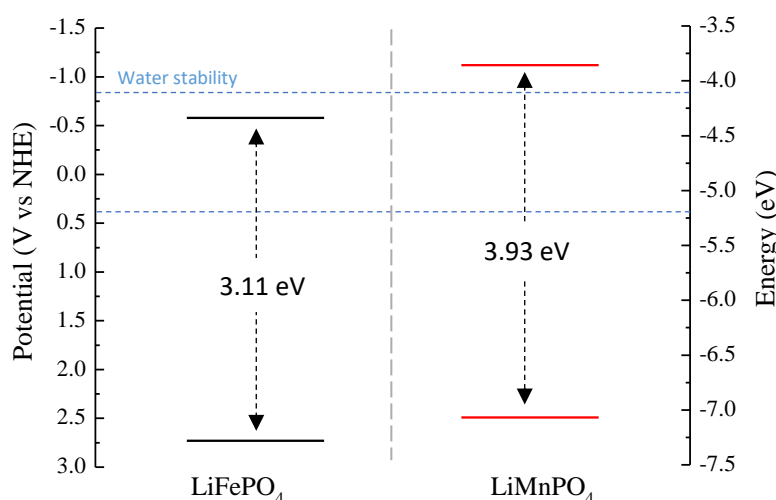


Figure 3.61. Comparison of the band edge positions of LiFePO_4 and LiMnPO_4 films in non-aqueous aprotic 1 mol/L TBAPF_6 EC/DMC-based electrolyte.

3.3.3. LiVPO_4F

The XRD diffractogram of LiVPO_4F is presented in Figure 3.62 (a) including its full-pattern matching refinement into a triclinic unit cell of P-1 space group. The sample is free of any impurities. The lattice cell parameters refined are $a = 5.168(4)$ Å, $b = 5.309(8)$ Å, $c = 7.263(6)$ Å, $\alpha = 107.599^\circ$, $\beta = 108.02^\circ$, $\gamma = 98.336^\circ$ ($V_{\text{cell}} = 174$ Å³). These values are in a good agreement with the crystallographic data reported by Ateba Mba et al. [179]. The SEM and TEM micrographs show the nanometer size of the particles forming rock-like agglomerates of few tenth of micrometers (Fig. 3.62 (b-c)). HR-TEM investigations confirmed the absence of amorphous regions while showing good crystallinity of the material to the edges of the particles (Fig. 3.62 (d-e)).

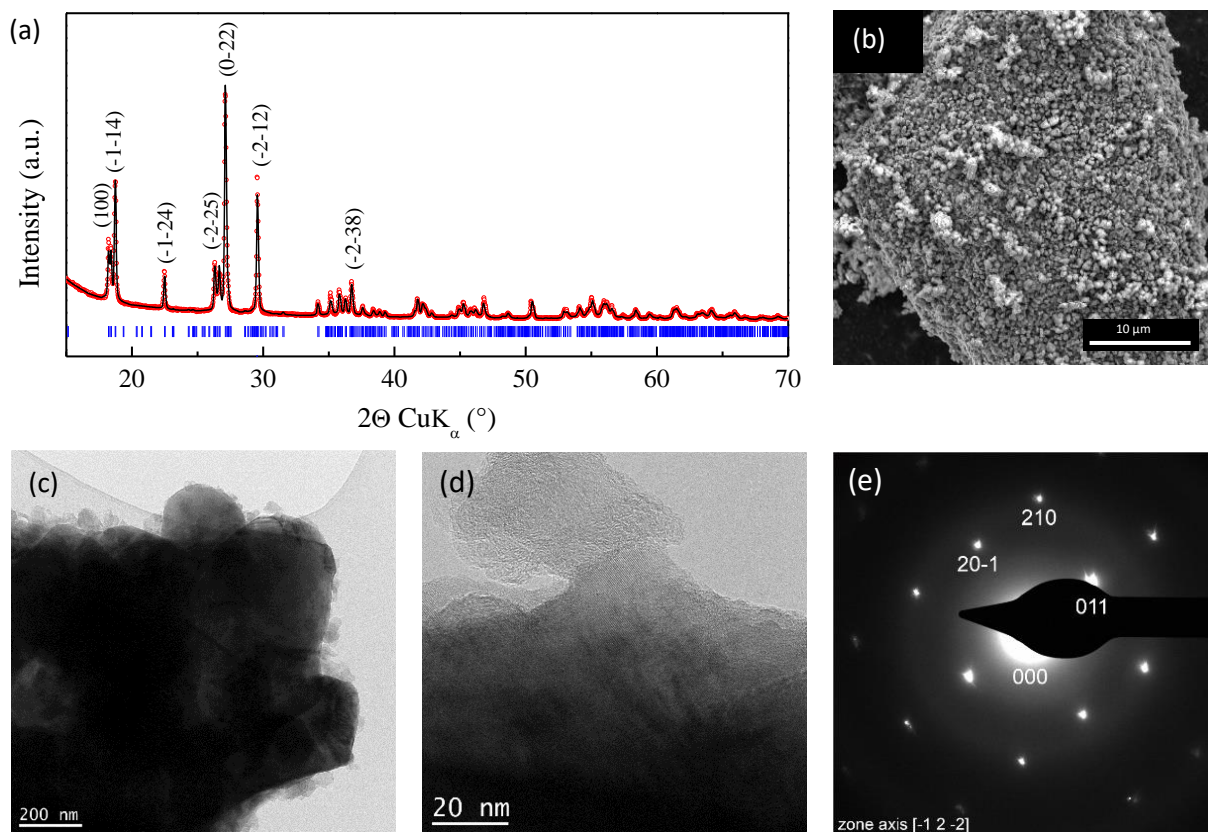


Figure 3.62. (a) Full pattern matching refinement of x-ray diffraction pattern of LiVPO_4F powder with its corresponding (b) scanning electron micrograph, (c) transmission electron micrograph and (d,e) high-resolution transmission electron micrograph including selected area electron diffraction pattern.

The band gap of LiVPO_4F was determined using 2 wt% of LiVPO_4F in KBr pressed pellet because of its low reflectivity in the portion of 200 - 1800 nm (Fig. 3.63 (a)). A band gap energy of 1.36 eV was determined assuming an indirect allowed transition (Fig. 3.63 (b)) and 1.71 eV for a direct allowed transition (Fig. 3.63 (c)). The latter assumption is supported in this work by the clear linear portion of the Tauc plot assuming direct transition by comparison to indirect. The experimental value of 1.71 eV is consistent with the value of 1.63 eV reported by Tang et al. based on the DFT band structure calculations [194].

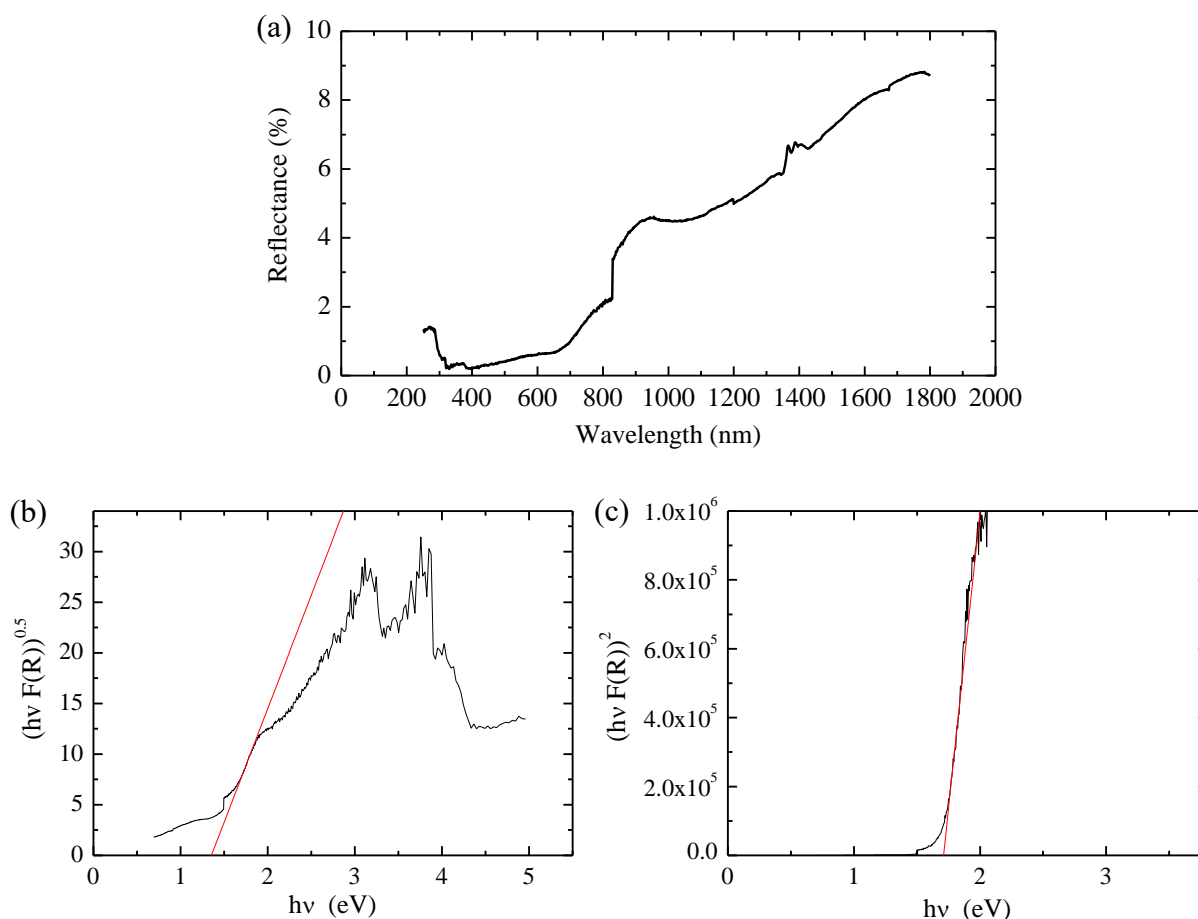


Figure 3.63. (a) Evolution of diffuse reflectance of LiVPO_4F powder as a function of wavelength and corresponding Tauc plot assuming (b) an indirect allowed transition ($n=2$) and (c) a direct allowed transition ($n=0.5$).

Unfortunately, we found that Mott-Schottky experiments on LiVPO_4F systematically failed regardless of the electrolyte nature. This latter, as for many fluorophosphates, is chemically not stable in water. It is however unclear why we faced irreproducible results in EC/DMC based electrolyte beside the possibility of excessive surface defects or a too porous film morphology, which makes us deviating too much from the initial assumptions of Mott-Schottky theory.

All the optoelectronic properties of the insertion materials studied in this part of the thesis and discussed above are gathered in the annex tables I-IV. The summarizing scheme of the band edge positions in aqueous and non-aqueous aprotic EC/DMC-based electrolytes for the materials, for which both Mott-Schottky and UV-visible measurements were successful, are gathered in Figure 3.64. For some of them, namely TiO_2 , LiCoO_2 , and WO_3 , a negative band edge energy shift is observed when this later is placed in contact with a non-aqueous aprotic EC/DMC-based electrolyte. For other materials investigated, i.e. $\text{Li}_4\text{Ti}_5\text{O}_{12}$, MoO_3 , Bi_2O_3 and

WS₂, this shift driven by the solvent interaction is positive. MoS₂ and LiFePO₄ are the only materials investigated which are showing no dependence of the band position with the electrolyte nature. Note that for MoS₂ a changeover from n to p-type semi-conduction was experienced when moving from aqueous to non-aqueous aprotic electrolyte.

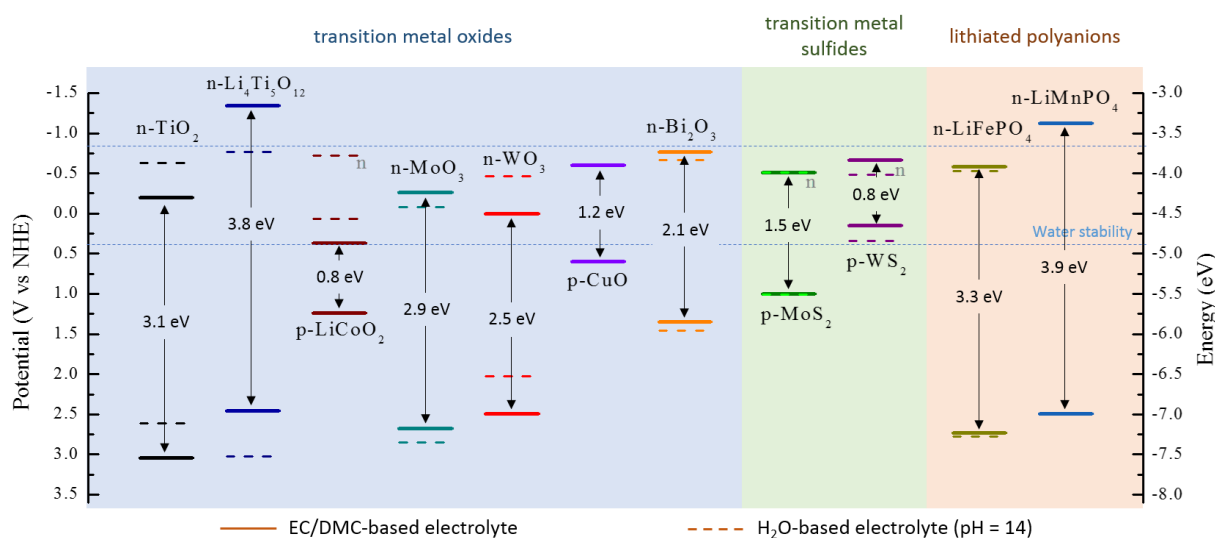


Figure 3.64. Representation of the database of optoelectronic properties of common insertion materials measured in aqueous protic electrolyte at pH = 14 (dashed line) and in non-aqueous aprotic EC/DMC-based electrolyte (solid line).

3.4. Fundamental evaluation of the possibility of Li⁺ photo-insertion / photo-deinsertion reaction.

In the late 1970s, Gerisher et al. have established that during the photo-induced charge separation in the depletion layer of a mixed semiconductor, the main charge carriers migrate into the bulk of the material while the minor carriers migrate towards the surface [195-196]. The latter can subsequently trigger an interfacial ion-transfer at the electrode / electrolyte interface induced by a redox reaction between the surface carriers and the transition metal center in the electrode [197–201]. Based on this pioneering work, we evaluated the possibility of the materials to be employed as a photorechargeable electrode relying on the information gathered in the database. To be used as a photorechargeable electrode, material needs to have an energy of the minor carriers adequate to the redox potential of the transition metal to allow its transfer. The figure 3.65 gathers the positions of the valence and conduction bands for different materials investigated in this thesis with respect to the type of semi-conduction and the redox energy of the transition metal.

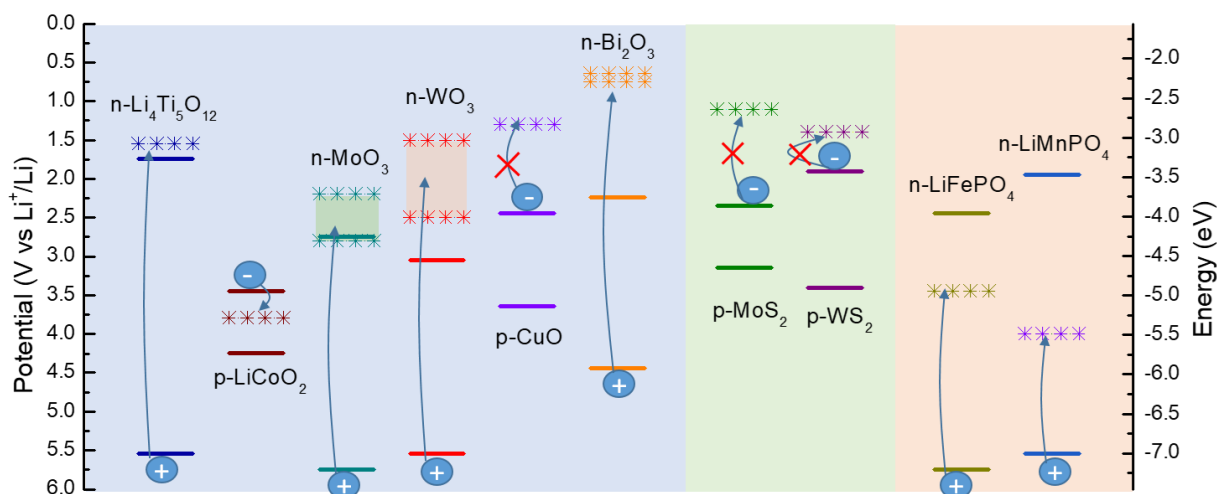


Figure 3.65. Schematic representation of the database including the redox energy of the transition metal for the different materials (in star lines) and the possibility or not for carrier transfer from the excited state.

Among the transition metal oxides herein studied, the photogenerated hole carriers (h^+) of the n-type $\text{Li}_4\text{Ti}_5\text{O}_{12}$, MoO_3 , WO_3 , and Bi_2O_3 have sufficient oxidizing strength to be transferred to the transition metal to onset the lithium deinsertion reaction from their lithiated composition (Table 3.14). This is the same case for the two polyanions LiFePO_4 and LiMnPO_4 . For the p-type LiCoO_2 , the electrons are also sufficiently reductive to conduct the lithium insertion reaction from its delithiated composition $\text{Li}_{1-x}\text{CoO}_2$, then making this material promising for a photorecharge application. In contrast, some materials can be discarded for thermodynamic reasons, such as the p-type CuO , MoS_2 , and WS_2 , for which the electrons are not reductive enough to reduce Cu^{2+} , Mo^{4+} and W^{4+} .

Table 3.14. Potential of the photogenerated minor charge carriers (h^+ for n-type and e^- for p-type SC) compared to the redox potential corresponding to lithium insertion/deinsertion (V vs. Li^+/Li) for the transition metal oxides, transition metal sulfides, and lithiated polyanions in study.

Material	Potential of minority charge carrier, V vs. Li^+/Li	Li^+ insertion / deinsertion potential, V vs. Li^+/Li	Overpotential for charge transfer (V)	[Reference]
n- $Li_4Ti_5O_{12}$	5.55	1.55	0.2-0.25	[202]
p- $LiCoO_2$	4.25	3.8	0.1	[39, 203]
n- MoO_3	5.75	2.2-2.8	0.5	[204]
n- WO_3	5.55	1.4-2.3	0.8	[205]
p- CuO	2.45	1.3	1.2	[206]
n- Bi_2O_3	4.45	0.64-0.75	0.6	[207]
p- MoS_2	3.55	1.1	1.0	[208]
p- WS_2	2.35	1.4	0.9	[209]
n- $LiFePO_4$	5.75	3.4	0.2	[176]
n- $LiMnPO_4$	5.55	4.0	0.2	[210]

3.5. First results on the photoelectrochemistry of chosen insertion materials

All photoelectrochemical studies developed in this part were carried out using the airtight three-electrode photoelectrochemical cell presented in chapter 2.

3.5.1. $LiCoO_2$

Figure 3.66 shows a comparison in dark and under illumination of the cyclic voltammogram of 16 μm thick film of $LiCoO_2$ at a scan rate of 0.1 mV/s. In dark, the first cycle shows an irreversible anodic peak between 4 and 4.2 V corresponding to the lithium extraction from $LiCoO_2$ leading to a current density of up to 106 $\mu A/cm^2$. In reduction, only a very low cathodic current of around -6 $\mu A/cm^2$ is observed, denoting the irreversible character of the lithium insertion into carbon-free electrode. This leads to a half wave redox potential of 3.84 V (vs. Li^+/Li) in a good agreement with literature [39]. No further capacity is observed in the subsequent cycle. Interestingly, there is an important modification under illumination. An

anodic current is starting to rise from 3.3 V (vs. Li^+/Li) leading to a current density almost six times higher than in dark. We estimate that this faradaic current is resulting from a combination of the lithium extraction from LiCoO_2 and a photo-activation of the electrolyte decomposition in contact with LiCoO_2 excited states. This role played by LiCoO_2 as a photoanode towards electrolyte degradation is somewhat surprising given its p-type semi-conduction. However, as discussed in the first part of this chapter, LiCoO_2 has a weak degenerated p-type semi-conduction which may either cross to n-type depending on the applied potential or lithium presence in the electrolyte, or, have a leak of electrons across the space charge layer. On top of this, it is also known that electrolyte degradation through LiPF_6 can be prominent under illumination [211]. As it will be discussed in the following, this reaction is here significantly catalyzed by the excited state of LiCoO_2 . Upon reverse scan, one can decipher a peak at around 3.8 V (vs. Li^+/Li) which still maintains a positive current. This is a result of two antagonist processes, namely lithium reinsertion into the structure (reduction) and the continuation of the electrolyte degradation (oxidation) at this potential; this latter being the predominant reaction. Nevertheless, a better reversibility observed under illumination can be a result of (i) the higher conductivity of the electrode, by photo-action (i.e. photoconductivity) and/or (ii) the possibility of photon-induced lithium insertion, which will lead to a higher reductive current.

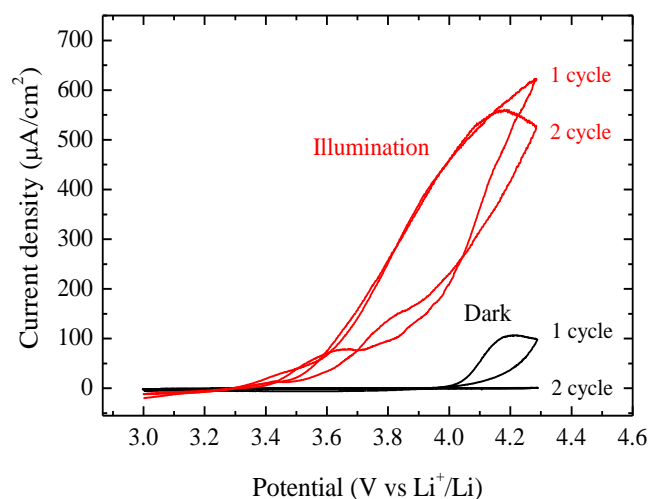


Figure 3.66. Comparison of the first two cycles of cyclic voltammetry recorded on $16 \mu\text{m}$ thick LiCoO_2 electrode at 0.1 mV/s scan rate in $1 \text{ mol/L LiPF}_6 \text{ EC/DMC}$, in dark (black curve) and under A.M. 1.5G illumination (red curve).

3.5.2. LiFePO₄

In order to evaluate the electrochemical behavior of LiFePO₄ in dark and under illumination, we carried out a cyclic voltammetry study on a 50 μm thick doctor-bladed film at different scan rates (v) from 0.5 to 20 mV/s (Fig. 3.67). The electrochemical behavior shows the typical redox activity of LiFePO₄ with a redox potential determined at half-wave at ca. 3.42 V vs. Li⁺/Li. In contrast to the case of LiCoO₂, we do not see here any predominant electrode degradation up to 4 V under illumination. This means that the excited states of LiFePO₄ have no photo-catalytic properties with respect to the electrolyte oxidation.

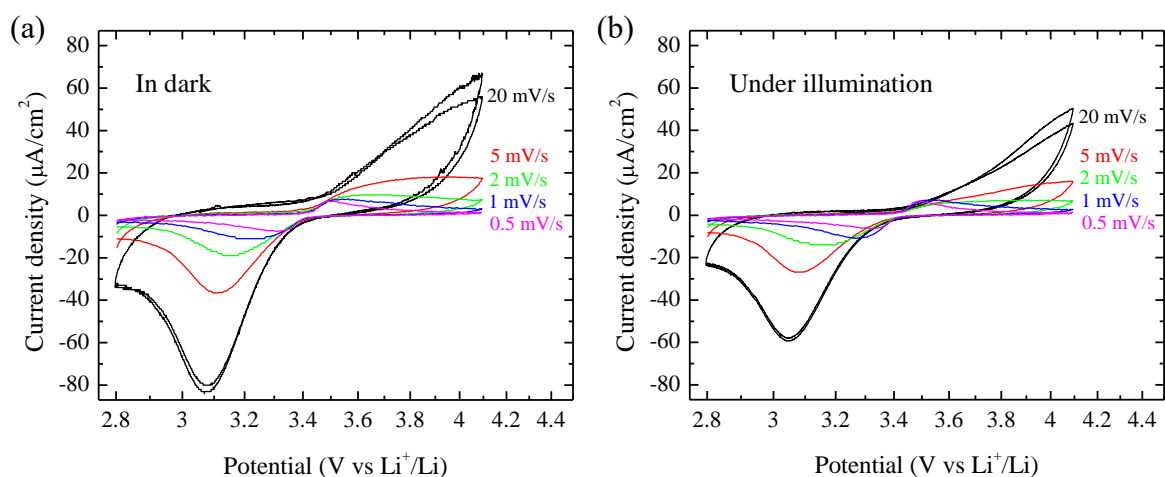


Figure 3.67. Evolution of the cyclic voltammograms of 50 μm thick LiFePO₄ film measured in 1 mol/L LiPF₆ EC/DMC as a function of the scan rate (0.5 mV/s < v < 20 mV/s) (a) in dark and (b) under standard A.M. 1.5G illumination conditions.

Comparison of the current density of anodic (J_{pa}) and cathodic (J_{pc}) peaks as a function of scan rate in dark and under illumination is presented in Figure 3.68 (a). Both in dark and under illumination, the non-linear dependence of the peak current density as a function of scan rate (v) and scan rate square root ($v^{0.5}$) indicates a kinetic behavior that is intermediate between capacitive and faradaic. This is ascribed to the low electro-activity of the carbon-free films, which undergo only surface reactions in agreement with the film capacity that is lower than 1 μAh/cm² (Fig. 3.68 (b)). We can notice a close to pure faradaic behavior only in reduction regardless in dark or under illumination conditions. There is no drastic differences under illumination in terms of film capacities (Fig. 3.68 (b)). We only found slightly higher peak current under illumination in a very reproducible manner.

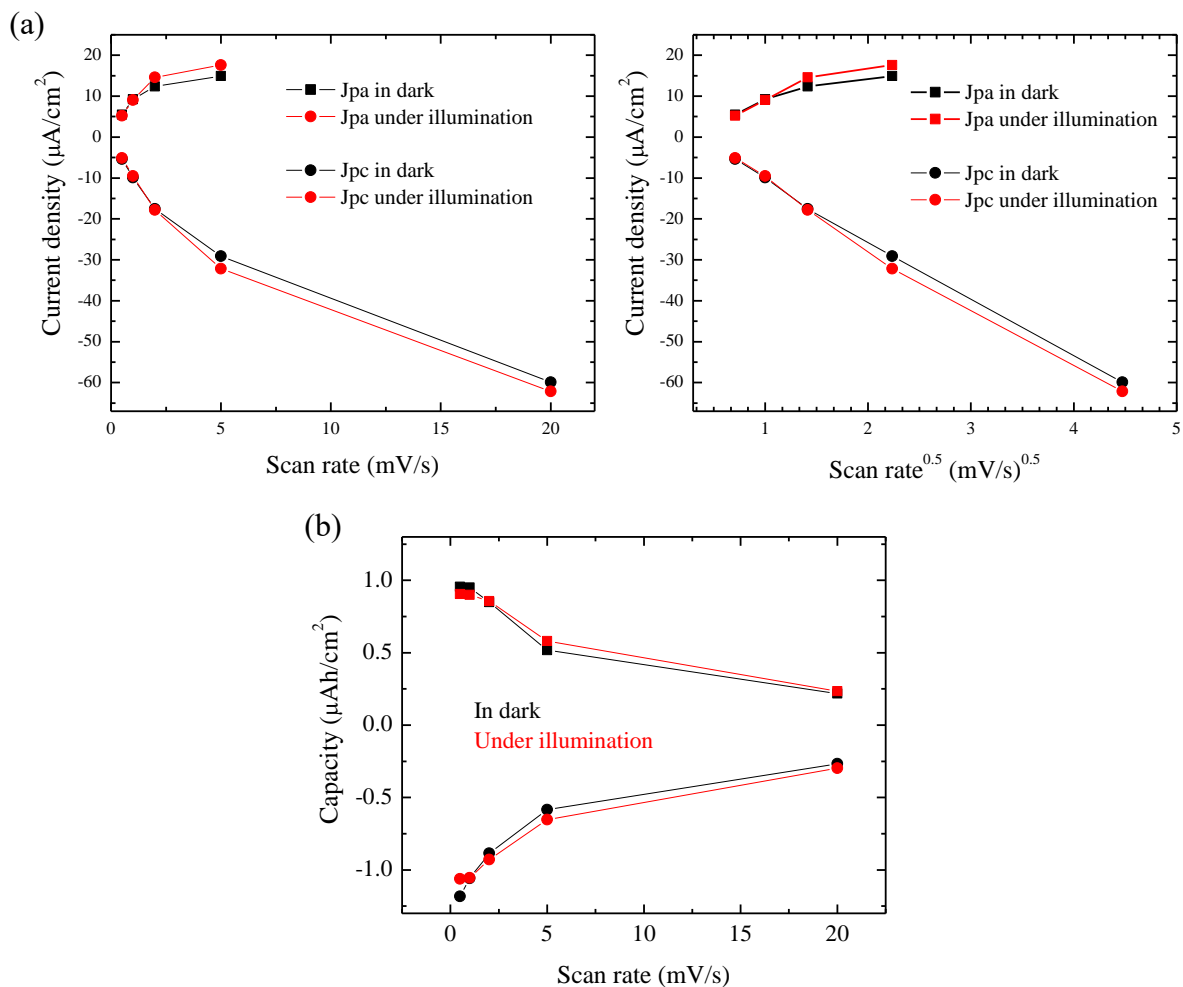


Figure 3.68. Evolution of the (a) peak current density as a function of scan rate and scan rate square root and (b) capacity as a function of scan rate derived from the cyclic voltammograms of 50 μm thick LiFePO_4 film in dark and under illumination.

This small improvement can be originating from a minor enhancement of electrode's conductivity under illumination. This can also explain why there is a ca. 40 mV smaller anodic/cathodic peak separation energy (ΔE_p) for scan rates greater than 1 mV/s, indicating lower kinetic issues for lithium insertion/deinsertion process (Fig. 3.69 (a)). This is also consistent with the global cell resistance that we determined from the linear portion of the current rise at low overpotentials, which shows lower but not drastic ohmic drop under illumination (Fig. 3.69 (b)).

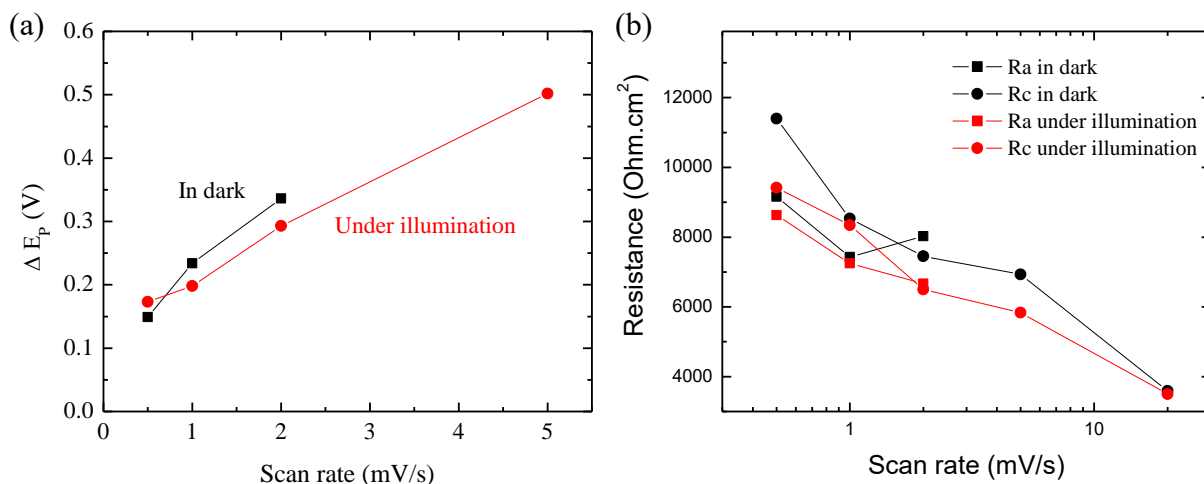


Figure 3.69. Evolution of the (a) potential of the faradaic peaks separation and (b) resistance of anodic and cathodic processes as a function of scan rate in dark and under illumination for $50 \mu\text{m}$ LiFePO_4 film in $1 \text{ mol/L LiPF}_6 \text{ EC/DMC}$.

To evaluate if LiFePO_4 can undergo a photorecharge process, the electrode was left at the open circuit condition under illumination for 120 hours (Fig. 3.70). The result shows that the electrode potential rises from the initial 3.36 V (vs. Li^+/Li) to 3.42 V (vs. Li^+/Li) in the first 20 hours and then increases steadily to 3.44 V (vs. Li^+/Li) in the next 100 hours. This slow increase of the electrode potential under open circuit condition indicates that the electrode has reached the equilibrium plateau without any photo-induced lithium deinsertion from the structure. This result in addition to the above presented observations indicates that LiFePO_4 has no photocatalytic activity, neither for electrolyte degradation nor for photo-rechargeability.

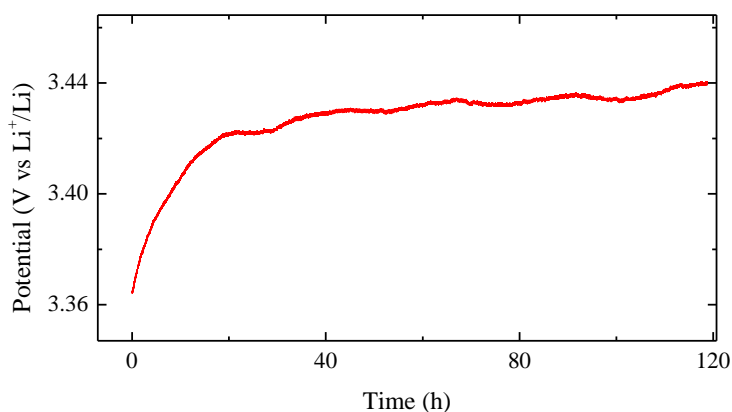


Figure 3.70. Evolution of the open circuit potential of LiFePO_4 film under standard A.M. 1.5G conditions.

Our result disagrees with the recent study of Paoella et al. reporting the light-assisted delithiation of LiFePO_4 (Fig. 3.71) [191]. The authors achieved a light-induced photorecharge to 3.62 V (vs. Li^+/Li) in ca. 70 hours at open circuit potential, which resulted in a consequent discharge capacity of 104 mAh/g. There are few major differences between our and their experiments. First, the authors used a film composed of colloidal LiFePO_4 nano-platelets. Second, LiFePO_4 was sensitized with a ruthenium-based complex N719 in analogy with a dye-sensitized solar cell photo-“anode” structure. Third, the electrode was composed of active carbon nanotubes and PVDF in a final composition of LFP:CNTs:PVDF with 90:5:5 ratio. Fourth, photo-recharge needs dry air and not argon in order to take place. The mechanism of the photo-recharge between N719 and LiFePO_4 is on the one hand very speculative (LiFePO_4 is assumed to be a p-type and N719 is an electron donor at excited state and not acceptor) and on the other hand very questionable based on energetic diagram proposed.

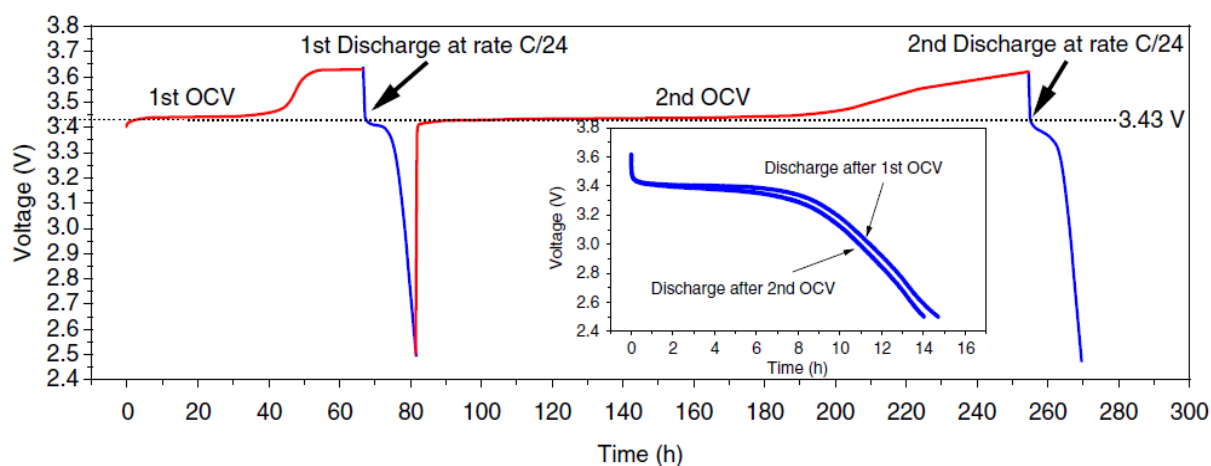


Figure 3.71. Open circuit voltage and discharge curves of LiFePO_4 on FTO glass reported by Paoella et al. [191]. OCV charge (red lines) were performed under illumination at 100 mW/cm^2 and galvanostatic discharge (blue lines) at $C/24$.

To clarify in some points if the photorecharge arises from the dye excitation or from the nano-size of LiFePO_4 , we collaborated with the group of Dr. Kulka (AGH University of Science and Technology, Cracow, Poland) who provided us nanoparticles of carbon-free LiFePO_4 . The synthetic procedure of this powder is reported in the following reference [212]. The full-pattern matching refinement of the x-ray diffractogram revealed minor impurities of Li_3PO_4 corresponding to ~4 wt% of the sample as reported in their publication (Fig. 3.72 (a)) [212]. All diffraction peaks of nano- LiFePO_4 are corresponding to the orthorhombic lattice adopting

Pnma space group. The refined lattice cell parameters are $a = 10.301(6)$ (9) Å, $b = 5.993(4)$ Å and $c = 4.694(5)$ Å ($V_{\text{cell}} = 290$ Å³). The result is close to the values obtained for the bulk LiFePO_4 ($a = 10.332(9)$ Å, $b = 6.019(3)$ Å and $c = 4.704(5)$ Å ($V_{\text{cell}} = 293$ Å³)), even though a small decrease of the unit cell volume by 3 Å³ is observed. These minor differences in the cell structure can be assigned to the higher number of the punctual defects present in the nanopowder. The TEM micrographs indicate that the particles are single crystals of LiFePO_4 with a platelet morphology of about 100-150 nm in diameter (Fig. 3.72 (b-d)).

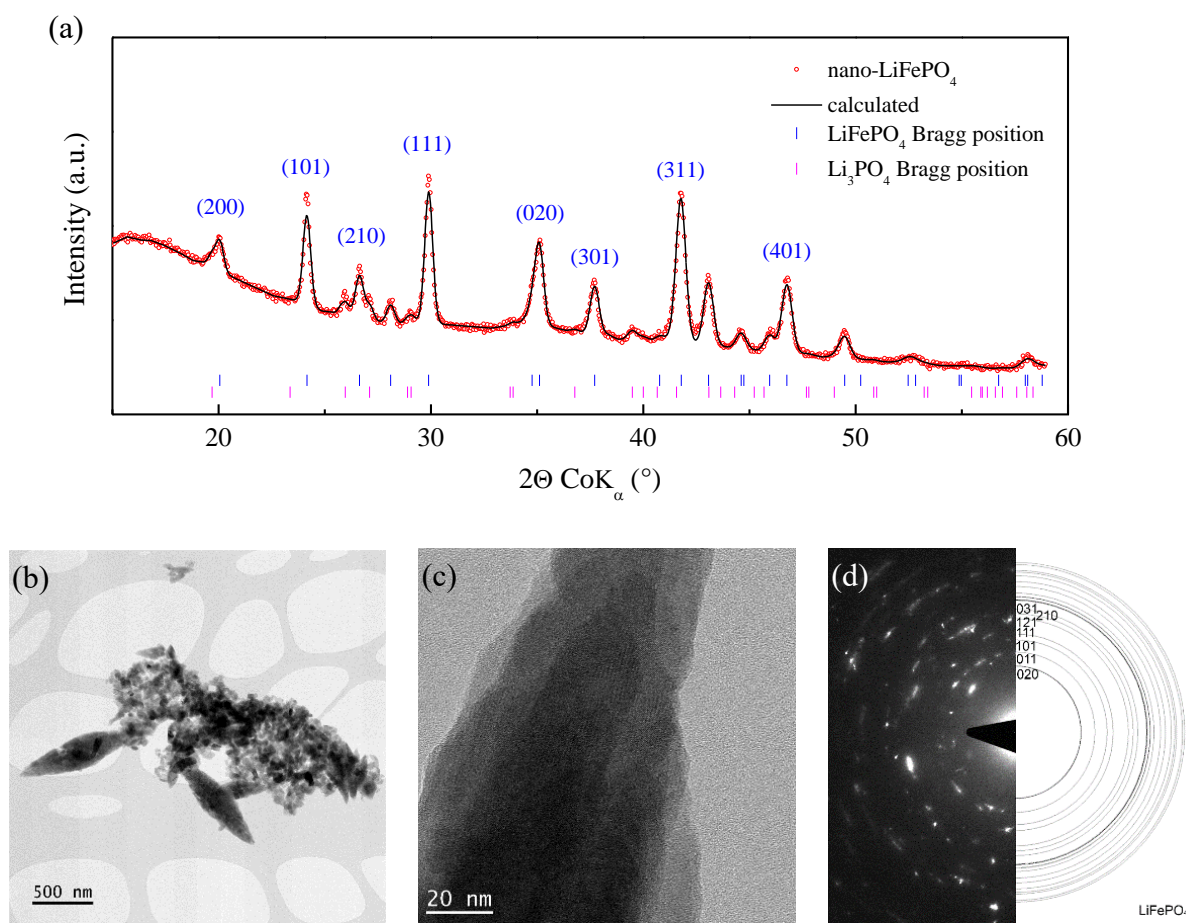


Figure 3.72. (a) Full pattern matching refinement of x-ray diffraction pattern of LiFePO_4 nanoparticles with the corresponding (b-d) transmission electron micrographs and selected area electron diffraction pattern.

The photoelectrochemical properties of a 30 μm thick electrode doctor-bladed films was investigated under open-circuit condition as a function of time, in dark and under illumination (Fig. 3.73 (a)). The difference in evolution of the open-circuit potential between the two conditions is not significant except the faster rise to equilibrium and potential perturbation after ca. 40 hours under illumination. We also evaluated the possibility of photo-induced lithium

insertion into FePO₄ phase by charging the electrode galvanostatically at 10 μA/cm² until 4.0 V vs. Li⁺/Li followed by dark vs. illumination open circuit condition (Fig. 3.73 (b)). First, the electrode reached 4.0 V in only few minutes indicating a very low level of the electrode activity. This is explained by the insulating nature of the lithium iron phosphate, which has an electronic conductivity of only 10⁻⁹ S/cm and is a poor ionic conductor [187]. As almost no lithium was extracted, the subsequent evolution of open circuit potential resulted in a fast electrode potential drop to the equilibrium value regardless of dark vs. illumination conditions.

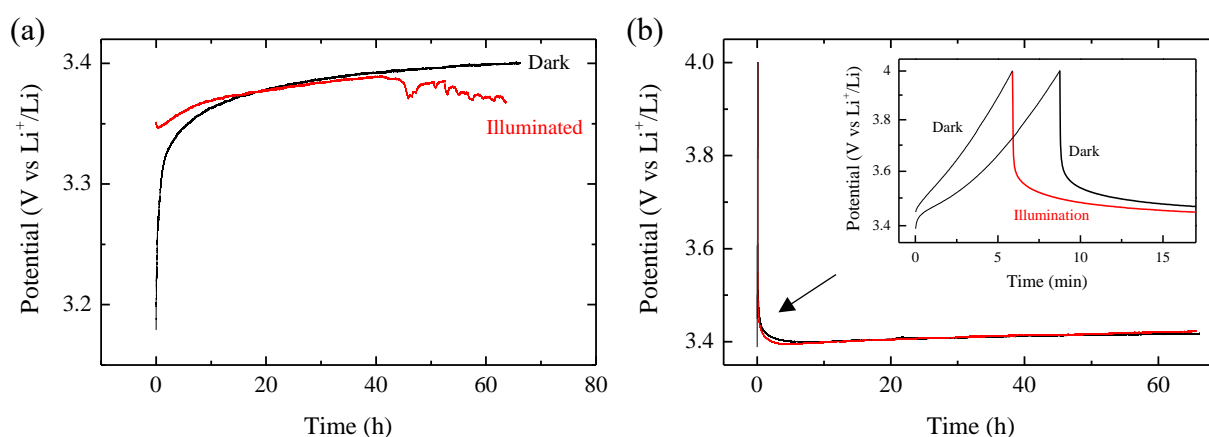


Figure 3.73. Evolution of open circuit potential in dark or under illumination under A.M. 1.5G conditions (a) from LiFePO₄ (b) from “FePO₄” obtained after galvanostatic charge to 4.0 V vs Li⁺/Li at 10 μA/cm².

The very low film activity is also reflected in the *in situ* UV-visible absorption spectroscopy experiments showing the evolution of the transmittance of the film as a function of the applied potential (Fig. 3.74). For this, the electrode was prepared by spin coating LiFePO₄ nanoparticles onto the FTO glass resulting in a ca. 300 nm thin film. The lithium insertion was performed by applying $j = 0.5 \mu\text{A}/\text{cm}^2$ current density and the transmission was recorded at different states of charge. No noticeable change in the transmission spectrum is observed depending on the applied potential. The main absorption bands are related to the electrolyte as discussed in chapter 2. This also suggest the very poor film electro-activity even using nanocrystalline particles and thinner films made by spin coating.

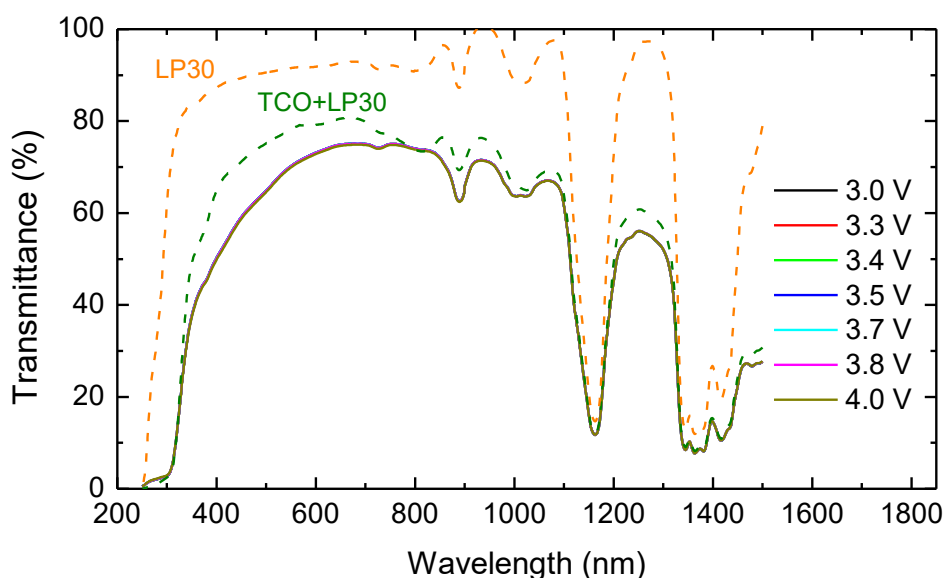


Figure 3.74. Evolution of the 300 nm thick nanoparticle LiFePO_4 film transmittance at different states of charge from 3.0 to 4.0 V vs. Li^+/Li . The transmittance spectra of the electrolyte (LP30) and transparent conducting glass (TCO) substrate of electrode in LP30 are provided for comparison.

We sensitized these nanoparticles with N719 dye. Figure 3.75 shows a comparison of the open circuit potential evolution of LiFePO_4 electrode in dark, under illumination, and under illumination when sensitized. Regardless of the electrode, there is no photorecharge process. There is an additional 20 mV when the film is sensitized, which is attributed to a photovoltage built-in from N719 excited states. This low compared to a dye-sensitized solar cells value indicates a very limited charge separation process induced by the low electronic coupling between the dye and LiFePO_4 . The triplet states of the N719 dye ($\text{LUMO} \approx -1.5$ V vs. NHE) can inject electrons into the conduction band of LiFePO_4 measured at -0.58 V vs. NHE, as determined in this thesis, but the dye cation formed after injection cannot be regenerated to its fundamental initial state (no redox mediator in electrolyte). It thus gives a clear clarification to the wrong charge transfer mechanism between LiFePO_4 and N719 presented by Paolella et al. [191].

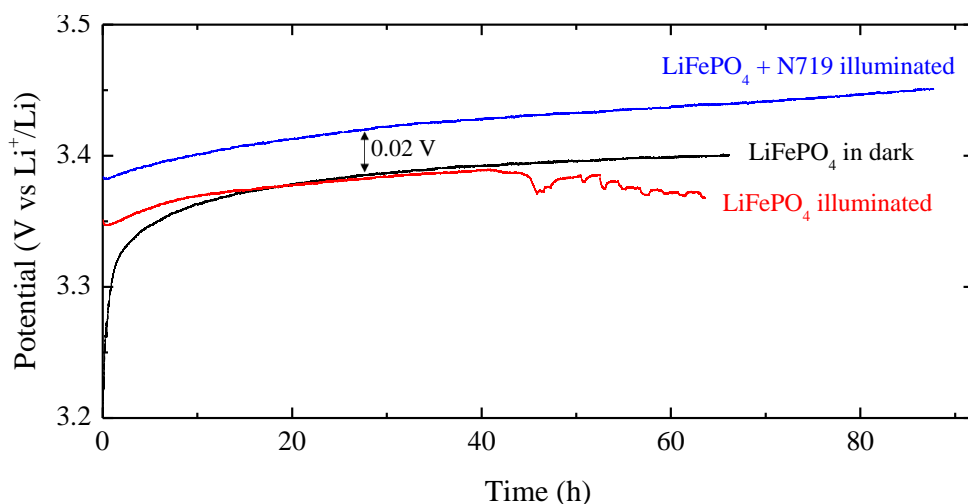


Figure 3.75. Evolution of the open circuit voltage of nanoparticles of LiFePO_4 measured in dark (black) and under standard A.M. 1.5G illumination conditions with (blue) or without (red) N719 dye.

One limitation of $\text{LiFePO}_4 / \text{FePO}_4$ system can also stem from the optoelectronic properties of the delithiated phase. For this, the iron phosphate was obtained by chemical oxidation of the lithium iron phosphate powder by means of a strong oxidizing agent [213]. First, 2 g of LiFePO_4 was added into a solution containing 3.36 g of NO_2BF_4 in 20 mL of acetonitrile. The mixture was stirred for four days at room temperature in an argon-filled glovebox to allow complete chemical oxidation of LiFePO_4 (800 to 1500 ppm of O_2 , 3.5 ppm of H_2O). The resulting powder was retrieved after three times centrifugation with acetonitrile. The XRD pattern of the resulting powder is presented in Figure 3.76. All diffraction peaks were indexed into Pnma space group in agreement with the heterosite FePO_4 phase without the presence of unoxidized LiFePO_4 . The lattice cell parameters are $a = 10.306(14) \text{ \AA}$, $b = 6.006(4) \text{ \AA}$ and $c = 4.704(7) \text{ \AA}$ ($V = 291 \text{ \AA}^3$), in agreement with literature [214-215].

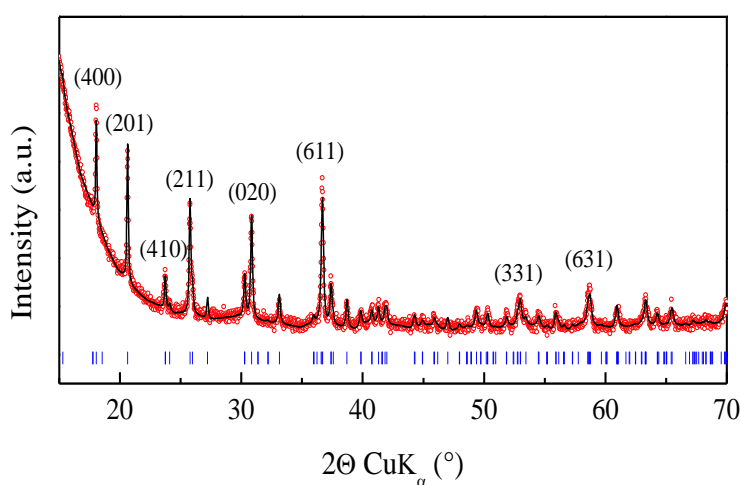


Figure 3.76. Full pattern matching refinement of the chemically obtained FePO_4 powder.

The band gap of FePO_4 was determined by UV-visible spectroscopy in diffuse reflectance mode (Fig. 3.77). The powder is highly reflective in the NIR part of the light, twice more than LiFePO_4 . Assuming an indirect allowed transition, we found a band gap value of 2.26 eV which is close to the range of values between 1.9 and 2.1 eV reported in literature based on DFT calculations [184, 216]. However, this value is not consistent with the light pink colour of the powder. Assuming a direct allowed transition as for LiFePO_4 , the onset of absorption is determined at 3.43 eV with a smaller transition at an energy of 2.73 eV that corresponds to the band gap value of FePO_4 . Lithium extraction leads then to a band gap narrowing of 0.58 eV.

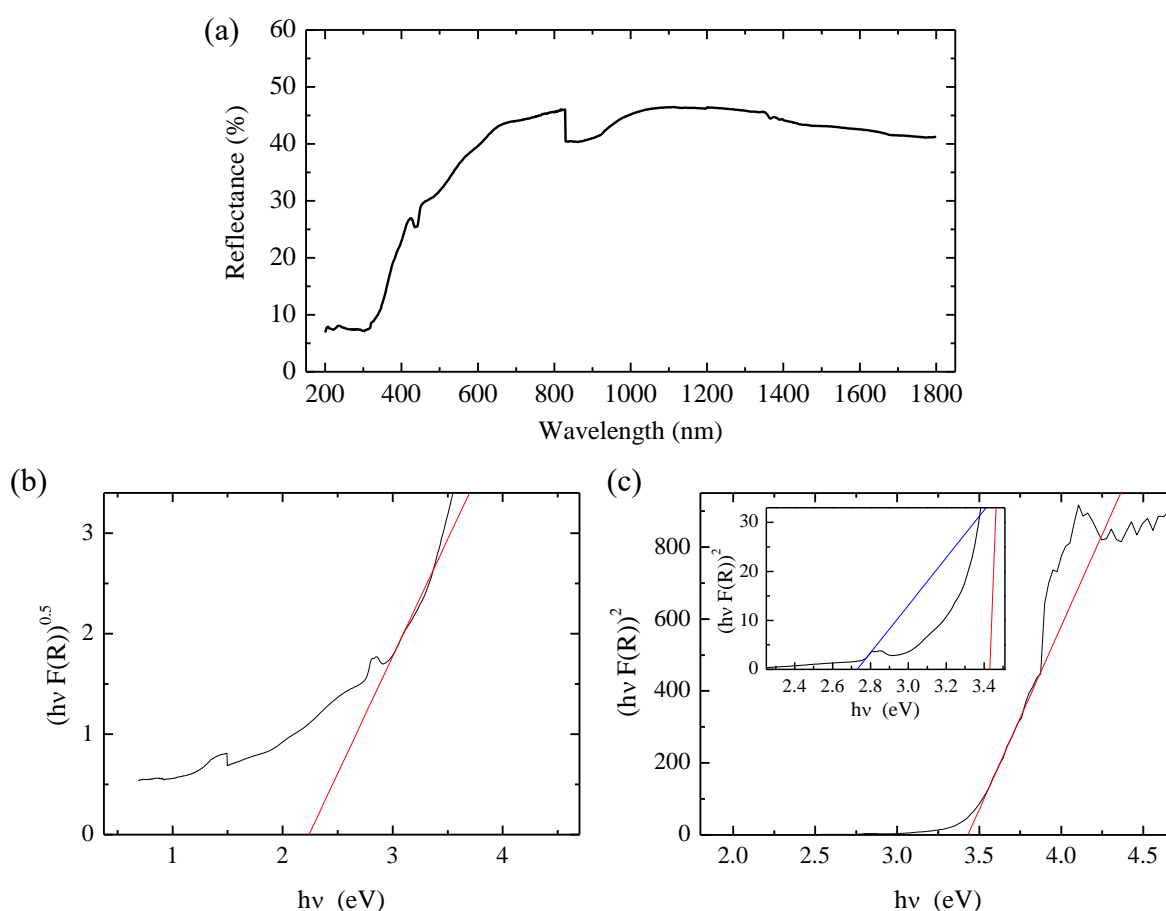


Figure 3.77. (a) Evolution of diffuse reflectance of the chemically obtained FePO_4 powder as a function of wavelength and corresponding Tauc plot assuming (b) an indirect allowed transition ($n=2$) and (c) a direct allowed transition ($n=0.5$).

With same procedure as previously described, we determined the band edge positions of FePO_4 by Mott-Schottky measurements in aqueous and non-aqueous aprotic electrolytes (Fig. 3.78). In both cases, the positive slope of the Mott-Schottky plot indicates that the material has a n-type conductivity as for LiFePO_4 in agreement with Zhu et al. [217]. Table 3.15 presents the

flat band potential and charge carrier concentration values. In an aqueous 0.5 mol/L TBANO₃ electrolyte, a flat band potential of -0.33 V vs. SCE was determined at pH = 6.1, which corresponds to -0.56 V vs. NHE at pH = 14. In a non-aqueous aprotic 1 mol/L TBAPF₆ EC/DMC electrolyte, the flat band potential value is equal to 2.36 V vs. Li QRE, corresponding to -0.83 V vs. NHE.

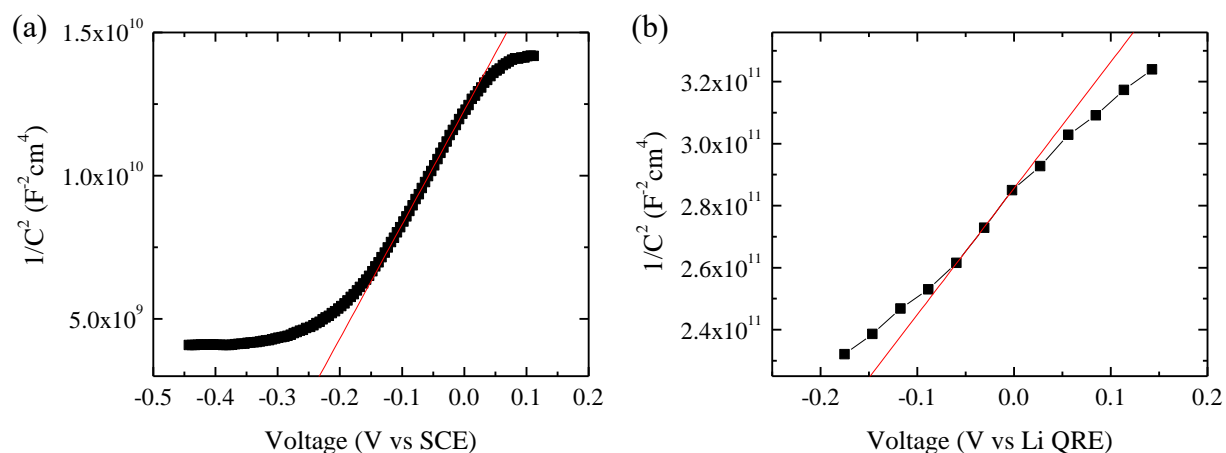


Figure 3.78. Mott-Schottky plot of $FePO_4$ measured in (a) 0.5 mol/L TBANO₃ aqueous electrolyte at 250 Hz and (b) 1 mol/L TBAPF₆ EC/DMC electrolyte at 200 Hz.

The charge carrier concentration was calculated with a dielectric constant of 30 as reported by Zhu et al. based on capacitance measurements [217]. In 0.5 mol/L TBANO₃ aqueous electrolyte, this latter was determined at $1.2 \cdot 10^{18} cm^{-3}$, and one order of magnitude higher in 1 mol/L TBAPF₆ in EC/DMC ($1.3 \cdot 10^{19} cm^{-3}$). These values are one order of magnitude lower than in LiFePO₄ in agreement with the literature stating that $FePO_4$ is more insulating than LiFePO₄ [217]. To the best of our knowledge, this is the first report of the flat band potential and charge carrier concentration in $FePO_4$.

Combining the flat band potential and the band gap values, the band edge positions were determined and compared to those of LiFePO₄ (Fig. 3.79). The results show that both conduction and valence band edges shift upwards in the energy scale upon lithium deinsertion. The delithiation of LiFePO₄ leads mainly to a destabilisation of the valence band position and lower effect on the conduction band position. This study shows clearly that N719 dye excited state (LUMO \approx -1.5 V vs. NHE) can inject into LiFePO₄ and $FePO_4$. It clarifies also the relative VB and CB position of $FePO_4$ which was wrongly speculated in the work of Paoletta et al. and also underlines that holes cannot be transferred from the dye (HOMO \approx 0.5 V vs. NHE) to the LiFePO₄ or $FePO_4$ [191].

Table 3.15. Flat band potential and charge carrier concentration of FePO_4 in 0.5 mol/L TBANO_3 aqueous electrolyte and 1 mol/L TBAPF_6 EC/DMC electrolyte.

Electrolyte	Flat band potential			Charge carrier concentration, cm^{-3}
	as measured	Recalculated		
		V vs. NHE	V vs. NHE at pH=14	
0.5 mol/L TBANO_3 in H_2O	-0.33 V vs. SCE	-0.09 (pH=6.1)	-0.56	$1.2 \cdot 10^{18}$
1 mol/L TBAPF_6 in EC/DMC	2.36 V vs. Li QRE	-0.83	-	$1.3 \cdot 10^{19}$

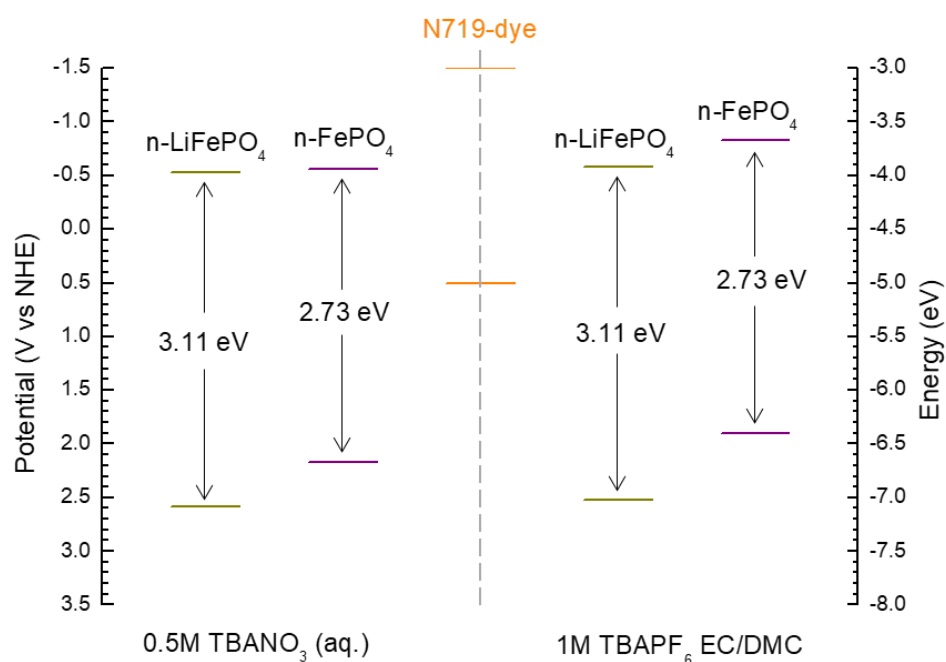


Figure 3.79. Energy diagram of the band edge positions of LiFePO_4 and FePO_4 measured in 0.5 mol/L TBANO_3 aqueous electrolyte and recalculated for $\text{pH} = 14$ (on the left), and in non-aqueous aprotic 1 mol/L TBAPF_6 EC/DMC-based electrolyte (on the right). The information on the HOMO and LUMO levels of N719-dye is provided for comparison [218].

3.5.3. $\text{Li}_4\text{Ti}_5\text{O}_{12}$

The kinetics of lithium insertion/deinsertion in the spinel $\text{Li}_4\text{Ti}_5\text{O}_{12}$ was investigated on 14 μm thick electrode by cycling voltammetry at different scan rates from 0.05 to 0.5 mV/s (Fig. 3.80). These experiments were performed under darkness and illumination. Higher scan rates lead to stronger kinetic limitations. Regardless of the scan rate, the degenerative influence of the light on the electrochemical cycling is observed. The small cathodic peak at around 2.3 V vs. Li^+/Li during the first cycle upon illumination is attributed to the filling of the surface trap states.

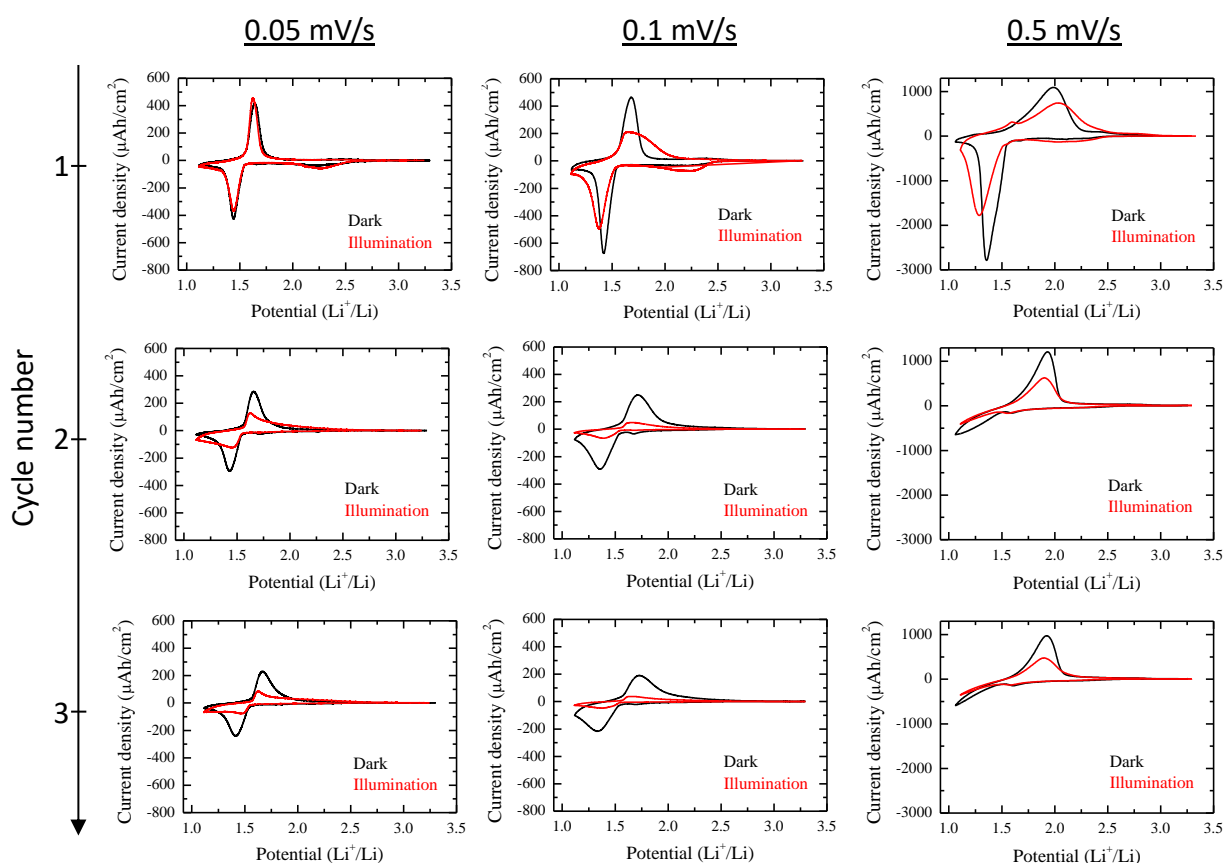


Figure 3.80. Comparison of the cyclic voltammograms of 14 μm thick $\text{Li}_4\text{Ti}_5\text{O}_{12}$ electrode measured in 1 mol/L LiPF_6 EC/DMC as a function of the scan rate from 0.05 to 0.5 mV/s (left to right) and cycle number (top down).

The comparison of the peak current density and capacity of the cyclic voltammograms in dark and under illumination is presented in Figure 3.81. For both conditions, a non-linear relationship between the current density and the scan rate or square root of scan rate suggests an intermediate behavior between capacitive and faradaic processes (Fig. 3.81 (a)). The comparable capacity of the film in dark and under illumination suggests that light has no or a negligible influence on film's capacity, even though systematically it leads to a lower peak current under illumination

(Fig. 3.81 (a-b)). Note that no significant influence of the light was observed neither on the energy of the peak separation nor on the global cell resistance extracted from the cyclic voltamperograms.

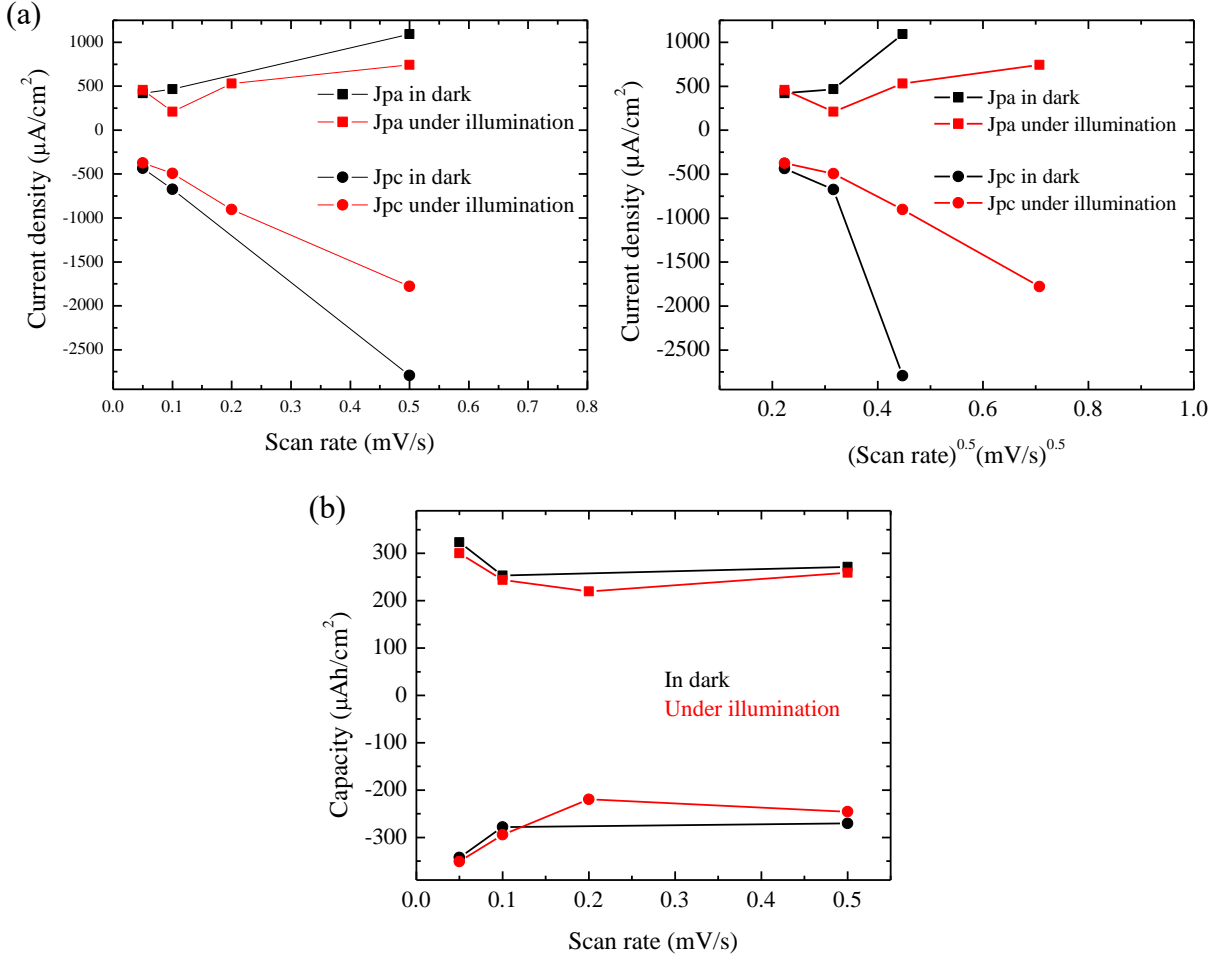


Figure 3.81. Evolution of (a) peak current density and (b) electrode capacity as a function of scan rate for a 14 μm thick $\text{Li}_4\text{Ti}_5\text{O}_{12}$ film in dark or under illumination.

Figure 3.82 (a) depicts the galvanostatic cycling of $\text{Li}_4\text{Ti}_5\text{O}_{12}$ electrode in dark and under illumination. Interestingly, we can observe that light illumination leads to a lower overpotential for the redox process at an applied current of $\pm 100 \mu\text{A}/\text{cm}^2$. This latter is more visible for the oxidation in agreement with the n-type character of $\text{Li}_4\text{Ti}_5\text{O}_{12}$. There is no drastic influence of light on the electrode's capacity in agreement with the presented above cyclic voltamperometry experiment. Nevertheless, as we also experienced in cyclic voltamperometry and for TiO_2 study, the electrode cyclability tends to fade faster when cycling under illumination. This is clearly showed by reporting the coulombic efficiency as a function of number of cycles (Figure 3.82 (b)). For the first cycle, the coulombic efficiency of the electrode

in dark and under illumination shows ca. 68-70%. The latter decreases nearly linearly in both conditions, however it declines more importantly under illumination reaching only 40% vs. ca. 50% under darkness after 10 cycles.

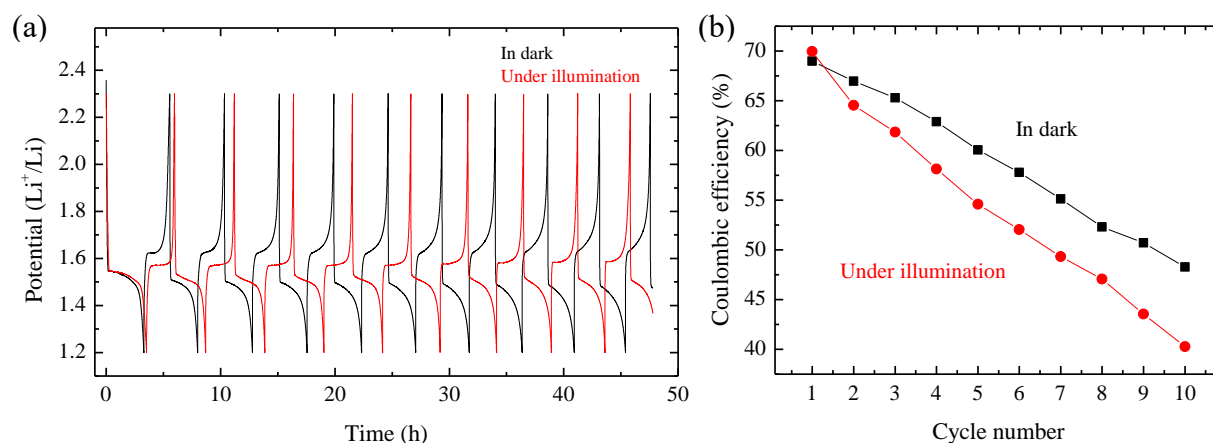


Figure 3.82. (a) Galvanostatic cycling of 13.5 μm thick $\text{Li}_4\text{Ti}_5\text{O}_{12}$ electrode versus lithium at 100 $\mu\text{A}/\text{cm}^2$ in dark or under illumination and (b) corresponding evolution of the coulombic efficiency as a function of cycle number.

To better understand this phenomenon, the TEM investigations were carried out and showed the formation of a SEI layer in both cases. Its thickness reaches up to 40 nm in dark and more than 50 nm under illumination with few isolated SEI parts, which can attain up to 100 nm (Fig. 3.83 (a-b)). This implies that the illumination of the electrode upon cycling promotes the formation of SEI. This was also observed for the samples cycled by cyclic voltamperometry. EELS analysis combined with electron diffraction study showed that the SEI layer formed under illumination is exclusively composed of LiF without any byproducts from carbonates decomposition as also deduced from Raman analysis of cycled electrodes.

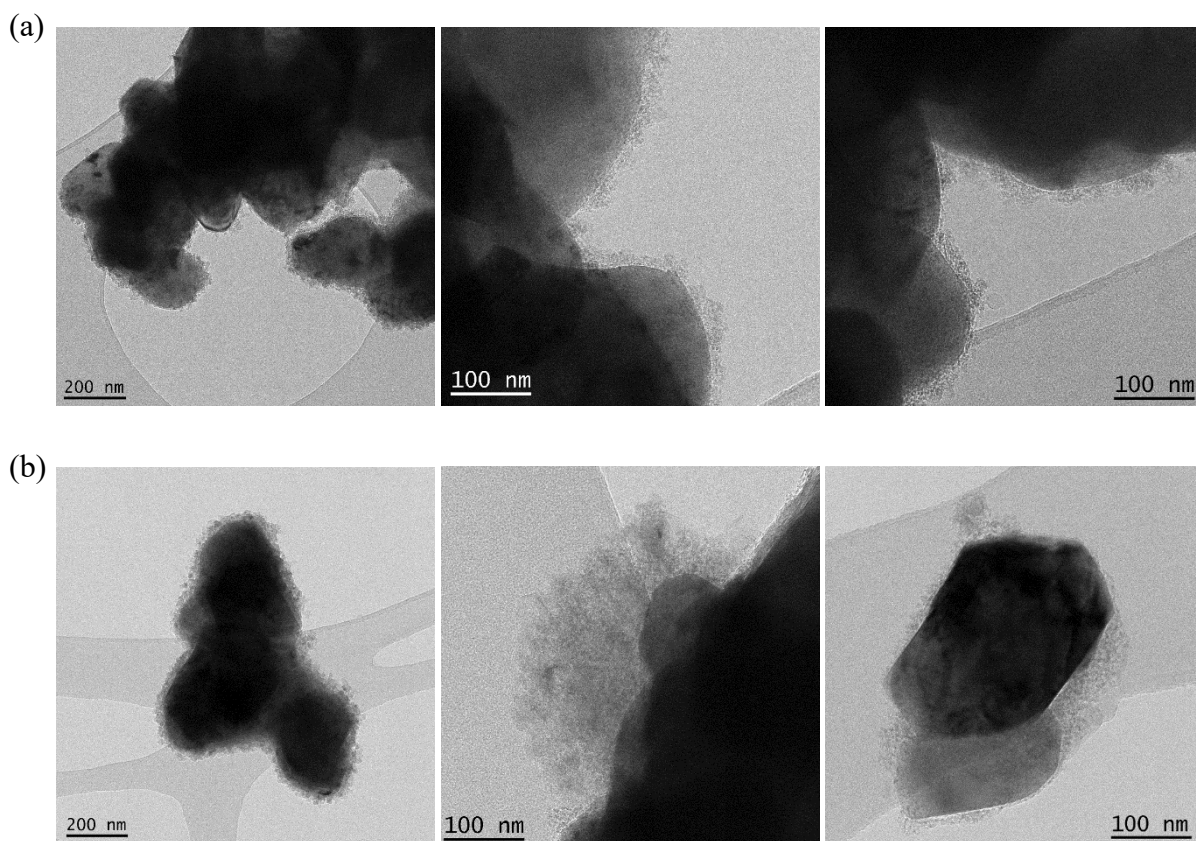


Figure 3.83. Transmission electron micrographs of $\text{Li}_4\text{Ti}_5\text{O}_{12}$ electrode after 10 cycles of galvanostatic cycling at $100 \mu\text{A}/\text{cm}^2$ (a) in dark and (b) under illumination.

Unfortunately, although the band structure allows a photorechargeable process, Figure 3.84 depicts the open circuit potential evolution of the discharged electrode down to 1.2 V vs. Li^+/Li in dark and under illumination, showing that the electrode cannot be photorecharged within 20 hours of light exposure. We can only see a faster rise of the electrode potential to equilibrium under illumination. After this time of relaxation, the subsequent discharge resulted in comparable capacity values of ca. $50 \mu\text{Ah}/\text{cm}^2$.

Time-correlated single-photon counting measurements of $\text{Li}_4\text{Ti}_5\text{O}_{12}$ electrode in 1 mol/L LiPF_6 EC/DMC electrolyte was performed under argon atmosphere using an EPL-375 picosecond pulsed diode laser at 2 MHz (Fig. 3.85). When compared to the lifetime decay of the $\text{Li}_4\text{Ti}_5\text{O}_{12}$ powder, a fluorescence quenching is experienced when in contact with the electrolyte. Indeed, it requires ca. 4 hours in electrolyte vs. ~ 1 hour for powder measurements. This means either that the contact with the electrolyte promotes non-radiative relaxation processes or that some carriers are transferred towards the electrolyte.

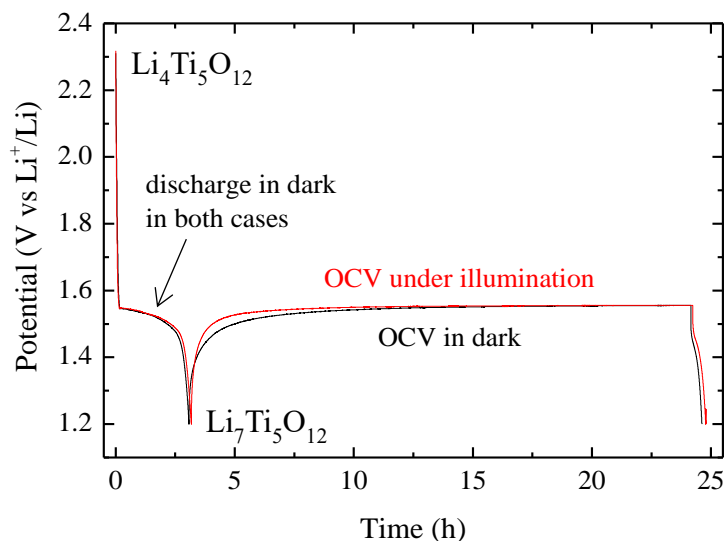


Figure 3.84. Galvanostatic discharge of 13.5 μm thick $\text{Li}_4\text{Ti}_5\text{O}_{12}$ electrodes in dark until 1.2 V (vs. Li^+/Li) at $-100 \mu\text{A}/\text{cm}^2$ followed by 21 hours of open-circuit relaxation either in dark (black curve) or under illumination (red curve), and subsequent discharge of the electrodes at $-100 \mu\text{A}/\text{cm}^2$ in dark.

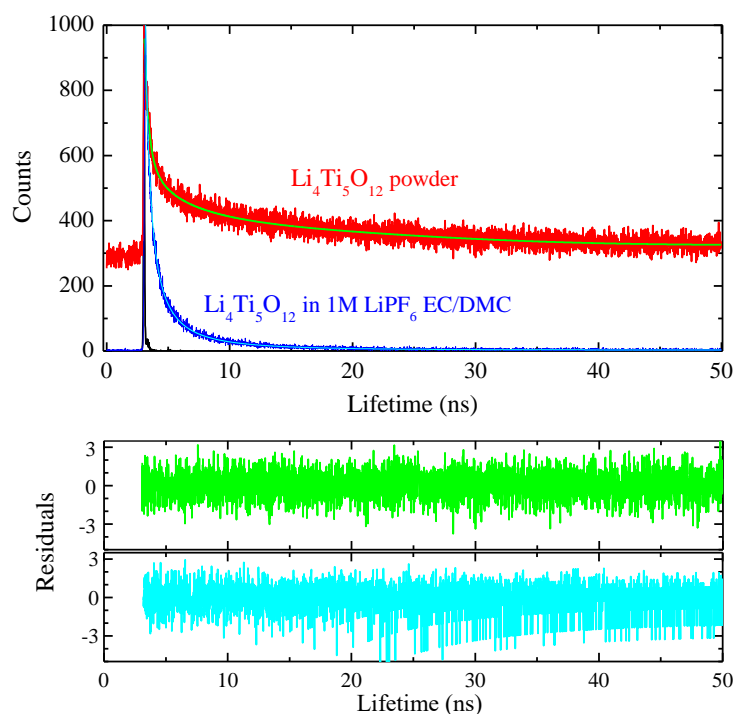


Figure 3.85. Comparison of the photoluminescence decay of $\text{Li}_4\text{Ti}_5\text{O}_{12}$ in contact with argon (red) and in contact with 1 mol/L LiPF_6 EC/DMC electrolyte (blue) recorded at 728 nm emission wavelength.

The results of the reconvolution of the lifetime decays with the IRF are gathered in Table 3.16. The lifetime values determined for $\text{Li}_4\text{Ti}_5\text{O}_{12}$ in contact with the electrolyte, i.e. 0.09 ns and

2.63 ns, are comparable with the first two components measured in contact with argon, i.e. 0.10 ns and 3.00 ns. The third very long component of 27.8 ns disappeared in contact with the electrolyte. The main difference comes from a redistribution of the lifetime values towards the fast component when in contact with the electrolyte (73.3 % in electrolyte vs. 6.9 % in argon). This confirms the quenching of $\text{Li}_4\text{Ti}_5\text{O}_{12}$ luminescence in the presence of LiPF_6 EC/DMC electrolyte.

Table 3.16. Reconvolution results of the time-correlated single photon counting decays recorded on $\text{Li}_4\text{Ti}_5\text{O}_{12}$ powder and $\text{Li}_4\text{Ti}_5\text{O}_{12}$ electrode in 1 mol/L LiPF_6 EC/DMC electrolyte.

	$\text{Li}_4\text{Ti}_5\text{O}_{12}$ powder			$\text{Li}_4\text{Ti}_5\text{O}_{12}$ electrode in 1 mol/L LiPF_6 EC/DMC		
	Pre-exponential factor B_i	Amplitude, %	Lifetime, ns	Pre-exponential factor B_i	Amplitude, %	Lifetime, ns
τ_1	0.572	6.9	0.10	0.395	73.3	0.09
τ_2	0.578	61.0	3.00	0.621	26.7	2.63
τ_3	2.752	32.1	27.87	-	-	-

The steady-state excitation/emission map of $\text{Li}_4\text{Ti}_5\text{O}_{12}$ electrode in 1 mol/L LiPF_6 EC/DMC electrolyte recorded over 250-700 nm excitation and 265-800 nm emission wavelengths is reported in figure 3.86 (a). It shows the presence of two bands. The high intensity band at 333 nm excitation and 735 nm emission wavelengths corresponds to the fluorescence of $\text{Li}_4\text{Ti}_5\text{O}_{12}$ (Fig. 3.86 (b)). However, when in contact with the electrolyte, the intensity of $\text{Li}_4\text{Ti}_5\text{O}_{12}$ emission drops tenfold due to the fluorescence quenching. The low intensity band at around 470 nm excitation and 520 nm emission wavelengths can be assigned to the tail of the electrolyte photoluminescence stemming from the solvated Li^+ and PF_6^- in EC/DMC (Fig. 3.86 (c)) [219]. Interestingly, the highest intensity band of 1 mol/L LiPF_6 EC/DMC electrolyte (LP30) located at 280 nm excitation and 310 nm emission wavelengths disappears completely when in contact with $\text{Li}_4\text{Ti}_5\text{O}_{12}$. This can be explained by a Förster resonance energy transfer (FRET) from the electrolyte to the electrode due to a partial overlapping of the electrolyte emission (centered at ca. 310 nm) with $\text{Li}_4\text{Ti}_5\text{O}_{12}$ excitation (excitation band at 333 nm).

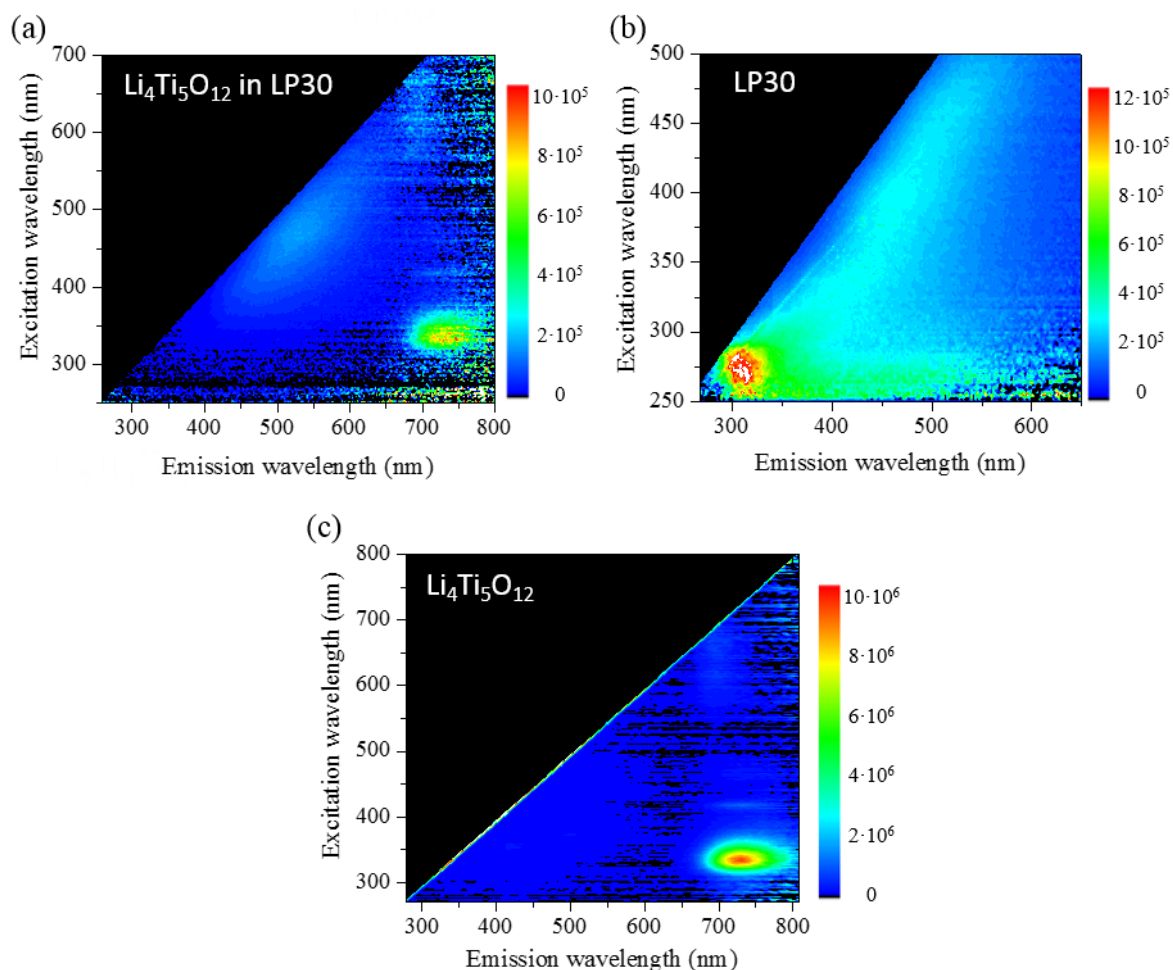


Figure 3.86. (a) Steady-state photoluminescence mapping of $\text{Li}_4\text{Ti}_5\text{O}_{12}$ powder in 1 mol/L LiPF_6 in EC/DMC electrolyte. The photoluminescence maps of (b) 1 mol/L LiPF_6 in EC/DMC electrolyte (LP30) and (c) $\text{Li}_4\text{Ti}_5\text{O}_{12}$ powder are provided for comparison.

Figure 3.87 presents the evolution of the emission spectra of $\text{Li}_4\text{Ti}_5\text{O}_{12}$ electrode in 1 mol/L LiPF_6 EC/DMC upon lithium insertion into the structure recorded *in situ* at 333 nm excitation wavelength. The emission spectrum of the fresh $\text{Li}_4\text{Ti}_5\text{O}_{12}$ electrode in 1 mol/L LiPF_6 EC/DMC at OCV has two emission bands: one at around 390 nm assigned to the electrolyte, and a second at 728 nm stemming from $\text{Li}_4\text{Ti}_5\text{O}_{12}$. Upon discharge down to 1.2 V vs. Li^+/Li , leading to $\text{Li}_7\text{Ti}_5\text{O}_{12}$, we observed a complete bleaching of the 728 nm emission band coming with a fluorescence decrease of the electrolyte at 390 nm. Because of this complete quenching, we have not been able to study the dynamics of the excited state of $\text{Li}_7\text{Ti}_5\text{O}_{12}$, which could have provided hints to explain if the absence of the photorecharge could be attributed to a too fast recombination dynamics. The quenching of the lithiated phase can stem either from the lithium insertion into $\text{Li}_4\text{Ti}_5\text{O}_{12}$ structure, too fast dynamics for the spectrometer, or from the formation of the LiF layer on the surface of the electrode, which completely quenches the luminescence. We argue that the two last

hypothesis are the most likely because: (i) the electrode recharge to 2.6 V vs. Li^+/Li does not allow retrieving the original luminescence signal of $\text{Li}_4\text{Ti}_5\text{O}_{12}$, even though there is a small irreversible capacity for the first recharge, which will still results in an electrode containing mostly $\text{Li}_4\text{Ti}_5\text{O}_{12}$ and a small part of $\text{Li}_7\text{Ti}_5\text{O}_{12}$; (ii) fluorescence of the chemically reduced $\text{Li}_7\text{Ti}_5\text{O}_{12}$ powder, which should not have a LiF layer, also shows a quenching of the luminescence (as well as that of the electrolyte). Note that the emission band of the electrolyte is partially but not totally retrieved during the electrode oxidation. This tends to suggest that the FRET mechanism might be more efficient in contact with $\text{Li}_7\text{Ti}_5\text{O}_{12}$.

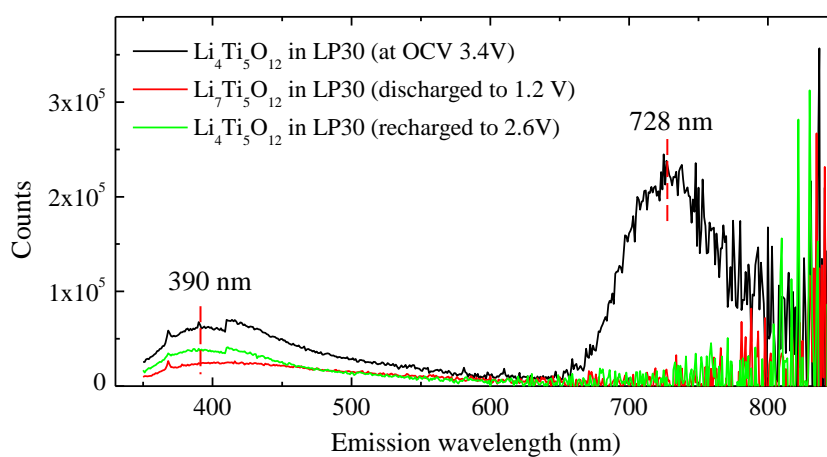


Figure 3.87. Evolution of the emission spectrum of $\text{Li}_4\text{Ti}_5\text{O}_{12}$ electrode in LiPF_6 EC/DMC recorded at 333 nm excitation wavelength in the initial state (OCV 3.4 V vs. Li^+/Li), discharged (1.2 V vs. Li^+/Li) and after first recharge (2.6 V vs. Li^+/Li).

The UV-visible absorption spectroscopy study of $\text{Li}_4\text{Ti}_5\text{O}_{12}$ in 1 mol/L LiPF_6 EC/DMC was carried out aiming at understanding the optical changes in $\text{Li}_4\text{Ti}_5\text{O}_{12}$ upon lithium insertion. For this, a semi-transparent 250 nm thick film of $\text{Li}_4\text{Ti}_5\text{O}_{12}$ was prepared by spin-coating on FTO glass and then discharged at $-10 \mu\text{A}/\text{cm}^2$. The transmittance spectra were recorded *in situ* at different states of discharge (Fig. 3.100 (a)). The changes in the transmission spectrum take place at 1.7 V vs. Li^+/Li and stay almost unaffected for all the potentials below. There is a significant decrease in the transmittance observed in a range from 300 nm to 1500 nm. The FTO glass absorbs all the light below 300 nm and all absorption bands are corresponding to the electrolyte fingerprint as detailed in chapter 2. The optical modifications are accompanied by a color change of the electrode turning from white to a dark blue. This is in agreement with the increase of absorbance in the visible and infra-red region as reported by Kanamura et al. [220].

This phenomenon is assigned to the absorption by the free carriers populating the conduction band. The derived Tauc plot assuming an indirect allowed transition shows that $\text{Li}_4\text{Ti}_5\text{O}_{12}$ has a band gap moving down to 3.48 eV when in contact with the electrolyte (Fig. 3.88 (b)). This is ca. 0.3 eV lower than the 3.79 eV determined for the powder in air. For the discharged to $\text{Li}_7\text{Ti}_5\text{O}_{12}$ composition electrode, the band gap decreases to 3.25 eV. It is assigned to the electron filling of the lower energy levels close to the conduction band (Ti^{3+} : ($4s^0 3d^1$) electronic configuration) [25].

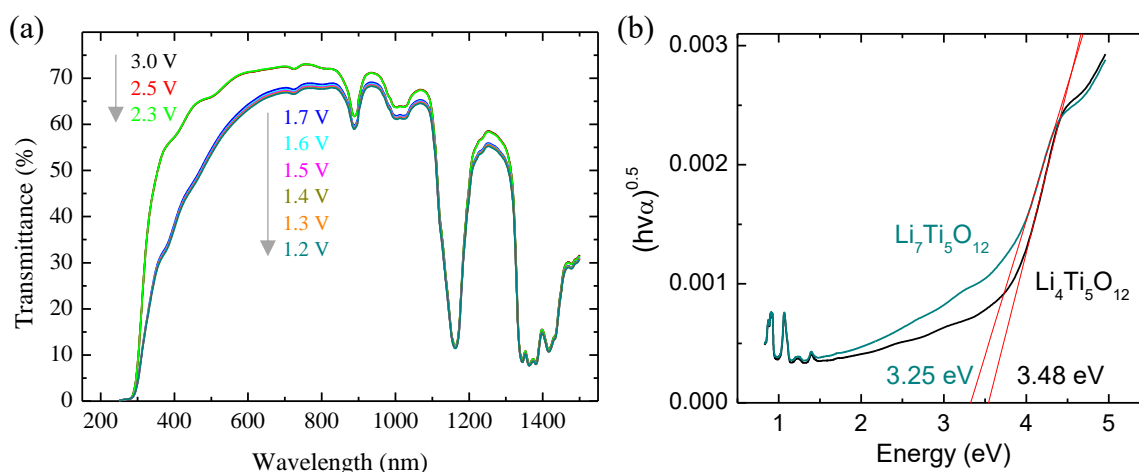


Figure 3.88. (a) Evolution of the transmittance spectrum of 250 nm thick film of $\text{Li}_4\text{Ti}_5\text{O}_{12}$ in 1 mol/L LiPF_6 in EC/DMC electrolyte as a function of lithium insertion at $-10 \mu\text{A}/\text{cm}^2$ and (b) Tauc plot of $\text{Li}_4\text{Ti}_5\text{O}_{12}$ (3.0 V spectrum) and its lithiated form $\text{Li}_7\text{Ti}_5\text{O}_{12}$ (1.2 V spectrum) assuming an indirect allowed transition.

The movement of the band edges and carrier concentration in $\text{Li}_4\text{Ti}_5\text{O}_{12}$ upon lithium insertion was investigated by Mott-Schottky measurements. For this, two types of electrodes were studied: a first directly measured in 1 mol/L TBAPF_6 EC/DMC corresponding to $\text{Li}_4\text{Ti}_5\text{O}_{12}$ and a second electrochemically discharged at $-100 \mu\text{A}/\text{cm}^2$ to 1.2 V vs. Li^+/Li in 1 mol/L LiPF_6 EC/DMC and then thoroughly washed with DMC before to be transferred in 1 mol/L TBAPF_6 EC/DMC electrolyte for the capacitance measurements. The corresponding Mott-Schottky plots are presented in Figure 3.89.

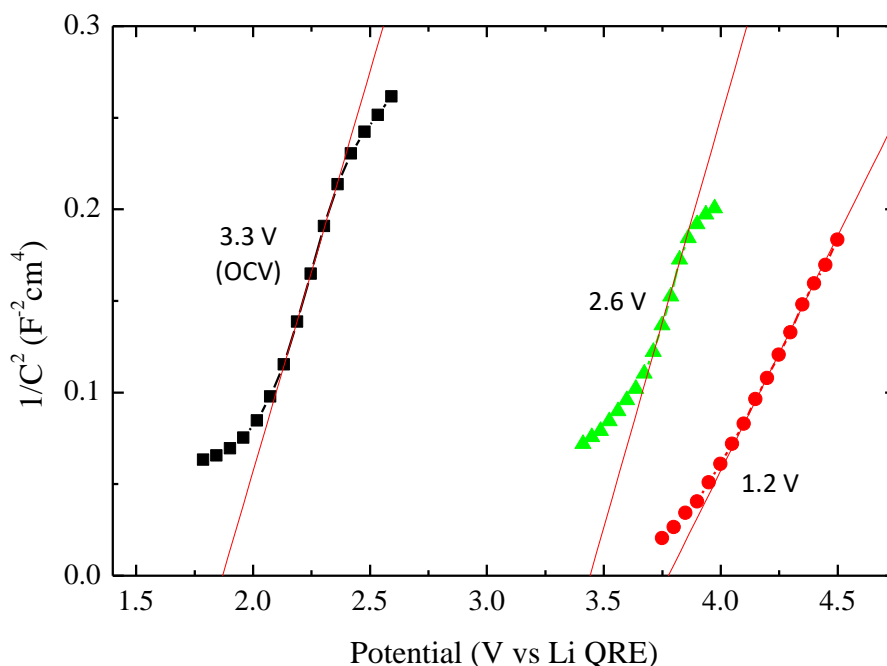


Figure 3.89. Evolution of Mott-Schottky analysis of $\text{Li}_4\text{Ti}_5\text{O}_{12}$ (3.3 V) and $\text{Li}_7\text{Ti}_5\text{O}_{12}$ (1.2 V) electrodes recorded at 200 kHz in 1 mol/L TBAPF₆ EC/DMC electrolyte. A recharged $\text{Li}_4\text{Ti}_5\text{O}_{12}$ (2.6 V) electrode is presented for additional information.

Table 3.17 gathers the information on the conductivity type, flat band potential and charge carrier concentration values. Regardless of the discharge state, the electrode remains n-type. For $\text{Li}_4\text{Ti}_5\text{O}_{12}$, the flat band potential is 1.91 V vs. Li QRE corresponding to - 1.28 V vs. NHE. Upon lithium insertion, the latter increases significantly to 3.60 V vs. Li QRE (+ 0.41 V vs. NHE). This means that upon lithium insertion, forming $\text{Li}_7\text{Ti}_5\text{O}_{12}$, the conduction band moves down by + 1.69 V in energy, which is hardly comprehensible based on the low structural modifications made by the lithium insertion. After electrode recharge, the flat band potential remains very close to $\text{Li}_7\text{Ti}_5\text{O}_{12}$, at 3.42 V vs. Li QRE (+ 0.23 V vs. NHE). This value cannot be solely explained by the first cycle irreversibility (coulombic efficiency ca. 65%). Most part of this irreversibility stems from the formation of LiF SEI layer. Based on these experiments, we argue that the band movement is not related to the lithium insertion. The important interfacial built-in capacitance is mainly controlled by the formation of LiF below 1.5 V vs. Li^+/Li . Note that a similar experiment has been carried out on pure FTO and the SEI formed on FTO. Even though the nature of the SEI is probably different on FTO, we found consistency with the results above, that the flat band potential of the FTO shifts up in potential by more than 1 V (Fig. 3.90 (a)).

Table 3.17. Conductivity type, flat band potential, and charge carrier concentration of $\text{Li}_4\text{Ti}_5\text{O}_{12}$ -based electrode measured at 200 kHz in 1 mol/L TBAPF_6 EC/DMC electrolyte under argon at initial state (OCV 3.4 V vs. Li^+/Li), discharged state down to 1.2 V vs. Li^+/Li and charge state after one cycle (2.6 V vs. Li^+/Li).

		$\text{Li}_4\text{Ti}_5\text{O}_{12}$	$\text{Li}_7\text{Ti}_5\text{O}_{12}$	$\text{Li}_4\text{Ti}_5\text{O}_{12}$ 1 cycle
Conductivity type		n	n	n
Flat band potential, V vs.	Li QRE	1.91	3.60	3.42
	NHE	-1.28	0.41	0.23
Charge carrier concentration, cm^{-3}		$2.9 \cdot 10^{19}$	$3.4 \cdot 10^{19}$	$2.4 \cdot 10^{19}$

The evolution of the charge carrier concentration was calculated using a dielectric constant of 6 [65] (Table 3.17). The initial $2.9 \cdot 10^{19} \text{ cm}^{-3}$ charge carrier concentration increases upon lithium insertion to only $3.4 \cdot 10^{19} \text{ cm}^{-3}$ whereas the literature reports a 6 orders of magnitude increase in conductivity between $\text{Li}_4\text{Ti}_5\text{O}_{12}$ and $\text{Li}_7\text{Ti}_5\text{O}_{12}$ [221]. This is an additional evidence that the interfacial capacitance become governed by LiF and not the insertion material anymore ($\epsilon \approx 10$ [222]). After the recharge, the charge carrier concentration decreases down to $2.4 \cdot 10^{19} \text{ cm}^{-3}$. The resulting donor density value is probably a combination of the charge carrier concentration of $\text{Li}_7\text{Ti}_5\text{O}_{12}$, which increases upon lithium insertion, and LiF. This would be also consistent with the carrier concentration measured on the SEI formed upon FTO, which is in same order of magnitude (Fig. 3.90 (b)).

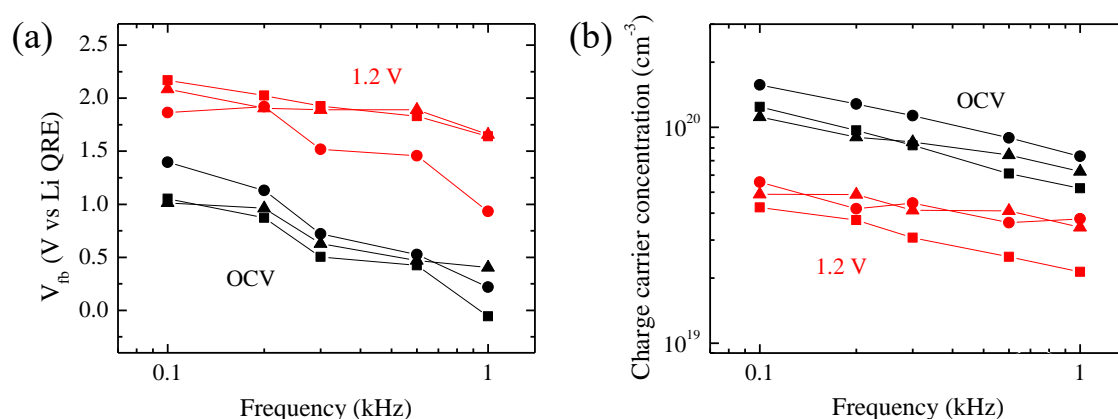


Figure 3.90. Frequency dependence of the (a) flat band potential and (b) the charge carrier concentration on pristine FTO glass (black line) and FTO glass discharged to 1.2 V vs. Li^+/Li for which SEI is formed on the surface (red line). The measurements were performed on three different samples between 100 Hz and 1 kHz in 1 mol/L TBAPF_6 EC/DMC electrolyte.

Conclusions

In this chapter, we focused on the development of a database gathering the optoelectronic properties of most common insertion materials used in lithium-ion batteries. The aim of this study was to decipher the materials, which can have perspective application in photorechargeable electrochemical device. Three groups of material were studied: transition metal oxides ($\text{Li}_4\text{Ti}_5\text{O}_{12}$, LiCoO_2 , MoO_3 , WO_3 , CuO , Bi_2O_3 , LiMn_2O_4 , $\text{LiMn}_{1/3}\text{Ni}_{1/3}\text{Co}_{1/3}\text{O}_2$), transition metal sulfides (TiS_2 , MoS_2 , WS_2), and lithiated polyanions (LiFePO_4 , LiMnPO_4 , LiVPO_4F).

All materials were characterized before studying the optoelectronic properties by using x-ray diffraction, scanning electron microscopy, and transmission electron microscopy techniques to ensure that materials are phase pure, lattice cell parameters to detect punctual defects, and evaluate size and morphology of the particles.

Using UV-visible absorption spectroscopy measurements in diffuse reflectance mode, the band gap values were determined. For a set of materials herein studied, we did not find optical bandgap likely owing to a too narrow band gap value below 0.7 eV (LiMn_2O_4 and $\text{LiMn}_{1/3}\text{Co}_{1/3}\text{Ni}_{1/3}\text{O}_2$) or to the semi-metallic nature of the material (TiS_2). We have identified that for all the materials, except $\text{Li}_4\text{Ti}_5\text{O}_{12}$, that the fluorescence cannot be measured in the range from 250 to 800 nm. This can be explained either by a band gap which is not in the visible range ($E_g < 1.6$ eV), an emission in the NIR region, or simply by materials' nature, which leads to exclusively non-radiative excited state relaxation.

By means of Mott-Schottky electrochemical impedance spectroscopy, we measured the type of conductivity, flat-band potential, and charge carrier concentration. In this chapter, three interesting phenomena are highlighted. First, for certain materials, i.e. LiCoO_2 , WS_2 , and MoS_2 , a change of semi-conduction type found depending on the nature of the electrolyte. More specifically, these materials are behaving as n-type semiconductor in aqueous electrolyte and turn p-type in non-aqueous aprotic EC/DMC-based electrolyte. This change is assigned to the weak degenerated nature of these semiconductors. Second, except the case of LiFePO_4 , all the materials have band edge positions that also depend on the nature of the solvent. Third, the charge carrier concentration is systematically higher in non-aqueous aprotic solution by one to two orders of magnitude, which means that materials can be “doped” depending on the electrolyte nature in contact through equilibrium process of Fermi level equalization.

Based on the band edge positions in EC/DMC-based electrolyte and the redox energy of the transition metal of the material, we deciphered materials which can or those which cannot trigger the Li^+ insertion / deinsertion from the structure by photo-induced minor carrier transfer. As a result, among all the materials herein studied, n-type $\text{Li}_4\text{Ti}_5\text{O}_{12}$, MoO_3 , WO_3 , Bi_2O_3 , LiFePO_4 , LiMnPO_4 and p-type LiCoO_2 are potential candidates for photorechargeable electrode application based on thermodynamic considerations. The p-type LiCoO_2 though should be discarded for application in a full device since p-type cathode material would lead to a photo-discharge process (i.e. lithium insertion under excited states).

In the second part of this chapter, we aimed to investigate the photo-electrochemical properties of some materials for the time being of this thesis. The first results clearly highlight the difficulties of this research field. Many materials, which were expected to have a photorecharge property did not express it, i.e. LiCoO_2 , $\text{Li}_4\text{Ti}_5\text{O}_{12}$, LiFePO_4 , Bi_2O_3 and MoO_3 (results for two latter are not reported in this manuscript). Besides the thermodynamic considerations, we think these difficulties are related to (i) the poor electronic conductivity of the electrode which leads to an excessive interfacial impedance value, (ii) the size of the particles which are often far from a threshold of few nanometers to lead to the Debye length comparable to particles radius, and (iii) faster excited state lifetimes compared to carrier transfer. Further research is therefore needed to point out which of these challenges is the most crucial to tackle. In addition, as showed in the case of LiCoO_2 and $\text{Li}_4\text{Ti}_5\text{O}_{12}$, the electrolyte's stability under electrodes excited states strongly limits the applicability of photorechargeable electrodes. We demonstrated for instance in the case of LiCoO_2 at excited states that this latter can be strongly photocatalytic towards the electrolyte's oxidation above 3.3 V vs. Li^+/Li or that LiF-SEI type formed at lower potential than 1.5 V vs. Li^+/Li totally quenches the excited state of the electrode ($\text{Li}_4\text{Ti}_5\text{O}_{12}$).

Even though the photorecharge was not observed in LiFePO_4 likely due to a too insulating nature of the electrode, we investigated further the possible reasons of its absence and potential solutions. Two strategies were attempted to overcome the possible obstacles: (i) decreasing the particle size to increase the electronic conductivity and (ii) grafting N719 dye on the particle's surface to increase light harvesting. None of these approaches led to noticeable improvements. However, this study enabled to discuss and clarify an important publication recently published in Nature Communication that we found very controversial in many aspects, more particularly in terms of type of semi-conduction in LiFePO_4 and FePO_4 , and, position of valence band and conduction band of these two semi-conductors with respect to N719 dye HOMO – LUMO levels. Our study enables to clarify the energy alignments and charge transfer processes under

illumination. Following this work, ps-transient absorption spectroscopy and time-resolved photoluminescence study are underway in the group to determine the rate constant of charge injection from the N719* into LiFePO_4 and FePO_4 conduction bands.

Even though we showed some kinetic improvements of the electrochemical processes of lithium insertion/deinsertion process in $\text{Li}_4\text{Ti}_5\text{O}_{12}/\text{Li}_7\text{Ti}_5\text{O}_{12}$ electrode, and faster reaching of equilibrium state under illumination, this spinel material did not express any sign of photorecharge neither. The in-depth study showed that on the one hand the $\text{Li}_7\text{Ti}_5\text{O}_{12}$ excited state may be ultrafast and faster compared to the carrier transfer, and on the other hand that SEI formation leading exclusively to insulating LiF on the electrode surface has an important influence in agreement with previous study on TiO_2 [219]. We showed by time-resolved fluorescence study that there is a strong quenching of electrolyte luminescence when including $\text{Li}_4\text{Ti}_5\text{O}_{12}$. This is explained by energy transfer via Förster resonance effect (FRET). This FRET mechanism is even more efficient for $\text{Li}_7\text{Ti}_5\text{O}_{12}$ owing to its band gap narrowing by 0.23 eV compared to $\text{Li}_4\text{Ti}_5\text{O}_{12}$ and its enhanced light absorption capability. The luminescence of $\text{Li}_4\text{Ti}_5\text{O}_{12}$ is also quenched when in contact with the electrolyte. The radiative part of the excited states relaxation is much accelerated. Unfortunately, we have not been able to study the radiative relaxation dynamics in $\text{Li}_7\text{Ti}_5\text{O}_{12}$ owing to the complete fluorescence quenching in this composition. Preliminary results that are not herein reported show that including a particular spin trap additive in the electrolyte can on the one hand significantly improve the electrode performance in capacity and reversibility without means of carbon and on the other hand enables to unlock the photorecharge barrier. An electrode of $\text{Li}_7\text{Ti}_5\text{O}_{12}$ can be completely photo-recharged in about 15 hours under standard A.M. 1.5G conditions (capacity of ca. $500 \mu\text{Ah}/\text{cm}^2$). A patent for the molecule included into the electrolyte is currently under filling process. We hypothesize that a function of this molecule is to avoid the formation of LiF upon discharge and under illumination, and it may also play a role in promoting the carriers transfer towards the transition metal.

References

- [1] A. Fujishima and K. Honda, *Nature*, **1972**, 238, 5358, 37.
- [2] T. Hisatomi, J. Kubota, and K. Domen, *Chem. Soc. Rev.*, **2014**, 43, 22, 7520.
- [3] K. Sivula and R. van de Krol, *Nat. Rev. Mater.*, **2016**, 15010.
- [4] A. Mills and S. Le Hunte, *J. Photochem. Photobiol. A Chem.*, **1997**, 108, 1, 1.
- [5] Y. Xu and M. A. A. Schoonen, *Am. Mineral.*, **2000**, 85, 3, 543.
- [6] M. D. Archer and A. J. Nozik, *Nanostructured and Photoelectrochemical Systems for Solar Photon Conversion*. London: Imperial College Press, **2008**.
- [7] S. R. Morrison, *Electrochemistry at semiconductor and oxidized metal electrodes*. New York: Plenum Press, **1980**.
- [8] Y. V. Pleskov and Y. Y. Gurevich, *Semiconductor photoelectrochemistry*. New York: Consultant Bureau, **1986**.
- [9] J. Schneider, M. Matsuoka, M. Takeuchi, J. Zhang, Y. Horiuchi, M. Anpo, D. W. Bahnemann, *Chem. Rev.*, **2014**, 114, 9919.
- [10] S. Basu, "Rechargeable battery", US4304825A, **1981**.
- [11] T. Morikawa, R. Asahi, T. Ohwaki, K. Aoki, Y. Taga, *Jpn. J. Appl. Phys.*, **2001**, 40, 561.
- [12] T. Umebayashi, T. Yamaki, H. Itoh, K. Asai, *Appl. Phys. Lett.*, **2002**, 81, 454.
- [13] X. H. Wang, J.G. Li, H. Kamiyama, M. Katada, N. Ohashi, Y. Moriyoshi, T. Ishigaki, *J. Am. Chem. Soc.*, **2005**, 127, 10982.
- [14] C. Gutierrez, P. Salvador, *J. Electroanal. Chem. Interfacial Electrochem.*, **1982**, 138, 457.
- [15] G. Redmond, D. Fitzmaurice, *J. Phys. Chem.*, **1993**, 97, 1426.
- [16] T. Ohzuku, A. Ueda, N. Yamamoto, *J. Electrochem. Soc.*, **1995**, 142, 1431.
- [17] K. Zaghib, M. Simoneau, M. Armand, M. Gauthier, *J. Power Sources*, **1999**, 81, 300.
- [18] C. H. Chen, J. T. Vaughey, A. N. Jansen, D. W. Dees, A. J. Kahaian, T. Goacher, M. M. Thackeray, *J. Electrochem. Soc.*, **2001**, 148, 102.
- [19] M. Wagemaker, E. R. H. van Eck, A. P. M. Kentgens, F. M. Mulder, *J. Phys. Chem. B*, **2009**, 113, 224.
- [20] O. Dolotko, A. Senyshyn, M. J. Mühlbauer, H. Boysen, M. Monchak, H. Ehrenberg, *Solid State Sci.*, **2014**, 36, 101.
- [21] P.-E. Lippens, M. Womes, P. Kubiak, J.-C. Jumas, J. Olivier-Fourcade, *Solid State Sci.*, **2004**, 6, 161.

- [22] C. Y. Ouyang, Z. Y. Zhong, M. S. Lei, *Electrochem. Commun.*, **2007**, 9, 1107.
- [23] H. Song, S.W. Yun, H.H. Chun, M.G. Kim, K.Y. Chung, H.S. Kim, B.W. Cho, Y.T. Kim, *Energy Environ. Sci.*, **2012**, 5, 9903.
- [24] Z. Ding, L. Zhao, L. Suo, Y. Jiao, S. Meng, Y.-S. Hu, Z. Wang, L. Chen, *Phys. Chem. Chem. Phys.*, **2011**, 13, 15127.
- [25] M. G. Verde, L. Baggetto, N. Balke, G. M. Veith, J. K. Seo, Z. Wang, Y. S. Meng, *ACS Nano*, **2016**, 10, 4312.
- [26] H. Ge, H. Tian, H. Song, D. Liu, S. Wu, X. Shi, X. Gao, L. Lv, X.-M. Song, *Mater. Res. Bull.*, **2015**, 61, 459.
- [27] T. Kostlánová, J. Dědeček, P. Krtíl, *Electrochim. Acta*, **2007**, 52, 1847.
- [28] Y.-R. Jhan, J.-G. Duh, *Electrochim. Acta*, **2012**, 63, 9.
- [29] C. Kim, N.S. Norberg, A.T. Caleb, R. Kostecki, J. Cabana, *Adv. Funct. Mater. Adv. Funct. Mater.*, **2012**, 23, 1214.
- [30] E. Kasper, Alternative Ge Applications. *Germanium-Based Technologies* / ed. by C. Claeys, E. Simoen, Oxford: Elsevier, **2007**, 387–415.
- [31] K. Rajkanan, R. Singh, J. Shewchun, *Solid State Electron.*, **1979**, 22, 793.
- [32] K. M. Reddy, S. V. Manorama, A. Ramachandra Reddy, *Mater. Chem. Phys.*, **2003**, 78, 239.
- [33] G. G. Macfarlane, T. P. McLean, J. E. Quarrington, V. Roberts, *Phys. Rev.*, **1958**, 111, 1245.
- [34] Y. Zhao, Y. Ding, X. Chen, W. Yang, *Sens. Actuator B-Chem.*, **2014**, 203, 122.
- [35] J. Zhang, R. Zuo, Y. Wang, S. Qi, *Mater. Lett.*, **2016**, 164, 353.
- [36] C. Liu, H. Zhang, H. Su, L. Jin, J. Li, Y. Liao, L. Jia, Y. Li, *Mod. Phys. Lett. B*, **2016**, 30, 1650287.
- [37] L. Wen, G. Liu, G.-Y. Liu, G. Liu, F. Li, H.-M. Cheng, *J. Chin. Chem. Soc.*, **2012**, 59, 1201.
- [38] K. Mizushima, P. C. Jones, P. J. Wiseman, J. B. Goodenough, *Mater. Res. Bull.*, **1980**, 15, 783.
- [39] R. Yazami, N. Lebrun, M. Bonneau, M. Molteni, *J. Power Sources*, **1995**, 54, 389.
- [40] E. Shinova, Ts. Mandzhukova, E. Grigorova, M. Hristov, R. Stoyanova, D. Nihtianova, E. Zhecheva, *Solid State Ion.*, **2011**, 187, 43.
- [41] M. C. Rao, *Int. J. Pure Appl. Phys.*, **2010**, 6, 365.
- [42] J. M. Rosolen, F. Decker, *J. Electroanal. Chem.*, **2001**, 501, 253.
- [43] H. Tukamoto, A. R. West, *J. Electrochem. Soc.*, **1997**, 144, 3164.

- [44] M. Menetrier, I. Saadoune, S. Levasseur, C. Delmas, *J. Mater. Chem.*, **1999**, 9, 1135.
- [45] F. Khatun, M. A. Gafur, M. S. Ali, M. S. Islam, M. a. R. Sarker, *J. Sci. Res.*, **2014**, 6, 217.
- [46] B. Nageswara Rao, M. Venkateswarlu, N. Satyanarayana, *Ionics*, **2014**, 20, 175.
- [47] A. Mizutani, K. Sugiura, H. Ohta, K. Koumoto, *Cryst. Growth Des.*, **2008**, 8, 755.
- [48] F. W. Dampier, *J. Electrochem. Soc.*, **1974**, 121, 656.
- [49] M. S. Whittingham, *J. Electrochem. Soc.*, **1976**, 123, 315.
- [50] C. Julien, G. A. Nazri, *Solid State Ion.*, **1994**, 68, 111.
- [51] L. Q. Mai, B. Hu, W. Chen, Y. Y. Qi, C. S. Lao, R. S. Yang, Y. Dai, Z. L. Wang, *Adv. Mater.*, **2007**, 19, 3712.
- [52] V. V. Atuchin, T. A. Gavrilova, T. I. Grigorieva, N. V. Kuratieva, K. A. Okotrub, N. V. Pervukhina, N. V. Surovtsev, *J. Cryst. Growth*, **2011**, 318, 987.
- [53] M. Anwar, C. A. Hogarth, *Phys. Status Solidi A*, **1988**, 109, 469.
- [54] Y. Zhao, J. Liu, Y. Zhou, Z. Zhang, Y. Xu, H. Naramoto, S. Yamamoto, *J. Phys.: Condens. Matter*, **2003**, 15, L547.
- [55] A. Chithambararaj, A. C. Bose, *J. Alloys. Compd.*, **2011**, 509, 8105.
- [56] M. Itoh, K. Hayakawa, S. Oishi, *J. Phys. Condens. Matter.*, **2001**, 13, 6853.
- [57] D. O. Scanlon, G. W. Watson, D. J. Payne, G. R. Atkinson, R. G. Egdell, D. S. L. Law, *J. Phys. Chem. C*, **2010**, 114, 4636.
- [58] M. Kroger, S. Hamwi, J. Meyer, T. Riedl, W. Kowalsky, A. Kahn, *Appl. Phys. Lett.*, **2009**, 95, 123301.
- [59] E. C. Dutoit, R. L. Van Meirhaeghe, F. Cardon, W. P. Gomes, *Berichte der Bunsengesellschaft für physikalische Chemie*, **1975**, 79, 1206.
- [60] A. Fujishima, A. Sakamoto, K. Honda, *Seisan-Kenkyu*, **1969**, 21, 450.
- [61] X. Tong, B. E. Lassiter, S. R. Forrest, *Org. Electron.*, **2010**, 11, 705.
- [62] J. Meyer, R. Khalandovsky, P. Görrn, A. Kahn, *Adv. Mater.*, **2011**, 23, 70.
- [63] J. C. Bernède, S. Houari, D. Nguyen, P. Y. Jouan, A. Khelil, A. Mokrani, L. Cattin, P. Predeep, *Phys. Status Solidi A*, **2012**, 209, 1291.
- [64] M. T. Greiner, M. G. Helander, Z. B. Wang, W. M. Tang, J. Qiu, Z. H. Lu, *Appl. Phys. Lett.*, **2010**, 96, 213302.
- [65] L. Lajaunie, F. Boucher, R. Dessapt, P. Moreau, *Phys. Rev. B*, **2013**, 88, 115141.
- [66] G. S. Nadkarni, J. G. Simmons, *J. Appl. Phys.*, **1972**, 43, 3650.
- [67] G. S. Nadkarni, J. G. Simmons, *J. Appl. Phys.*, **1970**, 41, 545.
- [68] J. S. E. M. Svensson, C. G. Granqvist, *Thin Solid Films*, **1985**, 126, 31.

- [69] M. Akiyama, J. Tamaki, N. Miura, N. Yamazoe, *Chem. Lett.*, **1991**, 20, 1611.
- [70] M. Green, W. C. Smith, J. A. Weiner, *Thin Solid Films*, **1976**, 38, 89.
- [71] A. Sclafani, L. Palmisano, G. Marci, A. M. Venezia, *Sol. Energy Mater. Sol. Cells.*, **1998**, 51, 203.
- [72] R. Abe, H. Takami, N. Murakami, B. Ohtani, *J. Am. Chem. Soc.*, **2008**, 130, 7780.
- [73] M. Yu, H. Sun, X. Sun, F. Lu, T. Hu, G. Wang, H. Qiu, J. Lian, *Mater. Lett.*, **2013**, 108.
- [74] S. Tanisaki, *J. Phys. Soc. Jpn.*, **1960**, 15, 573.
- [75] G. R. Bamwenda, K. Sayama, H. Arakawa, *J. Photochem. Photobiol. A Chem.*, **1999**, 122, 175.
- [76] J. Kleperis, J. Zubkans, A. R. Lasis, *International Conference on Advanced Optical Materials and Devices proceedings*, International Society for Optics and Photonics, **1997**, 186.
- [77] H. Yan, X. Zhang, S. Zhou, X. Xie, Y. Luo, Y. Yu, *J. Alloys. Compd.*, **2011**, 509, L232.
- [78] D. G. Barton, M. Shtein, R. D. Wilson, S. L. Soled, E. Iglesia, *J. Phys. Chem. B*, **1999**, 103, 630.
- [79] K. J. Lethy, D. Beena, R. Vinod Kumar, V. P. Mahadevan Pillai, V. Ganesan, V. Sathe, *Appl. Surf. Sci.*, **2008**, 254, 2369.
- [80] G. Wang, Y. Ling, H. Wang, X. Yang, C. Wang, J. Z. Zhang, Y. Li, *Energy Environ. Sci.*, **2012**, 5, 6180.
- [81] P. S. Patil, P. R. Patil, *Sol. Energy Mater. Sol. Cells.*, **1994**, 33, 293.
- [82] W. Gissler, R. Memming, *J. Electrochem. Soc.*, **1977**, 124, 1710.
- [83] H. Wang, X. Dong, S. Peng, L. Dong, Y. Wang, *J. Alloys. Compd.*, **2012**, 527, 204.
- [84] Q. Pan, H. Jin, H. Wang, G. Yin, *Electrochim. Acta*, **2007**, 53, 951.
- [85] J. Morales, L. Sánchez, F. Martín, J. R. Ramos-Barrado, M. Sánchez, *Electrochim. Acta*, **2004**, 49, 4589.
- [86] N. V. P. Chaudhary, J. K. Murthy, A. Venimadhav, *Solid State Commun.*, **2016**, 247, 36.
- [87] Y. K. Jeong, G. M. Choi, *J. Phys. Chem. Solids*, **1996**, 57, 81.
- [88] F. P. Koffyberg, F. A. Benko, *J. Appl. Phys.*, **1982**, 53, 1173.
- [89] K. Nakaoka, J. Ueyama, K. Ogura, *J. Electrochem. Soc.*, **2004**, 151, C661.
- [90] C.-Y. Chiang, Y. Shin, S. Ehrman, *J. Electrochem. Soc.*, **2011**, 159, B227.
- [91] D. Chauhan, V. R. Satsangi, S. Dass, R. Shrivastav, *Bull. Mater. Sci.*, **2006**, 29, 709.

- [92] A. A. Radhakrishnan, B. B. Beena, *Indian Journal of Advances in Chemical Science*, **2014**, 2, 158.
- [93] M. Umadevi, A. Jegatha Christy, *Spectrochim. Acta A Mol. Biomol. Spectrosc.*, **2013**, 109, 133.
- [94] K. L. Hardee, A. J. Bard, *J. Electrochem. Soc.*, **1977**, 124, 215.
- [95] W. Zuo, W. Zhu, D. Zhao, Y. Sun, Y. Li, J. Liu, X. W. (David) Lou, *Energy Environ. Sci.*, **2016**, 9, 2881.
- [96] O. Madelung, U. Rössler, M. Schulz (ed.), *Non-Tetrahedrally Bonded Elements and Binary Compounds I*, Berlin: Springer Berlin Heidelberg, **1998**.
- [97] S. K. Blower, C. Greaves, *Acta Crystallogr. C*, **1988**, 44, 587.
- [98] K. C. Chitrada, K. S. Raja, R. Gakhar, D. Chidambaram, *J. Electrochem. Soc.*, **2015**, 162, H380.
- [99] M. Schlesinger, M. Weber, S. Schulze, M. Hietschold, M. Mehring, *ChemistryOpen*, **2013**, 2, 146.
- [100] Y. Lu, Y. Zhao, J. Zhao, Y. Song, Z. Huang, F. Gao, N. Li, Y. Li, *Cryst. Growth Des.*, **2015**, 15, 1031.
- [101] Y. Yan, Z. Zhou, Y. Cheng, L. Qiu, C. Gao, J. Zhou, *J. Alloys. Compd.*, **2014**, 605, 102.
- [102] X. Yang, X. Lian, S. Liu, G. Wang, C. Jiang, J. Tian, J. Chen, R. Wang, *J. Phys. D: Appl. Phys.*, **2012**, 46, 035103.
- [103] X. Yang, X. Lian, S. Liu, C. Jiang, J. Tian, G. Wang, J. Chen, R. Wang, *Appl. Surf. Sci.*, **2013**, 282, 538.
- [104] Z. Liang, Y. Cao, Y. Li, J. Xie, N. Guo, D. Jia, *Appl. Surf. Sci.*, **2016**, 390, 78.
- [105] P. Hajra, S. Shyamal, H. Mandal, P. Fageria, S. Pande, C. Bhattacharya, *Electrochim. Acta*, **2014**, 123, 494.
- [106] K. C. Chitrada, K. S. Raja, *ECS Trans.*, **2014**, 61, 55.
- [107] S. W. Kang, S. W. Rhee, *Thin Solid Films*, **2004**, 468, 79.
- [108] K. C. Chitrada, K. S. Raja, *ECS Trans.*, **2014**, 61, 1.
- [109] M. M. Thackeray, P. J. Johnson, L. A. de Picciotto, P. G. Bruce, J. B. Goodenough, *Mater. Res. Bull.*, **1984**, 19, 179.
- [110] D. Guyomard, J. M. Tarascon, *J. Electrochem. Soc.*, **1992**, 139, 12.
- [111] K. Mukai, J. Sugiyama, K. Kamazawa, Y. Ikedo, D. Andreica, A. Amato, *J. Solid State Chem.*, **2011**, 184, 1096.

- [112] J. Nouri, T. Khoshravesh, S. Khanahmadzadeh, A. Salehabadi, M. Enhessari, *Int. J. Nano Dimens.*, **2016**, 7, 15.
- [113] C. Ouyang, H. Deng, Z. Ye, M. Lei, L. Chen, *Thin Solid Films*, **2006**, 503, 268.
- [114] G. E. Grechnev, R. Ahuja, B. Johansson, O. Eriksson, *Phys. Rev. B*, **2002**, 65, 174408.
- [115] H. Berg, K. Göransson, B. Noläng, J. O. Thomas, *J. Mater. Chem.*, **1999**, 9, 2813.
- [116] T. Ohzuku, Y. Makimura, *Chem. Lett.*, **2001**, 30, 642.
- [117] M. M. Thackeray, S.-H. Kang, C. S. Johnson, J. T. Vaughey, R. Benedek, S. A. Hackney, *J. Mater. Chem.*, **2007**, 17, 3112.
- [118] S. Muhammad, S. Lee, H. Kim, J. Yoon, D. Jang, J. Yoon, J.-H. Park, W.-S. Yoon, *J. Power Sources*, **2015**, 285, 156.
- [119] M. S. Whittingham, *Chem. Rev.*, **2004**, 104, 4271.
- [120] M. Winter, J. O. Besenhard, M. E. Spahr, P. Novák, *Adv. Mater.*, **1998**, 10, 725.
- [121] A. H. Thompson, *Phys. Rev. Lett.*, **1975**, 35, 1786.
- [122] E. M. Logothetis, W. J. Kaiser, C. A. Kukkonen, S. P. Faile, R. Colella, J. Gambold, *Physica B+C*, **1980**, 99, 193.
- [123] M. J. McKelvy, W. S. Glaunsinger, *J. Solid State Chem.*, **1987**, 66, 181.
- [124] C. Umrigar, D. E. Ellis, D.-S. Wang, H. Krakauer, M. Posternak, *Phys. Rev. B*, **1982**, 26, 4935.
- [125] G. A. Benesh, A. M. Woolley, C. Umrigar, *J. Phys. C: Solid State Phys.*, **1985**, 18, 1595.
- [126] C. M. Fang, R. A. De Groot, C. Haas, *Phys. Rev. B*, **1997**, 56, 4455.
- [127] Z. Y. Wu, G. Ouvrard, S. Lemaux, P. Moreau, P. Gressier, F. Lemoigno, J. Rouxel, *Phys. Rev. Lett.*, **1996**, 77, 2101.
- [128] Z. Y. Wu, F. Lemoigno, P. Gressier, G. Ouvrard, P. Moreau, J. Rouxel, C. R. Natoli, *Phys. Rev. B*, **1996**, 54, R11009.
- [129] Z. Y. Wu, G. Ouvrard, P. Moreau, C. R. Natoli, *Phys. Rev. B*, **1997**, 55, 9508.
- [130] S. Sharma, T. Nautiyal, G. S. Singh, S. Auluck, P. Blaha, C. Ambrosch-Draxl, *Phys. Rev. B*, **1999**, 59, 14833.
- [131] A. H. Thompson, K. R. Pisharody, R. F. Koehler, *Phys. Rev. Lett.*, **1972**, 29, 163.
- [132] G. Lucovsky, R. M. White, J. A. Benda, J. F. Revelli, *Phys. Rev. B*, **1973**, 7, 3859.
- [133] D. W. Fischer, *Phys. Rev. B*, **1973**, 8, 3576.
- [134] J. J. Barry, H. P. Hughes, P. C. Klipstein, R. H. Friend, *J. Phys. C: Solid State Phys.*, **1983**, 16, 393.
- [135] H. W. Myron, A. J. Freeman, *Phys. Rev. B*, **1974**, 9, 481.

- [136] J. A. Wilson, *Solid State Commun.*, **1977**, 22, 551.
- [137] B. Liu, J. Yang, Y. Han, T. Hu, W. Ren, C. Liu, Y. Ma, C. Gao, *J. Appl. Phys.*, **2011**, 109, 5, 053717.
- [138] C. Julien, I. Samaras, O. Gorochov, A. M. Ghorayeb, *Phys. Rev. B*, **1992**, 45, 13390.
- [139] H. Imai, Y. Shimakawa, Y. Kubo, *Phys. Rev. B*, **2001**, 64, 241104.
- [140] K. D. Bronsema, J. L. D. Boer, F. Jellinek, *Z. Anorg. Allg. Chem.*, **1986**, 540, 15.
- [141] T. S. Anand, *Sains Malays.*, **2009**, 38, 85.
- [142] L. F. Schneemeyer, M. S. Wrighton, *J. Am. Chem. Soc.*, **1979**, 101, 6496.
- [143] T. Cheiwchanchamnangij, W. R. L. Lambrecht, *Phys. Rev. B*, **2012**, 85, 205302.
- [144] W. Kautek, *J. Electrochem. Soc.*, **1980**, 127, 2471.
- [145] L. F. Mattheiss, *Phys. Rev. B*, **1973**, 8, 3719.
- [146] A. Kuc, N. Zibouche, T. Heine, *Phys. Rev. B*, **2011**, 83, 245213.
- [147] H. H. Guo, T. Yang, P. Tao, Z. D. Zhang, *Chinese Phys. B*, **2014**, 23, 017201.
- [148] R. B. Somoano, V. Hadek, A. Rembaum, *J. Chem. Phys.*, **1973**, 58, 697.
- [149] J. Heising, M. G. Kanatzidis, *J. Am. Chem. Soc.*, **1999**, 121, 11720.
- [150] B. Radisavljevic, A. Radenovic, J. Brivio, V. Giacometti, A. Kis, *Nat. Nanotechnol.*, **2011**, 6, 147.
- [151] Y. H. Lee, X. Q. Zhang, W. Zhang, M. T. Chang, C. T. Lin, K. D. Chang, Y. C. Yu, J. T. W. Wang, C. S. Chang, L. J. Li, T. W. Lin, *Adv. Mater.*, **2012**, 24, 2320.
- [152] M. R. Laskar, D. N. Nath, L. Ma, E. W. Lee, C. H. Lee, T. Kent, Z. Yang, R. Mishra, M. A. Roldan, J.-C. Idrobo, S. T. Pantelides, S. J. Pennycook, R. C. Myers, Y. Wu, S. Rajan, *Appl. Phys. Lett.*, **2014**, 104, 092104.
- [153] K. Dolui, I. Rungger, S. Sanvito, *Phys. Rev. B*, **2013**, 87, 165402.
- [154] Y. H. Lee, X. Q. Zhang, W. Zhang, M. T. Chang, C. T. Lin, K. D. Chang, Y. C. Yu, J. T. W. Wang, C. S. Chang, L. J. Li, T. W. Lin, *Adv. Mater.*, **2012**, Adv. Mater., 24, 17, 2320.
- [155] A. H. Reshak, S. Auluck, *Phys. Rev. B*, **2003**, 68, 125101.
- [156] A. Molina-Sánchez, L. Wirtz, *Phys. Rev. B*, **2011**, 84, 155413.
- [157] V. L. Kalikhman, *Inorg. Mater.*, **1983**, 19, 957.
- [158] B. F. Mentzen, M. J. Sienko, *Inorg. Chem.*, **1976**, 15, 2198.
- [159] G. Arora, Y. Sharma, V. Sharma, G. Ahmed, S. K. Srivastava, B. L. Ahuja, *J. Alloys. Compd.*, **2009**, 470, 452.
- [160] S. L. Xiao, W. Z. Yu, S. P. Gao, *Surf. Sci.*, **2016**, 653, 107.
- [161] J. J. Devadasan, C. Sanjeeviraja, M. Jayachandran, *J. Cryst. Growth*, **2001**, 226, 67.

- [162] J. A. Baglio, G. S. Calabrese, D. J. Harrison, E. Kamieniecki, A. J. Ricco, M. S. Wrighton, G. D. Zoski, *J. Am. Chem. Soc.*, **1983**, 105, 2246.
- [163] D. Braga, I. Gutiérrez Lezama, H. Berger, A. F. Morpurgo, *Nano Lett.*, **2012**, 12, 5218.
- [164] K. K. Kam, B. A. Parkinson, *J. Phys. Chem.*, **1982**, 86, 463.
- [165] G. Kline, K. K. Kam, R. Ziegler, B. A. Parkinson, *Sol. Energy Mater.*, **1982**, 6, 337.
- [166] R. Morrish, T. Haak, C. A. Wolden, *Chem. Mater.*, **2014**, 26, 3986.
- [167] S. Bassaid, B. Bellal, M. Trari, *React. Kinet. Mech. Cat.*, **2015**, 115, 389.
- [168] C. R. Cabrera, H. D. Abruña, *J. Electrochem. Soc.*, **1988**, 135, 1436.
- [169] S. Brunken, R. Mientus, K. Ellmer, *Phys. Status Solidi A*, **2012**, 209, 317.
- [170] J. Baglio, E. Kamieniecki, N. DeCola, C. Struck, J. Marzik, K. Dwight, A. Wold, *J. Solid State Chem.*, **1983**, 49, 166.
- [171] N. Li, Z. Liu, S. Hu, H. Wang, *Solid State Commun.*, **2018**, 269, 58.
- [172] L. Yadgarov, R. Rosentsveig, G. Leitus, A. Albu-Yaron, A. Moshkovich, V. Perfilyev, R. Vasic, A. I. Frenkel, A. N. Enyashin, G. Seifert, L. Rapoport, R. Tenne, *Angew. Chem.*, **2012**, 124, 1174.
- [173] H. Kawai, M. Sugahara, R. Okada, Y. Maniwa, Y. Yomogida, K. Yanagi, *Appl. Phys. Express*, **2016**, 10, 015001.
- [174] D. Tonti, F. Varsano, F. Decker, C. Ballif, M. Regula, M. Remškar, *J. Phys. Chem. B*, **1997**, 101, 2485.
- [175] T. Wang, C. Liu, X. Wang, X. Li, F. Jiang, C. Li, J. Hou, J. Xu, *J. Polym. Sci. B Polym. Phys.*, **2017**, 55, 997.
- [176] A. K. Padhi, K. S. Nanjundaswamy, J. B. Goodenough, *J. Electrochem. Soc.*, **1997**, 144, 1188.
- [177] C. Masquelier, L. Croguennec, *Chem. Rev.*, **2013**, 113, 6552.
- [178] J. Barker, M. Y. Saidi, J. L. Swoyer, *J. Electrochem. Soc.*, **2004**, 151, A1670.
- [179] J. M. Ateba Mba, C. Masquelier, E. Suard, L. Croguennec, *Chem. Mater.*, **2012**, 24, 1223.
- [180] J. J. Biendicho, A. R. West, *Solid State Ion.*, **2011**, 203, 33.
- [181] Y. N. Xu, W. Y. Ching, Y. M. Chiang, *J. Appl. Phys.*, **2004**, 95, 6583.
- [182] P. Tang, N. A. W. Holzwarth, *Phys. Rev. B*, **2003**, 68, 165107.
- [183] S. Shi, C. Ouyang, Z. Xiong, L. Liu, Z. Wang, H. Li, D. Wang, L. Chen, X. Huang, *Phys. Rev. B*, **2005**, 71, 144404.
- [184] F. Zhou, K. Kang, T. Maxisch, G. Ceder, D. Morgan, *Solid State Commun.*, **2004**, 132, 181.

- [185] S. Shi, H. Zhang, X. Ke, C. Ouyang, M. Lei, L. Chen, *Phys. Lett. A*, **2009**, 373, 4096.
- [186] Y. N. Xu, S. Y. Chung, J. T. Bloking, Y. M. Chiang, W. Y. Ching, *Electrochem. Solid-State Lett.*, **2004**, 7, A131.
- [187] C. Delacourt, L. Laffont, R. Bouchet, C. Wurm, J.-B. Leriche, M. Morcrette, J.-M. Tarascon, C. Masquelier, *J. Electrochem. Soc.*, **2005**, 152, A913.
- [188] K. K. Bharathi, L. N. Patro, C. V. Ramana, *J. Mater. Sci.*, **2013**, 48, 5063.
- [189] P. K. Chakraborty, G. C. Datta, K. P. Ghatak, *Physica B Condens. Matter*, **2003**, 339, 198.
- [190] Q. Wang, N. Evans, S. M. Zakeeruddin, I. Exnar, M. Grätzel, *J. Am. Chem. Soc.*, **2007**, 129, 3163.
- [191] A. Paolella, C. Faure, G. Bertoni, S. Marras, A. Guerfi, A. Darwiche, P. Hovington, B. Commarieu, Z. Wang, M. Prato, M. Colombo, S. Monaco, W. Zhu, Z. Feng, A. Vijn, C. George, G. P. Demopoulos, M. Armand, K. Zaghib, *Nat. Commun.*, **2017**, 8, 14643.
- [192] V. Koleva, R. Stoyanova, E. Zhecheva, *Mater. Chem. Phys.*, **2010**, 121, 370.
- [193] J. M. Osorio-Guillén, B. Holm, R. Ahuja, B. Johansson, *Solid State Ion.*, **2004**, 167, 221.
- [194] X. Tang, S.-K. Zhong, H.-F. Lu, *Chin. J. Inorg. Chem.*, **2011**, 27, 1065.
- [195] H. Gerischer, *J. Electroanal. Chem. Interfacial Electrochem.*, **1975**, 58, 263.
- [196] H. Gerischer, *J. Electrochem. Soc.*, **1978**, 125, 218C.
- [197] T. Nomiya, H. Kuriyaki, K. Hirakawa, *Synth. Met.*, **1995**, 71, 2237.
- [198] G. Betz, H. Tributsch, R. Marchand, *J. Appl. Electrochem.*, **1984**, 14, 315.
- [199] G. Betz, H. Tributsch, S. Fiechter, *J. Electrochem. Soc.*, **1984**, 131, 640.
- [200] G. Betz, S. Fiechter, H. Tributsch, *J. Appl. Phys.*, **1987**, 62, 4597.
- [201] C. Andriamiadamanana, I. Sagaidak, G. Bouteau, C. Davoisne, C. Laberty-Robert, F. Sauvage, *Adv. Sustainable Syst.*, **2018**, 1700166.
- [202] A. S. Prakash, P. Manikandan, K. Ramesha, M. Sathiya, J.-M. Tarascon, A. K. Shukla, *Chem. Mater.*, **2010**, 22, 2857.
- [203] Z. Qi, G. M. Koenig, *ChemistrySelect*, 2016, 1, 3992.
- [204] T. Tsumura, M. Inagaki, *Solid State Ion.*, **1997**, 104, 183.
- [205] N. Kumagai, N. Kumagai, Y. Umetzu, K. Tanno, J. P. Pereira-Ramos, *Solid State Ion.*, **1996**, 86, 1443.
- [206] R. Sahay, P. Suresh Kumar, V. Aravindan, J. Sundaramurthy, W. Chui Ling, S. G. Mhaisalkar, S. Ramakrishna, S. Madhavi, *J. Phys. Chem. C*, **2012**, 116, 18087.
- [207] H. Wang, H. Yang, L. Lu, *RSC Adv.*, **2014**, 4, 17483.

- [208] J. Xiao, D. Choi, L. Cosimbescu, P. Koech, J. Liu, J. P. Lemmon, *Chem. Mater.*, **2010**, 22, 4522.
- [209] C. Feng, L. Huang, Z. Guo, H. Liu, *Electrochem. Commun.*, **2007**, 9, 119.
- [210] G. Li, H. Azuma, M. Tohda, *Electrochem. Solid-State Lett.*, **2002**, 5, A135.
- [211] G. Bouteau, A. N. Van-Nhien, M. Sliwa, N. Sergent, J.-C. Lepretre, G. Gachot, I. Sagaidak, F. Sauvage, *Sci. Rep.*, **2019**, 9, 135.
- [212] A. Kulka, K. Walczak, W. Zając, J. Molenda, *J. Solid State Chem.*, **2017**, 253, 367.
- [213] L. Laffont, C. Delacourt, P. Gibot, M. Y. Wu, P. Kooyman, C. Masquelier, J. M. Tarascon, *Chem. Mater.*, **2006**, 18, 5520.
- [214] V. Palomares, A. Goñi, A. Iturrondobeitia, L. Lezama, I. de Meaza, M. Bengoechea, T. Rojo, *J. Mater. Chem.*, **2012**, 22, 4735.
- [215] Y. Janssen, D. Santhanagopalan, D. Qian, M. Chi, X. Wang, C. Hoffmann, Y. S. Meng, P. G. Khalifah, *Chem. Mater.*, **2013**, 25, 22, 4574.
- [216] M. E. A. Dompablo, J. M. Gallardo-Amores, U. Amador, *Electrochem. Solid State Lett.*, **2005**, 8, A564.
- [217] C. Zhu, K. Weichert, J. Maier, *Adv. Funct. Mater.*, **2011**, 21, 1917.
- [218] H. Zhang, J. F. Banfield, *Chem. Rev.*, **2014**, 114, 9613.
- [219] G. Bouteau, Etude des propriétés de l'interface semi-conducteur / électrolyte sous illumination pour batteries à ion-lithium photo-rechargeables. Ph.D. thesis, University of Picardie Jules Verne, **2019**.
- [220] K. Kanamura, T. Umegaki, H. Naito, Z. Takehara, T. Yao, *J. Appl. Electrochem.*, **2001**, 31, 73.
- [221] D. Young, A. Ransil, R. Amin, Z. Li, Y.-M. Chiang, *Adv. Energy Mater.*, **2013**, 3, 1125.
- [222] H. B. Gon, N. Veeraiah, *J. Mater. Sci.*, **1981**, 16, 2571.

General conclusions

This work is dedicated to the study of mixed electronic/ionic semi-conducting materials that can be capable of combining sunlight energy conversion reaction and its energy storage at the electrode and molecular levels. The objective of this thesis work is the exploration of other materials than the anatase TiO_2 . Our strategy, against simply blindly screening materials, was focused on deepening the current knowledge on the light-induced charge transfer through the semiconductor/electrolyte junction following up the example of the nanoparticles of anatase TiO_2 and to develop a database that can be used to decipher which materials can have potentialities for the application in photo-rechargeable electrode and in full devices that require a perfect band alignments between the two electrodes.

In the first part of this thesis, we developed an airtight photoelectrochemical cell allowing to monitor the change of the optoelectronic properties of TiO_2 upon lithium insertion. We have established that few factors stand behind the color changeover from white in TiO_2 to dark blue in $\text{Li}_{0.6}\text{TiO}_2$. On the one hand, there is a 0.3 eV increase in the bandgap value upon lithium insertion following Burnstein-Moss effect. On the other hand, the blue coloration is connected to the enhancement in absorption within the visible and near-infrared region of the solar spectrum as a result of the enrichment of free carriers in the conduction band of Li_xTiO_2 and electrons localized in Ti^{3+} centers occupying the 3d metal orbitals. The *in situ* Mott-Schottky measurements showed a positive shift in potential of 0.5 V of the conduction band. Our study also revealed that the charge carrier concentration increases by circa one order of magnitude upon lithium insertion into the structure.

We have established the ultrafast nature of the direct recombination, i.e. 29 ps, for both TiO_2 and $\text{Li}_{0.6}\text{TiO}_2$. We demonstrated that even though the majority of the photoluminescence stems from the direct recombination, a significant part of it belongs to the recombination through carrier traps associated with oxygen vacancies and surface states. This trap-mediated fluorescence was found to increase when electrode was put in contact with electrolytes. Depending on the electrolyte composition, the band gap, excitation/emission spectrum and photoluminescence dynamics can vary to a large extent. This phenomenon was assigned to an experimental demonstration of a Stark effect taking place in the nanocrystals as a result from the specific adsorption of lithium cation from the electrolyte. Today, Stark effect in nanocrystals is considered as being a beneficial effect for the electrode's photorecharge. We also demonstrated elsewhere that Stark effect is in part or in whole responsible for two phase vs. single phase transition during lithium insertion by downsizing the particles towards nanoscale.

Comparing the fluorescence decays in lithium ion-blocking vs. ion-conducting interface, we support that the half-time of the hole transfer to Ti^{3+} is in the scale of 100 ps, thus entering in direct competition with the deactivation of the excited states in crystals.

The second important part of this work was dedicated to the creation of a database describing the optoelectronic properties of common insertion materials. Three groups were studied: transition metal oxides ($\text{Li}_4\text{Ti}_5\text{O}_{12}$, LiCoO_2 , MoO_3 , WO_3 , CuO , Bi_2O_3 , LiMn_2O_4 , $\text{LiMn}_{1/3}\text{Ni}_{1/3}\text{Co}_{1/3}\text{O}_2$), transition metal sulfides (TiS_2 , MoS_2 , WS_2), and lithiated polyanions (LiFePO_4 , LiMnPO_4 , LiVPO_4F). This work reports for the first time that for some materials, i.e. LiCoO_2 , MoS_2 , and WS_2 , the type of conductivity can change of sign depending on the nature of the electrolyte in contact, i.e. from n-type in an aqueous (protic) electrolyte to a p-type in a non-aqueous aprotic EC/DMC-based electrolyte. We also show that the flat band potential can be drastically modified by the electrolyte up to 1.4 eV except for LiFePO_4 , and that the main carrier density is always increased by at least one order of magnitude in EC/DMC electrolyte. Comparing the minor charge carrier energy to the redox energy of the transition metal for the lithium insertion or deinsertion reaction, we established from this database that p-CuO, p-MoS₂ and p-WS₂ are materials which should not work for thermodynamic reasons. The case of LiCoO_2 is somewhat different. Although this material can be of interest from a fundamental point of view, this latter is not interesting for the application since its high redox potential associated to its p-type semi-conduction will lead to a photo-dischargeable electrode. By contrast, the photoelectrochemical recharge of the electrode is thermodynamically realizable in n- $\text{Li}_4\text{Ti}_5\text{O}_{12}$, n-MoO₃, n-WO₃, n-Bi₂O₃, n-LiFePO₄, and n-LiFePO₄.

Unfortunately, the photoelectrochemical study of some specifically chosen materials underlines that reaching the photo-rechargeable mechanism is not as straightforward as anticipated. None of the studied materials, i.e. n-type $\text{Li}_4\text{Ti}_5\text{O}_{12}$, MoO_3 , LiFePO_4 , Bi_2O_3 and p- LiCoO_2 , showed a process of light-induced ion transfer sometimes because of external reasons such as bad electrode adhesion or very poor electrochemical reactivity (MoO_3 , Bi_2O_3 and LiFePO_4) or for internal reasons mainly because of harmful electrolyte side-reactions under illumination (LiCoO_2 and $\text{Li}_4\text{Ti}_5\text{O}_{12}$).

We focused to extend this study in the case of two materials: LiFePO_4 and $\text{Li}_4\text{Ti}_5\text{O}_{12}$. A deeper study of LiFePO_4 revealed that neither downsizing of the particles nor grafting of a ruthenium polypyridyl dye on the surface improved the photoelectrochemical performance. However, this study clarified the charge transfer mechanism between LiFePO_4 and N719 dye and the band structure of LiFePO_4 and FePO_4 wrongly proposed/discussed in the literature. The extended

study of $\text{Li}_4\text{Ti}_5\text{O}_{12}$ showed that an important limitation of the system is related to the formation of a SEI layer exclusively made of LiF under dark but also under illumination with a thicker layer which can attain up to 100 nm. To present level of understanding, we estimate that LiF formation annihilates the photorecharge process of the electrode. On the other hand, we also speculate that excited state lifetime of $\text{Li}_7\text{Ti}_5\text{O}_{12}$ is too fast with respect to a possible charge transfer towards the transition metal. The formation of LiF on the surface prevented us from determination of how the band structure is modified in $\text{Li}_7\text{Ti}_5\text{O}_{12}$. However, in this part of the study, we revealed a FRET mechanism taking place in the UV from the electrolyte to the electrode. This FRET process, which induces the quenching of the electrolyte fluorescence, seems even more efficient in contact with $\text{Li}_7\text{Ti}_5\text{O}_{12}$ owing to its narrower bandgap by 0.23 eV and improved absorption capability in the whole visible range.

This study reveals mainly three important challenges that need to be addressed in the field: *(i)* electrode nanostructuralization to favor surface reactions and to bring the Debye length comparable to the particle size and carbon-free electrodes with high conductivity, *(ii)* developing electrolytes specific to photorechargeable systems with enhanced stability in both reduction and oxidation with respect to electrode's photo-excited states, and *(iii)* choosing the right photo-anode with the right photo-cathode that allows an adequate band energy alignments to collect carriers and thus yielding to a complete photorechargeable lithium-ion batteries. Preliminary results on the second point shows that the addition of a specific scavenger in the electrolyte can likely prevent the formation of LiF over the electrode, thus offering not only improved electrochemical performances of carbon-free electrodes but also a photo-rechargeable process in $\text{Li}_7\text{Ti}_5\text{O}_{12}$ under white light illumination in ca. 15 hours. The third point also remains very challenging, as the database herein developed shows that none of the materials can be associated to form a fully regenerative bifacial p-n photobattery.

This pioneering work in a complex subject of energy storage and energy conversion at the molecular level requires still a lot of profound investigations from fundamental standpoints, particularly in the field of the time-resolved spectroscopy. In our laboratory, further time-resolved spectrometers are under setting up, which will allow to provide more details on the different charge carrier transfer taking place in the photo-electrode (i.e. carrier transfer to the transition metal vs. to the electrolyte). This study will be able to be carried out by a picosecond-pump / three probes transient absorption spectrometer including a high dynamic range streak camera detection that is delivering today its first results and two other time-resolved spectrometers in fluorescence associating a fs tunable Ti:Sa laser with a streak camera in

synchroscan mode for TR-PL (ca. 4 ps time resolution) and a up-conversion setup (IRF ca. 200 fs) which will be able to monitor faster processes than ca. 30 ps. Establishing the time-scale of the different carrier transfer in the photo-electrode will allow understanding all limiting processes taking place in the electrode under illumination. It will be also a basis to improve the materials and the electrode mesostructuralization towards optimizing the electrode's performance.

As mentioned in the manuscript, this work has often faced a lack of data/knowledge from the literature to guide us more efficiently into this thesis development. However, the results of this work not only open up important lines of research that will be pursued in the laboratory to continue development of these systems, but can also establish a background for the pursuit of this field in the community. In addition, the created database of the optoelectronic properties of common insertion materials can be beneficial for a broad range of other applications like photocatalysis, electrochromic devices, and even to battery itself.

Résumé développé de la thèse en Français (Summary in French)

La croissance constante de la population mondiale et l'amélioration du niveau de vie entraîne une augmentation continue de la demande d'énergie, qui devrait atteindre environ +30% pour les prochaines deux décennies suivantes. Environ 80% de l'énergie actuellement produite provient de la combustion des énergies fossiles, par exemple: le charbon, le pétrole et le gaz naturel. Toutefois, en raison de la quantité limitée des ressources fossiles, son extraction est prévue de diminuer après 2025. En plus de sa disponibilité limitée, la combustion des carburants fossiles est la principale source d'émission de dioxyde de carbone dans l'atmosphère. Comptant pour 72% de tous les gaz à effet de serre émis, le CO₂ est le principal facteur du changement climatique. La première conséquence menaçante est le réchauffement planétaire qui génère l'augmentation du niveau de la mer, la fonte des glaces, des ouragans plus fréquents et plus violents, des chaleurs extrêmes et des incendies de forêt, inondations, etc.

Parmi les sources d'énergie renouvelables, toutes sauf la géothermie ($1,3 \cdot 10^{10}$ kWh) proviennent directement ou indirectement de l'activité solaire. L'énergie éolienne ($4,9 \cdot 10^{14}$ kWh), la biomasse ($1,1 \cdot 10^{11}$ kWh), l'énergie hydraulique ($1,1 \cdot 10^{12}$ kWh) et l'énergie marine ($3,6 \cdot 10^{13}$ kWh) sont des conséquences de l'irradiation solaire de la Terre. Cela est dû à la transformation du rayonnement solaire en chaleur thermique, photosynthèse ou évaporation de l'eau. Le soleil, avec une capacité de 10^{18} kWh / an atteignant la surface de la Terre, est la seule source d'énergie renouvelable capable de répondre pleinement aux besoins énergétiques actuels de $1,5 \cdot 10^{14}$ kWh. Son caractère intermittent constitue toutefois un obstacle majeur à une large utilisation de l'énergie solaire.

L'une des approches permettant de garantir une production d'énergie constante consiste à stocker l'excès d'énergies produites pendant les pics de production ou les périodes de basses consommations pour une utilisation ultérieure. L'énergie générée peut être stockée de manière chimique (batteries, condensateurs ou hydrogène), mécanique (énergie hydroélectrique pompée, air comprimé ou volants), ou dans des systèmes thermiques. Les plus attirants sont les systèmes de stockage électrochimique tels que les batteries en raison de leur intégration aisée et de la flexibilité pour l'application permettant une large gamme de densité d'énergie stockée allant du μ Wh au MWh. Cependant, malgré la maturité de la technologie, l'incorporation d'une partie de stockage électrochimique sur une implantation photovoltaïque double au minimum les coûts d'installation.

Cela pénalise le retour sur investissement financier (20-30 ans) par rapport à la durée de vie des panneaux photovoltaïque et des batteries Li-ion.

Dans le but de réduire les coûts d'installation et de faire germer de nouvelles innovations et de nouvelles filières scientifiques, la mise au point d'un seul système combinant à la fois la conversion et le stockage de l'énergie est hautement souhaitable. Toutefois, la réalisation d'un tel dispositif combinant conversion et stockage de l'énergie solaire à l'échelle du matériau et de la molécule est particulièrement complexe scientifiquement et requière donc de nombreuses recherches scientifiques. Une alternative à plus court terme est basée sur une hybridation des deux technologies qui consiste à développer un dispositif unique comprenant deux compartiments : un système de conversion PV, tel qu'une cellule solaire à colorant comme souvent proposé, et l'autre une batterie lithium-ion partageant ou non une même électrode. Cette approche est potentiellement moins coûteuse et plus facile à intégrer par rapport au couplage externe classique. La deuxième approche, avec des perspectives à plus long termes, consiste à adapter un assemblage moléculaire permettant de combiner la conversion de l'énergie solaire et son stockage chimique. C'est justement le cadre de ce travail de doctorat où l'approche consiste à créer des transferts d'ions à l'interface semi-conducteur mixte et électrolyte induit par l'excitation du niveau de la bande interdite du semi-conducteur. Ce transfert ionique résulte d'un transfert du porteur de charge minoritaire en phase homogène vers l'élément de transition. Un point bloquant de ce mécanisme provient de la nature purement surfacique de cette réaction qui est limitée par la longueur de Debye correspondant à la zone de déplétion du semi-conducteur.

Afin de contourner cette limitation importante du mécanisme de photo-recharge, notre équipe a mis au point des nanocristaux d'anatase TiO_2 de l'ordre de 4 à 5 nm de diamètre via une synthèse et thermolyse à température ambiante ou à basse température. Ces nano-cristaux ont permis de promouvoir considérablement le rapport surface / volume des particules. Une conséquence directe, ces particules permettent de maximiser la réactivité de surface vis-à-vis du volume, conduisant à un processus de photorecharge quantitatif. Une électrode mesoporeuse constituée par des nanoparticules de TiO_2 peut être photorechargée intégralement ($\approx 600 \mu\text{Ah}/\text{cm}^2$) en seulement 2 heures sous des conditions d'éclairage réaliste et standardisée (A.M. 1.5G, $100 \text{ mW}/\text{cm}^2$). Cette preuve de concept a démontré pour la première fois que l'excitation de la bande interdite peut induire une recharge complète d'une électrode de batterie. Cette recherche a permis d'ouvrir de

nouvelles perspectives scientifiques et technologiques sur le développement de matériaux bifonctionnels combinant la conversion et le stockage de l'énergie solaire à l'échelle moléculaire.

Des développements ultérieurs ont appelé à approfondir notre compréhension actuelle de ces processus de transfert de charge photoinduits afin de maximiser les performances en termes de stabilité et de temps de recharge. En plus, afin de passer d'une demi-cellule photorechargeable à une cellule complète, il est nécessaire de développer une contre-électrode appropriée permettant la collection des porteurs de charge majoritaires de l'électrode photo-active.

Il a déjà été discuté dans la littérature que le potentiel des ions intercalés peut contribuer à l'énergie libre des électrodes provoquant un décalage des bords de la bande d'énergie, de la bande interdite, et affectant la longueur de Debye et le champ électrique de la zone de déplétion. Dans ce but, nous nous sommes concentrés dans cette thèse sur l'étude approfondie de l'évolution des propriétés optoélectroniques et de la dynamique des processus de transfert de charges ultra-rapides à l'interface électrode/électrolyte de l'anatase TiO₂ lors de l'insertion du lithium. Pour cela, nous avons développé une cuvette en quartz à trois électrodes étanche permettant de coupler des expériences d'électrochimie et de spectroscopies optiques *in situ* / *in operando* du type absorption UV-Visible mais aussi de fluorescence à l'état stationnaire et résolue en temps.

Nos travaux décrivent l'évolution des spectres de transmittance des films de TiO₂ *in operando* à différents états de décharge. Nous avons établi que le changement de couleur passant du blanc au bleu foncé lors de l'insertion du lithium est associé d'une part à une augmentation de la valeur de la bande interdite par effet Burnstein-Moss, passant de 2,85 eV à 3,21 eV, et d'autre part liée à l'augmentation de l'absorbance dans la partie visible et dans le proche-infrarouge. Cette absorbance accrue est attribuée à l'absorption optique par des électrons libres dans la bande de conduction de TiO₂ et ainsi qu'à la localisation des électrons dans les centres Ti³⁺ occupant les orbitales métalliques 3d en raison de la taille nanométrique des particules. A ce titre, l'ajustement des spectres de transmittance à différentes profondeurs de décharge en utilisant le modèle de Drude montre que l'insertion de lithium dans TiO₂ augmente par un facteur 20 la concentration en porteurs de charges, passant de $1,3 \cdot 10^{19} \text{ cm}^{-3}$ à $2,9 \cdot 10^{20} \text{ cm}^{-3}$.

Afin de déterminer les positions des bords de bandes et leurs évolutions lors de l'insertion du lithium, des mesures en trois électrodes par la méthode Mott-Schottky ont été entreprises en combinaison avec la spectroscopie d'absorption UV-visible. Il est établi dans ce travail que

l'insertion de lithium dans la structure provoque un décalage important du potentiel de la bande plate vers des valeurs positives passant de 2,84 V à 3,36 V vs. Li^+/Li . Cela se traduit par un décalage négatif de 0,5 eV de la bande de conduction. Ce processus est accompagné par une augmentation d'un ordre de grandeur de la concentration d'électrons passant de $2,1 \cdot 10^{19} \text{ cm}^{-3}$ à $3,9 \cdot 10^{19} \text{ cm}^{-3}$ sans aucun changement dans la nature des porteurs principaux. De plus, nos résultats soulignent systématiquement une forte influence de la nature protique ou aprotique de l'électrolyte sur la valeur de potentiel de bande plate et la concentration des porteurs. Enfin, en confrontant les mesures Mott-Schottky avec celles de spectroscopie d'absorption UV-Visible à l'état solide, nos résultats montrent une diminution de l'énergie de la bande de valence de 800 mV, passant de 5,7 V à 6,5 V et de la bande de conduction de 500 mV, passant de 2,8 V à 3,3 V (vs. Li^+/Li) entre TiO_2 et sa forme réduite $\text{Li}_{0,6}\text{TiO}_2$.

Pour comprendre la dynamique des états excités de TiO_2 et de $\text{Li}_{0,6}\text{TiO}_2$ dans différents types d'électrolytes, la spectroscopie de fluorescence à l'état stationnaire et en temps de vie à comptage simple photon a été un outil important et incontournable durant ce travail de doctorat. Les cartes d'excitation/émission de fluorescence sur un film de TiO_2 à différentes profondeurs de décharge ont systématiquement montré la présence d'une bande principale pour laquelle le maximum se situe à 277 nm et 335 nm, ainsi qu'une seconde contribution moins intense et plus large vers 500 nm. Cette dernière se déplace de 498 à 515 nm lors de l'insertion de lithium. La première bande est attribuée aux phénomènes de fluorescence des ions solvatés Li^+ et PF_6^- dans l'EC/DMC. L'origine de la deuxième bande moins intense est attribuée à la fluorescence des nanocristaux de TiO_2 en équilibre avec l'électrolyte. Nos travaux mettent en évidence que les rendements de fluorescence de TiO_2 et de l'électrolyte diminuent drastiquement lors de l'insertion du lithium dans des nanocristaux de TiO_2 . Ce phénomène suggère très fortement qu'une partie de l'énergie radiative de l'électrolyte est transférée à l'électrode par résonance de Förster (FRET) et que ce processus de transfert d'énergie au bénéfice de l'électrode est plus efficace lorsque le TiO_2 est lithié en raison de ses meilleures propriétés d'absorption. En même temps, le rendement de fluorescence de l'électrode diminue à son état réduit. Ceci signifie que le processus radiatif de recombinaison dans le $\text{Li}_{0,6}\text{TiO}_2$ est désactivé comparé à TiO_2 . Ce phénomène est attendu en raison du transfert des trous d'électrons vers le Ti^{3+} , mécanisme responsable de la photorecharge de l'électrode. Un mécanisme de type FRET est clairement réalisable pour trois raisons : (i) le rendement quantique (QY) de luminescence de l'électrolyte est largement supérieur à celui du TiO_2 ($\text{QY}_{\text{LP30}} = 7,7\%$,

$QY_{TiO_2} < 1\%$), (ii) la proximité moléculaire entre le Li^+ et le PF_6^- solvaté responsable de la fluorescence de l'électrolyte et les nanocristaux de $Li_{0,6}TiO_2$, (iii) le recouvrement énergétique entre la bande d'émission de l'électrolyte et la bande d'excitation des nanocristaux de TiO_2 et de $Li_{0,6}TiO_2$.

Dans ce travail de doctorat, des mesures de spectroscopie de fluorescence résolue en temps en utilisant la technique du comptage à simple photon (TCSPC) a été utilisée pour étudier la dynamique de relaxation radiative des états excités dans le TiO_2 et le $Li_{0,6}TiO_2$ en contact avec différents types d'électrolyte. La dynamique de fluorescence a été enregistrée à une longueur d'onde d'émission de 455 nm en utilisant un détecteur refroidi par Peltier du type MCP-PMT (Hamamatsu) pour lequel le temps de réponse est < 25 ps. Tant dans le TiO_2 que pour le $Li_{0,6}TiO_2$ en contact avec l'argon, la reconvolution de la courbe de déclin avec la réponse instrumentale du spectromètre a abouti systématiquement à deux composantes. La contribution plus rapide, atteignant 29 ps, correspond à la recombinaison directe entre la bande de conduction et la bande de valence. La deuxième composante d'environ 2 ns est physiquement attribuée au processus de fluorescence passant par les pièges de surface. Une amplitude plus élevée de la recombinaison directe a été trouvée dans le cas de la phase lithiée, i.e. 18,1% pour $Li_{0,6}TiO_2$ contre 8,5% pour TiO_2 . Ceci provient d'une redistribution des pièges dans la bande interdite après l'insertion du lithium.

Afin d'estimer la cinétique des processus de transfert de charge dans la composition déchargée $Li_{0,6}TiO_2$, des mesures de fluorescence résolue en temps ont été effectuées sur une électrode au contact d'un électrolyte bloquant et passant en comprenant ou non des ions lithium. Dans cette expérience, nous avons utilisé deux types d'électrolyte: l'un basé sur le mélange de solvants organiques EC/DMC généralement utilisé dans les batteries et un second, plus inerte, à base de liquide ionique EMITFSI. Lorsque la photoluminescence des nanocristaux de $Li_{0,6}TiO_2$ est mesurée au contact des électrolytes, nous avons observé des déclins de fluorescence significativement plus longs que ceux sous argon. Cela provient du contact des nanocristaux avec une interface liquide dont la constante diélectrique supérieure tend à piéger les électrons à la surface des particules. Le contact interfacial avec l'électrolyte empêche la recombinaison direct inter-bandes au profit de processus plus lents via les pièges. Ce phénomène provient aussi du fait que les cations Li^+ et/ou TBA^+ forment des «quasi-particules» avec des électrons piégés à la surface des particules, prolongeant ainsi la durée de vie de l'état excité. Dans les deux milieux, les déclins enregistrés dans

des électrolytes contenant du Li^+ sont plus rapides que ceux déterminés avec des électrolytes sans lithium. La reconvolution des déclin dans les électrolytes à base de lithium nécessite systématiquement au recours d'une troisième contribution rapide. Cela suggère l'apparition d'un processus supplémentaire de transfert de charge rapide, que nous attribuons au transfert de trous vers le Ti^{3+} (mécanisme de photorecharge). Ce transfert de trous est rapide, nécessitant 145 ps dans un électrolyte à base d'EC/DMC (représentant 7,8 % du déclin), et il est de 97 ps avec un liquide ionique EMITFSI (représentant 12,5% du déclin). La différence d'amplitude indique que le processus de transfert de trous photogénéré est plus favorable dans l'électrolyte plus inerte. Le type de solvant influe également sur la fluorescence induite par les pièges, probablement dû à une redistribution de l'énergie et à la densité d'états des pièges situés dans la bande interdite. La plus longue durée de vie est obtenue dans le liquide ionique EMITFSI. Elle atteint jusqu'à 14,6 ns avec une amplitude de 69,4%.

Enfin, nous avons mis en évidence expérimentalement un effet Stark-Lo Surdo qui intervient sur nos particules de TiO_2 nanocristallines. Cette effet est induit par l'adsorption spécifique du cation lithium sur la surface des particules. Il a des conséquences visibles sur la dynamique de la photoluminescence qui, selon nous, est un mécanisme bénéfique pour la photorecharge de l'électrode.

Un obstacle important au développement d'un système de batterie photorechargeable consiste à trouver une contre-électrode appropriée. Cette électrode doit avoir une absorption optique complémentaire à celle de la photoanode, et en même temps présenter le type opposé de porteurs de charges principaux. Cette contre-électrode doit également posséder une position appropriée de la bande de conduction et de valence par rapport à l'autre électrode afin de collecter les charges photo-induites de l'autre électrode. Pour cette raison, la deuxième partie de cette thèse a été centrée sur la création d'une base de données des propriétés optoélectroniques des matériaux d'électrodes de batterie les plus utilisés afin de déterminer ceux qui présentent des potentialités pour cette application. Cette base de données constitue également un intérêt pour d'autres applications comme l'électrochromisme ou la photocatalyse. Trois familles de matériaux ont été étudiés: les oxydes de métaux de transition ($\text{Li}_4\text{Ti}_5\text{O}_{12}$, LiCoO_2 , MoO_3 , WO_3 , CuO , Bi_2O_3 , $\text{LiMn}_{1/3}\text{Ni}_{1/3}\text{Co}_{1/3}\text{O}_2$), les sulfures de métaux de transition (TiS_2 , MoS_2 , WS_2) et les charpentes polyanioniques (LiFePO_4 , LiMnPO_4 , LiVPO_4F). La caractérisation préliminaire de la structure, de la taille et de la

morphologie des matériaux a été réalisée avant l'étude principale en combinant diffraction des rayons X, microscopie électronique à balayage (SEM) et à transmission (TEM).

En utilisant les mesures de spectroscopie d'absorption UV-visible en mode de réflectance diffuse, les valeurs de bande interdite ont été déterminées à l'aide de la fonction Kubelka-Monk entre 200 et 1800 nm. Cependant, pour une partie des matériaux, aucun phénomène d'absorption n'est visible en raison probablement d'une valeur de bande interdite inférieure à 0,7 eV (LiMn_2O_4 et $\text{LiMn}_{1/3}\text{Co}_{1/3}\text{Ni}_{1/3}\text{O}_2$) ou par la nature semi-métallique du matériau (TiS_2).

Au moyen de la spectroscopie d'impédance électrochimique par la méthode Mott-Schottky, nous avons mesuré le type de conductivité, le potentiel de bande plate et la densité des porteurs de charge des matériaux dans deux types d'électrolyte: aqueux et aprotiques non aqueux à base d'EC/DMC. Trois phénomènes intéressants ont été mis en évidence. Premièrement, pour LiCoO_2 , WS_2 et MoS_2 , un changement du type de semi-conduction a été observé en fonction de la nature de l'électrolyte. En effet, ces matériaux se comportent comme des semi-conducteurs de type n dans un électrolyte aqueux et comme des semi-conducteurs de type p dans un électrolyte aprotique non-aqueux. Pour la majorité des matériaux, i.e. $\text{Li}_4\text{Ti}_5\text{O}_{12}$, MoO_3 , WO_3 , Bi_2O_3 , TiS_2 , MoS_2 , WS_2 , et LiFePO_4 , la conductivité est de type n et est indépendante de la nature de l'électrolyte. Le CuO est de type p et le LiMnPO_4 de type n. Deuxièmement, pour tous les matériaux étudiés à l'exception du MoS_2 , les positions des bords de bandes dépendent fortement de la nature de l'électrolyte. Cependant, aucune tendance systématique n'a pu être dégagée car pour certains matériaux ($\text{Li}_4\text{Ti}_5\text{O}_{12}$, MoO_3 , Bi_2O_3 , WS_2 , LiFePO_4 , and LiMnPO_4) l'énergie des bords de la bande augmente en passant d'un électrolyte aprotique aqueux à un électrolyte non aqueux, au contraire d'autres comme WO_3 et LiCoO_2 où c'est l'inverse qui se passe. Troisièmement, la concentration en porteurs de charge est systématiquement supérieure d'un à deux ordres de grandeur dans une solution aprotique non aqueuse. Nous attribuons ces changements à la nature faiblement dégénérée des semi-conducteurs, dans laquelle la concentration en électrons est comparable à celle des trous. Dans ces matériaux, le caractère donneur ou accepteur, ainsi que le potentiel de la bande plate et la densité des porteurs de charges dépendent de la nature de l'électrolyte lors du processus d'égalisation des niveaux de Fermi du semi-conducteur avec l'électrolyte.

Cette étude a permis d'évaluer les matériaux d'intérêt pour une application comme électrode photo-rechargeable en fonction de la valeur de la bande interdite, du type de conductivité et du

positionnement des bandes. Les résultats ont montré que parmi tous les matériaux, $\text{Li}_4\text{Ti}_5\text{O}_{12}$, MoO_3 , WO_3 , Bi_2O_3 , LiFePO_4 , LiMnPO_4 de types n et LiCoO_2 de type p sont des candidats potentiellement prometteurs. Toutefois, les résultats préliminaires de photo-rechargeabilité de ces matériaux ont toutefois montré que la recherche d'un matériau photorechargeable n'était pas aussi simple qu'attendu. En effet, de nombreux matériaux censés avoir une propriété de photorecharge n'ont pas montré les résultats escomptés pour des raisons encore peu claires. D'une part, la faible performance électrochimique peut être attribuée en partie à la faible conductivité électronique des matériaux purs. D'autre part, les particules utilisées ne sont pas systématiquement aussi divisées que celles du TiO_2 et enfin il est aussi possible pour certains matériaux que les temps de vie des états excités sont trop courts pour permettre un quelconque transfert de charge sous illumination.

Nous nous sommes attardés sur le cas de LiFePO_4 qui ne montre pas d'effet de photo-recharge. Tout d'abord, la première approche a été de réduire la taille des particules et deuxièmement de greffer un colorant (N719) à la surface des particules afin d'accroître l'absorption de lumière. Nos résultats montrent qu'aucune amélioration significative des propriétés photoélectrochimiques n'a été observée dans les nanoparticules de LiFePO_4 . La présence du colorant a augmenté le potentiel de tension ouverte de l'électrode d'un apport mineur de 20 mV ce qui est loin d'être suffisant pour déclencher une réaction de photorécharge. Nous avons également rencontré des difficultés pour désinsérer le lithium de la structure en absence de carbone en raison de la nature isolante du matériau.

Afin de mieux comprendre les mécanismes entravant la photorécharge de LiFePO_4 , nous avons déterminé les positions des bords de la bande de LiFePO_4 et de sa forme chargée FePO_4 obtenue par oxydation chimique. Notre étude montre que la valeur de la bande interdite diminue en fonction de la désinsertion du lithium, passant de 3,31 eV pour LiFePO_4 à 2,73 eV pour la phase délithiée. La conductivité de type n exprimée par FePO_4 est identique à celle de la phase lithiée. Le potentiel de bande plate et les valeurs de densité de donneur ont été déterminés et comparés à ceux de LiFePO_4 . Nous avons établis que les bords des bandes de valence et de conduction se déplacent vers le haut dans l'échelle d'énergie lors de la désinsertion du lithium. Le bord de la bande de conduction de FePO_4 est supérieur de 0,06 eV à celui de LiFePO_4 dans un électrolyte aqueux et de 0,25 eV dans un électrolyte aprotique non aqueux. Les décalages de la bande de valence et de conduction sont respectivement de + 0,64 eV et +0,83 eV. Les positions des bords des bandes de

conduction de LiFePO_4 et FePO_4 montrent que seulement l'injection d'électrons à partir du colorant est possible contrairement à ce qui a été publié récemment par Paolella et al.

Une étude plus approfondie des propriétés photoélectrochimiques de $\text{Li}_4\text{Ti}_5\text{O}_{12}$ a également été entreprise afin d'étudier l'évolution des propriétés optoélectroniques du matériau lors de l'insertion du lithium et l'influence de l'illumination. Dans cette partie de la thèse, nous avons montré la formation d'une couche de dégradation du type SEI qui se forme sur la surface des particules à la suite du cyclage. Son épaisseur est plus importante sous illumination et a priori de nature différente puisque cette dernière sous illumination est exclusivement constituée de LiF qui est composé isolant et qui provient de la dégradation photo-induite du sel de l'électrolyte (LiPF_6). Le cyclage galvanostatique de l'électrode $\text{Li}_4\text{Ti}_5\text{O}_{12}$ dans l'obscurité et sous illumination a montré que la surtension était plus faible sous illumination en raison de la photoconductivité apportée par l'absorption de lumière. D'autre part, l'électrode illuminée présente une polarisation qui augmente plus rapidement en raison de la formation de LiF et qui pénalise le rendement coulombique de l'électrode en cyclage.

Pour étudier l'influence de l'électrolyte sur la cinétique de la recombinaison des charges dans $\text{Li}_4\text{Ti}_5\text{O}_{12}$, une étude de fluorescence résolue en temps a été réalisée. La mesure du comptage à simple photon de l'électrode $\text{Li}_4\text{Ti}_5\text{O}_{12}$ dans un électrolyte 1 mol/L LiPF_6 EC/DMC à a été réalisée sous atmosphère d'argon. Dans ce cas, un déclin de fluorescence plus long a été obtenu par rapport à celui d'une poudre de $\text{Li}_4\text{Ti}_5\text{O}_{12}$. Ceci implique une extinction de la fluorescence de $\text{Li}_4\text{Ti}_5\text{O}_{12}$ au contact de l'électrolyte.

Les valeurs de durée de vie déterminées pour $\text{Li}_4\text{Ti}_5\text{O}_{12}$ en contact avec l'électrolyte, i.e. 0,091 ns et 2,63 ns, sont comparables aux deux premières composantes de durée de vie du déclin de fluorescence de la poudre de $\text{Li}_4\text{Ti}_5\text{O}_{12}$, soit 0,102 ns et 3,00 ns. La troisième composante de durée de vie observée sur la poudre a disparu lorsque le matériau a été mesuré dans l'électrolyte. La redistribution des valeurs de temps de vie vers la composante rapide (73,3% pour l'électrode dans l'électrolyte contre 6,9% pour la poudre) a confirmé l'extinction de la luminescence de $\text{Li}_4\text{Ti}_5\text{O}_{12}$ en présence d'électrolyte. Ceci résulte soit du transfert de charges photo-induites vers l'électrolyte conduisant à sa dégradation et/ou par une fraction plus importante d'un mode de désactivation de l'état excité de manière non radiative.

La carte de fluorescence à l'état d'équilibre de l'électrode de $\text{Li}_4\text{Ti}_5\text{O}_{12}$ dans un électrolyte LiPF_6 EC/DMC à 1 mol/L montre la présence de deux bandes. Une bande d'intensité élevée à une longueur d'onde d'excitation de 333 nm et d'émission de 735 nm, correspond à la fluorescence de $\text{Li}_4\text{Ti}_5\text{O}_{12}$. L'autre, avec une intensité plus faible correspondant à la queue de la photoluminescence de l'électrolyte. Il est également intéressant de noter que la bande d'intensité la plus élevée d'un électrolyte 1 mol/L LiPF_6 EC/DMC disparaît complètement en contact avec $\text{Li}_4\text{Ti}_5\text{O}_{12}$. Ceci s'explique par le transfert d'énergie d'émission de l'électrolyte vers la bande d'excitation de $\text{Li}_4\text{Ti}_5\text{O}_{12}$ (bande d'excitation à 333 nm). Lors de la décharge de l'électrode $\text{Li}_4\text{Ti}_5\text{O}_{12}$ à 1,2 V vs. Li^+/Li , la bande à 728 nm disparaît complètement et elle est également accompagnée par une diminution importante de l'intensité de la bande de fluorescence de l'électrolyte.

L'étude de $\text{Li}_4\text{Ti}_5\text{O}_{12}$ dans l'électrolyte 1 mol/L LiPF_6 EC/DMC par spectroscopie d'absorption UV-visible a été réalisée dans le but de comprendre les modifications optiques du matériau lors de l'insertion du lithium. Pour cela, les spectres de transmittance d'un film de 250 nm d'épaisseur de $\text{Li}_4\text{Ti}_5\text{O}_{12}$ ont été enregistrés *in situ* à différents états de décharge. Les changements importants du spectre de transmission commencent à partir de 1,7 V vs. Li^+/Li qui correspond au potentiel redox du matériau. Ceci se traduit par une diminution significative de la transmittance entre 300 nm et 1500 nm expliquant le changement visuel de la couleur du matériau passant du blanc au bleu foncé. Ce phénomène est attribué à l'absorption des électrons libres photogénérés dans la bande de conduction de $\text{Li}_4\text{Ti}_5\text{O}_{12}$ lors de l'éclairage en analogie directe avec ce qui se passe dans le TiO_2 . Les valeurs de la bande interdite ont été déterminées pour le $\text{Li}_4\text{Ti}_5\text{O}_{12}$ initial (3,48 eV) et sa forme déchargée $\text{Li}_7\text{Ti}_5\text{O}_{12}$ (3,25 eV). La valeur de bande interdite est inférieure de 0,30 eV à celle déterminée sur la poudre en contact avec l'air. Cela implique une diminution de 0,23 eV de la bande interdite de $\text{Li}_4\text{Ti}_5\text{O}_{12}$ lors de l'insertion du lithium dans la structure. Le rétrécissement de la bande interdite est attribué au remplissage des niveaux d'énergie inférieurs proches de la bande de conduction, provoqué par l'apparition de Ti^{3+} ($4s^0 3d^1$) dans la structure.

Les mesures Mott-Schottky réalisées *in situ* ont montré que le potentiel de bande plate de $\text{Li}_4\text{Ti}_5\text{O}_{12}$ est de 1,76 V vs. Li^+/Li et augmente de 1,69 V lors de l'insertion de lithium. L'insertion de lithium conduit également à une augmentation faible de la concentration en porteurs de charge passant de $2,9 \cdot 10^{19} \text{ cm}^{-3}$ à $3,4 \cdot 10^{19} \text{ cm}^{-3}$.

Les résultats préliminaires qui ne sont pas rapportés dans ce manuscrit montrent que l'inclusion d'un piègeur non sélectif de radicaux dans l'électrolyte montrent une considérable amélioration des performances de l'électrode en capacité et en réversibilité sans moyen de carbone. D'autre part, l'ajout de cette molécule permet de déverrouiller la barrière de photorecharge. En conséquence, une électrode en $\text{Li}_7\text{Ti}_5\text{O}_{12}$ peut être complètement photo-rechargée en 15 heures environ sous conditions d'éclairage standardisée (A.M. 1.5G, 100 mW/cm^2) avec une capacité d'environ $500 \mu\text{Ah/cm}^2$. Un brevet pour la molécule incluse dans l'électrolyte est en cours de remplissage. Nous émettons l'hypothèse qu'une fonction de cette molécule est de piéger les radicaux fluorés avant que ceux-ci réagissent pour former du LiF à la surface des particules, même s'il est nécessaire d'approfondir des mécanismes liant cette molécule à la photo-recharge et la dégradation de l'électrolyte.

Ce travail est pionnier dans un sujet complexe où l'on tente de combiner la fonction de conversion de l'énergie lumineuse avec celle du stockage électrochimique de cette énergie, ceci à l'échelle de l'électrode et de la molécule. Ce travail apporte une brique complémentaire aux choix possibles des matériaux. Toutefois elle laisse aussi place à un certain nombre de zones d'ombres qui nécessitent de nouvelles recherches plus approfondies, en particulier dans le domaine de la chimie douce pour concevoir des matériaux nanostructurés d'une part et d'autre part sur la spectroscopie résolue en temps en absorption et en émission. Dans notre laboratoire, l'installation de la spectroscopie d'absorption transitoire en régime picoseconde avec caméra Streak est finalisée, ce qui doit permettre d'étudier plus en profondeur la cinétique du transfert de charge photogénéré dans les électrodes seules et au contact de l'électrolyte. D'autres outils sont également en cours d'installation comme la photo-luminescence en associant une caméra streak avec un laser Ti:Sa qui permettra de descendre à une résolution temporelle de l'ordre de 5 ps et à la spectroscopie de fluorescence par up conversion permettant d'obtenir une résolution temporelle de l'ordre de 200 fs. L'établissement de la chronologie des processus dans le système permettra de reconnaître les processus limitants et offrira la possibilité d'améliorer les performances et la stabilité des cellules en guidant les expérimentalistes vers des orientations précises.

Comme il est mentionné dans le manuscrit, ce travail a souvent été confronté à un manque de données et d'observables de la littérature. Cependant, les résultats de ces travaux ouvrent à de nombreuses perspectives qui seront poursuivies au laboratoire pour continuer au développement de ces systèmes. Ce travail de thèse constitue une première démarche raisonnée dans la recherche

d'autres matériaux et d'une contre-électrode appropriée pour une photoanode de TiO_2 qui permettra de collecter les électrons photo-induits. Ceci ouvrira la voie vers une photo-batterie complète et régénérative. Enfin, il est également important de souligner que ce travail de thèse est aussi profitable pour d'autres applications telles que la photocatalyse, le stockage d'informations optiques, les dispositifs électrochromiques, etc...

Appendix

Table I. X-ray diffraction analysis results.

Material	Structure	Space group	Cell parameters						
			a	b	c	alpha	betha	gamma	Z
Li₄Ti₅O₁₂	face-centeredcubic	Fd-3m	8.3588(3)	8.3588(3)	8.3588(3)	90	90	90	-
LiCoO₂	rhomboherdal	R-3m	2.8149(3)	2.8149(3)	14.050(51)	90	90	120	-
MoO₃	face-centeredcubic	Fd-3m	13.825(8)	3.694(6)	3.954(6)	90	90	90	3
WO₃	orthorhombic	Pnma	7.300(6)	7.538(6)	7.689(6)	90	90.89	90	8
CuO	monoclinic	P21/n	4.690(8)	3.420(16)	5.131(3)	90	99.54	90	4
Bi₂O₃	base-centeredmonoclinic	C2/c	7.739(1)	7.739(1)	5.636(1)	90	90	90	8
LiMn₂O₄	tetragonal	P-421c	8.238(3)	8.2404(2)	8.2404(2)	90	90	90	4
LiMn_{1/3}Ni_{1/3}Co_{1/3}O₂	rhomboherdal	R-3m	2.859(2)	2.859(2)	14.155(9)	90	90	120	4
TiS₂	hexagonal	P-3m1	3.407(3)	3.407(3)	5.695(6)	90	90	120	3
MoS₂	hexagonal (β-MoS ₂)	P63/mmc	3.160(7)	3.160(7)	12.294(9)	90	90	120	1
WS₂	hexagonal	P63/mmc	3.154(5)	3.154(5)	12.362(12)	90	90	120	2
LiFePO₄	orthorhombic	Pnma	10.332(9)	6.0189(3)	4.704(5)	90	90	90	2
LiMnPO₄	orthorhombic	Pmnb	10.460(9)	6.100(6)	4.744(5)	90	90	90	4
LiVPO₄F	triclinic (tavorite structure)	P-1	5.168(4)	5.309(8)	7.263(6)	107.599	108.02	98.336	4

Table II. UV-visible absorption spectroscopy results. Band gap values determined from the Tauc plot of diffuse reflectance spectra using Kubelka-Munk function.

Material	Band gap, eV	Transition
TiO ₂	3.24	indirect allowed
Li ₄ Ti ₅ O ₁₂	3.79	indirect allowed
LiCoO ₂	0.79	indirect allowed
MoO ₃	2.93	indirect allowed
WO ₃	2.49	indirect allowed
CuO	1.19	indirect allowed
Bi ₂ O ₃	2.12	direct allowed
LiMn ₂ O ₄	-	-
LiMn _{1/3} Ni _{1/3} Co _{1/3} O ₂	-	-
TiS ₂	-	-
MoS ₂	1.52	indirect allowed
WS ₂	0.82	indirect allowed
LiFePO ₄	3.11	direct allowed
LiMnPO ₄	3.93	direct allowed
LiVPO ₄ F	1.71	direct allowed

Table III. Comparison of conductivity type, flat band potential, and charge carrier concentration derived from Mott-Schottky measurements with values reported in literature for transition metal oxides, transition metal sulfides, and lithiated polyanions.

Material	Aqueous media							Non-aqueousaprotic media			
	Mott-Schottky measurements			Literature				Mott-Schottky measurements			Literature
	Ty pe	V_{fb} , V vs NHE*	N_d/N_a , cm^{-3}	Ty pe	V_{fb} , V vs NHE	N_d/N_a	Ref.	Ty pe	V_{fb} , V vs NHE	N_d/N_a , cm^{-3}	Data - Ref.
TiO ₂	n	-0.63	$9.8 \cdot 10^{17}$	n	-0.8 to 0.26 * -1.6 to -0.57 *	10^{17} to 10^{20}	[1-12]	n	-0.20	$2.3 \cdot 10^{19}$	n-type; V_{fb} from -2.1 to -0.88 V* [49-51]
Li ₄ Ti ₅ O ₁₂	n	-0.76	$2.7 \cdot 10^{18}$	n	-1.13 *	-	[13]	n	-1.34	$6.9 \cdot 10^{19}$	Not reported
LiCoO ₂	n	-0.72	$4.9 \cdot 10^{19}$	-	-	-	-	p	+1.24	$2.6 \cdot 10^{20}$	p-type; 10^{20} [52-54]
MoO ₃	n	-0.08	$4.1 \cdot 10^{18}$	n	-2.2V to +2.3	10^{20}	[14-20]	n	-0.26	$1.2 \cdot 10^{20}$	Not reported
WO ₃	n	-0.46	$1.4 \cdot 10^{18}$	n	-0.59 to -0.22 *	10^{19} to 10^{20}	[21-24]	n	0.03	$2.8 \cdot 10^{19}$	Not reported
CuO	-	-	-	p	-1.33 to -0.60 *	10^{18} to 10^{21}	[2], [3], [25-28]	p	+0.60	$2.7 \cdot 10^{19}$	Not reported
Bi ₂ O ₃	n	-0.66	$9.9 \cdot 10^{17}$	n	-0.67 to +0.03 *	10^{16} to 10^{18}	[2], [29-32]	n	-0.77	$3.3 \cdot 10^{19}$	Not reported
TiS ₂	n	-0.62	$4.2 \cdot 10^{18}$	n	-	10^{20}	[33-37]	n	-1.18	$6.9 \cdot 10^{19}$	Not reported
MoS ₂	n	-0.51	$3.0 \cdot 10^{18}$	n p	-0.23 to -0.54 -	10^{19} 10^{17} to 10^{20}	[4], [38-39] [40-42]	p	+1.01	$4.0 \cdot 10^{19}$	Not reported
WS ₂	n	-0.48	$4.2 \cdot 10^{18}$	n p	-1.60 to -1.23 -0.43 to +0.37	10^{17} to 10^{20} 10^{17}	[43-48]	p	+0.15	$1.8 \cdot 10^{20}$	Not reported
LiFePO ₄	n	-0.53	$1.9 \cdot 10^{19}$	-	-	-	-	n	-0.58	$3.9 \cdot 10^{20}$	Not reported
LiMnPO ₄	-	-	-	-	-	-	-	n	-1.12	$6.6 \cdot 10^{20}$	Not reported

* Corrected to pH = 14

Notes: [1] = Schultze and Lohrengel 2000; [2] = Hardee and Bard 1977; [3] = Nozik 1978; [4] = Xu and Schoonen 2000; [5] = Butler and Ginley 1978; [6] = Kavan et al. 1996; [7] = Cao et al. 1995; [8] = Hengerer et al. 2000; [9] = Cameron and Peter 2003; [10] = O'Hayre et al. 2007; [11] = Tomkiewicz 1979; [12] = Redmond and Fitzmaurice 1993; [13] = Ge et al. 2015; [14] = Tong et al.; [15] = Meyer et al. 2011; [16] = Bernède et al. 2012; [17] = Kroger et al. 2009; [18] = Greiner et al. 2010; [19] = Nadkarni et al. 1970; [20] = Nadkarni et al. 1972; [21] = Wang et al. 2012 (*Energy Environ. Sci.*); [22] = Patil and Patil 1994; [23] = Gissler and Memming 1977; [24] = Wang et al. 1912 (*J. Alloys. Compd.*); [25] = Jeong et al. 1996; [26] = Koffyberg and Benko 1982; [27] = Nakaoka et al. 2004; [28] = Chiang et al. 2011; [29] = Chitrada and Raja 2014 (*ECS Trans.*, 61, 1); [30] = Chitrada and Raja 2014 (*ECS Trans.*, 61, 55); [31] = Chitrada et al. 2015; [32] = Hajra et al. 2014; [33] = McKelvy et al. 1987; [34] = Imai et al. 2001; [35] = Bronsema et al. 1986; [36] = Umnigar et al. 1982; [37] = Myron et al. 1974; [38] = Anand 2009; [39] Schneemeyer and Wringhton 1979; [40] = Guo et al. 2014; [41] = Bissessur et al. 1993; [42] = Heising et al. 1999; [43] = Bassaid et al. 2015; [44] = Tonti et al. 1997; [45] = Baglio et al. 1983; [46] = Devadasan et al. 2001; [47] = Morrish et al. 2014; [48] = Jäger-Waldau et al. 1994; [49] = Kabir-ud-Din et al. 1981; [50] = Heinzl et al. 1981; [51] = Schumacher et al. 1982; [52] = Rosolen & Decker 2001; [53] = Menetrier et al. 1999; [54] = Mizutani et al. 2008;

Table IV. Mott-Schottky measurements details and conditions.

Material		Aqueous protic media (measured vs SCE)			Non-aqueous aprotic media (measured vs Li QRE, stable vs Fc^+/Fc)		Dielectric constant in calculations	
Name	Film thickness, μm	Solution, atmosphere	pH	f, kHz	Solution, atmosphere	f, kHz	ϵ	Ref
TiO ₂	3	1M NaOHaq., air	14.00	0.75	1M TBAPF ₆ EC/DMC, Ar	0.1	31	[1]
Li ₄ Ti ₅ O ₁₂	12	1M NaOHaq., air	14.00	0.25		0.2	20	[2-3]
LiCoO ₂	18	0.5M TBANO ₃ aq., air	1.65	0.10		0.1	2	[4-5]
MoO ₃	13	0.5M TBANO ₃ aq., air	8.84	0.25		0.2	6	[6]
WO ₃	5	0.5M TBANO ₃ aq., air	1.65	0.25		0.1	20	[7]
CuO	3	-	-	-		0.3	10	[8]
Bi ₂ O ₃	5	1M NaOHaq., air	14.00	0.50		0.5	32	[9]
TiS ₂	12	0.5M TBANO ₃ aq., air	3.45	0.50		0.5	15	assumed
MoS ₂	4	1M NaOHaq., air	14.00	0.10		0.1	11	[10-12]
WS ₂	4	1M NaOHaq., air	14.00	0.10		0.1	8	[13]
LiFePO ₄	80	0.5M TBANO ₃ aq., air	1.65	0.25		0.1	3	[14]
LiMnPO ₄	5	-	-	-		0.1	3	assumed

Notes: [1] = Roberts 1949; [2] = Zhang et al. 2016; [3] = Liu et al. 2016; [4] = Nageswara Rao et al. 2014; [5] = Khatun et al. 2014; [6] = Lajaunie et al. 2013; [7] = Wang et al. 2012; [8] = Nakaoka et al. 2004; [9] = Kang et al. 2004; [10] = Reshak et al. 2003; [11] = Cheiwchanchamnangij et al. 1983; [12] = Molina-Sánchez et al. 2011; [13] = Bassaid et al. 2015; [14] = Bharathi et al. 2013.

Résumé

Le problème de la nature intermittente de l'énergie solaire est souvent résolu par le couplage traditionnel des unités PV et batterie. Notre approche plus fondamentale vise le développement de matériaux capables de combiner la conversion et le stockage de l'énergie solaire au niveau moléculaire. Les nanocristaux de TiO₂ d'anatase à 5 nm ont été synthétisés dans notre groupe, ce qui a permis une réaction quantitative de photorecharge par la seule contribution de l'illumination. Nous présentons ici une étude de l'évolution des propriétés optoélectroniques et de la dynamique du transfert de charge dans une électrode de TiO₂ à l'aide d'expériences *in situ / in operando* effectuées pendant le fonctionnement de la batterie (spectroscopies de UV-visible, Mott-Schottky, fluorescence). L'augmentation de la valeur de la bande interdite et de l'absorbance a été observée lors de l'insertion du lithium dans TiO₂. Un décalage négatif en énergie de la bande de conduction indique un potentiel plus oxydant des trous photogénérés dans le Li_{0.6}TiO₂ par rapport au TiO₂ initial. En analysant les processus de recombinaison dans Li_{0.6}TiO₂, nous avons établi une compétition entre les processus ultra-rapides (gamme ps) de recombinaison directe et de transfert de charge vers Ti³⁺ dans Li_{0.6}TiO₂, ce qui limite potentiellement le rendement de la réaction de photorecharge. Cette étude a été étendue à d'autres matériaux d'insertion généralement utilisés dans les batteries lithium-ion (Li₄Ti₅O₁₂, LiCoO₂, LiFePO₄, MoO₃, etc.). Les positions de bord de bande, la bande interdite, le type de porteurs de charge et leur concentration ont été mesurées et rassemblées dans une base de données. Basé sur ces résultats, la possibilité de photorecharge induite par la lumière a été évaluée et les premiers résultats discutés.

Mots-clés: photo-électrode, battery photo-rechargeable, photoelectrochimie, matériaux d'insertion, propriétés optoélectroniques, Mott-Schottky, photoluminescence, bande interdite

Abstract

The problem of intermittent nature of solar energy is often addressed by the traditional coupling of the PV and battery units. Our more fundamental approach targets the development of materials able to combine solar energy conversion and storage at the molecular level. The 5 nm anatase TiO₂ nanocrystals were synthesized in our group affording a quantitative photorecharge reaction by a sole contribution of illumination. Here, we present a study of the evolution of the optoelectronic properties and dynamics of charge transfer in TiO₂ electrode using *in situ / in operando* experiments performed during the battery functioning (UV-visible, Mott-Schottky, fluorescence spectroscopy). The increase of the bandgap value and the rise of absorbance are observed upon lithium insertion into TiO₂. A negative shift of the conduction band indicates a more oxidizing potential of the photogenerated holes in Li_{0.6}TiO₂ compared to TiO₂. By analysis of the recombination processes in TiO₂ upon lithium insertion, we established a competition of the ultra-fast (ps range) processes of direct recombination and charge transfer towards Ti³⁺ in Li_{0.6}TiO₂, potentially limiting the yield of the photorecharge reaction. This study was extended to other insertion materials typically used in lithium-ion batteries (Li₄Ti₅O₁₂, LiCoO₂, LiFePO₄, MoO₃, etc.). The measured band edge positions, band gap, charge carrier type and concentration were gathered into a database, based on which the fundamental evaluation of the possibility of the light-induced photorecharge was conducted. The first results of the photoelectrochemical study of chosen materials are also discussed.

Key-words: photoelectrode, photorechargeable battery, photoelectrochemistry, insertion materials, optoelectronic properties, Mott-Schottky, photoluminescence, band gap